# Towards CYGNUS-UK: Developments in Negative Ion Charge Amplification and Readout Technologies for Directional Dark Matter Detection

**Alasdair Gregor McLean**

Department of Physics & Astronomy
University of Sheffield

A thesis submitted in partial fulfilment for the degree of
*Doctor of Philosophy*

December 2024

I would like to dedicate this thesis to my friend Robert Earls (1997 - 2021)

# Abstract

Dark Matter (DM) is known to constitute the majority of mass in the Universe; however, its true particle nature remains a mystery. Particles in the Standard Model (SM) are not considered viable candidates for DM and thus alternatives must be pursued. The prevalence of one well motivated particle candidate called a Weakly Interacting Massive Particle (WIMP) could explain the observed influence of DM. Two-phase Time Projection Chambers (TPCs), using liquid and gaseous xenon, currently lead the direct search for rare WIMP-nucleon scattering events. The sensitivity of these experiments has improved by several orders of magnitude since their inception and are now faced with a new irreducible background of neutrinos, predominantly produced by processes in the Sun. However, the most viable method for irrefutably identifying a WIMP-induced signal, particularly in light of this neutrino background, is the directional measurement of recoiling nuclei; an approach which is not feasible with conventional two-phase experiments.

There are several detector technologies capable of directional detection; however, low pressure gaseous TPCs are the most developed and widely used. Previous directional searches like the Directional Recoil Identification From Tracks (DRIFT) experiment have established the groundwork for the next generation of directional searches, like that of the CYGNUS and CYGNO collaborations, by pioneering the fundamental principles of operation. These collaborations are largely in a phase of small scale research and development aiming to identify optimal technologies for a global network of nuclear recoil observatories. Major avenues for research include: the investigation of helium gas mixtures capable of more cost-effective atmospheric operation, which ideally possess Negative Ion Drift (NID) characteristics for high-fidelity event reconstruction; innovative gain stage devices, which are capable of producing large charge amplification in NID gases comparable to conventional gases; high-granularity charge readout technologies, which can improve the event reconstruction resolution compared to previous technologies used by DRIFT; and new scalable charge readout and data acquisition systems, which can handle the increased number of readout channels associated with high-granularity technologies.

In this thesis, significant developments towards these major research goals are presented. Charge amplification on the order of $10^4$ was successfully demonstrated in $CF_4$:He mixtures, which prioritised directional potential, at low and atmospheric pressures with a single Thick Gaseous Electron Multiplier (ThGEM) for the first time. Significant work with a novel multi-stage Multi-Mesh ThGEM (MMThGEM) demonstrated large charge amplification on the order of $10^4$ in an NID gas, low pressure $SF_6$, for the first time. The MMThGEM also showed promise for $SF_6$:He mixtures, demonstrating large $10^4$ gas gains up to 100 Torr. This device was then coupled to a high-granularity micromegas detector and demonstrated high gain of order $10^5$ in low pressure $SF_6$; constituting a gas gain in an NID gas which is an improvement of 2 orders of magnitude. This detector was also used to demonstrate 2-dimensional nuclear recoil detection in a large 1 $m^3$ volume of low pressure $SF_6$, with 32 channels, for the first time. Subsequent efforts focussed on scaling up the readout electronics and demonstration of full area instrumentation of the micromegas readout plane. This featured a comparison with alternative micromegas designs, and the first novel operation of the scalable readout system in low pressure pure $CF_4$. Ultimately, the results presented in this thesis successfully demonstrate order of magnitude improvements in the gas pressure of mixtures with directional potential, charge amplification in NID gases, and the granularity of charge measurements compared to the technologies utilised by the DRIFT experiments.

# Acknowledgements

I would like to acknowledge and express gratitude to my supervisor **Neil Spooner** for his guidance and support throughout my time at the University of Sheffield. I am grateful to **Tom Crane** and **AWE** for the opportunity and funding, without which I would not have been able to undertake this research project.

I would also like to thank past and present members of the local CYGNUS-DRIFT group including **Anthony Ezeribe**, **Andrew Scarff**, and **Callum Eldridge** for their support and guidance. A special thanks is expressed to **Robert Renz Marcelo Gregorio** for the productive conversations in the laboratory and your continued friendship. Thank you also to **Lan Nguyen** for your friendship, support, and the necessary fried chicken lunch breaks.

My thanks are extended to our international research partners from both the **CYGNUS** and **CYGNO collaborations**. I wish to thank Kentaro Miuchi, Satoshi Higashino, Dinesh Loomba, Gregory Lane, Lindsey Bignell, Ferdos Dastgiri, Lachlan McKie, Elisabetta Baracchini, Giorgio Dho, Cyprien Beaufort, Sven Vahsen, Majd Ghrear, and Hima Korandla for the invaluable support, insightful conversations, and kind hospitality you have shown me within an academic setting and beyond.

Finally, I would like to express my heartfelt gratitude to my friends and family. To my parents, **Wendy** and **Alan**, for your unwavering support which has helped me achieve more than I ever thought possible. Last, but by no means least, I would like to thank my partner **Lizze** for proofreading countless draft papers and chapters, supporting me throughout this process, and brightening up my every day.

# Author's Contributions

## Chapter 3 (publication)[1]

*Charge amplification in sub-atmospheric $CF_4$:He mixtures for directional dark matter searches, (2024) JINST* **19** P04038

The author constructed the experimental setup, based on previous work by A. Scarff, and designed the gas mixing procedure used prior to measuring the avalanche gain in low pressure and atmospheric mixtures of $CF_4$:He. Data acquisition was carried out by the author and code, supplied by R.R.M. Gregorio, was adapted for the gain and energy resolution analysis. Data analysis and interpretation of results was completed by the author. The author prepared the manuscript for publication and the co-authors reviewed the article before submission to the journal.

## Chapter 4 (publication)[1]

*Gas gains over $10^4$ and optimisation using $^{55}$Fe X-rays in low pressure $SF_6$ with a novel Multi-Mesh ThGEM for directional dark matter searches, (2024) JINST* **19** P03001

The author assembled the experimental setup, based on previous work carried out by C. Eldridge, and designed the optimisation study for maximising the gas gain produced by the MMThGEM in low pressure $SF_6$. The author wrote labview code for the data acquisition procedure, which utilised the signal integration method used previously by A. Scarff and C. Eldridge, and carried out all data acquisition. The analysis and interpretation of results was performed by the author, who adapted code supplied by R.R.M. Gregorio for the gain and energy resolution determinations. The author prepared the manuscript for publication and the co-authors reviewed the article before submission to the journal.

---

[1] This chapter was originally prepared as a manuscript for publication. It is therefore presented in line with the University of Sheffield guidelines regarding how to include published work in a thesis.

### Chapter 5

The author wrote python code to calculate and analyse the rise time of preamplifier pulses in $CF_4$ and $SF_6$ collected in Chapter 4. The author performed analysis of the pile-up probability calculation based on suggestions made by D. Loomba. The author conceptualised and wrote the root code for a comparative study between preamplifier rise times and simulated recoil ranges in DEGRAD, for which the author also wrote the input cards. The author identified and analysed the differences in the effective electronic gain produced by different methods in both $CF_4$ and $SF_6$, using python code written by the author, which was used to validate the signal integral method used in Chapter 4. The author wrote python code which implemented the deconvolution algorithm, suggested by C. Beaufort, used in this comparison.

### Chapter 6 (publication)[1]

*Charge amplification in low pressure $CF_4$:$SF_6$:He mixtures with a multi-mesh ThGEM for directional dark matter searches (2024) JINST* **19** P06021

The author applied the gas mixing procedure, developed for work presented in Chapter 3, to the experimental setup, constructed for work presented in Chapter 4, to measure the charge amplification produced by the MMThGEM in $SF_6$:He and $CF_4$:$SF_6$:He mixtures. The data collection, analysis, and interpretation of results was performed by the author using labview code written by the author and python code adapted from R.R.M. Gregorio. The manuscript was prepared by the author and reviewed by the CYGNO collaboration before publication.

### Chapter 7

The author organised the visit to Kobe University, with the assistance of N.J.C Spooner and R.R.M. Gregorio, through several meetings with K. Miuchi and S. Higashino held prior to the measurement campaign. The author optimised and constructed the coupled MMThGEM-Micromegas TPC, based on previous work performed by C. Eldridge and the optimisation performed in Chapter 4, inside the Kobe test vessel. The author performed the calibration, data acquisition, and data analysis which included the adaptation of code supplied by S. Higashino. The author hypothesised the origin of the charge discontinuity of tracks as the hole pitch of the MMThGEM and wrote root and python code which tested this hypothesis. A "Total Linear Regression" algorithm for 2-dimensional track reconstruction was developed and implemented in root code by the author. The author installed the detector in the BENTO vessel with the assistance of S. Higashino. SRIM and SREM simulations of electron and nuclear recoils were performed by the author as a method of identifying nuclear recoils in the BENTO vessel. The author analysed and interpreted the events in the BENTO vessel.

### Chapter 8

The author proposed and organised the research campaign at the University of Hawaii, through regular meetings with S. Vahsen and M. Ghrear prior to the visit. The author prepared the micromegas for compatible operation in an atmospheric vessel. The author identified and subsequently assisted in troubleshooting instabilities in the gas purity of the gas system. The author identified and resolved systematic errors experienced with the calibration equipment used at the University of Hawaii laboratory, which improved the accuracy of gain measurements. The author led the measurements collected on the mesh of the micromegas detectors. The author also participated in the collection of measurements on the strip electrodes by assembly of the experimental setup, troubleshooting noise issues and generation of the strip mapping file used during data acquisition and analysis. The author adapted python code written by R.R.M. Gregorio to perform and interpret the analysis of the measurements on the mesh. Analysis of the measurements collected on the micromegas strips was performed with the help of jupyter notebooks supplied by M. Ghrear, as well as root and python code written by the author.

### Chapter 9

The author identified the thermal challenges associated with operating the SRS system under low pressure conditions. The author designed and constructed the experimental setup used to test the options for thermal management of the chips in a novel low pressure environment. The author performed the data collection and wrote python code to determine the equilibrium temperature of the VMM chips. The author designed and assembled the experimental setup used to test the SRS electronics with the micromegas in low pressure $CF_4$ including the construction of a custom feedthrough, for VMM communications, with available materials in the laboratory. The author performed the data collection of measurements on the micromegas mesh and strips using python code adapted from R.R.M. Gregorio and root code written by the author. All data analysis and interpretation of results was conducted by the author.

### Other Contributions

The author has been an active contributor to the CYGNO and CYGNUS collaborations; attended monthly meetings, contributed towards several papers, and presented talks at five international conferences. The author supervised an MSc student, S. Wan, and performed all experimental radon emanation measurements for the project. The author visited Boulby Underground Laboratory to perform work related to the DRIFT experiment. The author also taught undergraduate laboratory students over two academic semesters.

# Contents

# List of Figures

# List of Tables

# Chapter 1

# The Search for Dark Matter WIMPs

Dark Matter (DM) is one of the greatest mysteries in modern physics today. This chapter will begin, in Section 1.1, by providing a brief historical overview of the evidence for DM in the Universe. This evidence motivates the search for possible candidate particles, including Weakly Interacting Massive Particles (WIMPs), which are discussed in Section 1.2. Finally, the method of direct detection is presented along with the status and limitations of current leading conventional detector technologies in Section 1.3, followed by some conclusions in Section 1.4.

## 1.1 Evidence for Dark Matter in the Universe

There is overwhelming evidence for the existence of DM in the Universe [1]. Much of this evidence has come from observations of its apparent gravitational influence. In this section, some of the major results which have motivated the modern search for DM are presented.

### 1.1.1 The Motion of Gravitationally Bound Galaxy Clusters

The first acknowledgement of DM was recorded by Fritz Zwicky in 1933 [2]. Zwicky coined the german name "dunkle Materie" for DM when he noted a large discrepancy between the expected amount of matter, from calculations using the virial theorem, and the observed luminous matter in the Coma cluster [3]. When applied to a galaxy cluster, the virial theorem states that the kinetic energy is equal and opposite to half the gravitational potential energy of the bound system, such that:

$$E_{KE} = -\frac{1}{2}E_{GPE}, \tag{1.1}$$

where the kinetic energy and gravitational potential energy are given respectively by:

$$E_{KE} = \frac{1}{2}M\langle v^2\rangle, \tag{1.2}$$

$$E_{GPE} = -\frac{3GM^2}{5R}. \tag{1.3}$$

Here $M$ is the mass of the cluster, $\langle v^2\rangle$ is the average square velocity obtained from measurements of red shifted light, $G$ is the gravitational constant, and $R$ is the radius of the cluster. By substituting into Equation 1.1 and rearranging for mass, the following relation can be deduced:

$$M = \frac{5\langle v^2\rangle R}{3G}. \tag{1.4}$$

When this relation was applied to the Coma cluster, Zwicky calculated a mass of $4.5 \times 10^{13} M_{\odot}$, $\approx$ 500 times larger than the mass he derived from observations of the luminous matter, via the mass-luminosity relationship [4]. This disparity lead Zwicky to believe that there must be a substantial amount of non-luminous matter in the cluster; numerous subsequent measurements have confirmed this significant discrepancy which strongly supported his conclusion [5]. Although this finding is regarded as the first gravitational measurement of DM, the significance of this result was generally ignored until 1970.

### 1.1.2 Flat Galactic Rotation Curves

In 1970, Vera Rubin and Kent Ford presented observations of the rotational velocities of objects in the Andromeda Galaxy as a function of radius from the galactic centre [6]. The results of the study were surprising as they did not follow Kepler's well established third law of orbital motion.

Under Kepler's third law, orbiting bodies are predicted to move with rotational velocities which are inversely proportional to the square root of the radial distance to the galactic centre, $v \propto r^{-\frac{1}{2}}$. This means that the orbital velocity decreases with increasing distance from the centre. However, the rotational velocity curves measured by Rubin and Ford showed distinctly flat rotation curves out to large radii. This result implies that there is a significant amount of matter at large radial distances which is not explained by the visible matter in the galaxy. Furthermore, this suggests that $M(r) \propto r$ and can be explained by a spherical distribution of mass, which has a density $\rho(r) \propto r^{-2}$, known as a DM halo. Although these findings were initially surprising, measurements of flat galactic rotation curves have since become very common, particularly in spiral galaxies [7].

An example of a flat rotation curve measured for the NGC 6503 dwarf spiral galaxy can be seen in Figure 1.1 [8]. This graph shows the velocity as a function of radial distance from the galactic centre. The observations are given by the data points with error bars. The dashed line shows the theoretical expectation from the luminous matter in the galaxy which follows an inverse relationship with $r$. The other contributions are from gas clouds, given by the dotted line, and a theoretical contribution from a DM halo, which is given by the dot-dashed line. The solid line in Figure 1.1 represents the sum of the three contributions to the measured velocity and agrees well with the experimental measurements.

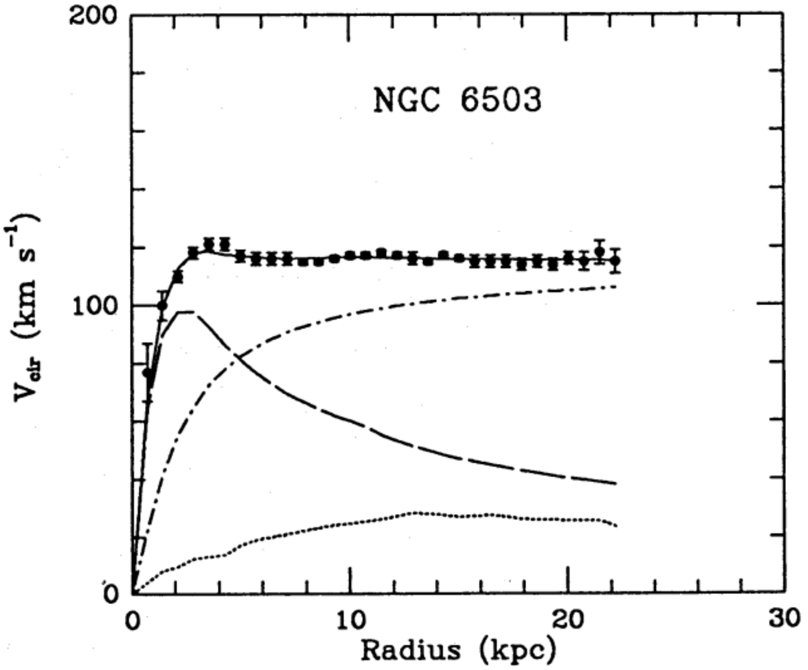

Figure 1.1 The galactic rotation curve for the NGC 6503 dwarf spiral galaxy showing the Keplarian expectation for the amount of observed visible matter (dashed line), contribution from gas clouds (dotted line), contribution of a dark matter halo (dot-dashed line), and the combined sum (solid line) [8].

Typically, the total mass of DM which can be deduced from flat rotation curves significantly outweighs the luminous matter. Modern measurements of galactic rotation curves continue to elude to large DM mass fractions > 90% [9]. Furthermore, rotation velocities measured in the Milky Way estimate a galactic DM fraction of 95% with a local density of 0.30 ± 0.03 GeV/cm$^3$ around Earth [10].

### 1.1.3 Modified Newtonian Dynamics

Modifed Newtownian Dynamics (MOND) was proposed originally in 1983 by Mordehai Milgrom as an alternative explanation for the peculiar shape of the galactic rotation curves, which did not evoke the existence of DM [11–13]. MOND fundamentally questions our understanding of gravitationally bound systems by proposing that:

$$F = m\mu(x)a, \tag{1.5}$$

where the introduction of the parameter in the standard case:

$$\mu(x) = \frac{x}{\sqrt{1+x^2}}, \quad x \equiv a/a_0, \tag{1.6}$$

depends on the acceleration of a test particle, $a$, and an acceleration constant, $a_0$, determined to be $\sim 1.21 \times 10^{-8}$ cm/s$^2$ [8]. Equation 1.5 returns to Newton's second law of motion in cases where $a >> a_0$, i.e. $\mu = 1$ at small radial distances where the acceleration is largest. On the other hand when $a$ is small, i.e. for objects with large radial distances from the galactic centre, this modified equation takes effect and has been used to explain flat rotation curves [8].

Despite presenting as a plausible explanation for the flat rotation curves, MOND is not widely accepted in favour of a DM halo theory. This is because MOND is not consistent with other significant observations from gravitational lensing measurements, discussed in the following subsection. Additionally, some galaxies have recently been discovered with an absence of DM; this finding provides paradoxical evidence favouring a DM solution as this is an impossibility under MOND [14–16]. However, the relevance of modified dynamics is still strongly debated, recent separate analyses of wide binaries from the same Gaia data set have drawn opposing conclusions to high levels of confidence [17, 18] whilst other theories even advocate for hybrid MOND-DM scenarios [19].

### 1.1.4 Gravitational Lensing and the Bullet Cluster

In contrast to MOND, Einstein's well established theory of General Relativity (GR) [20] provides the most complete understanding of gravity to date and still withstands scrutiny. Predictions from GR were most recently validated by the LIGO (Laser Interferometer Gravitational-wave Observatory) experiment via the measurement of distortions in space-time created by merging black holes [21–24]. The bending of space-time caused by massive celestial objects can also distort the path of photons. This phenomenon is known as gravitational lensing and the extent of the lensing can be used to determine the mass of the body inducing the effect [25, 26].

Strong lensing is the most obvious flavour of gravitational lensing and is observed as luminous arcs or Einstein rings when photons, emitted from a distant object, pass by large galaxy-sized objects in the line of sight of the observer on Earth [25–28]. A few examples of galaxy-scale lenses with differing luminous background sources can be seen in Figure 1.2 [27]. The radius of the Einstein ring is proportional to the amount of mass, including the amount of DM, contained within the lensing object [26].

Figure 1.2 False colour examples of galaxy-scale strong lenses with background sources of galaxies, quasar systems, and supernovae from left to right [27].

Weak lensing is a more common phenomena in the night sky, as the majority of photons reaching Earth do not pass by a strong lense. This is observed as more subtle magnifications and elliptical distortions known as shear [29]. Analysis utilising both strong and weak lensing regimes has been able to determine that the mass distribution within galaxies is consistent with an isothermal density profile ($\rho(r) \propto r^{-2}$) in agreement with DM halo predictions associated with the flat rotation curves [30].

Further gravitational lensing measurements of merging galaxy clusters have been able to determine that the majority of matter contained within the clusters is non-baryonic [31–34]. The most famous of which is credited to weak lensing analysis of the merging galaxy cluster 1E 0657–558, also known as the Bullet cluster, which has provided further compelling evidence for the existence of DM [31, 32]. The two galaxy clusters, which make up the Bullet cluster, collided with each other approximately $10^8$ years ago and the remnants of the collision can be seen in Figure 1.3. This figure shows the weak lensing measurements of the mass density as green contour lines superimposed on top of an image of the cluster (left) and a heat map of X-ray measurements (right).

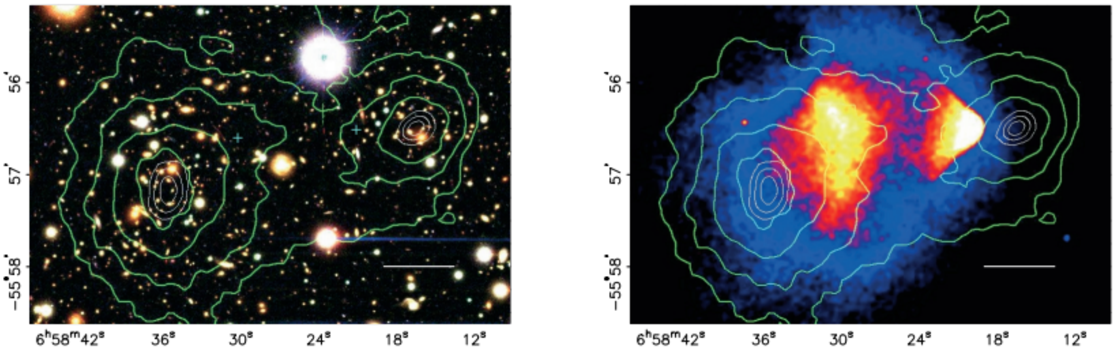

Figure 1.3 Weak lensing map of the Bullet cluster shown as green contour lines on top of an image of the cluster (left) and X-ray heat map (right) [32].

As shown, the majority of the mass contained in the two clusters passes through unhindered by the collision. The optical image shows how the galaxies within each cluster group together around the two points of high density, although the stars in these galaxies which generate this light only constitute around 1-3% of the total mass [35]. Instead, the majority of baryonic matter resides in the hot intergalactic gas [35], observed via the X-rays it emits, and is subject to ram pressure meaning that it trails behind the two clusters following the collision. This observation suggests that the majority of matter in the clusters is collisionless and non-baryonic; this can be explained by the preponderance of weakly interacting gravitationally bound DM [32]. Furthermore, this result made alternative explanations like MOND harder to justify.

### 1.1.5 Cosmic Microwave Background Power Spectrum

The Cosmic Microwave Background (CMB) provides us with a window to look back into the early universe at the point where expansion, following the Big Bang, had cooled the Universe sufficiently for neutral atoms to form. This event suddenly allowed photons to propagate freely and can still be observed as the CMB. Small temperature fluctuations at the point of recombination can be used to make estimates on the structure of DM in the early Universe.

This structure has been investigated via the power spectrum of these temperature fluctuations in the CMB [36–43]. The most recent results from the Planck Collaboration are shown in Figure 1.4 [43]. This spectrum represents the temperature fluctuations as a function of angular scale in the CMB. The relative intensity of the peaks and troughs can be used to make predictions about the mass and energy density of the early Universe. The shape of the temperature power spectrum is heavily dictated by oscillations caused by competing radiative pressure and gravitational collapse. Depending on the concentration of DM, the

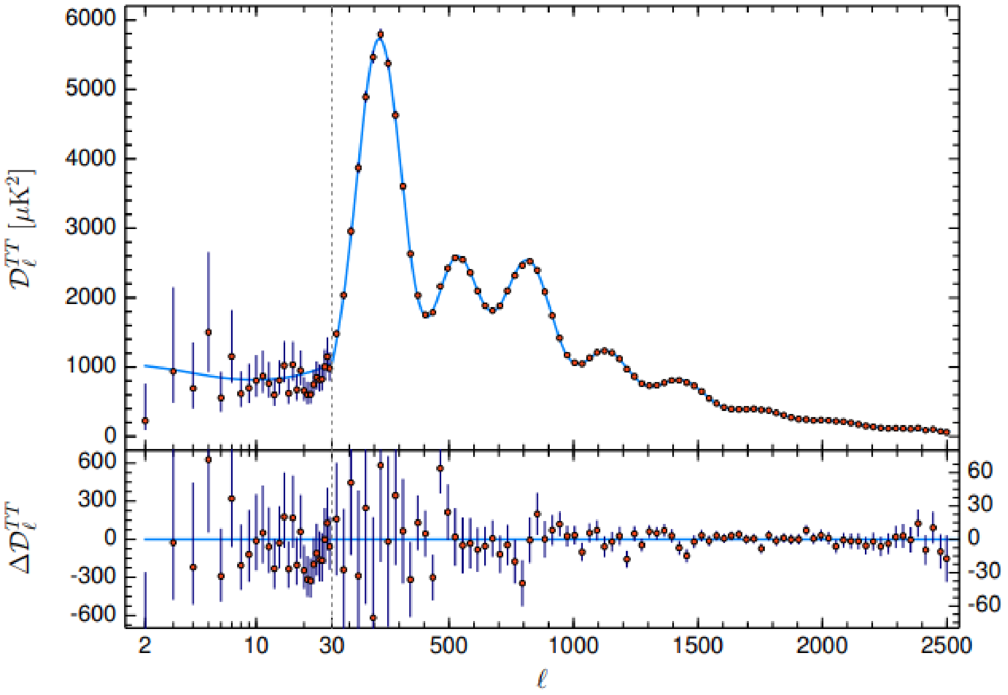

Figure 1.4 Power spectrum of the temperature fluctuations in the CMB fitted with a ΛCDM cosmological model [43].

relative difference in these competing forces changes the intensity of the oscillations. This is because baryonic matter participates in both gravitational collapse and radiative expansion of the oscillations, whereas DM only contributes gravitationally.

By fitting a ΛCDM cosmological model to the power spectrum, density parameters can be estimated for both the total matter density, $\Omega_m = 0.315 \pm 0.007$, and baryonic density, $\Omega_b h^2 = 0.0224 \pm 0.0001$. Utilising the hubble constant $H_0 = 67.4 \pm 0.5$, the power spectrum predicts that $\approx 84\%$ of the mass in the Universe is non-baryonic in nature [43].

### 1.1.6 Big Bang Nucleosynthesis

The process of Big Bang Nuceosynthesis (BBN) regards the formation of light elements in the first few minutes following the Big Bang and can be used to investigate the early Universe [44–46]. As the Universe expands and cools sufficiently for neutrons and protons to form, these particles are created and destroyed through weak interactions at an approximately equal rate and thus exist in thermal equilibrium according to [45]:

$$N_n/N_p = e^{(-Q_{np}/k_B T)}, \tag{1.7}$$

where $N_n/N_p$ is the neutron to proton ratio, $Q_{np}$ = 1.3 Mev is the difference in mass between the neutron and proton, $k_B$ is the Boltzmann constant and $T$ is the temperature of the Universe.

After $\sim$ 1 s, this equilibrium is disrupted due to the cooling temperatures and its lower mass favours a build up of protons 5 to 1 when $T \approx 10^{10}$ K [45]. This ratio was effectively frozen and only changed via the decay of neutrons through beta decay to end up with approximately 7 protons per neutron [46]. At this point in the evolution of the Universe, fusion reactions were able to begin producing light nuclei like Deuteron, $^3$H, $^3$He, $^4$He and $^7$Li. These reactions were halted after approximately 3 minutes following the Big Bang, due to further cooling, and the relative abundances of these light nuclei were fixed.

The most stable of the light nuclei is $^4$He and therefore almost all of the available neutrons contribute to its abundance. The mass fraction of $^4$He, $Y_p$, can thus be calculated via the ratio of neutrons and protons as [46]:

$$Y_p = \frac{2(n/p)}{1+n/p} \approx 0.25, \tag{1.8}$$

whereas the other nuclei are more sensitive to the nuclear reaction rates. The rate at which these fusion reactions can proceed depends strongly on the baryon density. Detailed simulations of the standard model of BBN have been carried out with varying baryon density, or equivalent baryon-to-photon ratio $\eta$, the results of which can be seen in Figure 1.5. The curves for $^4$He, D, $^3$He, and $^7$Li are shown plotted with a line width equivalent to a 95% confidence level. The white and yellow boxes indicate allowed regions from astronomical observations, with $\pm 2\sigma$ statistical and statistical + systematic errors respectively. The vertical blue hatched region represents the independent determination of the baryon density from the CMB, discussed in subsection 1.1.5, whilst the vertical orange hatched region represents the BBN concordance.

Apart from $^7$Li, there is good agreement between observations of the abundances of light nuclei, determinations from measurements of the CMB, and BBN concordance; the discrepancy associated with $^7$Li is known as the "Lithium Problem" and has been reaffirmed by analysis of the most recent Planck data of the CMB [47]. However, even though the $^7$Li fraction is not in perfect agreement, it is very promising that the order of magnitude of the predicted and measured mass fractions are in accord considering that the BBN abundances span 9 orders of magnitude. The agreement between the observations, CMB results, and BBN predictions tightly constrain the baryon content to $\Omega_b h^2 \leq 0.024$ [46]. Combining this with knowledge of the total mass density in the Universe, it is clear that the baryon contribution

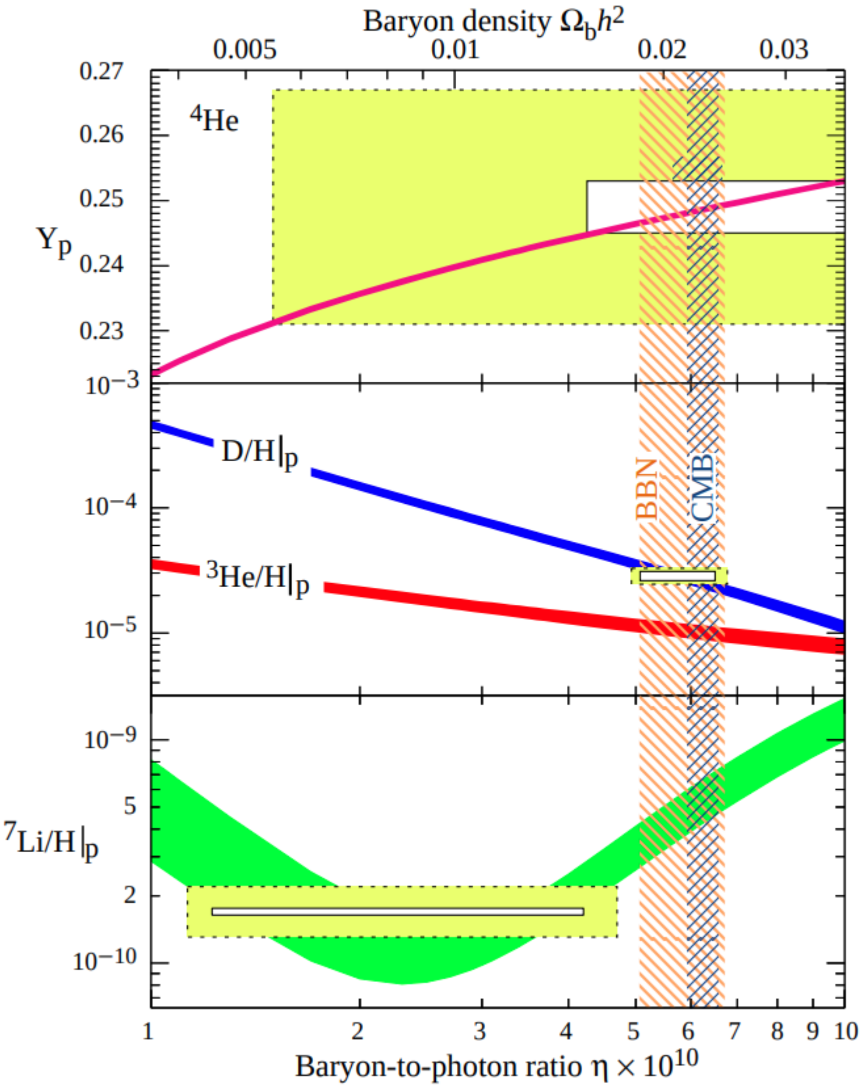

Figure 1.5 Compiled graph showing the primordial abundances as a function of baryon density, allowed regions from astronomical measurements, the CMB results and BBN concordance [46].

is only a minor component and thus leaves room for a significant quantity of non-baryonic DM. The apparent large amount of missing non-baryonic matter in the Universe has led to the postulation of various particle candidates, a few of which are outlined in Section 1.2.

## 1.2 Dark Matter Candidates

Early candidates for DM were baryonic and called MAssive Compact Halo Objects (MACHOs). A non-exhaustive list of MACHOs included objects like black holes, neutron stars, white dwarfs, and planets; however, gravitational lensing surveys have shown that MACHOs constitute less than 8% of the Milky Way's halo mass [48, 49]. Additionally, the evidence for DM presented thus far suggests that these baryonic candidates can not account for the observed influence of DM in the Universe. Instead we must consider new physics beyond the Standard Model (SM) of particle physics; the characteristics we associate with DM observations do not align with any known particle currently understood within the SM. Several candidate particles which have been strongly motivated elsewhere in the field of particle physics also conveniently fit the description of DM. In addition to being non-baryonic and weakly interacting, favourable candidates must be cold (non-relativistic), to allow for the structure formation we observe in the Universe; and stable within the lifetime of the Universe, so that their influence can be observed in the present day. One fitting candidate, which is the focus of this thesis, is called a WIMP.

### 1.2.1 Weakly Interacting Massive Particles

WIMPs are the most commonly studied DM candidate particles as they are highly favourable. This is because they are cold, stable, arise from multiple particle theories, possess the correct relic density, and offer a variety of detection avenues. The fact that WIMPs are produced with the correct relic density is known colloquially as the "WIMP miracle" and results from the prediction that WIMPs are initially created and exist in thermal equilibrium with other particles following the Big Bang [50].

In its primordial stage, the Universe is very hot and dense meaning that WIMP particles can be produced and destroyed via pair-production and annihilation mechanisms linked with SM particles. The cooling and expansion of the Universe results in the suppression of the pair production mechanism of WIMPs; however, the density is still sufficient for annihilation to prevail and WIMP numbers begin to fall. This decline of the WIMP relic density, $\Omega_X$, is shown in Figure 1.6 as equivalent functions of time and temperature of the Universe. Due to the expansion, WIMP annihilation into SM particles slowly becomes less likely to occur resulting in a "freeze-out" where the density of WIMPs reaches a plateau consistent with present day observations of the DM density.

The present day DM relic density is therefore strongly dependant on the annihilation cross section of WIMPs. The WIMP relic density at the point of freeze-out can be defined as [51]:

$$\Omega_X h^2 = \frac{m_X n_X}{\rho_c} \simeq \frac{3 \times 10^{-27} cm^3 s^{-1}}{\langle \sigma_A v \rangle} \tag{1.9}$$

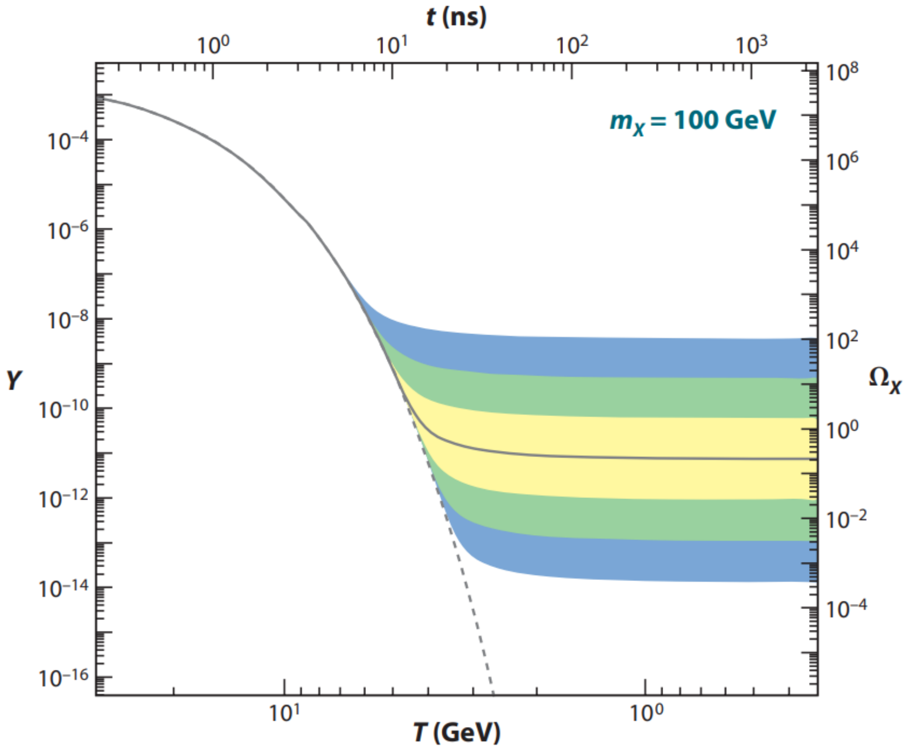

Figure 1.6 The number density and relic density as a function of time and temperature of the Universe following the Big Bang [50]. The solid colour bands indicate order of magnitude deviations from the present day relic density.

where $m_X$ is the WIMP mass, $n_X$ is the number density of WIMPs, $\rho_c$ is the critical density, and $\langle \sigma_A v \rangle$ is the thermally averaged cross section. The observed relic density, $\Omega_X h^2 = 0.120 \pm 0.001$ [43], can therefore be used to estimate the scale of the WIMP mass and annihilation cross section, $\sigma_A$. By substitution, this predicts a value of $\langle \sigma_A v \rangle = 2.5 \times 10^{-26} cm^3 s^{-1}$ which is comparable to particles on the weak-scale. This result suggests that new particles which interact with a strength no greater than the weak force are excellent DM particle candidates.

The Minimal Supersymmetric extension of the Standard Model (MSSM) is one of the most well known particle theories which offers a weak-scale candidate. The theory was originally motivated as a possible solution to the Gauge Hierarchy problem. Supersymmetry proposes that the particles in the SM have a supersymmetric partner and introduces a new symmetry called R-parity. R-parity is a property which must be conserved in particle interactions. SM particles are assigned an R-parity of +1 while supersymmetric partners have an R-parity of -1. The conservation of this new parity means that the Lightest Supersymmetric

Particle, called the neutralino, can not decay into an SM particle making it a stable DM candidate [52]. In recent years, enthusiasm for a supersymmetric WIMP candidate has begun to wane due to lack of evidence in collider searches [53].

Despite this, the search for WIMPs is not over as alternative particle theories which produce a weak-scale candidate, like Universal Extra Dimensions (UED), are also studied. The extra dimensions in this theory allow SM particles along with their Kaluza-Klein (KK) partners to propagate. Similar to MSSM, UED invokes a new property of particle interactions called KK-parity whose conservation stops the Lightest KK Particle (LKP) from decaying into SM particles. The LKP mass, which is consistent with the mass scale of the observed DM abundance, has been predicted between 500 - 600 GeV [54].

### 1.2.2 Prominent Alternative Candidates

#### Axions

Axions are an alternative DM candidate particle which are motivated by the strong Charge-Parity (CP) problem. The strong CP problem states that, if argued from a classical formulation, the electric dipole moment of a neutron should be on the order of $10^{-13}e$ cm [55]. However, experimental attempts to measure the dipole moment have lead to the conclusion that it can be no larger than $10^{-26}e$ cm [56]. This discrepancy between prediction and the experimental reality can only be explained if CP-symmetry is conserved. The Quantum Chromodynamics description for the strong force does not provide a reason for this conservation. This apparent conservation is made more peculiar by the fact that CP-symmetry is not conserved in measurements of the weak interaction. This unexplained observation has been dubbed the "strong CP problem" [55]. Axions were originally introduced by the Paccei-Quinn solution to the strong CP problem but this original model was ruled out by experiment. However, alternative axion models have also been put forward which are still permitted [57].

#### Sterile Neutrinos

There exists three flavours of neutrinos which currently fit into the SM; electron neutrinos ($\nu_e$), muon neutrinos ($\nu_\mu$), and tau neutrinos ($\nu_\tau$). These active neutrinos are left-handed and only interact gravitationally and via the weak force. These neutrino flavours have largely been ruled out as DM candidates because they are considered to be "hot" DM candidates which would produce structure in the Universe very differently to how it is observed today. Sterile neutrinos also called right-handed neutrinos, postulated due to the non-zero measurement of active neutrino masses, can be minimally inserted into the SM. They are predicted to only interact gravitationally and are much harder to detect than left handed neutrinos. These particles, if produced with masses on the keV scale, offer another potential candidate for DM [58].

## 1.3 Direct WIMP Dark Matter Detection

As they are a highly favourable DM candidate, the detection of WIMPs is the focus of this thesis. One of the main frontiers in the search for WIMP DM is called direct detection, although there are also methods like indirect detection and collider searches. Direct detection aims to measure the rare interaction between DM and SM particles inside a detector, situated in a deep underground radio-quiet environment, as we pass through the local DM distribution in the Milky Way [59]. Whereas, indirect searches aim to look for SM particles produced by DM annihilation processes [60] and collider searches aim to look for missing mass/energy, indicative of DM production, in high energy collisions of SM particles [61].

Direct detection searches work under the assumption of the Standard Halo Model, in which DM particles are enclosed in a halo encompassing the Milky Way. This implies that Earth is constantly sweeping through the local distribution of DM. These DM particles are gravitationally bound and assumed to have a Maxwell-Boltzmann velocity distribution. Therefore, by assuming a WIMP particle of mass 100 GeV/c$^2$, an average WIMP velocity of 220 km/s and a local DM distribution of 0.3 GeV/cm$^3$, the DM particle flux experienced on Earth is expected to be approximately $6.6 \times 10^4$ cm$^{-2}$ s$^{-1}$ [62].

Despite the expectation that any interaction between DM and SM particles would be rare, this large particle flux indicates that a small number of events could potentially be observed in a large detector volume in a laboratory on Earth. Several detector technologies exist in the field of direct detection; the following subsections highlight some of these and summarise the current status of leading conventional searches.

### 1.3.1 Direct Detection Technologies

#### Bubble Chambers

Figure 1.7 shows an example of a bubble chamber search planned by the PICO collaboration [63]. These detectors utilise a superheated liquid, typically refrigerants ("FREON") like $C_3F_8$, with temperatures maintained just below the boiling point. When a particle interacts with the superheated liquid, a localised phase transition is induced resulting in the nucleation of a bubble. The bubble formation depends on the amount of energy deposited and the size of the volume within which it is deposited. The thermodynamic threshold can be chosen in such a way that Electron Recoil (ER) backgrounds can not result in bubble formation; this

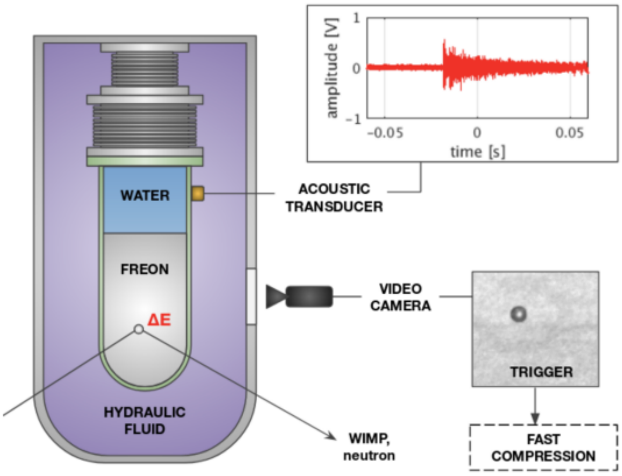

Figure 1.7 Diagram showing the principle of operation for a bubble chamber detector [63]

is important because WIMPs are expected to induce Nuclear Recoils (NRs). An acoustic transducer is used to further discriminate between NRs and alpha particles via the signal's amplitude [64]. Between each event the chamber must be compressed before the next event can be registered. The fast compression is triggered by a camera which detects the bubble; however, this still results in long dead times of the exposure [65]. Desite this, these detectors are able to set some of the most stringent limits on WIMP-proton Spin-Dependent (SD) cross sections [66].

### Inorganic Scintillating Crystals

As depicted in Figure 1.8, these detectors consist of high-purity scintillating crystal targets, typically NaI(Tl). Each crystal is coupled to two light sensitive Photo-Multiplier Tubes (PMTs), one at either end [67]. Particle interactions which take place inside the crystals cause bound electrons to become excited to higher energy levels and emit visible photons following relaxation back to the ground state; this process is made more efficient by the inclusion of the thallium activator [68]. The resulting scintillation photons are measured by the PMTs. These scintillating crystals can be stacked in large arrays and can be stably operated for extended periods. However, these detectors have relatively high levels of intrinsic background and are less capable of effectively discriminating against background signals [59].

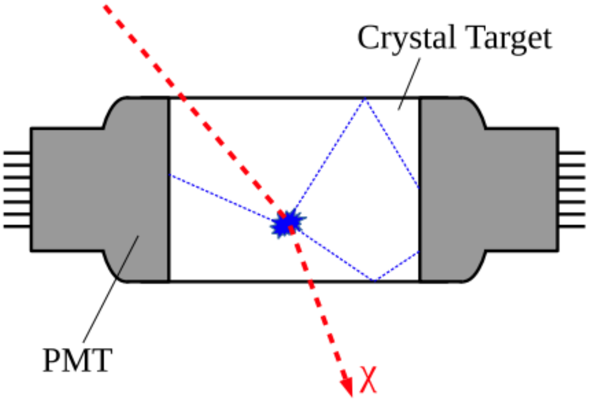

Figure 1.8 Diagram showing the operating principle of inorganic crystal scintillators [59].

### Cryogenic Detectors

Cryogenic detectors, like those used by the SuperCDMS experiment, are crystals which are kept under very cold conditions via coupling with a thermal bath, as shown in Figure 1.9. When a particle interacts with the crystal, energy is deposited which can be measured as both a temperature increase via phonons and concurrent ionisation via the current signal. The sensitivity of these detectors to phonons is dependent on the temperature, thereby necessitating cryogenic conditions $\leq$ 50 mK, and the heat capacity of the crystal. Silicon and germanium crystals are popular because they have very low heat capacities under these conditions [59]. Furthermore, the complementary measurement of simultaneous ionisation has been shown to allow for background discrimination [69]. Recently the sensitivity of

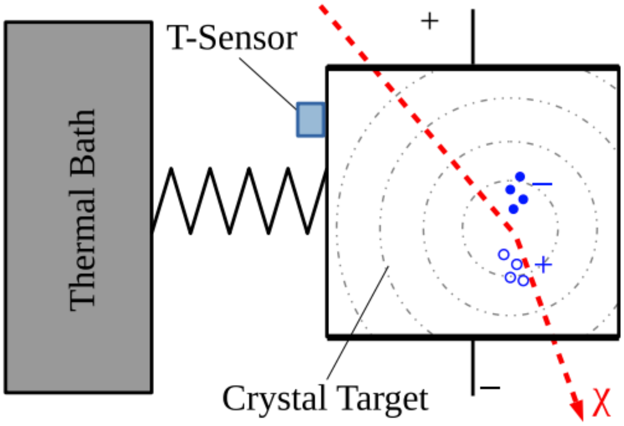

Figure 1.9 Diagram showing the operating principle of cryogenic detectors [59].

these detectors has been extended to lower energies, around 100 eV with eV resolution, by applying a large bias voltage to the crystal; however this is at the sacrifice of the background discrimination via ionisation [70].

### Two-phase Time Projection Chambers

Two-phase Time Projection Chambers (TPCs), like those of the LZ, XENON and PandaX collaborations [72–74], set some of the most competitive limits on direct WIMP interaction cross sections [75–77]. As shown in Figure 1.10, these detectors consist of a large tank filled with a liquid and gaseous phase of a noble element; typically xenon is favoured but argon is also used in some searches. Arrays of PMTs are positioned at the top and bottom of the tank which measure scintillation events. When particles interact in the liquid phase some electrons become excited and scintillate; this event is known as the S1 signal (left). As a result of the particle interaction, electrons are simultaneously liberated and become free to drift to the top of the liquid phase under the influence of an applied electric field. Upon arrival at the

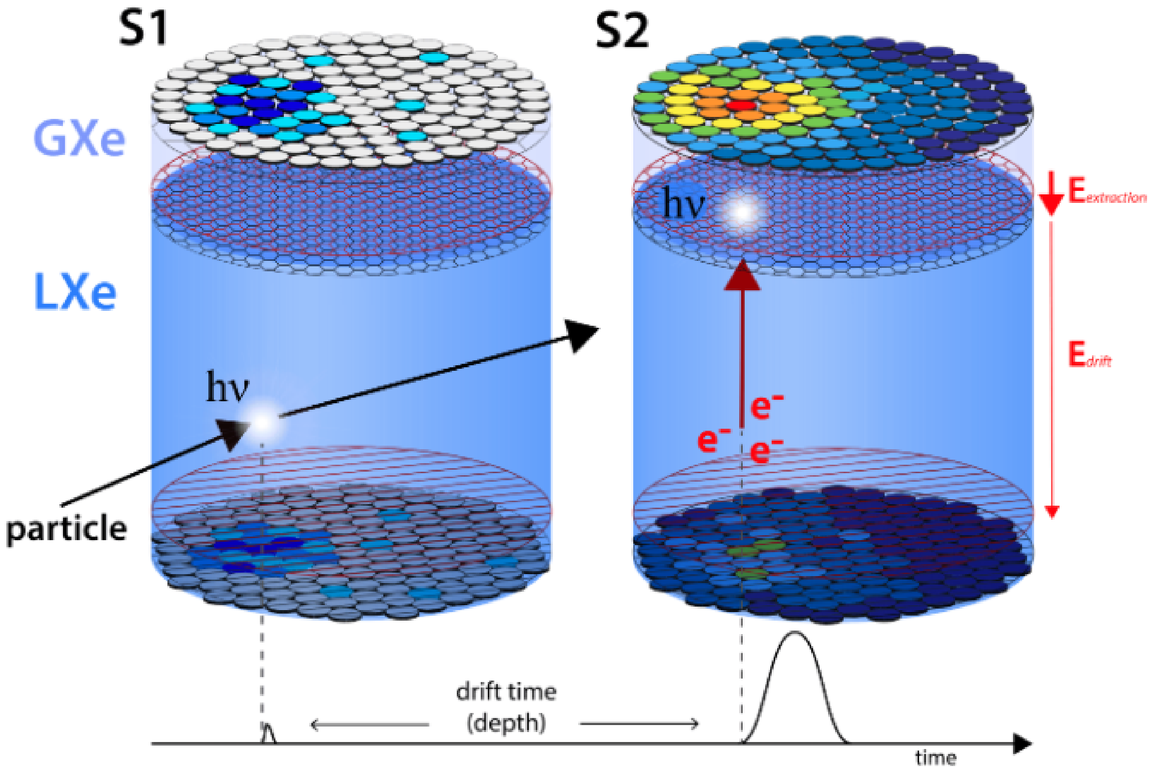

Figure 1.10 Diagram showing the detection principle of two-phase noble element detector technology [71].

liquid-gas interface, the free electrons are faced with a large extraction electric field which accelerates the charge and causes a secondary scintillation event known as S2 (right) [78].

The ratio of the S1 and S2 signals has proven to be a powerful method for ER and NR discrimination. Additionally, the time interval between S1 and S2 can be exploited to aid fiducialisation in the target volume in the vertical axis. Fiducialisation in the horizontal x-y plane is achieved by reconstructing the event position via the intensity of the signals measured by the PMT arrays. By ensuring that only events which occur in the fiducialised central bulk of the detector are considered, a significant number of background events can be rejected [78].

## 1.3.2 Detector Limits

Two-phase TPCs have improved in sensitivity by many orders of magnitude, in terms of both WIMP-nucleon cross sections and reduction of ER background rates, since they were first conceived and are currently at the forefront of the field [78]. Figure 1.11 shows the Spin-Independent (SI) WIMP-nucleon cross section limits for several direct detection experiments in recent years as a function of potential WIMP masses. As these detector limits are pushed

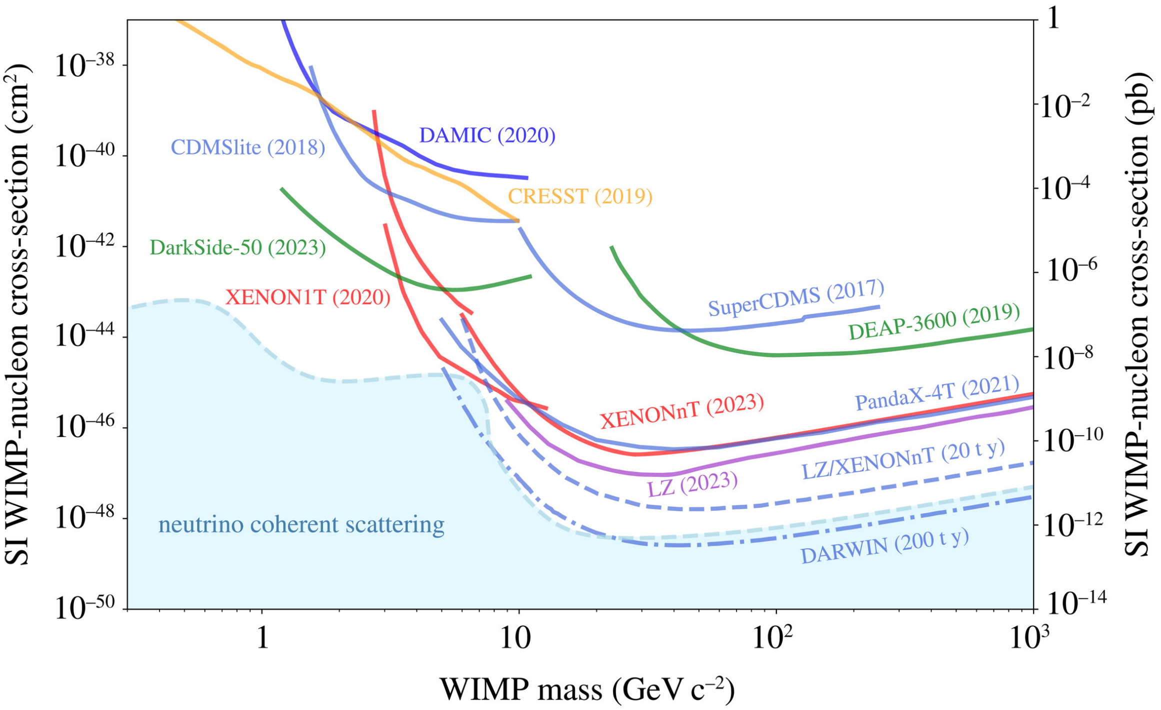

Figure 1.11 Current status on the SI WIMP-nucleon cross section limits for several direct detection experiments, including predictions for the leading LZ and XENONnT experiments and future limits with the next generation DARWIN/XLZD collaboration [78].

to lower cross sections, sensitivity to potential WIMP interactions improves. Predictions for the current leading detector collaborations, LZ and XENONnT, are indicated by dashed lines. These detector limits are becoming very close to a region of the parameter space, shaded in light blue, called the Neutrino "Fog" [79].

Below this region, these detectors are expected to become significantly influenced by neutrino interactions predominantly orginating from the Sun. This introduces a new irreducible background making the positive identification of a WIMP signal significantly more difficult [79]. Results from LZ, XENONnT and PandaX-4T indicate that there has been no excess in events near this region [75–77], suggesting that future searches will need to begin probing below the Neutrino Fog. The predicted limits for the next generation two-phase DARWIN/XLZD experiment [80, 81] is indicated by the dot-dashed line and can be seen below the Neutrino Fog. However, without a method of discrimination between neutrino and potential WIMP interactions, two-phase noble element detectors will struggle to establish an irrefutable WIMP signature. Future searches will therefore very likely need to employ an alternative method to achieve this goal. One possible solution is the search for a signal with a galactic origin.

### 1.3.3 Preface to Galactic Signatures

A galactic signature has the potential to definitively identify WIMP interactions beyond the Neutrino Fog. This can be achieved by one of two ways: through directional detection, discussed in Chapter 2, or with an annual modulation signal. Annual modulation of the event rate in a direct search has long been considered as a powerful signature of a positive DM signal. The galactic origin of annual modulation arises due to the motion of our solar system around the Milky Way Galaxy. This motion, shown in Figure 1.12, is relative to the local DM halo distribution of the galaxy and therefore induces the apparent DM "wind" experienced on Earth. The orbit of the Earth around the Sun modulates the relative velocity between Earth and the DM wind. For approximately half of the year the Earth is travelling into the wind, with the flux peaking in June, and travels away from the wind during the other half, reaching a minimum flux in December. The approximately cosinusoidal modulation of relative velocity is expected to result in a modulation of the DM event rate over the course of a year [82].

The DAMA experiment, previously known as DAMA/NaI and later as DAMA/LIBRA, have claimed to have measured an annual modulation signature consistent with the DM wind. The DAMA/LIBRA detector is located underground at Laboratori Nazionali del Gran Sasso in Italy and consists of an array of 25 highly radio-pure NaI(Tl) scintillating crystals [67]; discussed earlier in subsection 1.3.1. DAMA has continued to measure the annual modulation

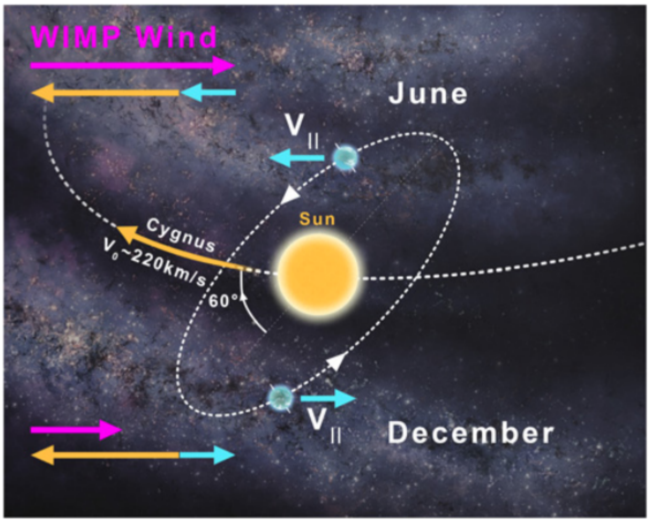

Figure 1.12 Diagram depicting the DM wind induced by the motion of the Earth through the Milky Way [83, 82].

signal for over 20 years with a confidence level of 13.7 $\sigma$ in the 2 - 6 keV range [84], as seen in Figure 1.13, and is argued by some to be the only positive DM signal measured to date.

However, DAMA's claim is widely considered to be controversial as this modulation is also consistent with background sources [85, 86] and possible artifacts of the analysis method [87–89]. Several other experiments, which utilise the same detector technology as DAMA, have been set up to elucidate the annual modulation result. This includes the ANAIS-112 [90] and COSINE-100 [91] experiments whose results, at the time of writing, are either compatible with no modulation [92] or can not conclusively challenge the DAMA results [93]. Crucially this annual modulation signal has not been detected by independent searches

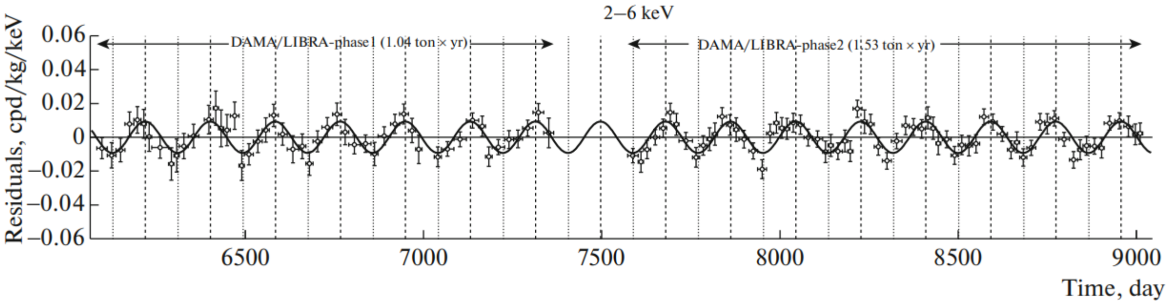

Figure 1.13 Annual modulation signature measured by the DAMA experiment spanning over 20 years [84].

with different detector technologies which boast far superior sensitivity, like two-phase TPCs [82].

Furthermore, the prospect of two-phase TPCs measuring an annual modulation signal below the Neutrino Fog is poor. This is because annual modulation is a %-level effect and would require a significant number of detected events to successfully observe the oscillations. Therefore, the alternative directional galactic signature is more favourable; this will be explored in more detail in the following chapter.

## 1.4 Conclusions

The broad range of evidence for the existence of DM presents the unavoidable reality that this mysterious substance exists and is made of a non-baryonic material constituting the majority of mass in the Universe. Several particle candidates, which currently exist outside the SM of particle physics, conveniently fit the profile of a DM suspect; the most commonly studied candidate is the WIMP. Several experimental efforts have endeavoured to detect the rare scattering event between one of these WIMPs and an SM particle in underground laboratories. All of which, aside from the widely disputed DAMA annual modulation result, ascertain that no signals consistent with a WIMP-nucleon scattering event have been observed. Leading two-phase xenon TPCs are fast approaching the irreducible background below the Neutrino "Fog". These ongoing and future experiments are poised to begin probing this region and will inevitably struggle to positively identify a WIMP signal to a high degree of certainty. The logical progression for the future of the field beyond the Neutrino Fog with directional detection is discussed in the following chapter.

# Chapter 2

# The Case for Directional Dark Matter Detection

Some of the major evidence for DM and the motivation for direct WIMP detection experiments was presented in the previous chapter. However, the most sensitive of these searches, two-phase xenon TPCs, are currently probing the limits close to the so-called Neutrino Fog. Below this limit the positive identification of WIMP interactions could be overlooked due to spurious interactions caused by neutrinos predominantly coming from the Sun. To overcome this limitation, it is likely that an alternative search method will be required. This chapter presents the case for a directional approach to direct DM detection beyond this limit.

Firstly, the main challenge of the Neutrino Fog, which provides strong motivation for a directional search, is presented in Section 2.1. An overview of low pressure gaseous techniques, which can be used to perform directional recoil detection, is then presented in Section 2.2 followed by a brief description of other viable detector technologies. This is succeeded by a review of the status of current and future directional search efforts in Section 2.3. Finally, a few areas of detector development which are of interest to the next generation of gaseous detectors are discussed in Section 2.4 before drawing some conclusions in Section 2.5.

## 2.1 The Neutrino Fog

As discussed in the previous chapter, there is a relatively large density of DM particles in the vicinity of Earth, 0.3 GeV/cm$^3$ [10]. Despite this, the interaction cross section is anticipated to be very small, which means that the successful identification of WIMP interactions is challenging. World leading direct detection experiments have devoted significant efforts to reduce sources of background signals, by employing low-background radioactivity techniques [94], to thereby improve the chances of detecting rare WIMP-nucleon elastic scattering events. However, the Neutrino Fog has been an impending source of irreducible background signals for around a decade [95].

### 2.1.1 The Irreducible Neutrino Background

The Neutrino Fog is a region of the cross section and mass parameter space below which the gradient of discovery limit for WIMPs, $n$, increases due to the uncertainties associated with various sources of neutrinos. This can be seen in Figure 2.1 as the majoritively blue region below several previous direct detection limits in the SI parameter space. The discovery limit, $\sigma$, is proportional to the number of background events, $N$, such that $\sigma \propto N^{-1/n}$ and the edge of the Neutrino Fog, previously known as the neutrino floor, is defined as the transition where $n > 2$. Therefore, the large variations in the gradient of discovery limit, indicated by the colour scale, results in larger WIMP discovery limits relative to the number of background events at lower cross sections [79]. Ultimately this makes the identification of excess WIMP events more difficult.

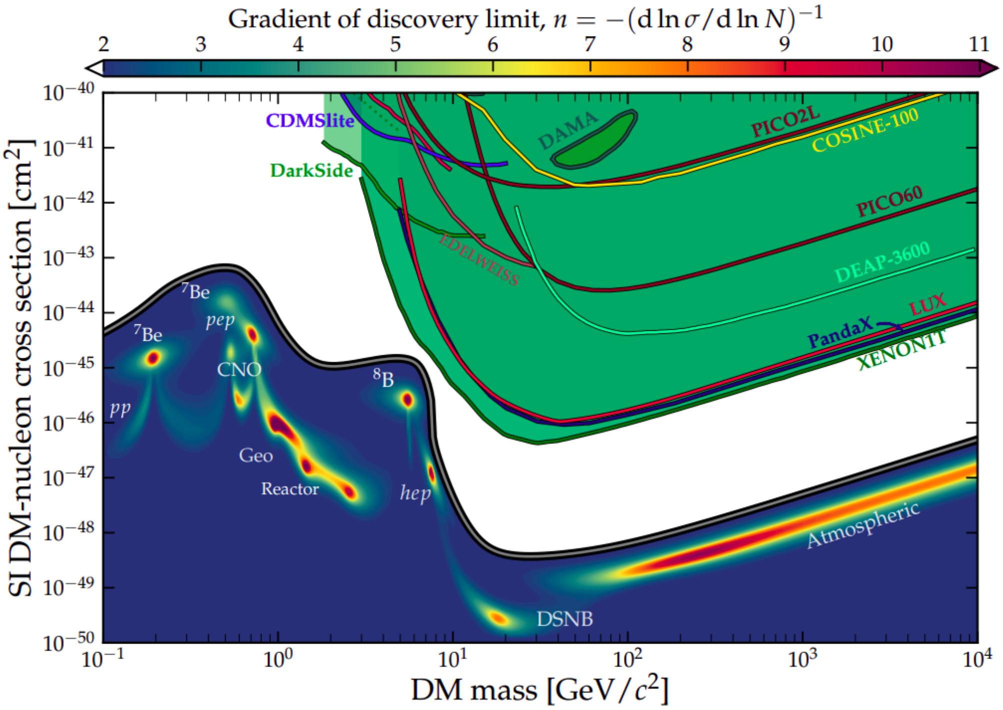

Figure 2.1 An annotated map of the Neutrino Fog, as it would appear to a xenon target, including some previous SI WIMP-nucleon detector limits for comparison [96].

The neutrino background signals are caused by coherent elastic neutrino-nucleus scattering (CE$\nu$NS) and the different neutrino sources, labelled in Figure 2.1, are able to mimic WIMPs of varying masses and cross sections [95]. The most imminent source of neutrinos for current leading DM searches, the so-called $^8$B neutrinos, are produced in the Sun. These neutrinos are produced when the proton-proton (pp) chain terminates in $^8$B which then decays via the emission of a positron and neutrino. The total $^8$B neutrino flux has been measured to be 5.95 $^{+1.03}_{-1.01}$ $\times$ $10^6$ cm$^{-2}$ s$^{-1}$[97]. The *hep* neutrinos, which mimic a similar WIMP mass to the $^8$B neutrinos at lower cross sections, are also produced as a by-product of the pp chain in the Sun. These *hep* neutrinos are produced by the fusion reaction $^3$He + p $\rightarrow$ $^4$He + e$^+$ + $\nu_e$ and have a predicted flux of 9.3 $\times$ $10^3$ cm$^{-2}$ s$^{-1}$ [98]. Less energetic neutrinos produced in the Sun including *pp*, $^7$Be, CNO, and *pep* neutrinos also produce significant fluxes on Earth. However, these sources are less imposing for current leading DM searches due to the sharp reduction in sensitivity to lower WIMP masses.

In addition to Solar neutrinos, other sources of neutrinos will arise in future searches as lower limits to the WIMP-nucleon cross section and recoil threshold are pursued. These sources include atmospheric neutrinos, the Diffuse Supernova Neutrino Background (DSNB), geoneutrinos, and reactor neutrinos. Atmospheric neutrinos are produced by high energy cosmic ray collisions in the Earth's atmosphere [99] and will become a dominate background for larger WIMP masses $\gtrsim 10^2$ GeV/c$^2$. The DSNB is the cumulative product of core-collapse supernovae neutrinos which have accumulated over the course of cosmological history [100]. Geoneutrinos and reactor neutrinos produce fluxes which are location dependant on Earth. The geoneutrinos are produced in radioactive decays of naturally occurring uranium, thorium, and potassium and the flux depends on the radiopurity of the rock surrounding an experiment in an underground laboratory [101]. The reactor neutrinos are produced by fission processes in nuclear power plants and such a flux will depend on the number and proximity of nuclear power stations to the laboratory [102].

The impact that the Neutrino Fog will have on future efforts to conclusively detect a WIMP-like signal should not be understated. Although some methods have been suggested for bypassing the Neutrino Fog [103–105], the large statistical uncertainties associated with neutrino fluxes will make the positive identification of WIMP-nucleon scattering events very difficult with current conventional counting experiments [79]; as they heavily depend on the accuracy of background models to identify excess WIMP events. Discriminating a WIMP signal from the neutrino background with absolute certainty will therefore likely require an alternative search technique. This challenge has been long anticipated for leading searches; however, recent landmark announcements from both the PandaX-4T [106] and XENONnT experiments [107], regarding the first detection of $^{8}$B neutrinos, have made it clear that the era of navigating the Neutrino Fog has begun.

### 2.1.2 Overcoming the Neutrino Fog with Directional Signatures

The recent results from the PandaX and XENON collaborations are consistent with expectations of $^{8}$B neutrinos. However, using this current leading technology, the presence of a WIMP contribution to this signal can not be refuted. Therefore, an alternative detection technique must be employed to robustly search for WIMP-like DM in the future.

The directional measurement of NRs has long been regarded as a conclusive way to identify a DM signature [108, 109] and, particularly in light of recent results, is also considered to be a feasible way of probing the Neutrino Fog [110]. Similar to a galactic annual modulation signal, the directional measurement of WIMP-nucleon scattering events will be influenced by the motion of the Earth. As discussed in the previous chapter, the Solar System orbits around the Milky Way constantly sweeping through the local DM distribution. This orbital motion is directed towards the Cygnus constellation. Therefore, an excess of events originating from this region of space would constitute a compelling galactic signature of WIMPs.

The top panel of Figure 2.2 shows the angular distribution for the rate at which 9 GeV/c$^{2}$ WIMPs would arrive on Earth, represented in blue. As shown, the peak in the WIMP event rate almost coincides perfectly with the Cygnus constellation in galactic coordinates. Additionally, the majority of the neutrino background is produced by the Sun; the position of which is indicated by the star shaped marker. The direction from which these neutrinos originate is therefore known at all times and can be reasonably separated from the peak direction in the WIMP wind distribution. Furthermore, as shown in the bottom panel of Figure 2.2, the rotation of the Earth on its own axis causes an auxiliary angular modulation. The apparent direction of the DM and neutrino signals will oscillate over the course of a day but will always be separated [110]. The angular distribution of any terrestrial background signals will be invariant with respect to time. Consequently, the observation of an oscillation in the apparent origin of the DM wind and neutrino signals would constitute powerful evidence for WIMPs.

The measurement of such a directional signal is considered to be the most promising for future searches beyond the Neutrino Fog [111]. It has been shown that large regions of the Neutrino Fog parameter space can be removed with minimal directionality [110, 111]. However, the ultimate goal of a high performance WIMP detector with 3-dimensional directional sensitivity would be able to completely remove the Neutrino Fog as it is currently depicted in Figure 2.1 [96].

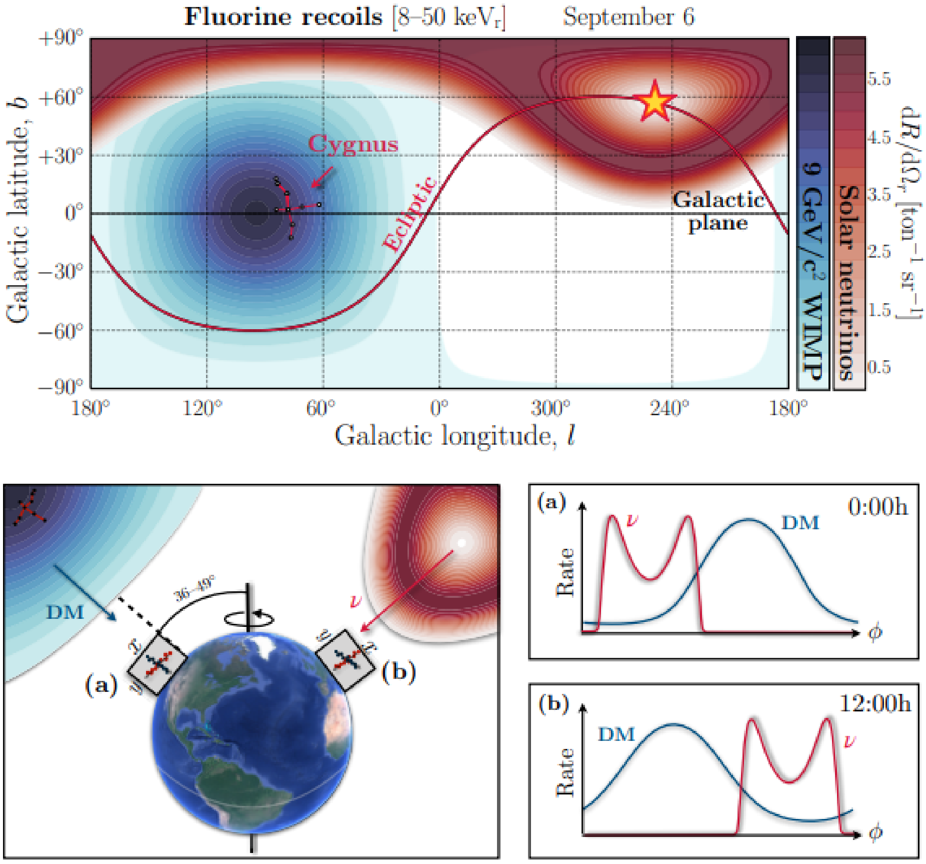

Figure 2.2 The rate of WIMPs and Solar neutrinos plotted as a function of their origin in galactic coordinates (top). Diagram showing the angular modulation over the course of a day due to the Earth's axial rotation (bottom) [110].

## 2.2 Methods of Directional Detection

The case for developing a detector with directional sensitivity is very well motivated, particularly beyond the Neutrino Fog. However, feasibility studies for observing directional signals in two-phase TPCs have indicated that this is not possible [112]. Therefore, the future of direct detection will require an alternative technology to progress the field. The principles of operation for several detector technologies, which are capable of directional detection, are highlighted in this section. Particular attention is paid to low pressure gaseous TPCs, as this is the most widely adopted approach and the main focus of this thesis.

### 2.2.1 Low Pressure Gaseous Time Projection Chambers

Low pressure gaseous TPCs consist of a gas target volume situated between a cathode and anode readout plane. The low pressure gas facilitates NR tracks with ranges extending to the mm-scale, making it possible to determine the direction of the recoiling nucleus. When an NR is induced in the gas target, Figure 2.3, electrons are liberated along the path of the recoil and this charge is drifted towards a readout plane due to the influence of an applied electric field. The charge is then amplified by large electric fields before being measured by a segmented 2-dimensional readout technology with suitable positional resolution. This method allows the track of the recoiling nucleus to be reconstructed and is one of the most developed methods of directional detection. Several experimental efforts have demonstrated this method, the most successful of which is attributed to the Directional Recoil Identification From Tracks (DRIFT) experiment, discussed in Section 2.3 [113].

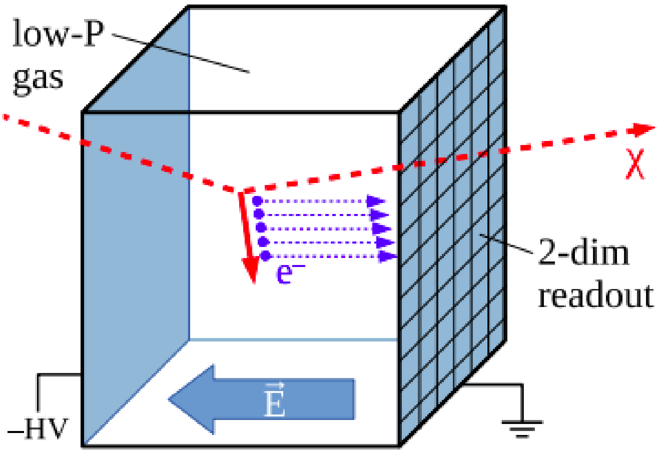

Figure 2.3 Diagram showing the low pressure gaseous TPC concept for directional DM searches [59].

#### Nuclear Recoils in Low Pressure Gas

When an ER or NR is induced, the subject of the recoil moves through the target material colliding with electrons and nuclei, causing its kinetic energy to dissipate. Collisions with electrons along the path of the recoil, which are energetic enough to liberate an electron, produce electron-ion pairs. The average amount of energy required to liberate an electron is called the W-value of the gas.

In the case of ERs, the average ionisation produced is equal to the initial recoil energy divided by the W-value of the gas target. For NRs on the other hand, the energy of the recoil is not equal to the amount of charge produced because this energy can dissipate through other channels. This effect is quantified by the Ionisation Quenching Factor (IQF) which is equal to the fraction of energy that contributes to ionisation. The Lindhard model [114, 115] provides a semi-empirical method for determining the IQF for a recoiling nucleus of energy $E_r$. This model is expressed in terms of the reduced energy of the recoil, $\varepsilon$, and a constant, $k$, related to the stopping power of the gas which takes the form:

$$\varepsilon = 11.5 E_r Z^{-\frac{7}{3}}, \qquad k = 0.133 Z^{\frac{2}{3}} A^{-\frac{1}{2}}, \tag{2.1}$$

where Z and A are the atomic and mass numbers of the nucleus under recoil. The reduced recoil energy is further parameterised by the function $g(\varepsilon)$ which is defined as:

$$g(\varepsilon) = 3\varepsilon^{0.15} + 0.7\varepsilon^{0.6} + \varepsilon. \tag{2.2}$$

Using these definitions, the IQF according to the Lindhorn model is given by the following equation:

$$IQF = \frac{kg(\varepsilon)}{1 + kg(\varepsilon)}. \tag{2.3}$$

This is an important correction factor for the energy of measured recoils because energies are often given in units of $\text{keV}_r$ or $\text{keV}_{ee}$. The absolute energy of the recoil is given in $\text{keV}_r$, whereas, $\text{keV}_{ee}$ is defined as the electron equivalent energy of the recoil. There is no distinction between these units for ERs. However, for an NR the $\text{keV}_{ee}$ energy is equal to the $\text{keV}_r$ multiplied by the IQF.

### Negative Ion Drift Gases

Following the ionisation caused by a recoil in conventional gas targets, the liberated electrons are drifted towards the readout plane. These electrons are subject to a significant amount of diffusion, the extent of which increases with increasing drift length [116]. This diffusion reduces the precision to which the recoil track can be reconstructed and therefore limits the drift length of the detector volume.

Alternatively, Negative Ion Drift (NID) gases can be used. These gases are highly electronegative and therefore have an affinity to capture free electrons, forming Negative Ions (NIs). Consequently, after a recoil ionises the gas, the free electrons are captured and NIs are drifted towards the anode readout plane instead. Due to their larger mass, the speed at which NIs travel, $v_{drift}$, is much slower than free electrons and is defined by [117]:

$$v_{drift} = \mu_0 E \frac{P_0 T}{P T_0}, \tag{2.4}$$

where $\mu_0$ is the reduced mobility, $E$ is the electric field strength, $P$ is the pressure, $T$ is the temperature, and the zero subscript indicates standard temperature and pressure conditions. As a side effect of this slower velocity, special consideration is required for the charge integration time of the readout [118, 119]; some work regarding this issue in the NID gas $SF_6$ is presented later in Chapter 5. However, the main reason for using an NID gas is because the NIs are subject to less diffusion than the electrons would have otherwise experienced. This effect is demonstrated in Figure 2.4 which shows the difference in diffusion between pure $CF_4$, a conventional electron drift gas, and following a small addition of $CS_2$, an NID gas.

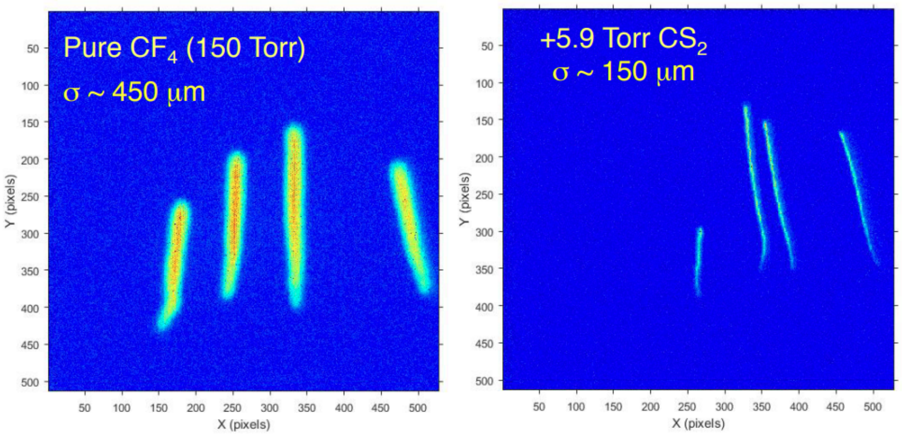

Figure 2.4 Example alpha particle tracks taken in an optical TPC, described in Ref. [120], demonstrating the effects of electron diffusion in $CF_4$ (left) and the significant improvement seen following a small addition of the NID gas $CS_2$ (right) [96].

This diffusion is close to the thermal limit in the case of the NIs and can be defined by the Nernst-Townsend-Einstein relation, in term of the thermal diffusion constant, D [116]:

$$D = \frac{\mu k T}{e}, \tag{2.5}$$

where $\mu$ is the mobility without an applied field, $k$ is the Boltzmann constant, and $e$ is the unit charge. Under the assumption that the diffusion is thermal, the 1-dimensional diffusion width, $\sigma$, can be defined as a function of drift time, $t$:

$$\sigma = \sqrt{2Dt}, \tag{2.6}$$

which can be related to the drift length, $L$, such that:

$$\sigma = \sqrt{\frac{2kTL}{eE}}. \tag{2.7}$$

These types of gases have demonstrated that sub-mm diffusion is achievable for drift distances on the order of a metre [121]. NID gases are considered to be important for future directional searches with large target volumes, because extending the drift length is more cost-efficient per unit volume than the production of larger readout planes [122].

### Charge Amplification

Once charge arrives at the readout plane it must be amplified so that it can be easily registered by charge sensitive electronics. This is done by subjecting the charge to a region with a high electric field strength. The large electric field causes the charge to accelerate and subsequently collide with other gas molecules, initiating an avalanche of ionisation. Several detector geometries exist for amplifying charge [123, 124], subsection 2.4.2 will later present some options which are of particular interest for future directional searches.

The extent of amplification is quantified by the gas gain of the detector, defined as the multiplication factor between the initial liberated charge and the total charge following the avalanche. The amplification can be parameterised such that [125]:

$$ln(Gain) = dPAe^{-\frac{BP}{E}}, \tag{2.8}$$

where $d$ is the length of the amplification gap, $P$ is the gas pressure, and the Townsend coefficients are given by $A$ and $B$. An alternative parameterisation is outlined by the Rose-Korff equation which takes the form [126, 127]:

$$ln(Gain) = \frac{d}{\lambda}e^{-\frac{-I_e}{\lambda E}}, \tag{2.9}$$

where $I_e$ is the ionisation potential of the gas and $\lambda$ is the mean free path which depends on the molecular number density, $N_m$, and the primary ionisation cross section, $\sigma_p$, such that [116]:

$$\lambda = \frac{1}{N_m \sigma_p}. \tag{2.10}$$

The amplification process is more complex in the case of NID gases because of its strong electronegative nature. When the NIs arrive at the amplification field, they are accelerated but the electron must first be stripped from the NI before the charge amplification can occur [119].

This results in gas gains which are typically orders of magnitude smaller than conventional gases; this is a limitation which is addressed by work presented in Chapter 4 - 7.

### Electron Recoil Discrimination

Ionising particles produce signatures with characteristic traits which can be used for particle identification. These characteristic traits are heavily dependent on the type of ionising event and detector medium. For direct DM detection experiments, the ability to correctly identify ERs and NRs is very important because ERs are a background for WIMP-nucleon scattering searches. Therefore proficient detector technologies should be able to achieve ER discrimination to a high level of accuracy.

In low pressure gaseous TPCs the interaction processes associated with gamma radiation, like Compton scattering and photoelectric absorption, initiate ERs. Due to the relatively high charge-to-mass ratio of electrons, the tracks of ionisation they typically leave behind are not straight and they deposit a relatively low amount of energy per unit length, $\frac{dE}{dx}$. On the other hand, neutrons and theoretical WIMPs induce NRs in the gas volume. The larger mass of the recoiling nucleus means that the recoils are much shorter, more rectilinear, and produce larger $\frac{dE}{dx}$ than ERs of comparable energy. These characteristic traits can be used for ER discrimination in directional searches. In particular, the higher charge density of NRs has previously been leveraged for ER rejection by enforcing $\frac{dE}{dx}$ cuts in low pressure gaseous TPCs [128].

### Head-Tail Effect

There are varying degrees of directionality which can be extracted from a recoiling nucleus. Figure 2.5 illustrates the different levels of directional information which can be extracted

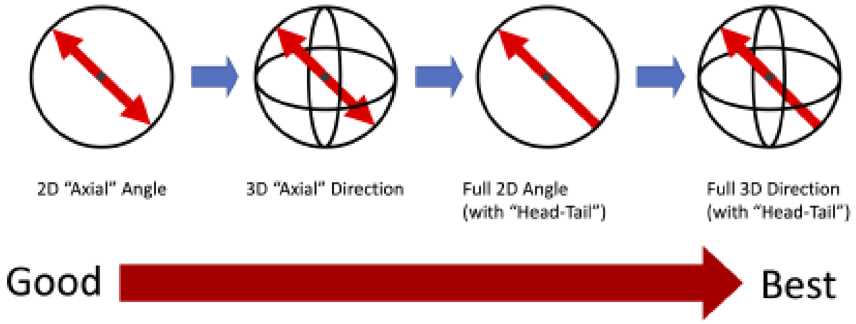

Figure 2.5 Illustration showing the varying degrees of directionality which can be achieved [129].

from "good" to "best". A detector with good directionality should be able to determine the principle axis of a recoil in 2-dimensions. A greater measure of axial directionality is achieved if the track is reconstructed in 3-dimensions. Axial directionality in 3-dimensions can still be improved upon if the sense of the recoil, i.e. the direction along the principle axis, is also known. Sense recognition is an incredibly powerful tool because it can reduce the number of recoils required for confirmation of an anisotropic signature, consistent with the WIMP wind, from hundreds to tens of events [130]. Knowledge of both the principle axis and recoil sense in 3-dimensions is therefore the ultimate goal for directional DM searches.

The head-tail effect has been shown to encode the sense information of NRs in low pressure gaseous TPCs [131]. The head-tail effect takes advantage of the asymmetrical deposition of energy along the path of a recoiling nucleus. Figure 2.6 shows how a recoiling nucleus deposits more energy, thereby liberating more charge, at the beginning of the track (tail) compared to the end (head). This is opposed to what is observed with charged heavy particles as the recoiling body is neutral. A high-granularity $\frac{dE}{dx}$ measurement can therefore be used to determine the direction along the principle axis of the recoiling nucleus.

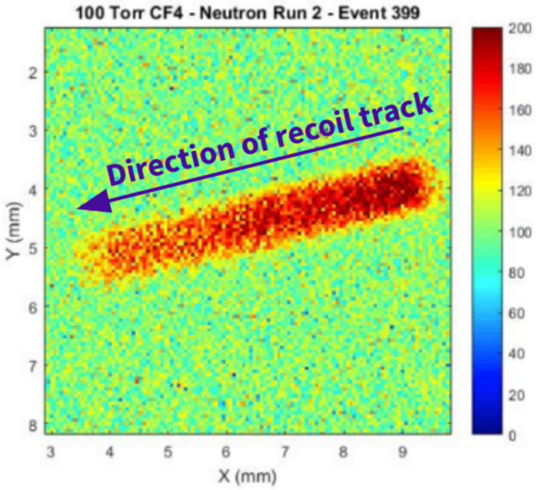

Figure 2.6 High resolution optical CCD image of scintillation light from a 12.3 keV$_r$ NR in 100 Torr$^2$ of CF$_4$ demonstrating the head-tail asymmetry. Adapted from Ref. [132].

### Minority Carriers

Fiducialisation of the detector volume is an important consideration in low background direct DM experiments. The 2-dimensional readout plane in a gaseous TPC can be easily

---

[2] The Torr is a unit of pressure commonly used in low pressure gaseous TPC literature. For the convenience of the reader it is useful to know that 760 Torr = 1 atm = 101325 Pa.

fiducialised by implementing a veto region close to the edge of the detector volume; however, fiducialisation in the z-axis, along the drift field, is not as trivial. Unlike the S1 event in two-phase xenon and argon experiments (see Chapter 1 for details), low pressure gaseous TPCs with charge readout do not have an initialisation event which can be used to determine the absolute depth of an event in the target volume. Without the knowledge of the absolute distance at which an event occurred from the anode plane, it can be challenging to filter NR backgrounds caused by radioactive decays on either the cathode (high z) or anode readout (low z) plane.

Minority carriers in NID gases can provide relief for the challenge of fiducialisation in gaseous TPCs. As discussed, NID gases transport charge via NIs rather than electrons. As shown in Figure 2.7, depending on the gas mixture, it is possible for different species of NIs to form in a single event. In this instance, an event from $SF_6$ is shown which has a majority carrier, $SF_6^-$, and a minority carrier, $SF_5^-$. Minority carriers are a NI species which constitute a small fraction of the total charge produced by an event and have a mass which is different to the majority carrier species. The difference in mass has implications for the mobility of the NI and, by extension, for the drift velocity. This results in two signal pulses per event and the absolute distance of the event from the readout plane, $Z$, is related to the time difference between the pulses, $\Delta t$, according to [119]:

$$Z = \frac{v_s \times v_p}{v_s - v_p} \Delta t, \tag{2.11}$$

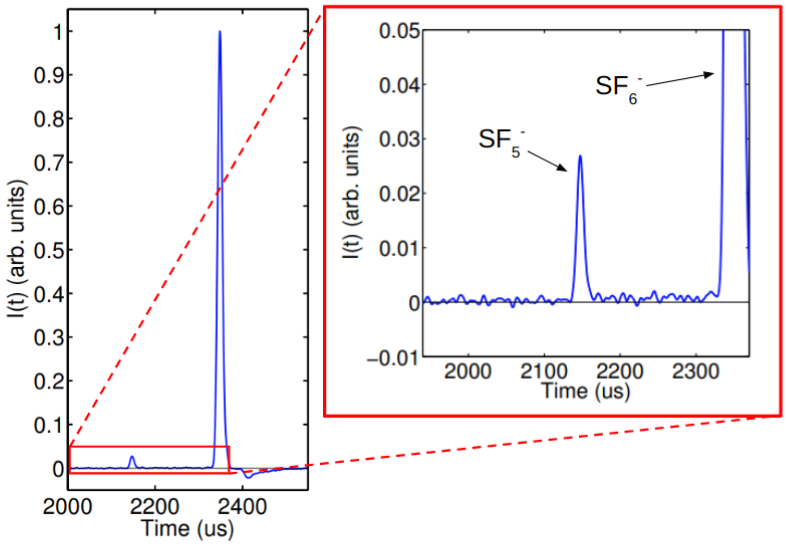

Figure 2.7 An example of the minority carrier principle in the NID gas $SF_6$ at low pressure. Adapted from Ref. [119].

where $v_p$ is the drift velocity of the primary/majority NI species and $v_s$ is the drift velocity of the secondary/minority species. The drift velocities can be determined via the reduced ion mobility via Equation 2.4. Therefore, the absolute depth of an event can be determined via the time difference between the signal pulses of different NI species. Thus, minority carriers provide a means for total fiducialisation of a gaseous TPC volume.

### 2.2.2 Alternative Methods of Directional Detection

Low pressure gaseous TPC technology is relatively well established as a method of directional detection and is the main focus of the work presented in this thesis. However, other detector technologies are also being developed for directional DM detection. In this subsection, a few alternative viable detector technologies are discussed.

#### Anisotropic Scintillators

Normal scintillating materials produce visible/UV light proportional to the excitation, and subsequent de-excitation, caused by a particle interaction. An anisotropic scintillating crystal, like stilbene [133] and $ZnWO_4$ [134], produce a scintillation response which depends on the orientation of the NR. The light yield of this scintillator depends on the orientation of an NR with respect to the crystal lattice. When applied in the context of a directional DM search, the amplitude of NR events will vary over the course of a sidereal day depending on the orientation relative to the WIMP wind. This technology is not ideal for future recoil observatory applications because the full reconstruction of the recoil is not possible. However, one experiment proposing to utilise $ZnWO_4$ crystals, similar to the one shown in Figure 2.8, is the ADAMO experiment [135].

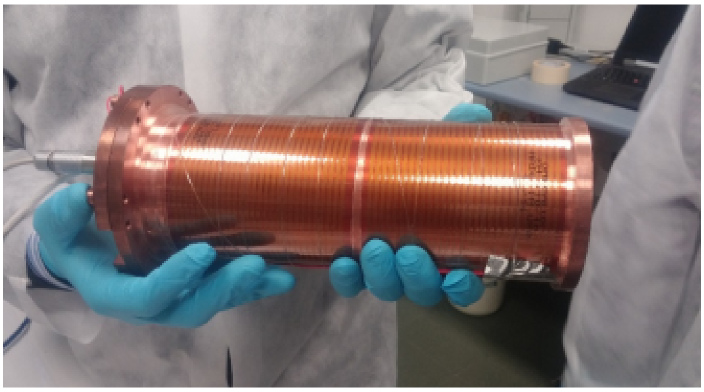

Figure 2.8 Image of a $ZnWO_4$ scintillating crystal encapsulated and coupled to a PMT [136].

### Nuclear Emulsions

Nuclear emulsions are a very high-granularity solid state detector capable of reconstructing NRs. They are typically made of AgBr crystals suspended in gelatine. The diameter of the Ag grains influences positional resolution. Emulsions with a grain size $\leq$ 200 nm are known as Nano Imaging Trackers (NITs) [137], whereas those with $\leq$ 25 nm are referred to as Ultra-Nano Imaging Trackers (UNITs) which can have a granularity as fine as 40 nm [138]. When a recoil occurs in the emulsion it leaves behind a trail of ionisation which can be observed as a track after the material has been developed. The length of a recoiling nucleus in a solid is small, on the order of a few hundred nm for a recoil of tens of keV, however the ultra fine granularity makes the high resolution imaging of these short tracks possible [139]. Figure 2.9 shows some examples of 100 keV carbon recoils in a NIT following development. The NEWSdm experiment is known to be driving the development of this technology for the application to a directional DM search [140]. However, this type of search is complicated by the long exposure times and lack of instantaneous readout. It is therefore necessary for the detector to maintain a constant orientation with respect to the WIMP wind. In the NEWSdm experiment, this is achieved by mounting the detector to an equatorial telescope [141].

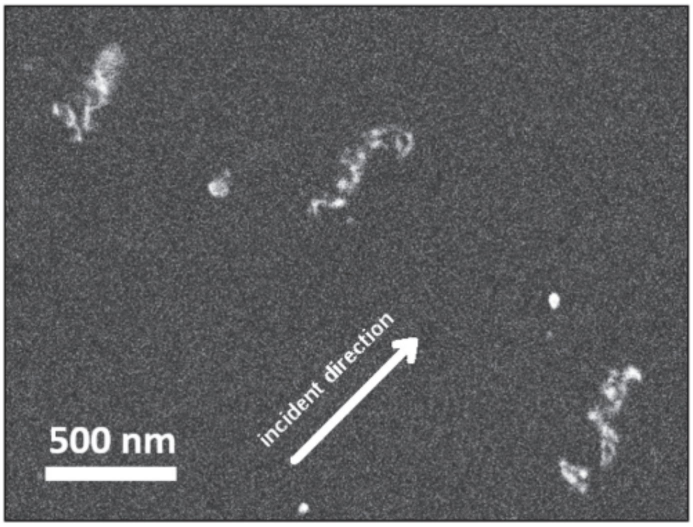

Figure 2.9 Scanning electron microscope image of 100 keV carbon recoils in a NIT following development of the emulsion [138].

### Diamond

Diamond target volumes have also been proposed as a method of probing below the Neutrino Fog with directionality [142]. By utilising a method of diamond growth called chemical vapor deposition, large uniform volumes with semiconductor properties are relatively quick to produce. When recoils occur in the diamond volume, either phonons, photons, or charge can be measured. This signal is used to triangulate the event in the crystal to the mm-scale and provides a timestamp for the event. The diamond crystal can then be removed at a later time and inspected for damage using high resolution optical and X-ray imaging techniques. This damage is caused by the particle interaction and can be used to determine the direction of the recoil. This hybrid readout method allows the direction of the recoil to be determined with respect to the orientation of the WIMP wind at the time of the event. Although this method provides a large and dense target volume, the readout method is cumbersome.

## 2.3 The Status of Directional Searches

Gaseous TPC technology is the most mature and widely practiced method of directional detection. Several research groups from around the world are currently developing and running WIMP searches using this methodology. In this subsection, the status of the field is briefly summarised and the future scope of the field with the CYGNUS collaboration is introduced.

### 2.3.1 The DRIFT Experiments

The DRIFT experimental programme is widely renowned as the World's leading directional DM search. The series of experiments started in 2001 and is hosted at Boulby underground laboratory in North Yorkshire in the UK. These experiments have pioneered numerous techniques in the field which are now considered to be standard practice.

A diagram and image of the DRIFT detector can be seen in Figure 2.10. As shown, the detector consists of a vertical central cathode wire plane design which has two 0.5 $m^3$ volumes either side. The two detector volumes utilise Multi-Wire Proportional Counter (MWPC) anode planes which are used to amplify and readout charge.

The DRIFT-I experiment was the first of its kind to implement an NID gas for the target material. The detector demonstrated stable operation with the NID gas $CS_2$ at 40 Torr which, as discussed in subsection 2.2.1, was a new initiative at the time capable of reducing the diffusion to thermal levels [143, 144]. This detector also demonstrated insensitivity to gamma/ER events by implementing a threshold cut. As discussed in subsection 2.2.1, this was possible due to the much lower density of ionisation caused by ERs [144].

The DRIFT-II experiment was the successor to the DRIFT-I experiment. During its operation, developments were made towards the study and observation of the head-tail effect

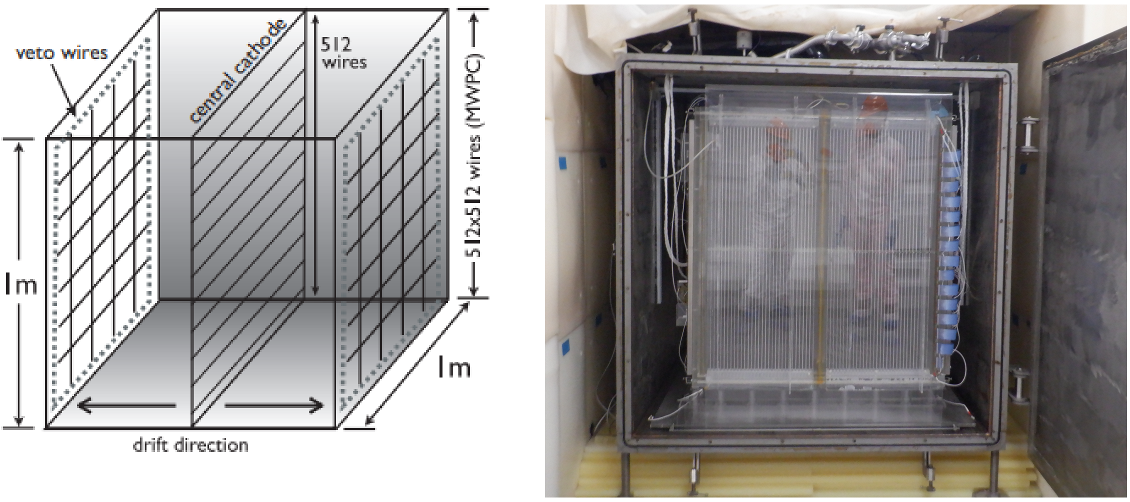

Figure 2.10 Diagram of the DRIFT-II detector (left) [143]. Image of the DRIFT-IId detector inside the open vacuum vessel (right).

[145, 146] and the fiducialisation of the detector volume through the concept of minority carriers [147]. These minority carriers were observed previously in pure $CS_2$, with possible trace amounts of $O_2$, however the amplitude of the minority peaks were only $\sim 0.1\%$ of the main peak. The amplitude of the minority peaks was found to significantly improve with the addition of a 1 Torr $O_2$ admixture to the nominal $CS_2$:$CF_4$ mixture with partial pressures 30:10 Torr. The time difference between consecutive peaks could therefore be used to fiducialise the drift volume of DRIFT-II [148]. The concept of minority peaks is still studied for fiducialisation in recent Research and Development (R&D) efforts [119, 149].

Following these breakthrough developments, the DRIFT experiment was able to set world leading directional WIMP-nucleon cross section limits. Figure 2.11 shows the published SD results from the experiment compared to other searches; only two other experiments of those shown, NEWAGE and DMTPC, have directional capability. As can been seen, the DRIFT experiment was able to achieve a limit of 0.28 pb at 100 GeV/$c^2$. This result is still competitive with new directional limits published recently by the NEWAGE experiment [150].

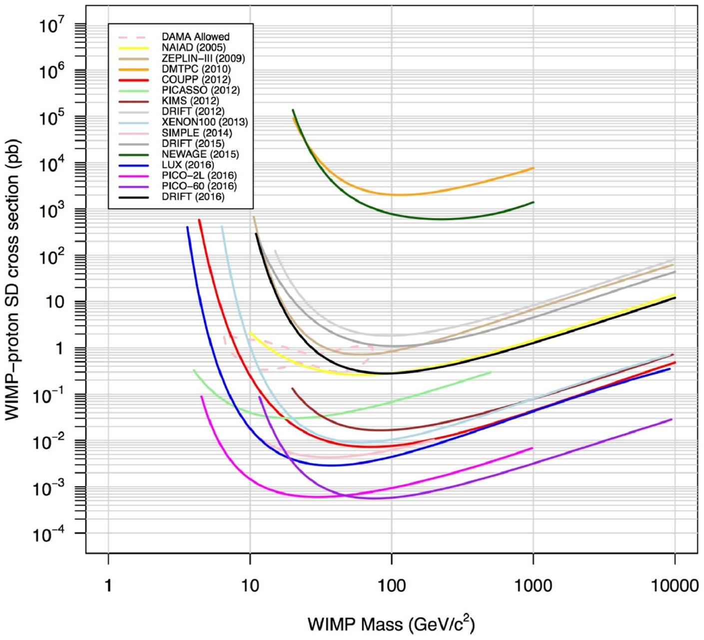

Figure 2.11 The SD WIMP-nucleon cross section limits of the DRIFT-II search (black) compared to other previous search results. Alternative directional experiments include NEWAGE (dark green) and DMTPC (orange). Other experimental limits are from searches which are not capable of observing a directional signal [151].

## 2.3.2 Other Directional Gaseous Searches

Several other directionally sensitive gaseous TPC searches, similar to DRIFT, have also been carried out; images of a few notable detectors used in some of these searches can be seen in Figure 2.12. The most competitive of which is the NEWAGE experiment hosted at Kamioka Observatory in Japan [150]. This experiment utilises a one-sided TPC design with a cathode mounted 41 cm from the anode plane. The anode plane consists of a Gaseous Electron Multiplier (GEM) coupled to a type of Micro-Pattern Gaseous Detector (MPGD), called a Low $\alpha$ emitting Micro-PIxel Chamber ($\mu$-PIC) [152]. These detector technologies are discussed in more detail later in Section 2.4. The target gas used in this search is pure $CF_4$ at 76 Torr. This gas, although not an NID gas, is favourable due to the fluorine content which is predicted to have an improved SD WIMP-nucleon interaction cross section [153].

This gas has other beneficial properties, like scintillation, which was utilised in the DMTPC search [158]. The DMTPC experiment used two CCD cameras for capturing the scintillation light produced by events in a 10-L back-to-back TPC, filled with 75 Torr of $CF_4$, during a surface run. The surface run with this detector identified that background events induced by radioactivity in the CCD chip can be removed by requiring coincidence with a

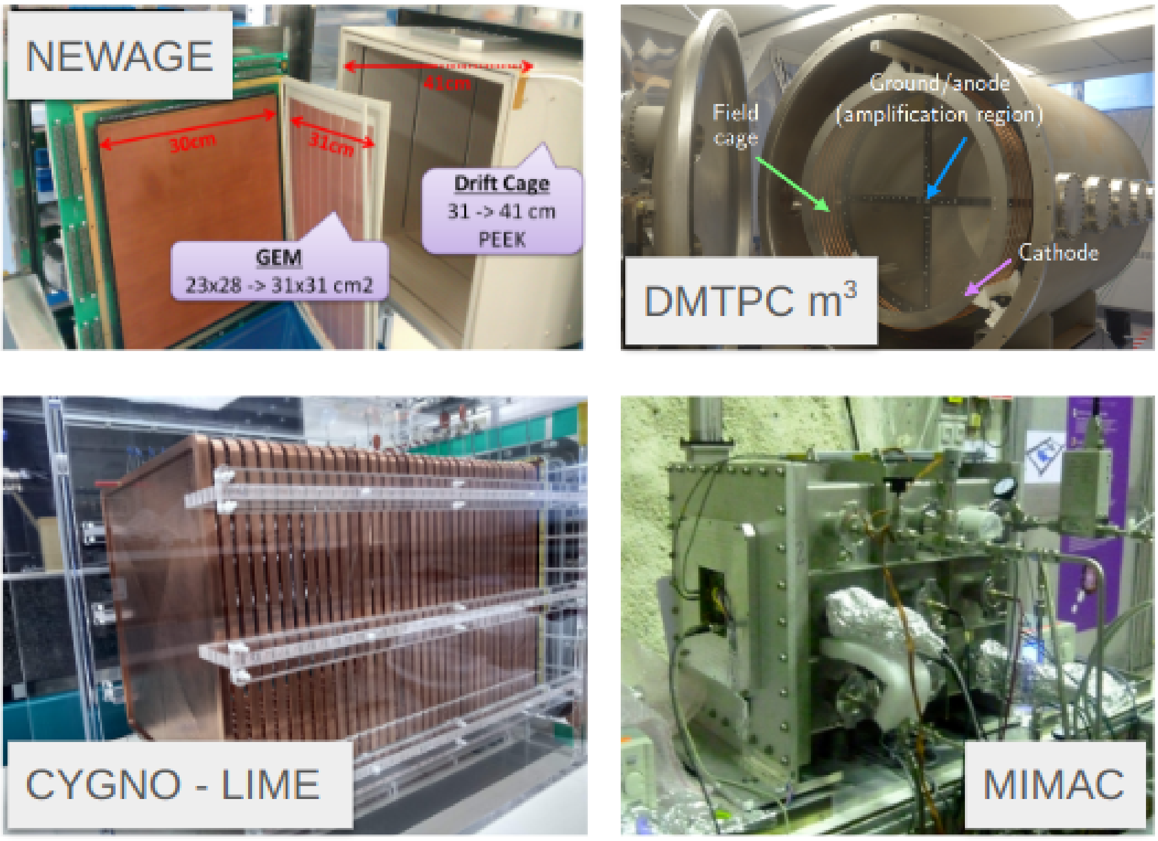

Figure 2.12 A few notable directional DM detection experiments which utilise the gaseous TPC approach similar to DRIFT; including the NEWAGE detector (top left), the DMTPC $m^3$ prototype (top right), the CYGNO LIME prototype (bottom left), and the MIMAC detector (bottom right). Images adapted from Ref. [154–157].

PMT [158]. The scale up of this approach is planned for implementation in an underground search at SNOLAB with a larger 1 $m^3$ volume [159].

The scintillation property of $CF_4$ is also used by the CYGNO collaboration which is currently in a prototyping and R&D phase with the LIME experiment at Laboratori Nazionali del Gran Sasso in Italy. This prototype currently uses a single-sided TPC design featuring a 50 cm drift length with an anode plane consisting of a triple GEM structure for charge amplification. The optical readout plane is implemented with 4 PMTs, used for triggering, and a scientific CMOS camera capable of imaging a $33 \times 33$ $cm^2$ readout area. The CYGNO collaboration currently uses a gas mixture of $CF_4$:He in ratio 40:60 at atmospheric pressure which reduces the cost of the containment vessel. The He nuclei offer improved sensitivity to lower WIMP masses in the range 1-10 GeV. This readout method has proven to provide a high-granularity positional sensitivity and the next phase of the CYGNO roadmap will see this technology applied to a 1 $m^3$ back-to-back demonstrator called CYGNO_04 in the next few years [160, 161].

The MIcro-TPC MAtrix of Chambers (MIMAC) experiment is a low pressure directional DM search experiment hosted at Modane Underground Laboratory in France [162]. The detector prototype is a 25 cm drift back-to-back TPC filled with a gas mixture of $CF_4$ + 28% $CHF_3$ + 2% $C_4H_{10}$ at 50 mbar (37.5 Torr). Although the majority of the mixture consists of the scintillating gas $CF_4$, the readout is based on charge amplification with a type of MPGD called a pixelated micromegas [163]. Studies conducted by the MIMAC group have found that a 10 kg detector similar to the MIMAC prototype would be very competitive with other DM searches in the SD parameter space [164]; however, explicit search results have not yet been published.

### 2.3.3 The CYGNUS Collaboration

As discussed in the previous subsections, there is a diverse community of directionally sensitive gaseous TPC experiments searching for the WIMP wind. As the issue of the Neutrino Fog becomes more encumbering for conventional counting experiments, the unique research and development performed by this community will form the basis for the next generation of direct DM searches beyond the Neutrino Fog. One such experiment has been proposed by the CYGNUS collaboration [122].

The CYGNUS collaboration brings together the majority of groups working on gaseous TPCs for directional detection and has proposed a global network of nuclear recoil observatories in underground sites including: Boulby (United Kingdom), Stawell (Australia), Kamioka (Japan) and Gran Sasso (Italy) among others. The proposed detectors, shown in Figure 2.13, are very similar in design and dimensions to the DRIFT experiment; consisting of a back-to-back TPC called a CYGNUS-$m^3$ module. Multiple detector modules will be positioned together inside layers of shielding at each observatory location. The modular design allows the experiment to be easily scalable for future expansion and the multi-site aspect will provide further evidence of the galactic origin of any observed signal.

The CYGNUS consortium is currently in an R&D phase which aims to identify the most suitable next generation technologies which can be used in the CYGNUS-$m^3$ module. There are several avenues of current research including different gas target mixtures and new technologies for charge amplification and readout. Despite the ongoing detector development, the collaboration has made some predictions about the discovery reach of a global CYGNUS search. These predictions for the SI and SD limits for different detector scales, ranging from 10 $m^3$ to 100,000 $m^3$, can be seen presented in purple alongside other experimental search limits in Figure 2.14. These limits are calculated with the angular resolution, head-tail

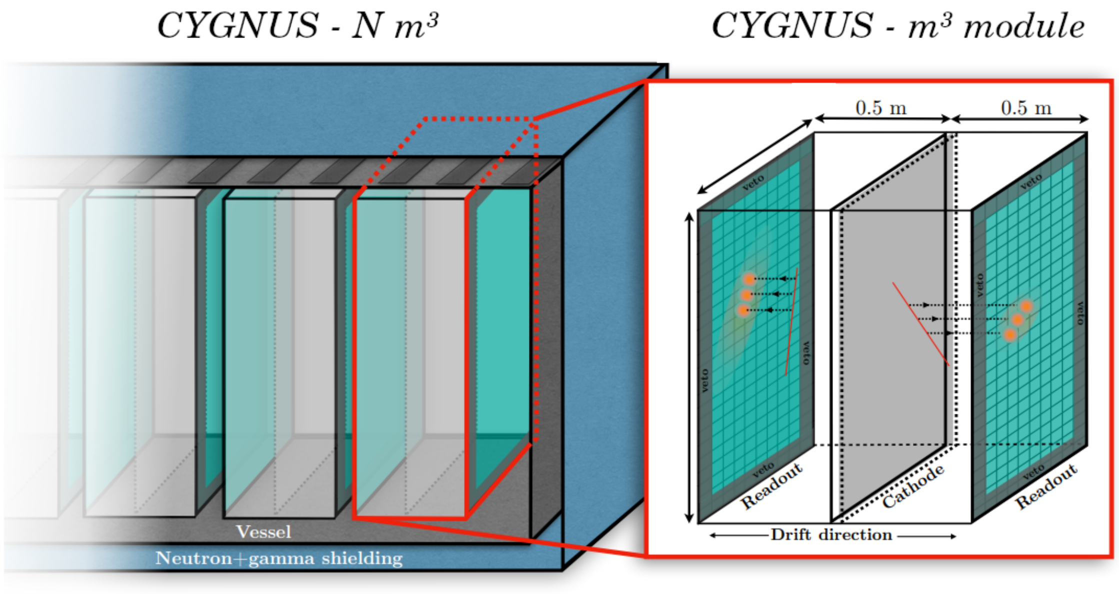

Figure 2.13 Diagram of the modular CYGNUS $N \times 1$ m$^3$ detector with $N$ back-to-back TPCs housed inside a single vessel surrounded by appropriate shielding. Adapted from Ref. [122].

recognition efficiency, energy resolution, and charge detection efficiency estimates based on a simulated strip detector response [122]. The large fluorine content, in the proposed He:SF$_6$ target mixture, makes this search particularly competitive in the SD parameter space even for

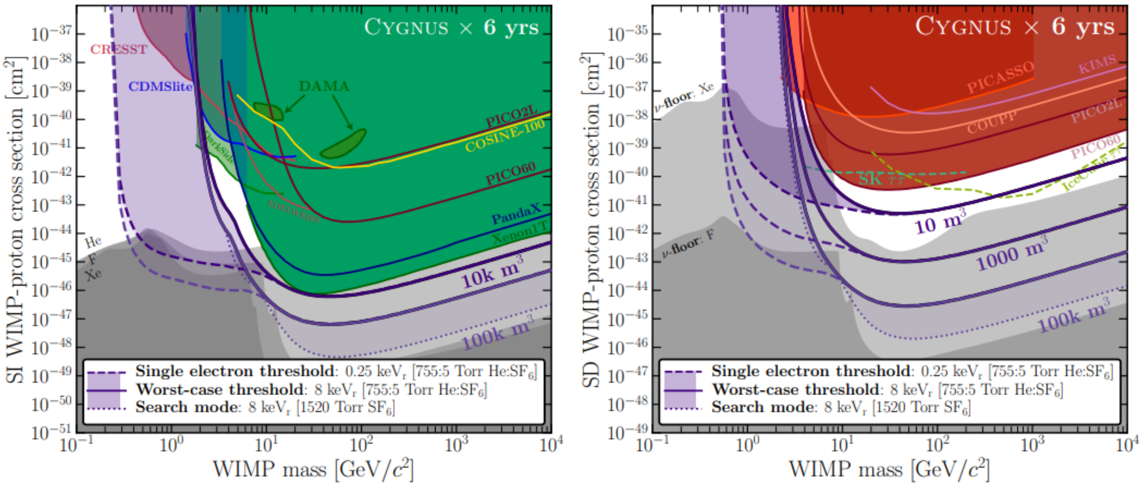

Figure 2.14 Spin independent (left) and spin dependent (right) limits predicted for the CYGNUS experiment with increasing volumetric exposures projected for a 6 year measurement [122].

a relatively modest 10 $m^3$ volume. Additionally, the low threshold limits demonstrate the ability to examine the previously unexplored parameter space below 10 GeV/$c^2$.

## 2.4 Next Generation Detector Development

The CYGNUS-$m^3$ module, discussed in the previous section, is conceptually identical to the DRIFT experiment. Although the detector limits presented in Figure 2.14 were based on a specific detector design and gas targets, the specification of the detector has not yet been confirmed and is subject to much research. In this section, a few of the major avenues for next generation detector development are outlined.

### 2.4.1 Gas Mixture Targets

The use of NID gases for high-fidelity positional resolution was developed by the DRIFT experiments. At the time, $CS_2$ was identified as a suitable electronegative gas target. However, $CS_2$ is not an ideal gas to work with in an underground laboratory environment. This is because it is toxic, flammable, and can even be explosive under certain circumstances [165]. It is therefore advantageous to find an alternative gas target which is electronegative and safer to use.

Since the demonstration of the NID concept with $CS_2$, directional detection experiments have begun investigating the use of $SF_6$ as an alternative NID gas [122, 149, 166]. $SF_6$ is commonly used as a insulating gas for High Voltage (HV) applications because of its electronegative properties; this makes it a prime candidate as an NID gas. Additionally, $SF_6$ is non-toxic and non-flammable which makes it more practical to work with in an underground facility. Furthermore, similar to the motivation for using $CF_4$, discussed previously, the large proportion of fluorine significantly improves the SD WIMP-nucleon cross section due to the odd number of protons contained in the nucleus. These properties all suggest that $SF_6$ is an ideal NID gas candidate for next generation directional DM detectors.

Another important consideration for a next generation gas target is the operating pressure. Low pressure is used in the majority of gaseous TPC searches because this facilitates NR tracks on the mm-scale which are more suitably matched to the resolution of charge readout technologies. One challenge associated with this low pressure requirement is the limited number of target nuclei available for WIMP-nucleon scattering. Additionally, operation at low pressure requires expensive containment vessels which are capable of sustaining a vacuum. These concerns can not be addressed by simply increasing the gas pressure without also sacrificing directionality. Although, the addition of helium to low partial pressures of $SF_6$ to achieve atmospheric pressure operation has been suggested by the CYGNUS collaboration. Simulations, shown in Figure 2.15, indicate that both helium and fluorine recoils will be on the mm-scale; this is possible because the lighter helium nuclei do not significantly impede the length of the fluorine recoils. Furthermore, the lower mass of helium nuclei will significantly improve sensitivity to lower WIMP masses. The CYGNUS limits presented in Figure 2.14 consider a mixture of He:$SF_6$ with ratio 755:5 Torr. Work is presented in Chapter 3 and 6 which investigates charge amplification in helium gas mixtures which contain $CF_4$ and $SF_6$.

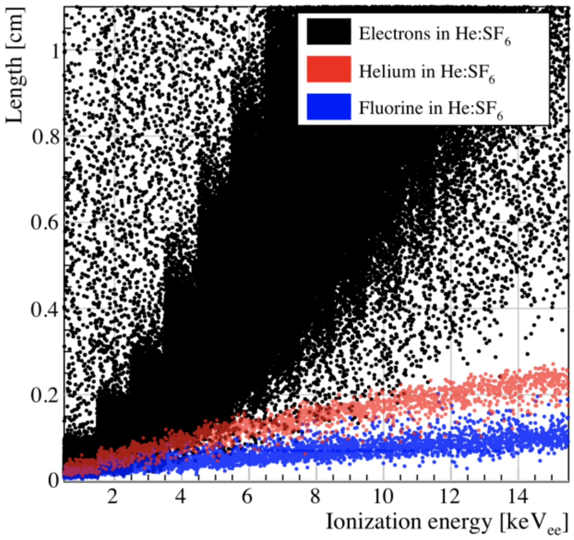

Figure 2.15 Simulated electron (black), helium (red) and fluorine (blue) recoils in a mixture of He:$SF_6$ with partial pressures 755:5 Torr [122].

### 2.4.2 Charge Amplification Technology

Finding a technology which can produce a significant amount of charge amplification in a given gas mixture is fundamentally important for improving the minimum detectable energy threshold. The DRIFT experiment utilised large amplification fields between planes of wire readouts to amplify the charge. In more recent years, the production and use of MPGDs has become commonplace. MPGDs take advantage of the improvements in manufacturing techniques like photolithography, doping, coating and etching to create structures at the sub-mm scale [167].

A popular MPGD technology called a Gaseous Electron Multiplier (GEM) is now widely used across the field of particle physics. An electron microscope image and cross sectional diagram of this technology can be seen in Figure 2.16. The GEM consists of a dielectric material intercalated between two copper electrode layers; GEMs with a thicker dielectric layer are often referred to as Thick GEMs (ThGEMs). Holes are etched, typically using chemical techniques, into the layers of the GEM in a regular pattern. When mounted with a cathode to form a TPC, the copper electrodes are biased with high voltage to establish a large amplification field in the holes of the GEM. As free electrons approach the GEM, they are guided into the holes by the field lines at the interface between the drift volume and amplification gap. The electrons are then accelerated to large velocities and the subsequent collisions with gas molecules cause an exponential avalanche of ionisation. The avalanche electrons are then collected on the electrode on the opposite side of the GEM and measured with charge sensitive electronics.

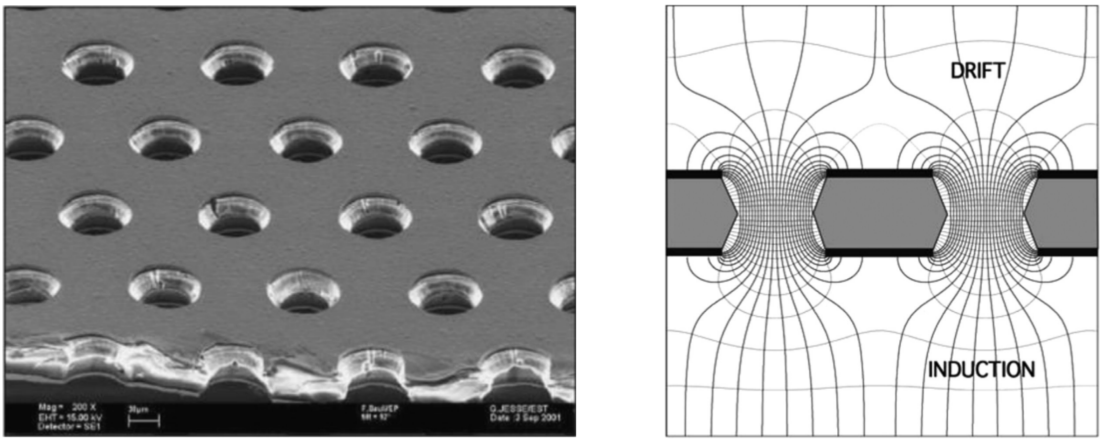

Figure 2.16 Electron microscope image of a Gaseous Electron Multiplier structure (left). Cross sectional diagram indicating the electric field lines established once the top and bottom planes have been biased (right) [168].

GEMs and ThGEMs have proven to be effective planar charge amplification devices in conventional electron drift gases, like $CF_4$, which are readily capable of producing gas gains on the order of $10^5$ or greater [123]. The use of this technology in NID gases is still relatively uncommon. The maximum attainable gas gains produced in an NID gas with GEMs or ThGEMs are typically on the order of $10^3$ and often require double or even triple GEM configurations [119, 169–171]; this amplification is comparable to previous proportional counter technology [172]. The difficulties of charge amplification in an NID gas has been attributed to the requirement to first strip the electron before an avalanche can ensue. This comparatively low level of amplification has implications on the energy threshold of future WIMP searches. Therefore, the challenge of producing a level of amplification which is comparable to conventional drift gases requires significant attention. The recent development of multi-layer GEM structures, like the M-ThGEM [173] and MMThGEM [174], which reduce charge losses between transfer regions are one possible avenue for development.

Work which focusses on the use of a ThGEM and MMThGEM for producing large charge amplification in both helium mixtures and NID gases and mixtures is presented in Chapter 3 - 6.

### 2.4.3 High-granularity Charge Readout Technology

As discussed, charge amplification is fundamental for the realisation of next generation readout technology in NID gases. Following the amplification stage, the amplified charge needs to be measured by a segmented readout plane in order to facilitate 3-dimensional track reconstruction. This readout technology is required to have a level of granularity which is suitable to the length of NRs in the target gas.

MWPCs, used by the DRIFT experiment [177], and a ThGEM-multiwire hybrid [178] have demonstrated wire pitches of 1 - 2 mm. This mm-scale is a physical limitation of the wire readout technology caused by the electrostatic forces between neighbouring wires. This meant that the wires could not be positioned closer together without experiencing significant mechanical deformation. This level of granularity was suitable for low pressure operation; however, with the desire for atmospheric operation with an He:SF$_6$ mixture in future searches, devices with a sub-mm granularity would be better suited.

Strip and pixel based MPGD designs provide an alternative to wire based readouts which are not limited to mm-scale resolution. The micromegas and the $\mu$-PIC, shown in Figure 2.17, are two MPGD readout designs which are currently under investigation by the directional community; these particular designs both feature strip electrodes which have

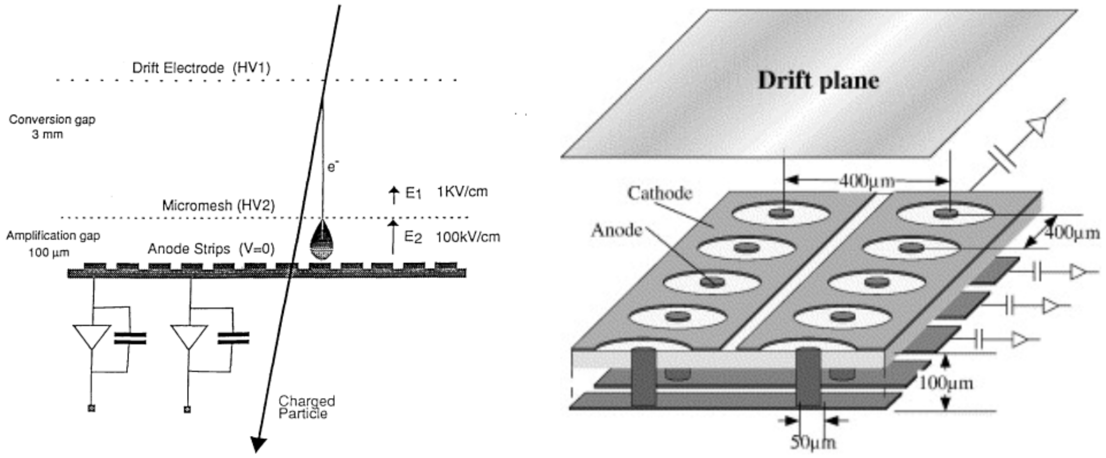

Figure 2.17 Diagrams showing the different geometries of a simple micromegas (left) [175] and $\mu$-PIC detector (right) [176].

been highlighted as a cost-effective scalable geometry for a CYGNUS search [122]. The micromegas utilises a mesh electrode above the strip readout plane for charge amplification. The positional resolution of the micromegas is set by the pitch of the strips in perpendicular x and y-axis planes. Due to the insulating support structure, which the strips are printed on, a pitch on the order of hundreds of microns can be easily achieved. The $\mu$-PIC utilises an alternative geometry for charge amplification. As shown, each strip in the upper electrode layer features equally spaced holes along the length. The lower strip layer features projections which protrude though the holes in the upper strip layer. A large potential difference is then applied between the lower and upper strip layers which establishes the avalanche region. The manufacture of $\mu$-PIC designs with a granularity of 400 $\mu$m has been successfully demonstrated [152, 176]. For comparison, the MIMAC collaboration has demonstrated a micromegas with pitch of 200 $\mu$m [179] and finer granularity down to 100 $\mu$m has also been demonstrated elsewhere [180]. Work which utilises micromegas designs is presented in Chapter 7 - 9.

The fine sub-mm pitch, associated with MPGD designs, requires an order of magnitude more electrodes to cover the same readout area as an MWPC. This can drastically increase the number of channels requiring charge sensitive readout electronics and dedicated data acquisition channels. Some techniques have been implemented previously, like grouping channels together [177] and multiplexing [181], to circumvent the need for more channels. However, the significant increase in the number of electrodes means that considerable attention to the choice of electronics and data acquisition system will be required for the future CYGNUS search. Work which implements a scalable electronic system with a micromegas detector is presented in Chapter 8 and 9.

## 2.5 Conclusions

In summary, the Neutrino Fog has now begun to impose an irreducible background signal for the current leading conventional direct WIMP detection experiments. The only conclusive method for measuring the WIMP wind, beyond the Neutrino Fog, is through the directional measurement of recoiling nuclei induced by WIMP-nucleon scattering. Several detection methods for performing a directional DM search are available; the most developed method thus far is the use of low pressure gaseous TPCs. The next generation of these searches have been proposed by the CYGNUS collaboration and will encompass a global network of nuclear recoil observatories. The detector specification of the CYGNUS-m$^3$ module is currently subject to small scale testing. To this effect, major avenues for next generation detector development include the target gas mixture and technologies for improved charge amplification and higher-granularity charge readout.

# Chapter 3

# Charge Amplification in Sub-atmospheric $CF_4$:He Mixtures with a ThGEM

This chapter is a reproduction of the *Journal of Instrumentation* publication titled *"Charge Amplification in Sub-atmospheric $CF_4$:He Mixtures for Directional Dark Matter Searches"* and consequently contains some repetition of information stated in previous chapters.

As discussed in Chapter 2, the fluorine content of $CF_4$ makes it a favourable candidate for SD directional DM searches, with a caveat that it must be operated at low pressure to achieve significant NR lengths. Introducing helium to low pressure $CF_4$ offers the possibility for atmospheric operation and thus reducing the cost of a containment vessel; whilst also offering improved sensitivity to lower WIMP masses. Furthermore, the helium atoms are not expected to significantly impede the length of the $^{12}$C and $^{19}$F recoils. In this chapter, charge amplification in an extensive range of $CF_4$:He gas mixtures is demonstrated with a single ThGEM.

To begin, the experimental method and gas mixing procedure is first introduced in Section 3.2. Following this, charge amplification measurements in low pressure pure $CF_4$ is presented in Section 3.3 before helium is gradually added incrementally in Section 3.4. Finally conclusions are presented in Section 3.5.

## 3.1 Introduction

Dark Matter (DM) comprises 85% of the mass in the observable Universe. The existence of Weakly Interacting Massive Particles (WIMPs) is one of the possibilities that could transpire to account for DM, yet the direct measurement of such a particle has not been confirmed. In the field of DM detection, many attempts have been made to measure the rare low energy events expected when WIMPs elastically scatter off nuclei; despite significant improvements in the sensitivity of WIMP detectors in recent years, the positive identification of recoils instigated by WIMPs has not been established [182]. Results from the leading two-phase xenon Time Projection Chamber (TPC) experiments, LZ and XENON, indicate that there is no excess in the number of events close to the Neutrino Fog [75, 76]. The future generations of these detectors will struggle to discriminate between Nuclear Recoils (NRs) induced by neutrinos, predominately coming from the Sun, and NRs induced by WIMPs [79, 95].

Discrimination between NRs induced by WIMPs and Solar neutrinos is theoretically possible by utilising low pressure gaseous TPCs; the direction of an NR can be determined by reconstructing the track of ionisation left behind in its wake. Such a measurement would provide a galactic signature which can be used as a means for discrimination. Solar neutrinos could be distinguished from WIMP signals which, due to the motion of the Solar System around the Galaxy, are expected to originate from the direction of the Cygnus constellation. This galactic signature is further modulated by the motion of the Earth around the Sun [108, 183] and by the rotation of the Earth on its own axis which causes a directional shift over the course of a sidereal day [144]. Unlike an annual modulation experiment, a DM detector with directional capability would be able to measure a galactic signal with confidence as it could not easily be replicated by a terrestrial source [85, 86, 184].

The DRIFT detector currently holds the best published sensitivity for directional DM searches by utilising a $CS_2$:$CF_4$:$O_2$ mixture at the low pressure of 41 Torr (30:10:1 Torr) [146]. These low pressures are required in order to facilitate longer NR tracks on the millimeter scale. Since DRIFT's latest published search results, gases containing fluorine like $CF_4$ have become more popular as the $^{19}$F content is suspected to improve the spin-dependent elastic scattering rates with a possible WIMP candidate [153, 185, 186]. Additionally, $CF_4$ is proven to be readily capable of producing sufficient gas gains with a single Thick Gaseous Electron Multiplier (ThGEM) at low pressures [125, 129].

One challenge of using low pressure $CF_4$ gas is the resulting low target mass. In order to probe meaningful cross sections such a low pressure detector would need to be $\mathscr{O}(10 - 100)$ cubic meters [187, 188]. This issue can not be addressed by simply increasing the pressure without also sacrificing the directional sensitivity of the detector. Several studies have shown that the recoil length of $^{12}$C and $^{19}$F are on the order of millimeters in low pressure $CF_4$ [119, 158, 188–190]; including the successful observation of the head tail effect [131, 132], which is important for determining the direction along the principle axis of a recoil. It has also been found that the separation of NR and Electron Recoil (ER) populations at lower energy thresholds could be improved by reducing the pressure of $CF_4$ below 100 Torr [128].

To address this low pressure limitation one possibility could be to add He to gases like $CF_4$. The addition of He would increase the target mass and improve sensitivity to lower WIMP masses, without having a detrimental effect on the recoil track length of $^{12}C$ and $^{19}F$ nuclei due to its much lower density [122]. A number of researchers have already begun testing these He mixtures [169, 191–196]. Atmospheric mixtures of $CF_4$:He in molar ratios of 40:60 and 20:80 have already been successfully demonstrated [193, 195]. Sub-atmospheric $CF_4$:He mixtures with a molar ratio of 20:80 have also been tested before with a double GEM configuration but the gas mixture could not be operated at pressures lower than 400 Torr [193]. Additionally, these measurements were done with a premixed gas bottle, so the partial pressure of $CF_4$ could not be managed independently of total pressure; as discussed, the partial pressure of $CF_4$ should take priority to ensure directionality of both $^{12}C$ and $^{19}F$ recoils.

In this paper, efforts to evaluate the charge amplification performance of $CF_4$:He mixtures at sub-atmospheric pressures, while also prioritising constant low partial pressure of $CF_4$, are presented. To begin, a description of the ThGEM TPC used and methodology is discussed along with the gas filling procedure. Following this, gas gain curves and energy resolution results are presented for both pure $CF_4$ and $CF_4$:He mixtures at pressures which could produce a significant gas gain. Finally, the results are concluded and possible avenues for future work are discussed.

## 3.2 Single ThGEM TPC Setup and Methodology

The ThGEM used in this work, denoted as ThGEM-B previously in [129], was produced at CERN. The device has a thickness of 0.4 mm and, as can be seen in Figure 3.1a, the holes have a diameter of 0.4 mm and a pitch of 0.6 mm. The ThGEM top and bottom Cu layers around the holes have been etched in such a way to create a rim structure. This rim is important primarily because it reduces the probability of electrical discharge [197, 198]. Moreover, charge which collects on the surface of the rim helps to shape the field close to the holes [199]. The rim of the holes of this particular ThGEM have a width of 0.04 mm.

This ThGEM was then mounted with a cathode to a fibre glass base and was placed inside a small vacuum vessel. An image of this mounting setup can be seen in Figure 3.1b. The cathode was offset by 1.5 cm above the base and the ThGEM was then offset by 2 cm above the cathode. The cathode was biased with a negative High Voltage (HV), the bottom plane of the ThGEM was grounded, and the top plane was biased with a positive HV via the biasing line of a CREMAT CR-150 evaluation board. The potential difference between the ThGEM top and bottom planes is defined as $\Delta V_{\mathrm{ThGEM}}$. Both HV channels were provided by an NHQ

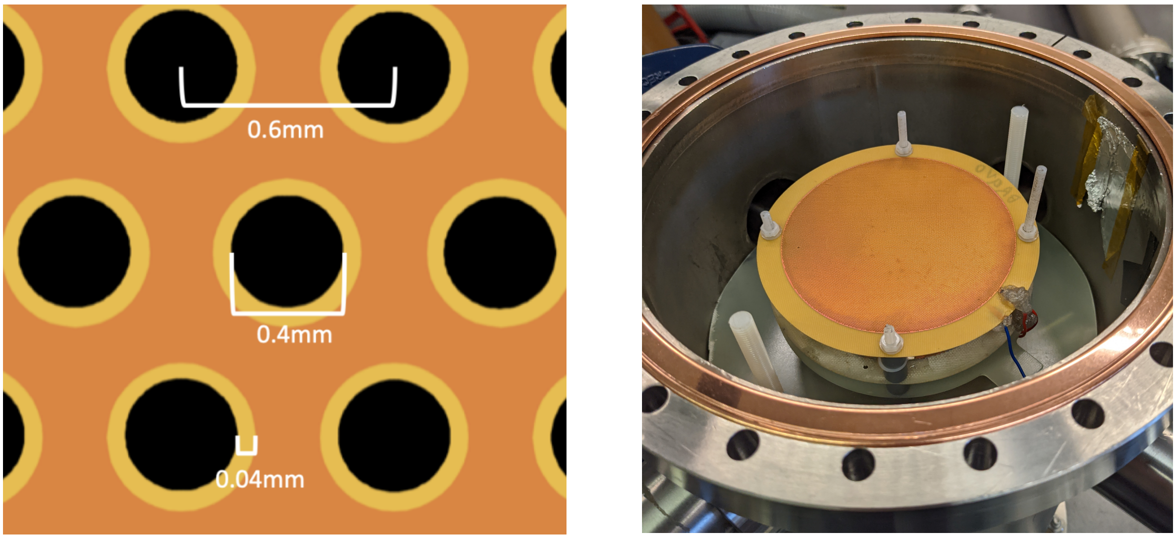

(a) (b)

Figure 3.1 Magnified top down diagram depicting the dimensions of the hole structures of the ThGEM [129] (left). Image of small scale TPC assembly inside the open vacuum vessel (right).

202M iseg HV supply. The evaluation board utilised a CREMAT CR-111 charge sensitive preamplifier chip. The exposure of the TPC assembly to an $^{55}$Fe X-ray source was controlled by securing a magnet to the source and then using a secondary magnet externally to hold the source at the desired height. This assembly was then enclosed in the vessel and evacuated for a minimum of 48 hours using a vacuum scroll pump and achieved a vacuum $< 10^{-2}$ Torr. The vessel had a leak rate < 0.1 Torr per day.

The output of the preamplifier was connected externally to a CREMAT CR-200-4$\mu$s shaper module on a CREMAT CR-160 shaper evaluation board. The output of the shaper was connected to an Ortec 926 ADCAM MCB which interfaced with the software package Maestro [200]. This allowed the signals to be binned according to their amplitude. The charge sensitive electronics were calibrated by injecting test pulses from an Ortec 480 Pulser into a 1 pF capacitor on the CREMAT CR-150 evaluation board. For all presented results, the ADC bin number was calibrated against gas gain via the W-value of pure CF$_4$, 34 eV [201], and energy of the $^{55}$Fe X-ray, 5.89 keV, by varying the amplitude of the test pulses. This is a valid approximation for the CF$_4$:He mixtures as previous weighted calculations have shown that the W-value of CF$_4$ dominates that of He, even despite being a minority component [193]. The variation in the number of initial electron-ion pairs across all mixtures is expected to be $\sim 5$ pairs.

Following an exposure to the $^{55}$Fe source, energy spectra were obtained, examples of which can be seen in Figure 3.2. The gain was then extracted by fitting a Gaussian and an exponentially falling component to the spectrum. The mean of the Gaussian was used to determine the gas gain via the calibration of the electronics. The energy resolution was then extracted by calculating the FWHM (Full Width at Half Maximum) of the Gaussian and then dividing by the mean. The spectrum on the left in Figure 3.2 shows an example with a relatively small energy resolution, conversely the spectrum on the right shows an example with a relatively large energy resolution.

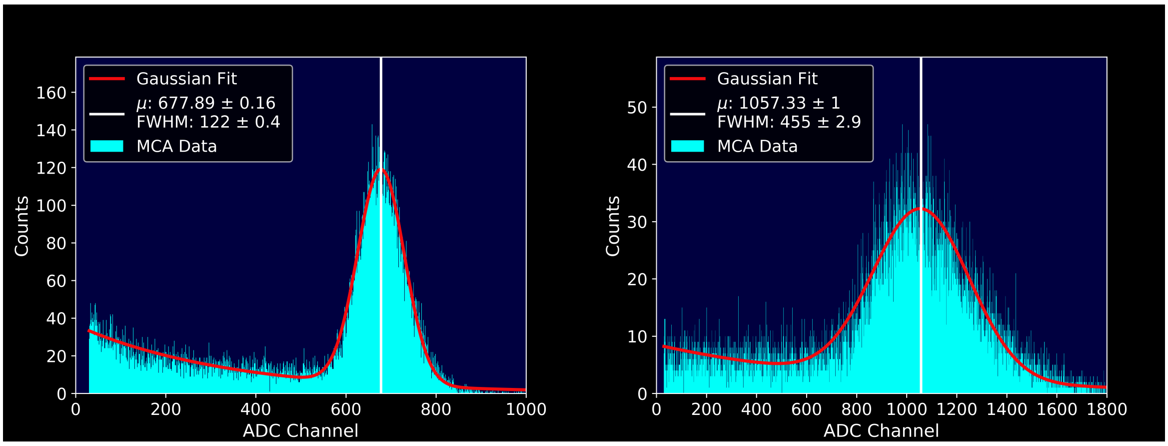

Figure 3.2 Example $^{55}$Fe spectrum in 40 torr of pure $CF_4$ with $\Delta V_{\text{ThGEM}}$ = 640 V (left). Example $^{55}$Fe spectrum in a $CF_4$:He mixture with partial pressures 40:720 Torr with $\Delta V_{\text{ThGEM}}$ = 740 V (right).

When the vessel was ready to be filled with the target gas mixture, a filling procedure was followed in an attempt to mix the gas in a repeatable way. Figure 3.3 shows a diagram which aids the explanation of the filling procedure. During the evacuation phase: the gas bottles were closed, the pump was turned on and valves V1 - V4 were all opened. The filling procedure begins by closing all the valves and turning off the pump. Both gas bottles were then briefly opened and closed to reduce the chance of gas contaminants leaking into the gas lines due to a large pressure differential. Starting with $CF_4$, the gas bottle and V1 were opened. V4 was then used as a throttle to fill the vacuum vessel to the desired pressure in a slow and controlled manner. Once the desired pressure of $CF_4$ ($p_{CF_4}$) was reached on the pressure gauge, V4 was closed along with V1 and the gas bottle. If only pure $CF_4$ was required for a measurement then this concluded the filling procedure. However when a mixture was required, the pump was then turned back on and V3 was opened to evacuate the gas line for 5 minutes. Afterwards, V3 was closed and the pump was turned off again. Then the He gas bottle and V2 were opened and V4 was again used as a throttle to fill the vessel to the desired partial pressure. Once at the correct pressure, both valves were closed along with

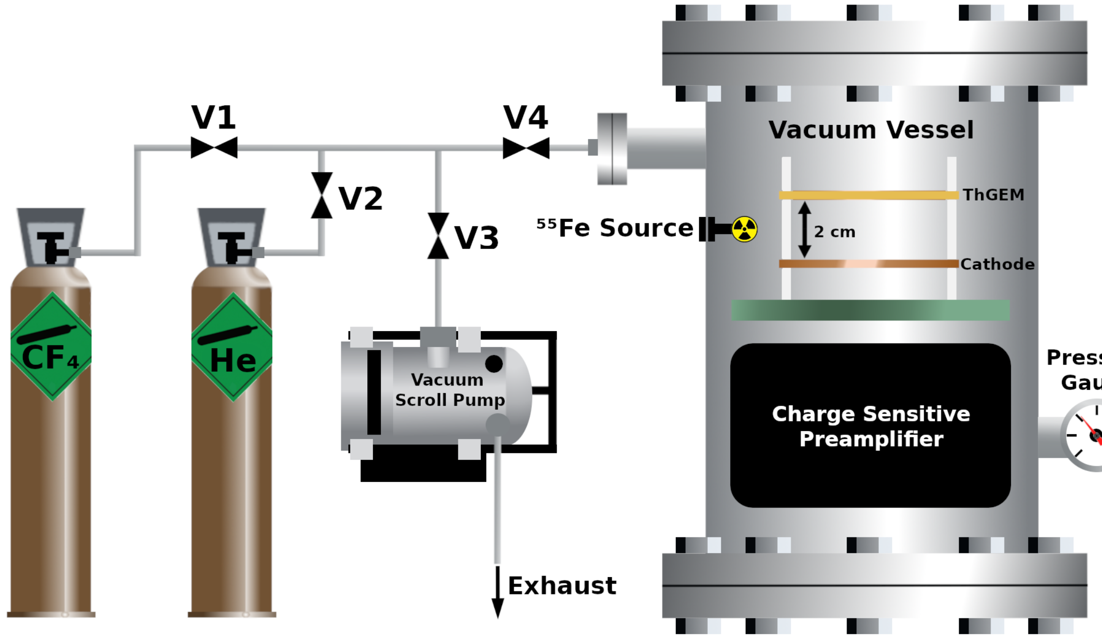

Figure 3.3 Diagram of the experimental setup and gas system used to evacuate and fill the vacuum vessel with $CF_4$ and $CF_4$:He mixtures to the desired partial pressures.

the gas bottle. Finally, after the measurements were complete, the gas system was returned to the evacuation phase.

## 3.3 Low Pressure Pure $CF_4$

As mentioned, the pressure of $CF_4$ should be low and ideally lower than 100 Torr in order to improve directional sensitivity and ER/NR discrimination. For this reason, a range of low pressures of pure $CF_4$ were tested; 5, 10, 20, 30, 40, 50, and 100 Torr. The filling procedure, as described in Section 3.2, was followed for each pressure.

Once the vessel was filled, the cathode voltage was set to -300 V; any possible systematic effects regarding the reduced drift field strength are assumed to be negligible. Then the ThGEM top voltage was increased until a clear $^{55}$Fe photopeak could be observed in the energy spectrum. Following this, the voltage was increased gradually in increments of 10 V until sparking occurred between the ThGEM top and bottom; indicated by the tripping of the current limiter on the HV supply connected to the ThGEM top. This allowed a range of operational voltages to be determined for a given pressure. Once this range was determined, the upper voltage limit was set by reducing the voltage by 10 V below the sparking limit. Intermediate voltage settings were determined by dividing the operational voltage range into five sample voltages. The result of these gain measurements can be seen in Figure 3.4.

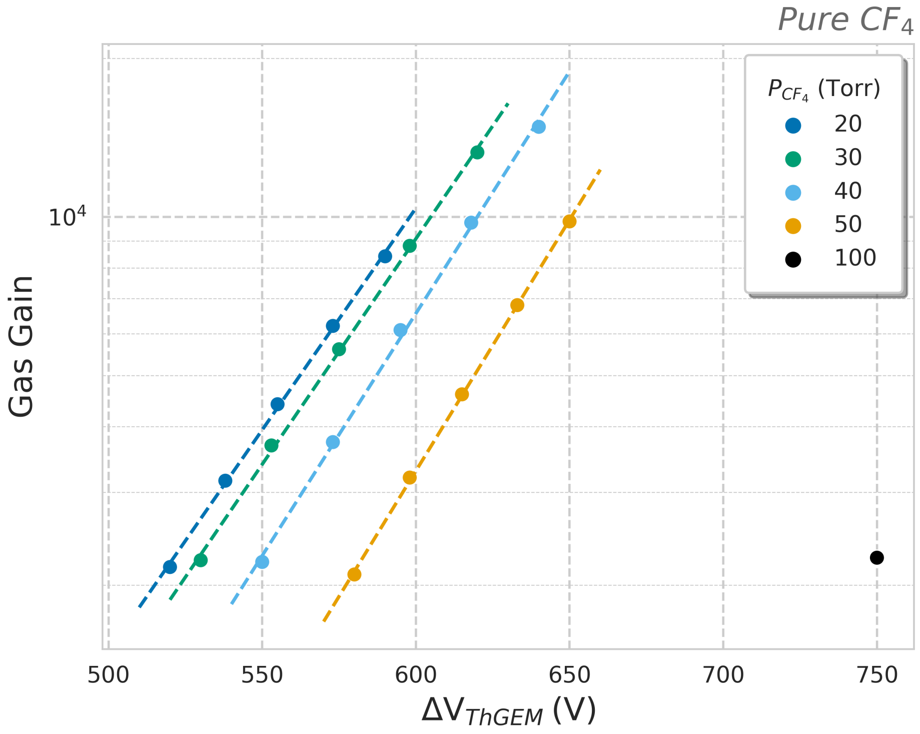

Figure 3.4 Gas gains measured in pure $CF_4$ at a range of low pressures presented on a log scale.

As can be seen in Figure 3.4, gain curves were obtained for 20 - 50 Torr of pure $CF_4$ and exhibit an exponential increase in gas gain with increasing voltage. Accordingly, exponential curves were fitted for each pressure and are displayed as dashed lines. Only a single data point was captured at 100 Torr due to a very narrow range of operating voltages before sparking occurred. Gain measurements could not be established in 5 and 10 Torr of pure $CF_4$ because sparking was observed before a clear photopeak could be seen on the energy spectrum. For the observed gain curves, it can be seen that as the pressure of $CF_4$ increases, larger $\Delta V_{\text{ThGEM}}$ voltages were required to achieve the same gas gain. This causes the gain curves to shift to the right with increasing pressure. The 40 and 50 Torr curves in Figure 3.4 are consistent with previous measurements conducted with ThGEMs with identical dimensions [125, 129]. However, the maximum gas gains achieved in Figure 3.4 are smaller than those previous results and could be a result of sparking damage discussed in [129].

The energy resolution was also calculated for each pressure and can be seen presented as a function of $\Delta V_{\text{ThGEM}}$ in Figure 3.5. The figure shows that the energy resolution decreases with increasing voltage; as expected because larger gains result in smaller variation during avalanche [202]. For a given potential difference, the energy resolution generally increases with increasing pressure. The energy resolution curves of 20, 30 and 40 Torr are very similar; however at 50 Torr the energy resolution increases significantly. The best energy resolution in 50 Torr is comparable to the worst energy resolutions measured in 20, 30 and 40 Torr. Furthermore, the energy resolution measured at 100 Torr is significantly worse than all the measurements at lower pressure. This suggests that, in addition to being beneficial for directionality, lowering the pressure of $CF_4$ below 100 Torr improves the energy resolution.

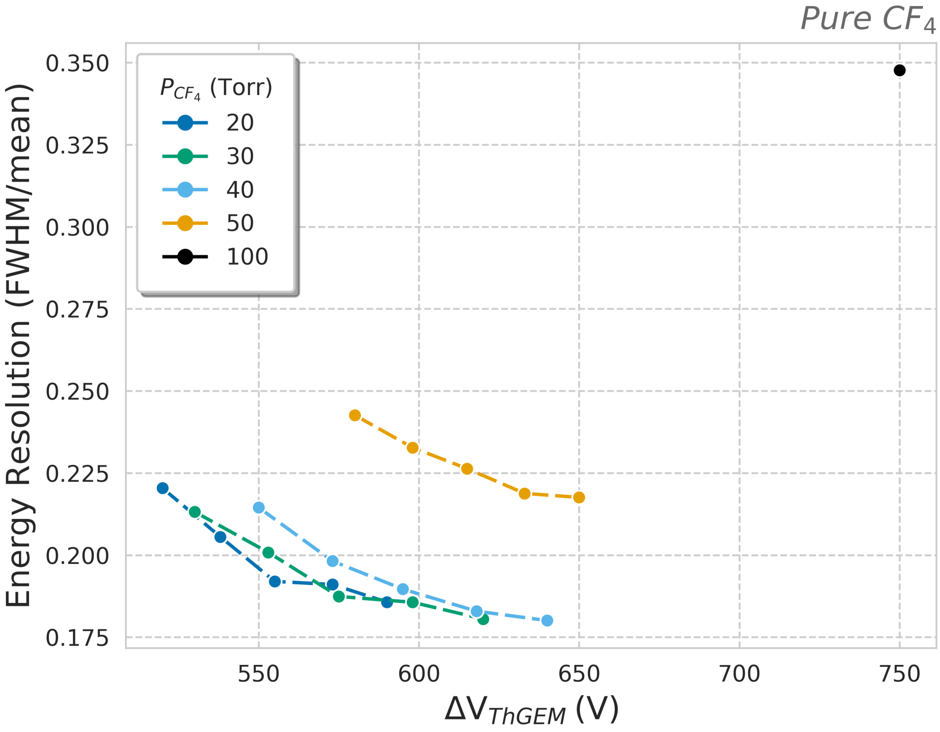

Figure 3.5 Energy resolution measured in pure $CF_4$ at a range of low pressures.

The best energy resolution, 0.1801 ± 0.0006, was achieved during the 40 Torr run and occurred at a $\Delta V_{\text{ThGEM}}$ of 640 V. Conversely, the worst energy resolution was measured to be 0.3477 ± 0.0007 at 100 Torr with a $\Delta V_{\text{ThGEM}}$ of 750 V. In the following section, we will discuss how the addition of He affects the gain and energy resolution.

## 3.4 Sub-atmospheric $CF_4$:He Mixtures

After the measurements in pure $CF_4$, He was added to the vessel using the filling procedure described in Section 3.2. For each $CF_4$ pressure, He was added gradually and gas gain measurements were taken at total pressures of 95, 190, 380, and 760 Torr. These pressures were chosen to give a broad range of sub-atmospheric pressures equivalent to 1/8, 1/4, 1/2, and 1 atm respectively. The same procedure for determining the operational voltage range, as described in Section 3.3, was used. The subsequent gas gain measurements can be seen in Figure 3.6.

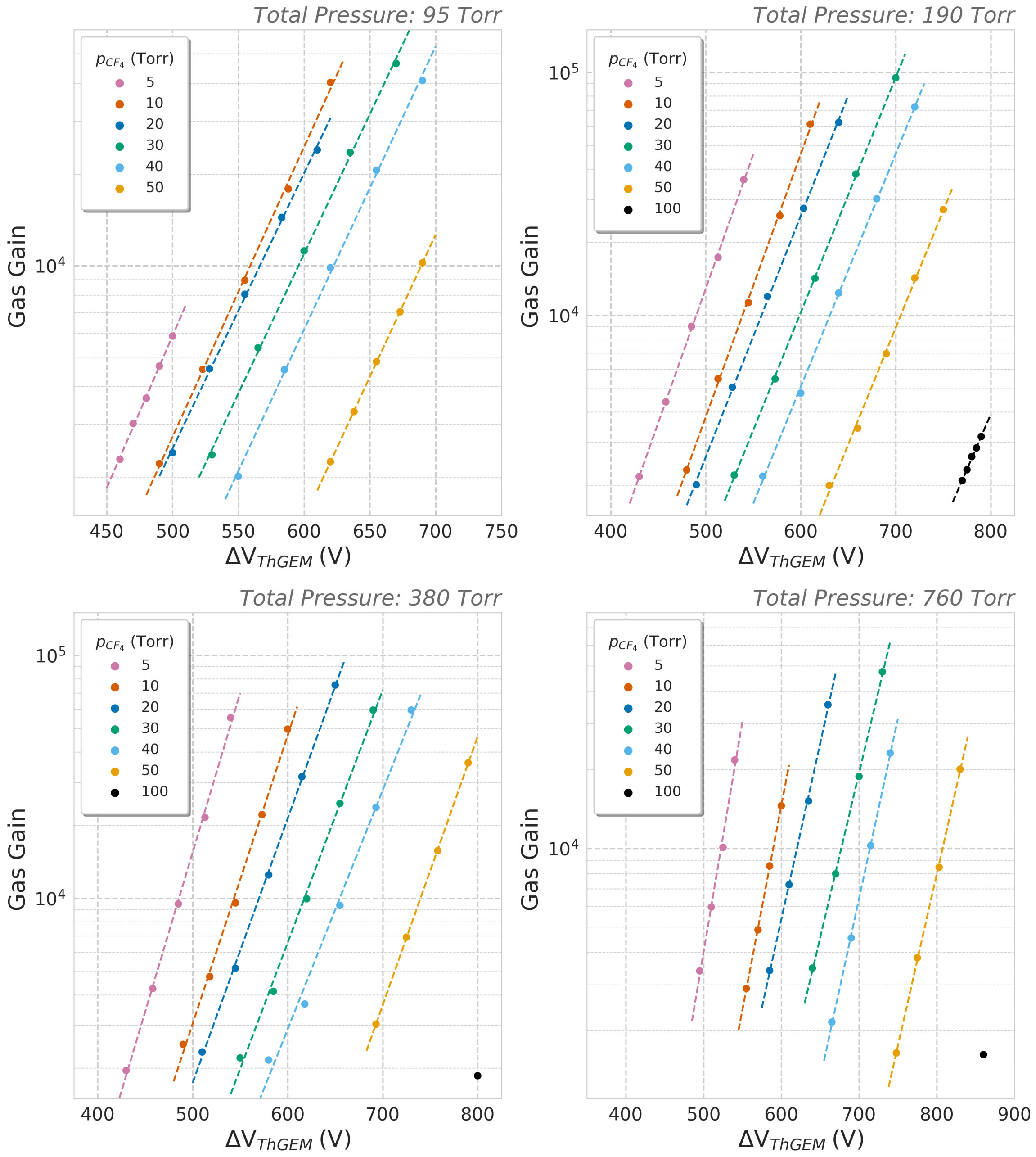

Figure 3.6 Gas gains measured in $CF_4$:He mixtures grouped together by total pressure presented on log scales.

The gain curves in Figure 3.6 are grouped together with mixtures of equal total pressure; 95, 190, 380, 760 Torr from left-to-right, top-to-bottom. The colour represents the partial pressure of $CF_4$. Gain curves exhibiting exponential behaviour were obtained for all gas mixtures except in the case of 100 Torr. The gain curves follow a similar trend to that observed in the pure $CF_4$ measurements, i.e. as the partial pressure of $CF_4$ increases the $\Delta V_{\mathrm{ThGEM}}$ required to achieve the same gas gain increases. This trend is consistent for each given total pressure.

As can be seen, the addition of helium to $CF_4$ appears to stabilise the gas by increasing the maximum attainable gas gain before breakdown occurs in the gas. Previously in Section 3.3, sparking was observed in both 5 and 10 Torr of pure $CF_4$ before a photopeak could be resolved above the noise. However with the addition of He, all mixtures with a $CF_4$ partial pressure of 5 and 10 Torr were able to yield gain curves. Furthermore, the operational voltage range with 100 Torr of $CF_4$ appears to increase with the addition of He as a range of voltages can be seen at a total pressure of 190 Torr in Figure 3.6. As the partial pressure of He increases further, the operational voltage range is limited again and only one stable voltage could be measured at 380 and 760 Torr. This dramatic change in gas gain and stability for a given partial pressure of $CF_4$ is unsurprising as the mixing ratio is changing with increasing partial pressure of helium.

This improvement in gas gain is seen across all partial pressures of $CF_4$. If the maximum gas gains achieved in Figure 3.4 are compared with those in Figure 3.6 at 95 and 190 Torr, it can be seen that the addition of He has significantly improved the maximum stable gas gain. This improvement is almost an order of magnitude in some cases. At higher total pressures, 380 and 760 Torr, it can be seen that the maximum stable gas gains begin to recede. It is interesting to note however, that the gas gains at atmospheric pressure are still larger than their low pressure pure $CF_4$ counterpart. This could be due in part to $He^*/CF_4$ penning ionisation because the ionisation potential of $CF_4$ is smaller than the excitation potential of He. Further work is required in order to understand the penning nature of these mixtures.

The energy resolution of these $CF_4$:He mixtures was also evaluated. These results can be seen in Figure 3.7. If we consider first the mixtures with a $CF_4$ partial pressure of 20 - 50 Torr, we see that the energy resolution generally decreases with increasing $\Delta V_{\mathrm{ThGEM}}$ at a total pressure of 95 and 190 Torr. As the total pressure increases to 380 and 760 Torr, the energy resolution in these curves initially decreases with increasing $\Delta V_{\mathrm{ThGEM}}$ before exhibiting a slight increase at the highest operating voltages. This produces a minimum on many of the curves coinciding with a relatively high gas gain which, if so desired, could be used for $\Delta V_{\mathrm{ThGEM}}$ optimisation. Energy resolution curves with minima have been observed in $CF_4$ mixtures during ThGEM measurements before. This has previously been attributed

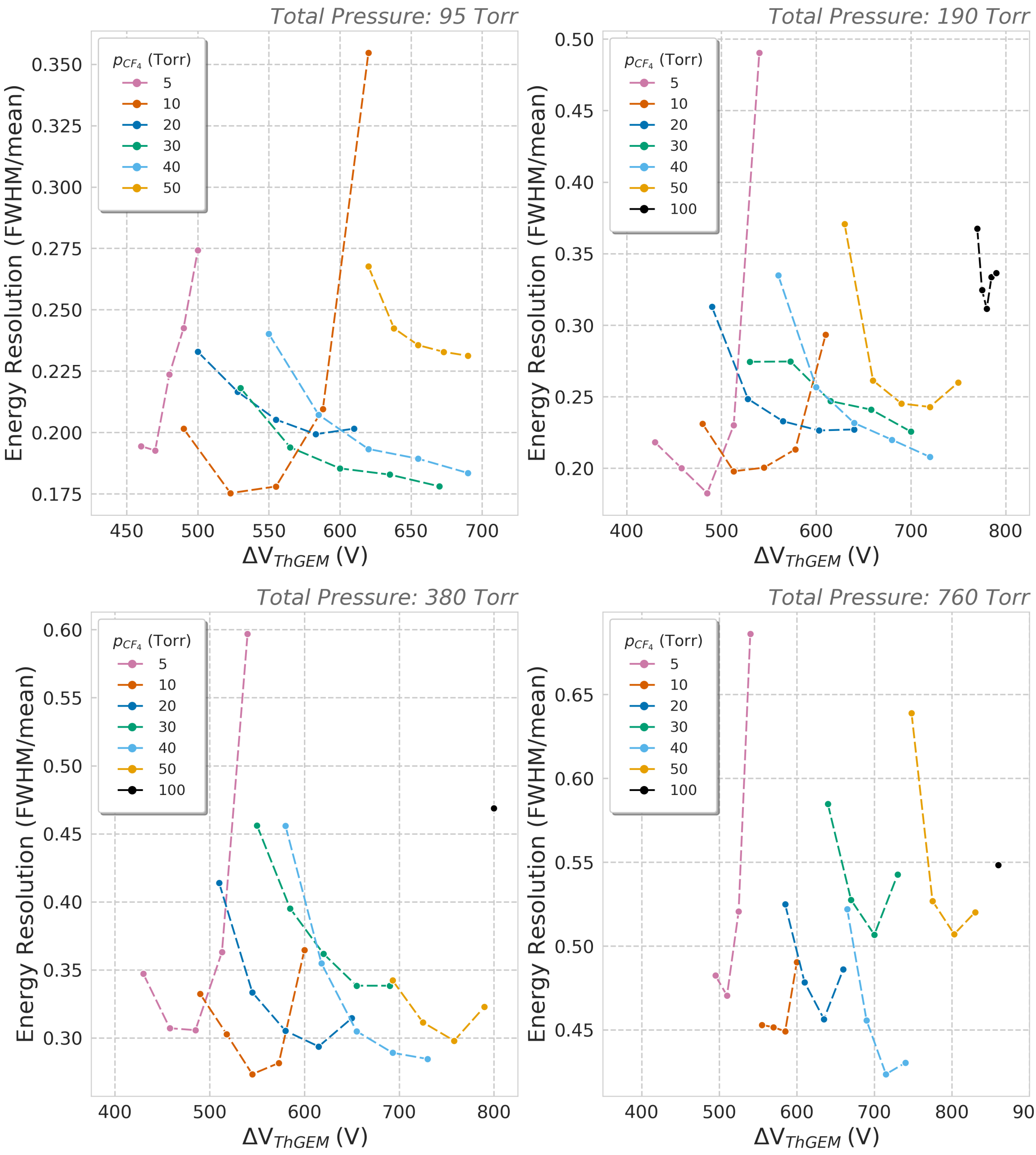

Figure 3.7 Energy resolution measured in $CF_4$:He mixtures grouped together by total pressure.

to the shape and strength of the field lines extending past the top and bottom planes of the ThGEM. This is suspected to cause degradation in the energy resolution via photon feedback and variation in electron pathways through the ThGEM [203].

Local minima can also be seen in the mixtures containing a $CF_4$ partial pressure of 5 and 10 Torr; however, these occur at the lower end of the operating voltage range and would therefore not be ideal for optimising both energy resolution and gain simultaneously. A similar optimisation could be made for the mixture at a total pressure of 190 Torr with a $CF_4$ partial pressure of 100 Torr. Although this would not be very valuable as the gas gains in this case were relatively small compared to the lower $CF_4$ partial pressures, as seen in Figure 3.6.

It can also be seen that the observed lowest energy resolution increases with each increase in total pressure. For example the lowest energy resolution achieved for pressures 95, 190, 380 and 760 Torr was found to be $0.175 \pm 0.001$ ($p_{CF_4}$:10 Torr), $0.183 \pm 0.002$ ($p_{CF_4}$:5 Torr), $0.282 \pm 0.003$ ($p_{CF_4}$:10 Torr), and $0.424 \pm 0.002$ ($p_{CF_4}$:40 Torr) respectively. This suggests that the energy resolution worsens as more He is added to the vessel and the total pressure increases. A similar trend of degrading energy resolution with increasing pressure was also observed in pure $CF_4$ in Section 3.3. However, for a given total pressure in Figure 3.7, the predictive power of the variation in energy resolution with $\Delta V_{\mathrm{ThGEM}}$ as the proportion of $CF_4$ changes is very low; highlighting the importance of doing these measurements experimentally.

The results presented in Figure 3.6 and 3.7 demonstrate that $CF_4$:He mixtures can produce significant charge amplification with a single ThGEM at sub-atmospheric pressures down to 95 Torr. It is believed that this success is partially due to the thickness of the ThGEM used in these measurements. Previous work with a double GEM configuration, each with a thickness of 50 $\mu$m, utilising a premixed gas bottle of $CF_4$:He with molar ratio 20:80 was not able to produce a measurable gas gain at pressures lower than 400 Torr [193]. The smaller amplification gap likely resulted in earlier onset sparking at lower pressures. Additionally, the ability to vary the partial pressure of both constituent gases means that the mixtures tested in this paper at atmospheric pressure are more suitable for preserving the length of $^{12}$C and $^{19}$F recoils than the previously tested 20:80 atmospheric mixture. This is because the partial pressure of $CF_4$ in a 20:80 molar ratio mixture at atmospheric pressure is greater than 100 Torr.

These results also present the opportunity for optimisation of a gas mixture at atmospheric pressure. This would be beneficial as operation at atmospheric pressure can reduce the cost of a containment vessel; this consideration will be significant when scaling the detector volume up to reach meaningful cross sections. As mentioned, the lowest energy resolution achieved at atmospheric pressure can be seen to occur at 40 Torr in Figure 3.7. This curve also exhibits a local minima at a relatively high gas gain. It would therefore be recommended to use an atmospheric mixture with 40 Torr of $CF_4$.

Following the $CF_4$:He mixtures, pure helium was also tested at pressures of 5, 10, 20, 30, 40, 50, 95, 195, 380, and 760 Torr. However no peaks were observed in the energy spectrum before sparking occurred. This may not be surprising as He is typically mixed with a small amount of a quenching gas in gaseous ionisation detectors. Despite this result, successful charge amplification in pure He has been demonstrated before with various single/double ThGEM and WELL-ThGEM configurations; as low as 100 Torr with UV-light and 350 Torr with 5.5 MeV alpha particles [204]. This could suggest that future measurements in pure He at low pressure would benefit from multiple amplification stages.

## 3.5 Conclusions

In conclusion, gas gain and energy resolution measurements were conducted in pure $CF_4$ at low pressures of 5, 10, 20, 30, 40, 50, and 100 Torr. For pressures 20 - 50 Torr, full gain curves exhibiting exponential behaviour could be achieved. Sparking occurred in both 5 and 10 Torr before a measurable gas gain could be reached and only one measurement could be made at 100 Torr. The energy resolution in pure $CF_4$ was below 0.22 in 20 - 40 Torr but appeared to increase significantly at 50 and 100 Torr. These findings suggests that lowering the pressure below 100 Torr would not only benefit directionality but also offers improvement in energy resolution.

Following these measurements, He was added to the vessel to bring the total pressure up to 95, 190, 380, and 760 Torr. The addition of He appeared to raise the breakdown voltage and maximum stable gas gain. Above 190 Torr the maximum stable gas gain began to decrease but was still larger at 760 Torr compared to its low pressure pure $CF_4$ counterpart. The energy resolution of these mixtures worsened with increasing total pressure but some local minima were observed to coincide with relatively high gas gains, which could be used for optimisation. Besides improving the sensitivity to low WIMP masses, these results suggest that the addition of He to low pressure $CF_4$ also improves the gas gain which is beneficial to the detection of low energy recoils.

These results have demonstrated that mixtures, which prioritise a partial pressure of $CF_4$ $<$ 100 Torr, can be successfully operated at sub-atmospheric pressures down to 95 Torr with a single ThGEM. This is lower than previously achieved with premixed ratios of $CF_4$:He and is believed to be due to the larger amplification gap used in these measurements. Additionally, the mixtures tested here are more suitable for preserving the length of both $^{12}$C and $^{19}$F recoils when compared to the previously tested 20:80 atmospheric mixture. This is due to the fact that an atmospheric mixture of 20:80 results in a partial pressure of $CF_4$ greater than 100 Torr.

These results also present the possibility of gas mixture optimisation at atmospheric pressure which is beneficial for reducing the cost of a containment vessel. This will be a significant consideration when scaling up the detector volume to reach meaningful cross sections. If an atmospheric mixture of $CF_4$:He is to be used with a ThGEM of comparable dimensions, then it is recommended that $CF_4$ contributes a partial pressure of 40 Torr to the mixture; this was found to produce the lowest energy resolution at atmospheric pressure in this case. Alternatively, when using a ThGEM of comparable dimensions under sub-atmospheric conditions, it is recommended to use a partial pressure of $CF_4$ between 20 and 40 Torr due to its stability of operation and coinciding high gain with low energy resolution.

Finally, pure He was tested with the ThGEM setup at pressures of 5, 10, 20, 30, 40, 50, 95, 195, 380, and 760 Torr but a measurable gas gain could not be achieved before sparking occurred in each case. Further work is required to test charge amplification in pure He with multi-stage amplification options and to understand the possible penning effects in the $CF_4$:He mixtures.

# Chapter 4

# Charge Amplification with a Multi-Mesh ThGEM in Low Pressure $SF_6$

This chapter is a reproduction of the journal article titled *"Gas Gains Over $10^4$ and Optimisation using $^{55}$Fe X-rays in Low Pressure $SF_6$ with a Novel Multi-Mesh ThGEM for Directional Dark Matter Searches"* which was published in the *Journal of Instrumentation*. As the text was originally intended as a journal article, it is a self contained account and therefore contains some repetition with other chapters.

As discussed in Chapter 2, NID gases can be used as the target medium in low pressure gaseous directional DM detectors in order to improve the positional resolution and, by extension, the track reconstruction capability. This is possible because the drifting NIs are less susceptible to diffusion than electrons. The electron affinity of NID gases, responsible for the formation of the NIs, is also accountable for the limited gas gains for which they are typically associated. In this chapter, it is shown that significant gas gains, which are comparable to those readily obtained in electron drift gases, can also be achieved in the NID gas $SF_6$ given the careful design of a suitable charge amplification device and comprehensive optimisation procedure.

Firstly, a novel multi-stage Multi-Mesh ThGEM is introduced in Section 4.2 followed by the experimental setup in Section 4.3. The calibration of the electronics with reference to an electron drift gas is then presented in Section 4.4. Then charge amplification measurements are made in low pressure pure $SF_6$ following a comparison with previous results and an optimisation procedure in Section 4.5 before finally drawing conclusions in Section 4.6.

## 4.1 Introduction

The Multi-Mesh Thick Gaseous Electron Multiplier (MMThGEM) presented in this paper is a novel multi-stage design variation on the original single stage MMThGEM [174]. It was designed as a gain stage device for coupling to a micromegas readout plane in a low pressure Negative Ion (NI) gas Time Projection Chamber (NITPC). Such experiments are used in directional searches for Weakly Interacting Massive Particles (WIMPs).

WIMPs are a hypothetical candidate particle for Dark Matter (DM) which constitutes 85% of the mass in the known Universe. Attempts to detect rare events in which WIMPs elastically scatter off nuclei have made significant improvements in sensitivity in recent years. However, the WIMP-nucleon cross section limits produced by leading two-phase xenon TPC experiments, like those of the LZ and XENON collaborations [75, 76], are approaching the Neutrino Fog [79]. In this region of sensitivity, these detectors are expected to measure Nuclear Recoils (NRs) induced by neutrinos predominately coming from the Sun [95]. With this current leading technology, these recoils will make the positive identification of an NR induced by a WIMP significantly more difficult.

Low pressure gaseous NITPCs are seen as a viable method for probing into the Neutrino Fog because the reconstruction of ionisation tracks, produced by NRs in such a target medium, can be used to determine the direction of the incoming particle, resulting in a so-called galactic signature [122]. This is advantageous when trying to discriminate between neutrinos originating from the Sun and WIMP signals which, due to the motion of the Solar System around the Galaxy, are expected to originate from the direction of the Cygnus constellation [108, 110]. Unlike the DAMA/LIBRA experiment which seeks a galactic signature via an annual modulation of events [205], which has already been ruled out by more sensitive experiments [206–208] and tightly constrained by similar NaI target experiments like COSINE-100 [209], a directional galactic signal can not be mimicked by terrestrial background events [85, 86, 184].

The direction of a recoiling nucleus can be reconstructed from the track of ionisation it leaves behind in the gas by utilising a readout plane with positional sensitivity. The DRIFT experiment pioneered this method using back-to-back Multi-Wire Proportional Counters (MWPCs), filled with the NI gas $CS_2$ around 40 Torr, and so far has the best published sensitivity for directional DM searches [146]. NI gases, like $CS_2$ and $SF_6$, are preferred over electron drift gases like $CF_4$ because they exhibit significantly less diffusion during the drift phase. However, the NI nature of these gases means that it is more difficult to achieve significant gas gains [119]. For instance, gas gains achieved in $CS_2$ and $SF_6$ typically have an order of magnitude $\leq 10^3$ compared to $\geq 10^4$ in $CF_4$ [119, 125, 129, 169–171, 210–212]. This is likely due to the requirement of the electron to be stripped from the NI before amplification can occur [119]. As a result, the sensitivity to low energy recoils in Negative Ion Drift (NID) gases is limited by at least one order of magnitude. One exception to this was demonstrated with a triple Gaseous Electron Multiplier (GEM) setup in 100 Torr of $SF_6$ which produced maximum gas gains around $\sim$10000, however the vast majority of measurements achieved with that setup were on the order of $10^3$ or lower [171] and ideally the pressure should be lower than this in order to elongate potential NR tracks.

In this paper, we start by introducing the design and operation of the MMThGEM in a low pressure gas. Then the experimental setup and method of measuring the gas gain is discussed along with a calibration run in 40 Torr of $CF_4$. Following this, we expand on previously reported results with the MMThGEM [213] to push the device to its sparking limit in 40 Torr of $SF_6$. This process reveals that the device is capable of achieving gas gains in $SF_6$ on the order of $10^4$. Further optimisation of the collection and transfer fields in the device demonstrate that this gain can be improved further. Finally, gas gain results are presented comparing the fully optimised device in $SF_6$ to the $CF_4$ calibration run.

## 4.2 MMThGEM Design and Operating Principles

The multi-stage MMThGEM presented here was designed and fabricated in 2018 at the micropattern detector production facility at CERN following the initial demonstration of a single stage MMThGEM design [174, 213]. It was designed as an amplification stage device which could be coupled to a micromegas for use in directional DM searches utilising an NID gas. The device, as shown in Figure 4.1, is similar in structure to a regular ThGEM [214]. It consists of a dielectric layer between two copper electrode layers with a hexagonal lattice of holes drilled through the device. The addition of four mesh layers embedded in the dielectric layer differentiates the MMThGEM from a regular ThGEM structure. These mesh layers span across the holes and can be seen in Figure 4.1a.

As shown in the cross sectional diagram of Figure 4.1b, the meshes are situated at depths of 200 $\mu$m, 400 $\mu$m, 1400 $\mu$m, and 1600 $\mu$m from the top plane of the device. The holes have a diameter of 0.8 mm and a pitch of 1.2 mm. The device has a total thickness of 2600 $\mu$m and a total active area of 10 $\times$ 10 cm. The addition of the meshes establishes five distinct regions in the detector; the collection field, amplification field 1, transfer field 1, amplification field 2 and transfer field 2. All the layers can be biased individually in order to establish electric fields of varying strengths between neighbouring electrodes. As described further in [129], multi-stage amplification requirements for a low pressure NID gas were motivated by the low gas gains produced by a single ThGEM in $SF_6$. Unlike double/triple ThGEM configurations and other multi-stage devices like Multi-layer Thick

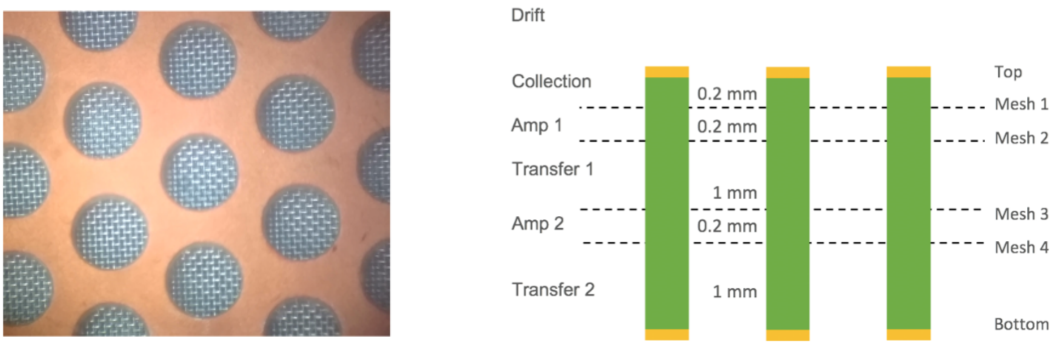

(a) (b)

Figure 4.1 (a) Image of the MMThGEM hole structure as viewed from above. (b) Cross sectional diagram of the MMThGEM device.

Gaseous Electron Multipliers (MThGEMs) [173], the meshes in the MMThGEM ensure that the electric fields are uniform and should therefore provide better amplification properties.

When a particle interacts with the gas in the drift region between the top layer and a cathode, the resulting ionised negative charge is drifted towards the MMThGEM under the applied drift field. When the charge reaches the MMThGEM, it is focused into the holes by the collection field applied between the top layer and mesh 1. The charge is accelerated when it reaches the first amplification field due to a large electric field applied between mesh 1 and mesh 2. This acceleration of the charge causes further ionisation through subsequent collisions with gas molecules and causes an avalanche of ionised charge. After the first amplification stage, the first transfer field between mesh 2 and mesh 3 transports the charge to the second amplification stage. The charge is then amplified for a second time between mesh 3 and mesh 4. Under its intended use, this amplified charge would be transported towards a micromegas plane by the second transfer field between mesh 4 and the bottom electrode plane. In the following section, the experimental setup and biasing circuitry is discussed.

## 4.3 Experimental Setup and Biasing Circuitry

An image of the experimental setup can be seen in Figure 4.2a and shows the MMThGEM mounted to an acrylic base with a standoff of 1 cm and includes a cathode mounted 3 cm above the top surface of the MMThGEM to form a TPC. A black 3D printed source holder was secured to the acrylic such that X-rays from an $^{55}$Fe source could be directed towards the center of the TPC volume in a repeatable way.

All the electrodes were biased individually with HV power supplies according to the circuit diagram shown in Figure 4.2b. Five HV power supplies were used in the experiment;

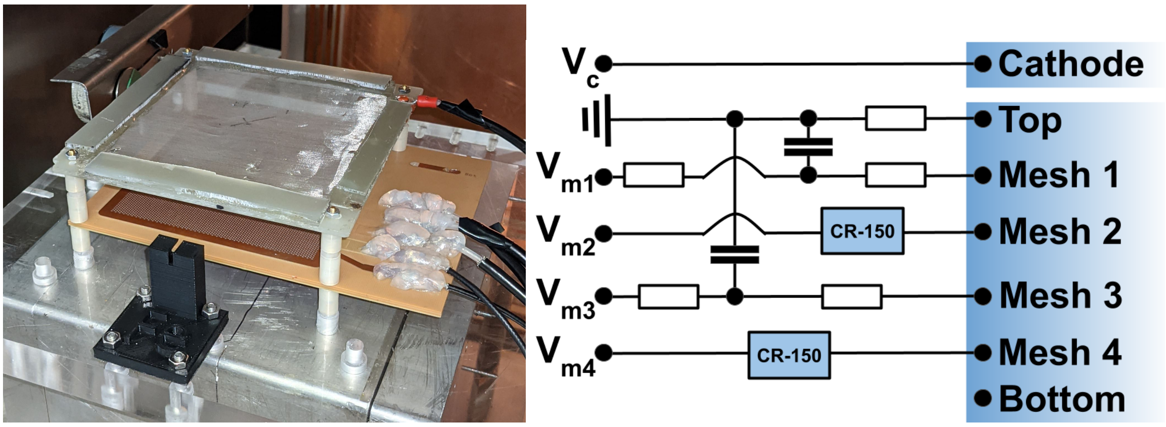

(a) (b)

Figure 4.2 (a) Photograph of MMThGEM assembly. (b) HV biasing circuit diagram. All resistors and capacitors are 200 MΩ and 10 nF respectively.

$V_c$, $V_{m1}$, $V_{m2}$, $V_{m3}$, and $V_{m4}$. These provided biasing voltages for the cathode, mesh 1, mesh 2, mesh 3 and mesh 4 respectively. $V_c$ produced a negative HV and was connected directly to the cathode. The top layer of the MMThGEM was connected to ground via a resistor to reduce the number of HV supplies required. $V_{m1-4}$ all produced positive voltages of increasing magnitude. $V_{m1}$ and $V_{m3}$ were connected to meshes 1 and 3 respectively via a resistor and low pass filter to reduce capacitative coupling between meshes. $V_{m2}$ and $V_{m4}$ were connected to meshes 2 and 4 via the biasing input on separate CREMAT CR-150 evaluation boards. The bottom electrode of the MMThGEM was left floating. All the HV channels were provided by three NHQ 202M iseg Nuclear Instrumentation Modules (NIMs). The evaluation boards utilised a CR-111 charge sensitive preamplifier whose output was connected to a CR-200-4$\mu$s shaper module on a CR-160 shaper evaluation board. The output of the shapers were connected to an NI USB-5132 8-bit 50MS/s Digitizer which interfaced with a simple labview program so that the amplified charge could be monitored on mesh 2 and measured on mesh 4. The MMThGEM assembly and biasing circuitry were placed inside a vacuum chamber and the vessel was sealed.

## 4.4 Calibration with Electron Drift Gas $CF_4$

An energy spectrum is usually acquired by recording the amplitude of pulses from the output of the shaper. This method of acquisition is sufficient for gain measurements in electron drift gases like $CF_4$ because the charge collection time of electrons in the gas is shorter than the integration time of the shaper. Due to the NI nature of $SF_6$ the charge collection period of the NIs, $\sim$80 $\mu$s for measurements presented in this paper, is longer than the integration time of the shaper. This means that the pulse height of the shaper signal does not necessarily account for all the collected charge in an NI gas, therefore the integral of the shaper signal must be acquired instead. In this section we calibrate the integral of the shaper signal above a threshold of 5 mV, using Simpson's method [215], against the amplitude of the shaper signal in $CF_4$ to establish a self consistent method of comparing the gas gain of an electron drift gas and an NID gas [3].

To begin the calibration, the air inside the vacuum chamber was evacuated using a vacuum scroll pump for 72 hours to allow sufficient time for out gassing. Before filling, the vessel was purged with $CF_4$ and evacuated for a further 10 minutes to ensure that the gas line was free from contaminants. The vessel was then filled with 40.0 ± 0.1 Torr of $CF_4$. The leak rate of the vessel was < 0.1 Torr per day. The electronics were then calibrated by injecting test pulses from a 480 Ortec Pulser NIM onto the CREMAT evaluation boards via a 1 pF capacitor. By using the amplitude of the test pulse and the capacitance, the amount of charge reaching the preamplifier was determined. The electronic gain for the amplitude and integral methods were found to be 1.39 ± 0.04 V/pC and 17.5 ± 0.5 V$\cdot\mu$s/pC respectively. The gas gain associated with this amount of charge was determined via the energy of the $^{55}$Fe X-ray (5.89 keV) and the W-value of the gas. The W-value is the same for $CF_4$ and $SF_6$ at 34 eV [201, 216]. The gas gain is defined as the amount of amplified charge reaching the preamplifier on mesh 4 divided by the initial amount of charge liberated from the gas.

Following the calibration of the electronics, the HV power supplies were ramped up to set up electric fields of varying strengths in the different detector regions. $V_c$, $V_{m1}$, and transfer field 1 were held constant at -300 V, 100 V, and 500 V/cm respectively. The amplification fields were increased in tandem from 18500 V/cm to 22500 V/cm in increments of 500 V/cm. These voltages were chosen as they allowed for the measurement of a broad range of gas gains and previously indicated good collection efficiency [213]. For each amplification field strength, the shaper output from mesh 4 was passed to the labview program and the pulses were histogrammed according to their amplitude and integral value.

After a 30 minute exposure, spectra could be observed in the amplitude and integrated signal histograms, examples of which can be seen in Figure 4.3. These spectra exhibit a clear photopeak, caused by the complete absorption of the $^{55}$Fe X-ray, and an exponentially falling component; caused by partial/inefficient collection, transfer and amplification of the initial charge. The spectra were then fitted with both an exponential curve and a Gaussian to the photopeak, shown in red. The mean of the Gaussian was then determined, indicated by the

---

[3] This rationale is thoroughly investigated in Chapter 5.

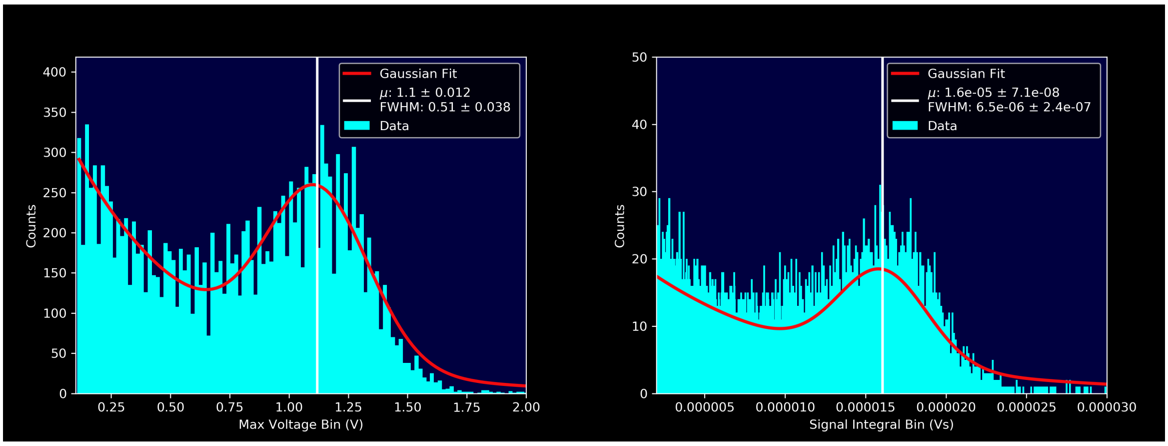

Figure 4.3 Shaper amplitude spectrum with both amplification fields set to 21000 V/cm in 40 Torr $CF_4$ (left). Shaper signal integral spectrum with both amplification fields set to 21000 V/cm in 40 Torr $CF_4$ (right).

white vertical line, and the gas gain calibrations were applied to the mean of the Gaussian curves.

The resulting gas gains from both the amplitude and integral methods can be seen plotted against each other in Figure 4.4. A linear regression analysis was performed with the intercept

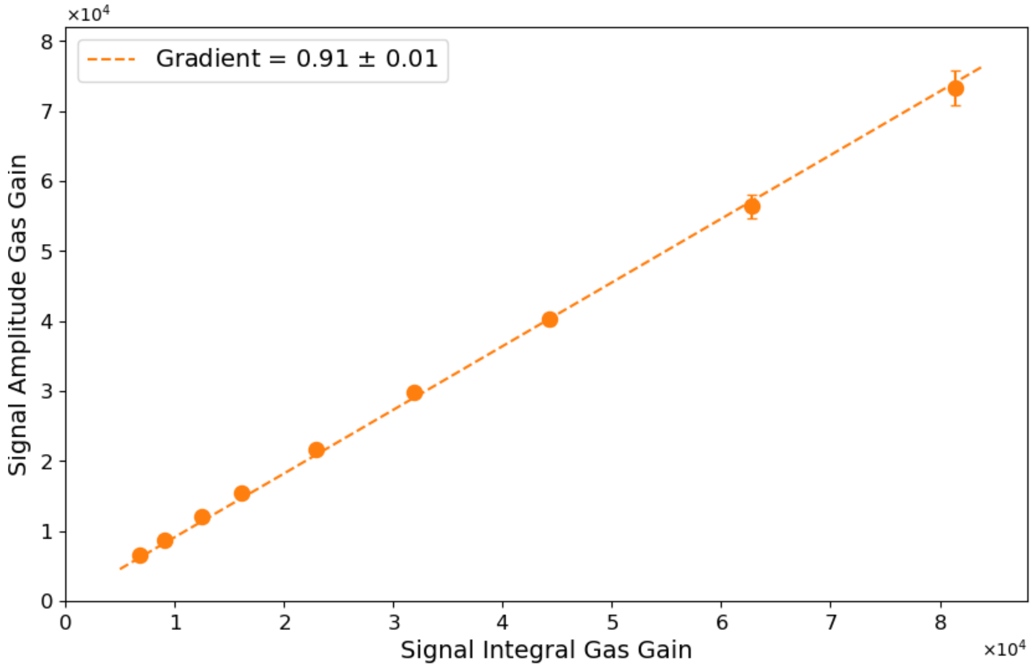

Figure 4.4 Gas gain measurements according to the amplitude method vs those of the integrated signal method in 40 Torr $CF_4$.

passing through (0, 0). The gradient of this line should be equal to unity, however it was found that the gradient was $0.91 \pm 0.01$. This slight discrepancy is likely an artifact of the integral method. For the purpose of establishing a self consistent method of comparing the gas gains in $CF_4$ to that of $SF_6$, all further gas gain measurements using the integral method were re-calibrated against the signal amplitude method according to Figure 4.4.

## 4.5 Gas Gains in $SF_6$ with the MMThGEM

Previous work conducted with the MMThGEM in 20 and 30 Torr of $SF_6$ has shown that gas gains were limited by a ringing effect[4] at larger amplification field strengths. This caused the shaper signal to oscillate and was unable to return to its baseline without intervention via reduction of the bias voltage. However, this ringing effect was not observed at 40 Torr as the device was not pushed to its physical limitations out of caution [213]. In this section, the MMThGEM is pushed to its sparking limit and then an optimisation procedure is performed on both the collection and transfer field 1 to explore the maximum achievable gas gain in 40 Torr of $SF_6$.

To begin, the vessel was filled with $SF_6$ in an identical manner to that of the $CF_4$ measurements. $V_c$, $V_{m1}$, and transfer field 1 were then set to -500 V, 30 V, and 600 V/cm respectively. The drift field was chosen to give good collection efficiency while the collection and transfer settings were chosen because they were previously used in 40 Torr of $SF_6$ [213]. The amplification fields were then increased in tandem until a photopeak could be observed on the integrated signal spectrum, which occurred above 27000 V/cm. Integral spectra were acquired and subsequent gas gains were calculated for amplification field strengths between 27000 and 30000 V/cm in increments of 500 V/cm. Above 30000 V/cm sparking and ringing events which did not return to baseline were observed. The gas gain measurements were plotted as a function of the amplification field strengths and can be seen in blue in Figure 4.5. As expected, the gas gain measurements exhibit an exponential increase with amplification fields strength. The gas gains achieved range from $4400 \pm 400$ to a maximum of $45200 \pm 500$. This maximum gas gain is an order of magnitude larger than what has been observed previously in $SF_6$ with the MMThGEM [213] and other MPGD devices [119, 169, 170]. Moreover this is comparable to the gas gains achieved in the $CF_4$ calibration run.

Previous results in 40 Torr of $SF_6$, as presented in [213], have also been included in Figure 4.5 and can be seen in green. The exponential curve which was fitted to the present results was extrapolated down to these lower field strengths. It can be seen that the fitted

---

[4] The ringing effect regards the motion of positive ions, liberated in the second amplification field, flowing back towards the first amplification field where these ions are accelerated to produce secondary ionisation.

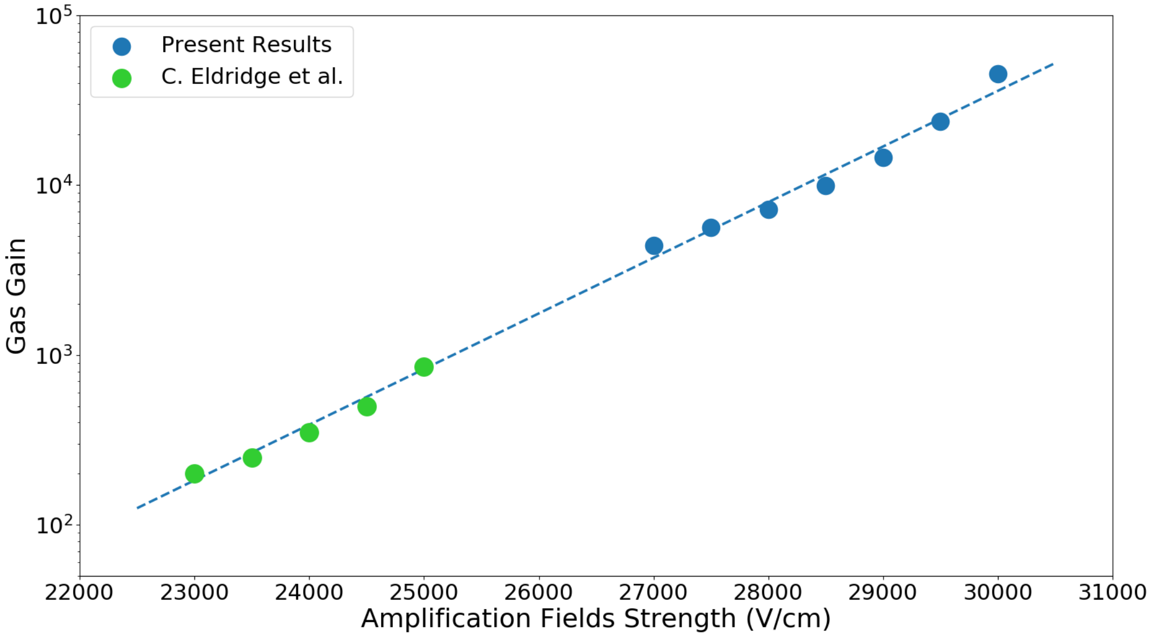

Figure 4.5 Gas gain vs amplification fields strength in 40 Torr $SF_6$. Error bars are smaller than the marker size and therefore not observed.

line appears to have good agreement with the previously obtained results. To quantify this agreement, an $R^2$ test was performed between the extrapolated fit and previous measurements which produced a value of 0.97. This result provides strong evidence that the work presented in this paper is consistent with previously obtained results. Direct measurement at these lower amplification fields could not be made because the dynamic range of the digitiser used in these measurements was not sufficient to see these smaller signals above the electronic noise.

Although this gas gain result is a significant improvement on previous results with $SF_6$, this is not a thoroughly optimised detector regime. To push the device to its physical limits in $SF_6$, the collection and transfer fields underwent methodical optimisation. To optimise the collection field; $V_c$, the amplification and transfer fields were held constant at -500 V, 29000 V/cm and 600 V/cm respectively as this produced a mid range gas gain in Figure 4.5. The collection field was varied by increasing $V_{m1}$ from 20 V to 140 V in increments of 10 V. Figure 4.6 shows the resulting gas gains plotted against $V_{m1}$. It can be seen that, as $V_{m1}$ increased to 40 V, the gas gain increased from $11100 \pm 300$ to $14300 \pm 300$. Above 40 V the gas gain began to decrease slowly down to $10500 \pm 300$ at 140 V. The clear peak in gas gain observed at 40 V was determined to be the optimal collection field strength for maximising gas gain.

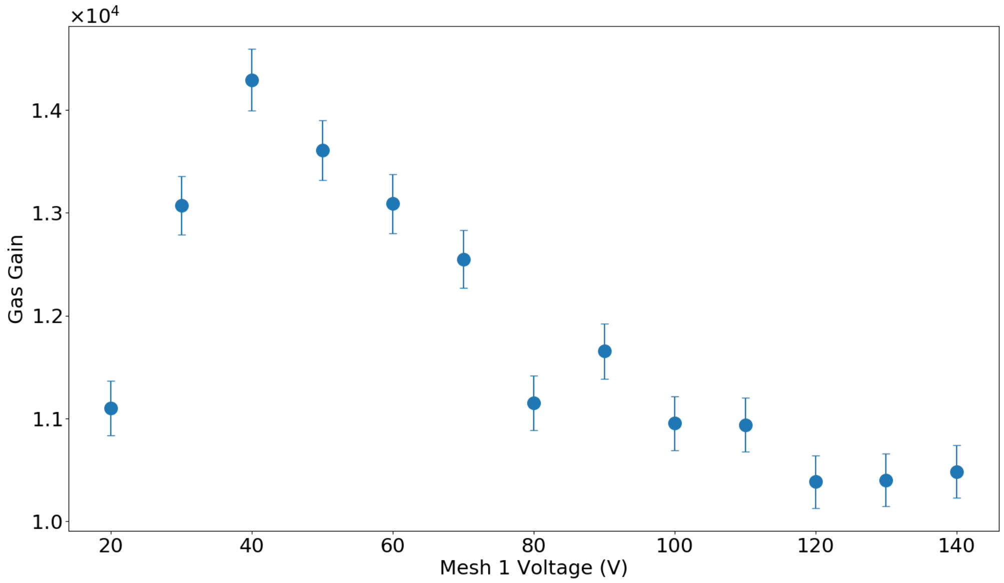

Figure 4.6 Gas gain vs $V_{m1}$ showing optimum collection voltage at 40 V in 40 Torr $SF_6$.

Now that the optimum collection field has been determined, the transfer field strength can be subjected to a similar gain optimisation procedure. This was achieved by holding $V_c$, $V_{m1}$, and the amplification fields constant at -500 V, 30 V, and 29000 V/cm respectively. The transfer field was then increased from 300 to 2300 V/cm in increments of 100 V/cm and resulting gas gains were determined. These results can be seen in Figure 4.7 and show that,

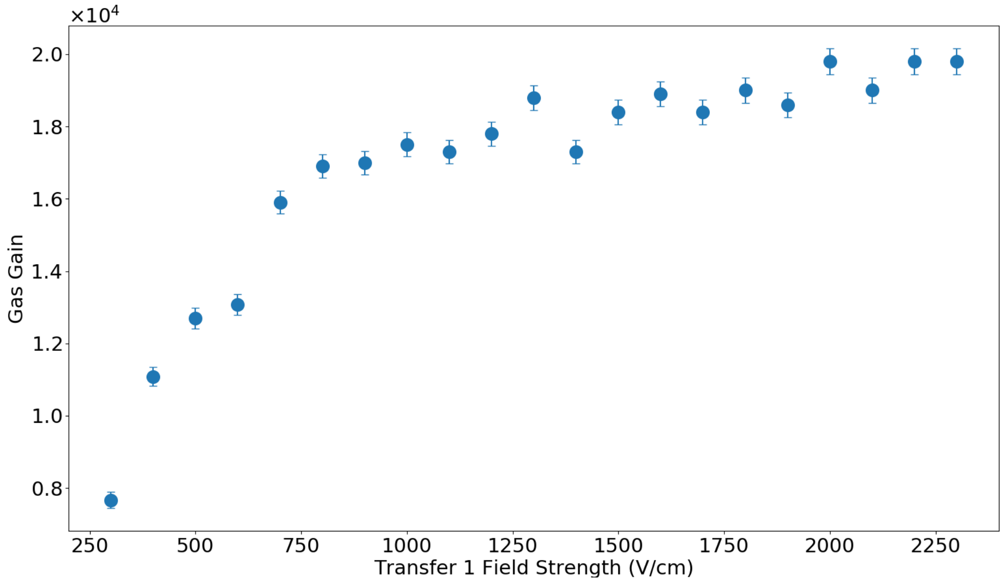

Figure 4.7 Gas gain vs transfer 1 field strength exhibiting a plateau above 900 V/cm in 40 Torr $SF_6$.

as the transfer field increases from 300 to 900 V/cm, the gas gain increases from 7700 ± 200 to 17000 ± 300. Above 900 V/cm the gas gain begins to plateau and the improvement in gas gain becomes less significant with increasing strength. Therefore increasing the transfer field strength beyond the plateau was not beneficial for performance and thus 900 V/cm was taken as the optimised transfer field strength.

Once the optimised field strengths for both the collection and transfer fields were determined, the gas gain of the fully optimised device could be tested. By holding $V_c$, $V_{m1}$, and the transfer field strength constant at -500 V, 40 V and 900 V/cm, the amplification fields were once again increased in tandem from 27000 to 30000 V/cm in increments of 500 V/cm. The gas gain measurements that resulted can be seen in Figure 4.8.

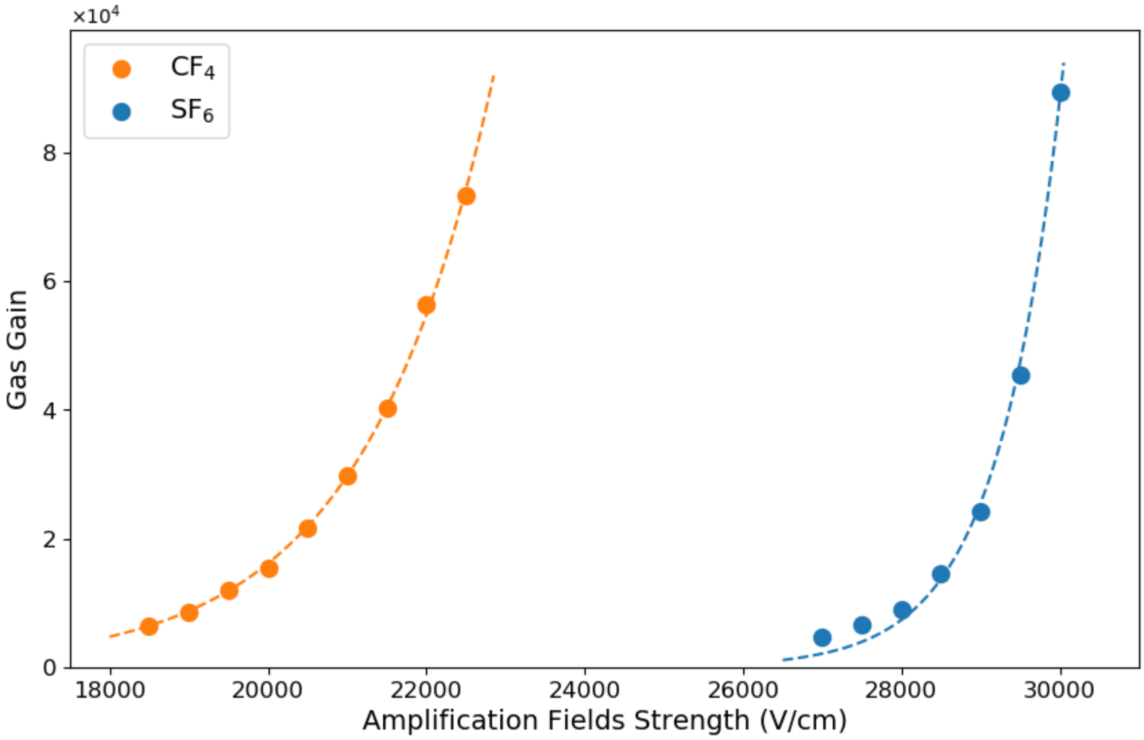

Figure 4.8 Gas gain vs amplification field strengths in 40 Torr $CF_4$ and fully optimised in 40 Torr $SF_6$.

Figure 4.8 shows that as the amplification fields increase from 27000 to 30000 V/cm, the gas gain increases exponentially from 4700 ± 200 to a maximum of 89300 ± 600 before sparking and continuous ringing was observed at higher field strengths. The optimisation process constitutes an improvement in gas gain by a factor of $\sim 2$ compared to the maximum gain achieved in Figure 4.5 prior to the optimisation. This demonstrates that the gas gain is strongly dependent on the field strengths of all the regions in the MMThGEM, not just the amplification field strengths. It is worth mentioning that a minority of ringing events were observed during the 29500 and 30000 V/cm measurements, however these operating voltages were stable as the signal voltage was able to return to baseline without intervention and these signals did not account for a significant portion of events. Further investigation is required to fully understand the suppression of this ringing phenomenon.

The gas gains achieved with the fully optimised device are comparable to the readily attainable gas gains achieved during the $CF_4$ calibration run. However, the amplification fields required were significantly larger in $SF_6$. While $CF_4$ could produce gas gains on the order of $10^4$ above 19000 V/cm, $SF_6$ required amplification field strengths greater than 28000 V/cm. This large increase of 9000 V/cm is unsurprising for $SF_6$ due to the electronegative nature of the gas. Despite the much larger field strengths required, these results show significant promise for the MMThGEM as an amplification stage in the next generation of NITPC directional DM searches. The order of magnitude improvement demonstrated throughout this paper will ultimately benefit the sensitivity of these detectors to low energy NRs.

For completeness, a comparison of the energy resolution between the $CF_4$ and $SF_6$ measurements has been included in Figure 4.9. It can be seen that the energy resolution in

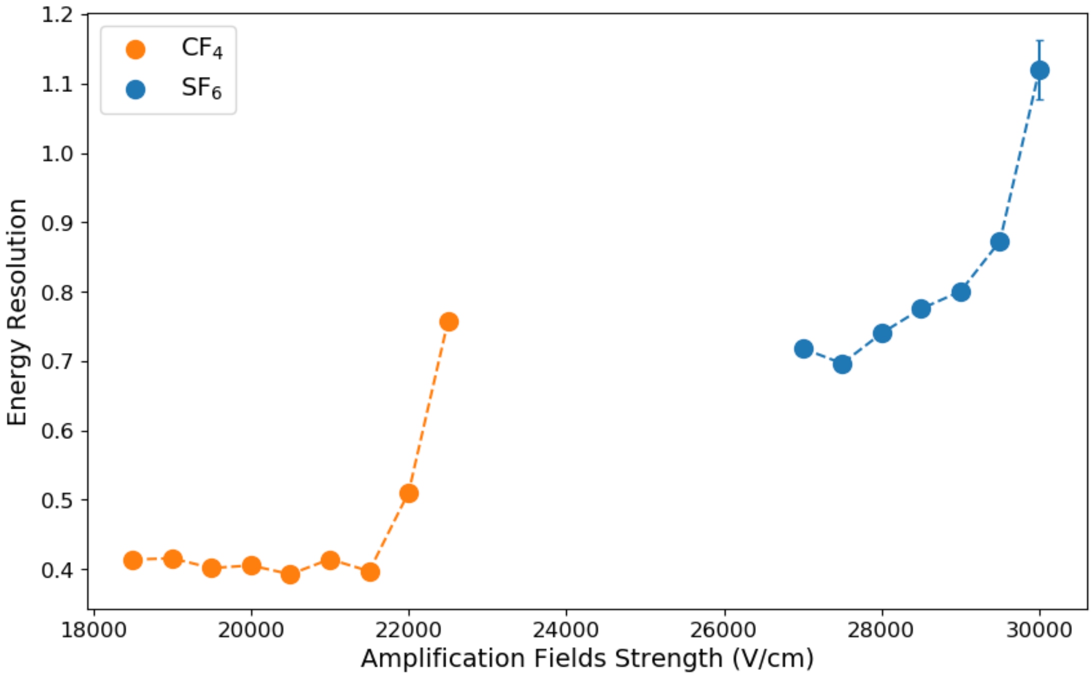

Figure 4.9 Energy resolution vs amplification fields strength in 40 Torr $CF_4$ and 40 Torr $SF_6$ after the gain optimisation.

$CF_4$ is generally better than that of $SF_6$. As the amplification fields increase from 18500 to 21500 V/cm, the energy resolution mostly decreases from 0.4136 ± 0.0008 to 0.397 ± 0.002 with the smallest energy resolution of 0.392 ± 0.001 occurring at 20500 V/cm. It then increases significantly to 0.758 ± 0.005 at 22500 V/cm. The best energy resolution observed in $SF_6$ is comparable to this. At 27000 V/cm the energy resolution starts at 0.7180 ± 0.0005 before dropping slightly to its lowest of 0.696 ± 0.001 at 27500 V/cm. The energy resolution then becomes progressively worse up to 1.12 ± 0.04 at 30000 V/cm. Although the gain in $SF_6$ is excellent at 30000 V/cm, the energy resolution is poor and could possible benefit from a similar optimisation procedure in future.

## 4.6 Conclusions

In conclusion, the integral method required for measuring the gas gain of $SF_6$ was first calibrated against the standard amplitude method in $CF_4$. Then the MMThGEM was pushed to its sparking limit in 40 Torr of $SF_6$. These initial results were able to produce a maximum gas gain of 45200 ± 500, which was larger than previously demonstrated results by an order of magnitude. The collection and transfer field 1 were then isolated and subjected to an optimisation process. The device was found to produce optimum gas gains when $V_{m1}$ and transfer field 1 strengths were set to 40 V and 900 V/cm respectively. The optimised field settings were then tested by holding $V_c$, $V_{m1}$, and transfer field 1 constant while increasing both the amplification fields in tandem. This yielded an absolute maximum gas gain of 89300 ± 600 before sparking occurred. These results are significant because they demonstrate gas gains in an NID gas greater than $10^4$ for the first time. This is at least an order of magnitude improvement on what was previously considered possible with the gas at this low pressure and ultimately offers a significant advancement in the sensitivity of NITPCs to low energy recoils in the context of a directional dark matter search. The energy resolution was also evaluated in both $CF_4$ and fully optimised $SF_6$. It was found that the energy resolution was generally better in $CF_4$ with the lowest value reaching 0.392 ± 0.001 compared to 0.696 ± 0.001 in $SF_6$. The energy resolution could benefit from a similar optimisation procedure in future. Finally, it is recommended that future MMThGEM designs should focus on reducing the pitch and diameter of the hole structures to aid positional resolution and track reconstruction when coupled to a micromegas.

# Chapter 5

# Validation of Integration Method for Negative Ion Signals in the MMThGEM

In the previous chapter, gas gains in the NID gas $SF_6$ on the order of $10^4$ were presented. These results offer an order of magnitude improvement over what was generally considered possible with such a gas. A brief discussion was presented in Chapter 4 regarding how the slower drift velocity of NIs likely necessitated the use of the signal integration method for the gas gain calculations in $SF_6$. In this chapter, a thorough investigation of this hypothesis is presented in order to ascertain a complete understanding of the use of the integral method with NIs in the previous chapter.

Section 5.1 first contains a discussion of the main differences between typical pulse shapes measured during the $CF_4$ and $SF_6$ exposures. Simulations of ERs are then compared to the measurements, obtained in Chapter 4 with the MMThGEM using $SF_6$, in Section 5.2. Following this, work examining how NIs affect the electronic gain, by comparing the $CF_4$ and $SF_6$ exposures, is presented in Section 5.3. Finally, concluding remarks are provided in Section 5.4.

## 5.1 Electron vs Negative Ion Pulse Shapes

As discussed in Chapter 2, the drift velocity of NIs in $SF_6$ is much slower than that of electrons in $CF_4$. This results in a longer time period over which the charge arrives on mesh 4 of the MMThGEM during the $SF_6$ measurements (see Chapter 4 for details of the MMThGEM design and measurements). This should be reflected in the rise time of the preamplifier pulses [217]. For the purpose of comparison, it is useful to start by reviewing the composition of the fast signals observed during the $CF_4$ measurements.

### 5.1.1 MMThGEM Pulse Shapes in $CF_4$

Figure 5.1 shows an example of a typical preamplifier (orange) and corresponding shaper signal (blue) produced by an $^{55}$Fe X-ray in 40 Torr of $CF_4$. This event was taken from one of the exposures presented earlier in Chapter 4 with $V_c$, $V_{m1}$, amplification fields and transfer field 1 set to -300 V, 100 V, 19000 V/cm and 500 V/cm respectively. It can be seen that the preamplifier has a fast rise time and slow decay. Vertical dotted lines can be seen superimposed on top of the preamplifier signal which represent the point at which the preamplifier exceeds 10% (green) and 90% (red) of the preamplifier amplitude. The times at which these thresholds are breached are presented in the legend and the difference is used to calculate the rise time. This particular pulse exhibits a rise time of 1.6 $\mu$s which is less than the integration time of the shaper, 4 $\mu$s. As a result, the shaper signal exhibits a smooth Gaussian appearance. The shape of this preamplifier and shaper signal is consistent with all the observed $CF_4$ pulses on mesh 4.

The fast electron signal is likely not limiting the rise time in Figure 5.1 but the rise time can be influenced by other factors including sampling frequency and detector capacitance. The sampling frequency of the digitiser is 10 MHz (0.1 $\mu$s) which is faster than the measured rise time indicating that the sampling frequency is not a limitation. However, the detector

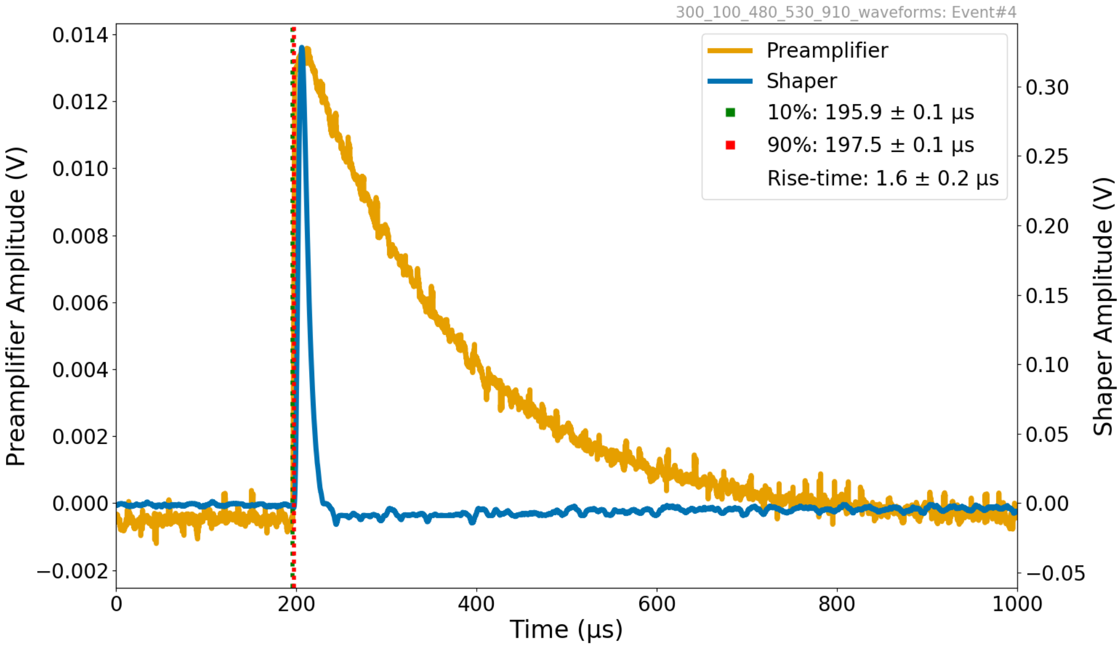

Figure 5.1 Typical $CF_4$ preamplifier and shaper pulses measured during the exposure with $V_c$, $V_{m1}$, amplification fields, and transfer field 1 set to -300 V, 100 V, 19000 V/cm and 500 V/cm respectively.

capacitance is expected to have a linear relationship with the practical rise time. According to the CREMAT CR-111 specification [218], a detector capacitance of $\sim$ 14.5 nF can be calculated. This is comparable to the 10 nF capacitors used in the low pass filters, indicating that these low pass filters could be influencing the rise times in the case of $CF_4$ pulses.

### 5.1.2 MMThGEM Pulse Shapes in $SF_6$

When the $CF_4$ signals are compared to the $SF_6$ preamplifier and shaper signals, a significant difference in pulse shape between the two gases is observed. Figure 5.2 shows a typical preamplifier (orange) and shaper signal (blue) produced by an $^{55}$Fe X-ray in 40 Torr of $SF_6$ during the optimised run with $V_c$, $V_{m1}$, amplification fields, and transfer field 1 set to -500 V, 40 V, 28000 V/cm, and 900 V/cm respectively. This exposure was selected because it provided a gas gain similar to that of the $CF_4$ exposure; from which the example pulse in Figure 5.1 is taken. It can be seen in Figure 5.2 that the rise time of the preamplifier, 59.6 $\mu$s, is significantly longer than that observed in $CF_4$ and is more than 10 times longer than the integration time of the shaper. The shaper signal is also observed to be asymmetric and has an appearance similar to that of event pile-up; the circumstance where the charge

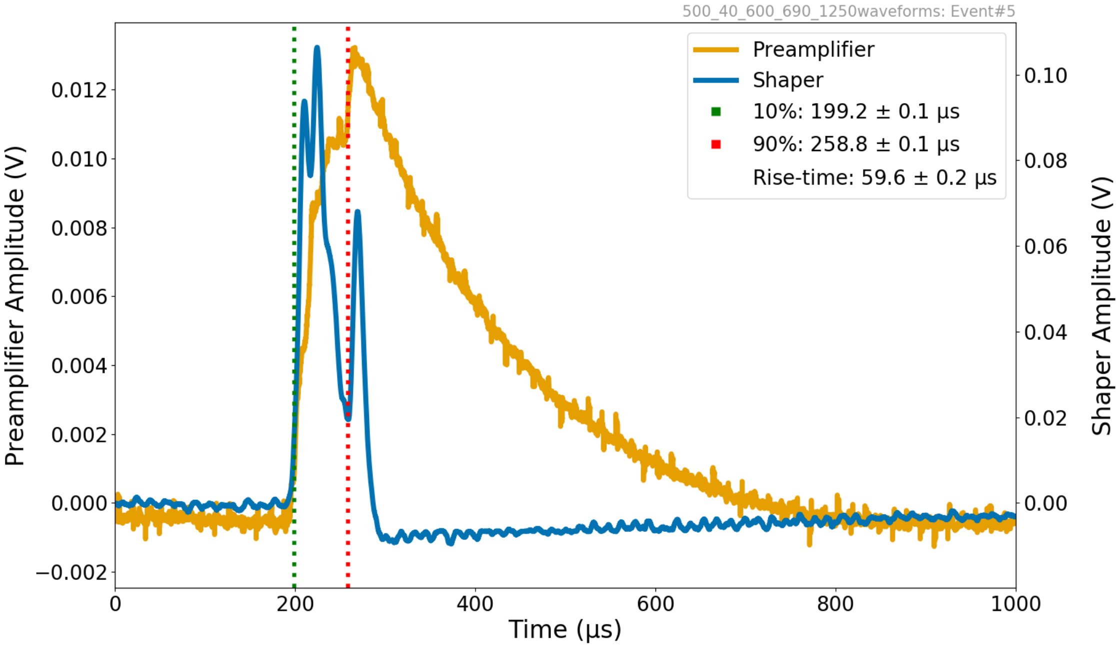

Figure 5.2 Typical $SF_6$ preamplifier and shaper pulses measured during the exposure with $V_c$, $V_{m1}$, amplification fields, and transfer field 1 set to -500 V, 40 V, 28000 V/cm and 900 V/cm respectively; showing a more complex shaper response than seen with $CF_4$.

from multiple different events arrives in quick succession, resulting in a shaper signal which is a superposition of events [217]. Before this pulse shape can be attributed to a physical phenomenon, like the slower drift velocity of NIs, the possibility of pile-up must be excluded first.

### 5.1.3 Evaluation of Event Pile-up

Pile-up is well known for causing erroneous measurements during the acquisition of Pulse Height Analysis (PHA) spectra. If two or more events occur simultaneously, then the pulse height registered by the PHA system will measure an artificially inflated pulse height. This is particularly problematic in high radiation fields which produce large count rates. This can be assessed by the probability of two events being separated by a time interval greater than the effective width of the shaper signals, $\tau_w$, which can be calculated via the count rate, $n$, according to [217]:

$$P(>\tau_w) = e^{-n\tau_w}. \tag{5.1}$$

During the $CF_4$ exposures, an average of 9360 ± 90 events were registered over a 30 minute period, resulting in a count rate of 5.20 ± 0.05 $s^{-1}$. The effective width can be approximated as the FWHM of the shaper signal [217] which is 2.4 times larger than the shaping time [219], estimating a FWHM of 9.6 $\mu s$. As at least two events are required for pile-up, $\tau_w$ is estimated to be 19.2 $\mu s$. By substitution into Equation 5.1, it is found that > 99.99% of all $CF_4$ events will be separated by a time interval greater than twice the effective pulse width. Therefore, it is very unlikely that the events measured during the $CF_4$ exposure will experience pile-up; in agreement with the appearance of the shaper signal in Figure 5.1.

This conclusion, regarding the likelihood of measuring pile-up, should be transferable to the $SF_6$ exposures. An average of 12700 ± 100 events were recorded during the 30 minute $SF_6$ exposures, resulting in a count rate of 7.06 ± 0.06 $s^{-1}$. This is slightly larger than, but comparable to, the count rate during the $CF_4$ exposures; this is expected because $SF_6$ attenuates the $^{55}$Fe X-rays more than $CF_4$ due to its larger molar mass attenuation coefficient [220]. Applying Equation 5.1, this count rate indicates that > 99.98% of events will be separated by a time interval which is greater than two effective pulse widths, thereby avoiding event pile-up in the $SF_6$ exposures.

The result above strongly suggests that the longer preamplifier rise time and asymmetric appearance of the shaper pulses in $SF_6$ are not caused by pile-up and is therefore most likely due to a different phenomenon. As mentioned earlier, this could be caused by the longer charge collection times associated with the slower drift velocity of $SF_6^-$ ion clusters. To investigate this hypothesis, DEGRAD simulations were developed and are presented in the following section.

## 5.2 Electron Recoil Range Simulation with DEGRAD

As discussed earlier, pulses observed during the $SF_6$ exposures had preamplifier rise times far exceeding the shaper's integration time, which is likely due to the slower drift velocity of NIs compared to electrons. To investigate this, DEGRAD [221] simulations were performed. This software is capable of simulating the cluster size and primary cluster distributions in gases and mixtures instigated by the interaction of minimum ionising particles and X-rays. It is considered to be the most accurate simulation package for electron and X-ray interactions with gaseous detectors [222] and includes a large database of different gases. This software is able to simulate an extensive list of physics processes including: cascades, photon absorption, electron scattering, and atomic de-excitation [223].

The DEGRAD program takes five "input cards" which contain information regarding the gas mixture, pressure, temperature, electric field strength, number of events, type of ionising radiation, energy of incident ionising radiation, and orientation of incoming particles. Output files contain the number of ionised electrons per event and the (x, y, z) coordinates of each ionisation electron per event.

### 5.2.1 Simulating $^{55}$Fe X-ray Events in 40 Torr of $SF_6$

For the purpose of comparing the preamplifier rise times to simulated events, DEGRAD was run with 10000 X-rays with energy 5.89 keV in a target of 40 Torr of pure $SF_6$. The temperature was set to 20 °C and the electric field was set to 166.7 V/cm in line with the drift field strength used in the experiment described in Chapter 4. As the z-range of the simulated events is the main focus for comparison with the experimental preamplifier rise times, and because the electric field is oriented parallel to the z-axis in DEGRAD, the X-rays were directed randomly in the x-y plane to best simulate the experimental configuration in Chapter 4. The coordinates of primary ionisation electrons liberated along the ER track of event #10, indicated by the solid blue circles beginning with coordinates (0,0,0), can be seen presented as an example in Figure 5.3. The z-range was calculated as the maximum difference between the z-coordinates of the liberated electrons in each event and can be seen presented in the legend for event #10. These simulations assume that diffusion is a minor effect for two reasons: firstly, electron diffusion is negligible due to the large electron capture cross section of $SF_6$, which results in a capture mean free path of around a micron [119];

and secondly, the subsequent NIs have a maximum drift length of only 3 cm, resulting in minimal NI diffusion.

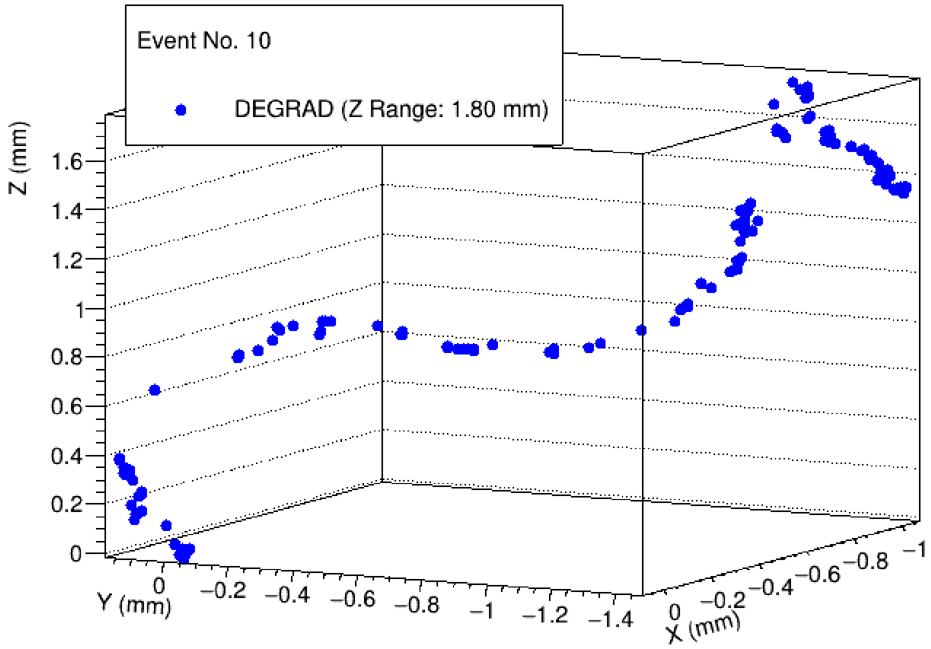

Figure 5.3 Example of primary ionisation sites along the path of an ER event induced by an $^{55}$Fe X-ray in 40 Torr of $SF_6$ simulated in DEGRAD.

To facilitate comparison with the simulated z-ranges, the rise time of the experimental preamplifier signals can be converted to z-range via the drift velocity of $SF_6^-$ ions according to:

$$r_z = v_{drift} \cdot t_{rise}, \tag{5.2}$$

where $r_z$, $v_{drift}$, and $t_{rise}$ are the z-range, ion drift velocity, and preamplifier rise time respectively. As mentioned in Chapter 2, the drift velocity can be calculated via the reduced ion mobility, $\mu_0$, which is 53 mm$^2$ V$^{-1}$ s$^{-1}$ in the case of $SF_6^-$ [224]. By substituting into Equation 2.4, we arrive at a drift velocity of 0.018 mm/$\mu$s; interestingly this suggests that structure in events on the sub-mm scale should be observed beyond the 4 $\mu$s shaping time. In the following subsection, the simulated z-ranges are compared to those extracted from the experimental preamplifier rise times.

### 5.2.2 Simulation Results and Comparison with Measured Rise Times

The simulated z-ranges were calculated and binned into a histogram, shown in blue in Figure 5.4a. Additionally, all the measured preamplifier rise times taken from the $SF_6$

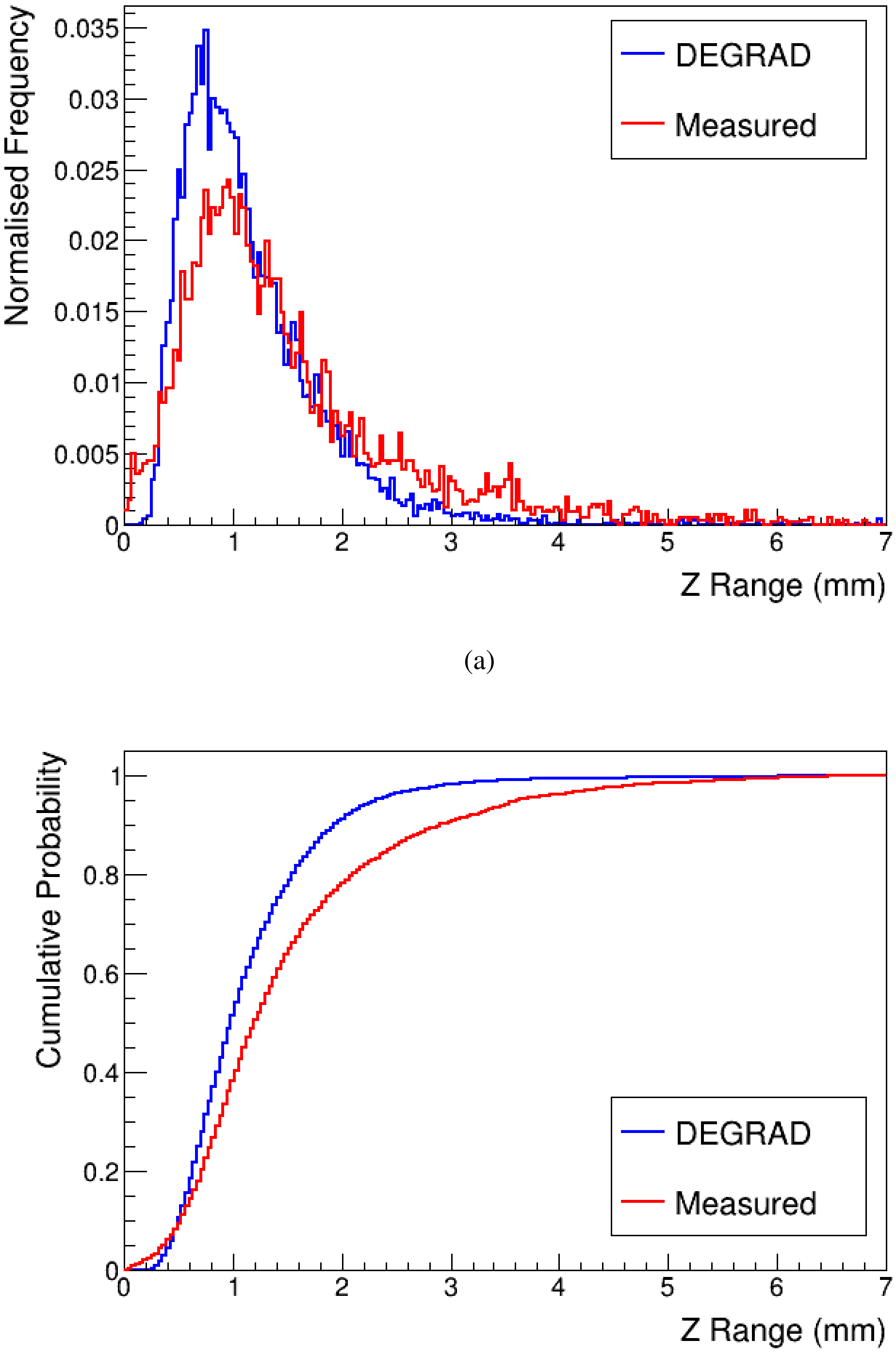

(a)

(b)

Figure 5.4 (a) Z-range of simulated events in DEGRAD (blue) and z-range of events calculated using the rise time of real events with the MMThGEM (red). (b) Cumulative distribution used for calculating the Kolmogorov-Smirnov test statistics. The real experimental preamplifier rise times were taken from the $SF_6$ exposure with $V_c$, $V_{m1}$, amplification fields, and transfer field 1 set to -500 V, 40 V, 28000 V/cm and 900 V/cm respectively.

exposure were converted to z-range via Equation 5.2 and are presented alongside the DEGRAD results in red. Both histograms were normalised to unity.

Qualitatively, the simulated and measured z-range histograms are very similar and exhibit a peaking distribution with a longer tail on the trailing side of the distribution. Furthermore, both distributions peak close to 1 mm. This is significant because it corresponds to a preamplifier rise time of 56.2 $\mu s$, which is very similar to the typical $SF_6$ pulse seen earlier in Figure 5.2. This provides evidence that the elongated rise time observed during the $SF_6$ exposures are likely a direct result of the slow drift velocity of $SF_6^-$ ions.

To establish a quantitative comparison between the DEGRAD simulation and the measured results, the distributions were plotted cumulatively. The cumulative distributions can be seen in Figure 5.4b which shows that both distributions are very similar in shape. The measured distribution can be seen to begin rising earlier and plateauing later than the DEGRAD distribution; this is due to the broader base observed in the measured distribution in Figure 5.4a. A Kolmogorov-Smirnov two-sample test was then performed [225] in order to quantify the similarity between the measured and simulated distributions. This is done via the test statistic D which quantifies the maximum absolute difference between the two cumulative distributions. In Figure 5.4b, the test statistic D was found to be 0.15, corresponding to a p-value of 0.79. This high p-value suggests that there is no significant difference between the simulated DEGRAD ranges and the measured ranges from the preamplifier rise times, supporting the hypothesis that both sets of data are likely drawn from the same distribution. This result provides further evidence that the long rise time of the preamplifier signals during the $SF_6$ exposures is caused by the slower drift velocity of the NIs.

In this section, evidence has been presented which supports the correlation between preamplifier rise time and the $SF_6^-$ drift velocity. This was achieved by comparing the measured z-range, calculated via the experimental preamplifier rise times, to the z-range of simulated $^{55}$Fe X-ray induced ER events. With the physical origin of the extended preamplifier rise time now understood, the impact on the shaper signal and the use of the signal integral method in the context of NIs are explored in the following section.

## 5.3 Slow Negative Ion affect on Electronic Gain

Thus far, significant evidence has been presented which supports the hypothesised relationship between preamplifier rise times and the drift velocity of $SF_6^-$ ions. In this section, the affect that the slow rise time has on the preamplifier and shaper signals is investigated. This is done to further understand the use of the integral method, instead of the standard signal amplitude method, during the $SF_6$ gas gain measurements presented in Chapter 4.

### 5.3.1 Maximum Amplitude Method

As can be seen earlier in Figure 5.2, the shaper signal in $SF_6$ begins its initial return to baseline before all the charge has arrived. This is due to the slow rise time of the preamplifier, found to be caused by the drift velocity of the NIs in the previous section, being longer than the charge integration time of the shaper. This results in multiple peaks in the shaper signal pulse. Therefore, the maximum amplitude of the shaper signal significantly underestimates the amount of charge arriving on mesh 4 in these events. This can be shown explicitly by looking at the electronic gain provided by the shaper circuitry. Figure 5.5 shows the maximum shaper voltage plotted as a function of maximum preamplifier voltage by sampling the first 100 events per exposure in both $CF_4$ (orange) and $SF_6$ (blue).

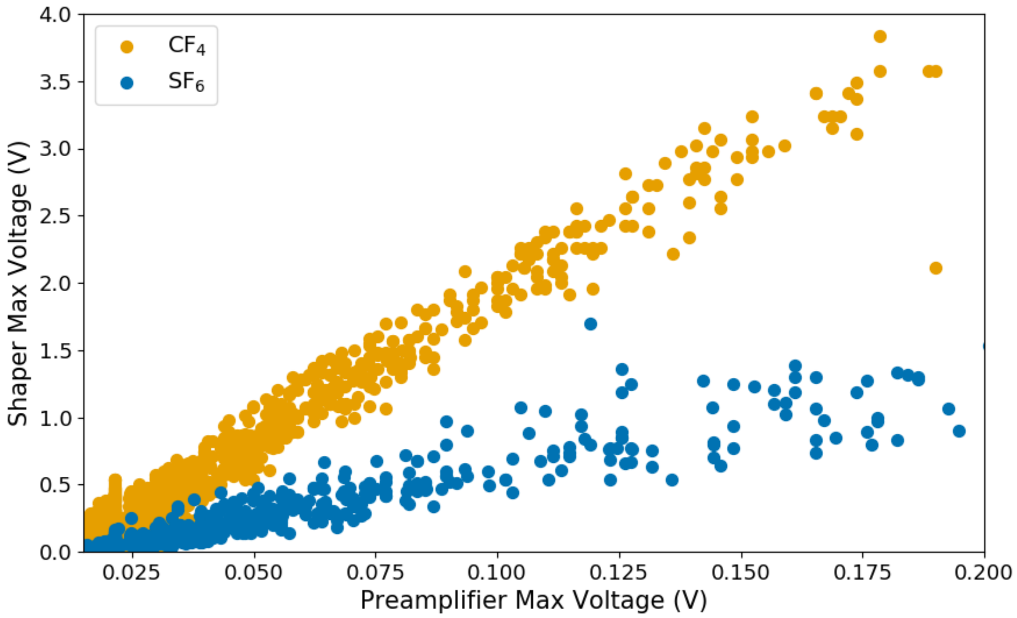

Figure 5.5 Maximum amplitude of the shaper signal vs maximum amplitude of the preamplifier signal in both $CF_4$ (orange) and $SF_6$ (blue) demonstrating the effective electronic gain of the shaper circuitry in both cases.

It can be seen that a linear relationship is demonstrated in both $CF_4$ and $SF_6$, the gradient of which can be used to estimate the effective electronic gain provided by the shaper circuitry. The gradient should be independent of the gas being used; however, there is a clear difference between $CF_4$ and $SF_6$. A linear regression analysis was applied to both the $CF_4$ and $SF_6$ data and the gradient of the resulting fit was extracted.

The electronic gain of the shaper circuitry observed during the $CF_4$ exposures was determined to be 21 ± 1, whereas this was found to be 5 ± 1 for the $SF_6$ measurements. The accompanying $R^2$ values for the linear regression analysis in both $CF_4$ and $SF_6$ are 0.97 and 0.91 respectively. This result indicates that the effective electronic gain of the shaper circuitry is more than 4 times smaller for the $SF_6$ pulses. Thus, the shaper amplitude does not provide a method for calculating the amount of measured charge in an NID gas which is consistent with an electron drift gas, in agreement with the discussion presented previously in Chapter 4.

### 5.3.2 Simpson's Integral Method

A similar analysis can be applied to the electronic gain if Simpson's integral method [215] is used to calculate the area under the shaper signal above a threshold of 5 mV; as done in Chapter 4. Figure 5.6 shows the shaper integral values as a function of preamplifier voltage for 100 events per exposure in both $CF_4$ (orange) and $SF_6$ (blue). The gradient of the linear regression fit to the $CF_4$ data points was found to be $2.6 \pm 0.3 \times 10^{-4}$ s compared to $3.4 \pm 0.4 \times 10^{-4}$ s in $SF_6$. The associated $R^2$ values are 0.96 and 0.94 respectively. This means

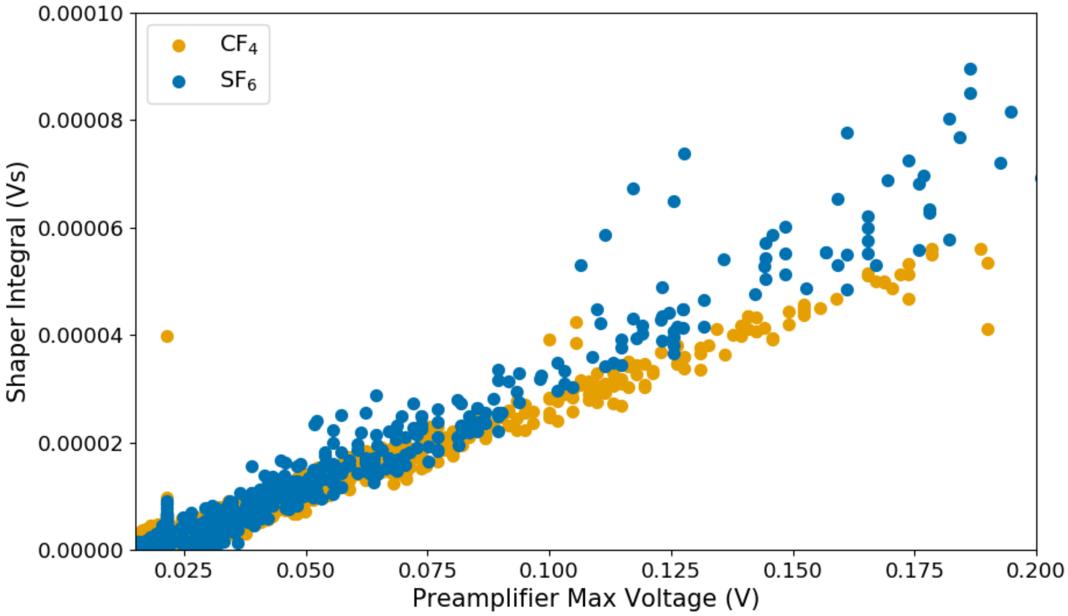

Figure 5.6 Shaper signal integral vs maximum amplitude of the preamplifier signal in both $CF_4$ (orange) and $SF_6$ (blue) comparing the relative effective electronic gain of the shaper circuitry in both cases.

that the effective electronic gain is only different by a factor of 1.3 between the two gases, indicating a significant improvement in the agreement. However, it can also be seen that the $SF_6$ data points with a preamplifier voltage greater than 0.1 V begin to deviate more significantly from the trend observed in $CF_4$. This discrepancy is most likely due to the phenomenon of ballistic deficit.

Ballistic deficit is a result of the preamplifier rise time being similar to the electronic decay constant of the preamplifier [217]. The decay of the preamplifier signal following an event seeks to return the signal to baseline and is purely electronic in nature. If the rise time is not much faster than the decay constant, then the preamplifier signal can begin decaying before all the charge from a given event has been collected; resulting in an underestimate of the true preamplifier amplitude. The decay constant in the case of the CR-111 preamplifier used in these measurements is 150 $\mu s$ [218]. As the majority of $SF_6$ preamplifier rise times were around 56 $\mu s$, it is very likely that the majority of $SF_6$ pulses will experience ballistic deficit.

### 5.3.3 Correcting for Ballistic Deficit

By definition, ballistic deficit is the difference between a measured signal and the equivalent signal with a decay constant which tends to infinity, i.e. the preamplifier output signal will remain at the peak voltage never to return to baseline [217]. However, using a preamplifier with an infinite decay constant is not practical because the output voltage would become very large after several registered events. It is proposed here to perform this correction with a deconvolution algorithm which is capable of removing the electronic decay component of the preamplifier signal; effectively simulating the infinite decay constant. This deconvolution algorithm has been used previously to correct the amplitude of preamplifier signals caused by the slow collection of oxygen ions and takes the recursive form [118]:

$$V_i^{rec} = \begin{cases} V_i, & i = 1, \\ V_{i-1}^{rec} + V_i - V_{i-1} \times e^{(-\Delta t/\tau)}, & 1 < i \leq n, \end{cases} \tag{5.3}$$

where $n$ is the total number of data points in the digitised time series, $V_i$ is the preamplifier voltage of the $i$th data point in the time series, $\Delta t$ is the inverse of the digitiser sampling frequency, and $\tau$ is the decay constant of the preamplifier. The result of this algorithm, following application to the typical $SF_6$ preamplifier signal discussed earlier, can be seen in Figure 5.7 plotted in green.

The algorithm appears to be working as intended by removing the decaying component of the preamplifier signal; once the preamplifier signal has finished rising and begins to decay,

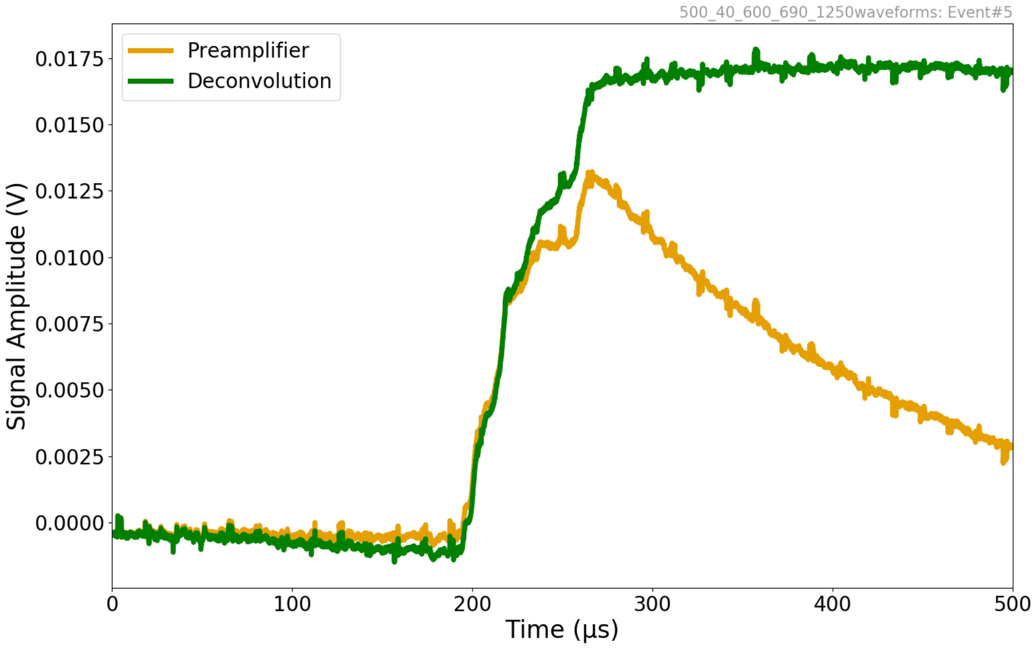

Figure 5.7 Deconvolution algorithm (green) applied to the typical $SF_6$ preamplifier signal (orange) measured during the exposure with $V_c$, $V_{m1}$, amplification fields and transfer field 1 set to -500 V, 40 V, 28000 V/cm and 900 V/cm respectively.

the deconvolution signal plateaus. It can be seen that the plateau of the deconvolved signal is greater than the peak amplitude of the raw preamplifier signal. This indicates that the amount of ballistic deficit experienced in this instance is $\approx 4$ mV which constitutes 24% of the total amplitude of the deconvolved signal. It can be concluded from this result that the true amplitude of the preamplifier signals, during the $SF_6$ exposures, are being significantly underestimated due to ballistic deficit; particularly as the signals become larger in amplitude. This would explain the discrepancy between the $CF_4$ and $SF_6$ gradients in Figure 5.6.

The integral of the shaper signals can be seen plotted as a function of the amplitudes recovered from the deconvolution algorithm in Figure 5.8. The gradients calculated for the $CF_4$ and $SF_6$ exposures were found to be $2.5 \pm 0.2 \times 10^{-4}$ s and $2.2 \pm 0.2 \times 10^{-4}$ s respectively. This suggests that the effective electronic gain between the $CF_4$ and $SF_6$ exposures only differ by a factor of 1.1. It can also be seen that the spread of the data points is much narrower; this is reflected in the $R^2$ value which increased to 0.99 in Figure 5.8 for both $CF_4$ and $SF_6$.

As the gradient of the linear regression applied to the $CF_4$ data is unchanged, it can be assumed that the pulses measured during the $CF_4$ exposures did not experience any appreciable amount of ballistic deficit; this result is reasonable because the rise time of the

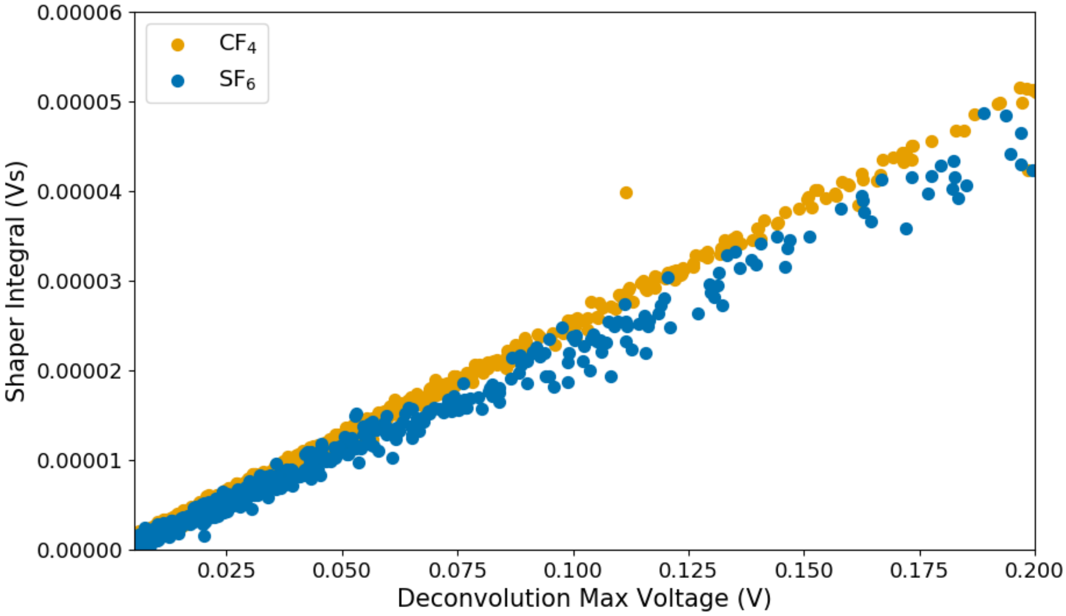

Figure 5.8 Shaper signal integral vs maximum voltage of the deconvolved preamplifer signal in both $CF_4$ and $SF_6$ comparing the relative effective electronic gain of the shaper circuitry in both cases.

$CF_4$ pulses are two orders of magnitude smaller than the decay constant of the preamplifier. As the electronic gain in the $CF_4$ and $SF_6$ exposures are within estimated errors, this suggests that the deconvolution algorithm can be used to correct for the significant amount of ballistic deficit experienced by the preamplifier during the $SF_6$ exposures. Ultimately, this result indicates that the shaper integral method provides an accurate measurement of charge in an NID gas, which is not significantly affected by ballistic deficit and is consistent with measurements made in an electron drift gas. Importantly, this finding provides further validation of the large NI gas gain measurements presented in Chapter 4.

## 5.4 Conclusions

In this chapter, the pulse shapes resulting from ERs induced by an $^{55}$Fe X-ray source, collected for the purpose of gain measurements in Chapter 4, in both $CF_4$ and $SF_6$ were analysed. Typical $SF_6$ pulses were shown to exhibit preamplifier rise times which were more than an order of magnitude larger than those observed in $CF_4$. This resulted in shaper signals reminiscent of pile-up. However, it was shown that the probability of pile-up occurring was less than 0.02% indicating that pile-up can not explain the difference in pulse shapes.

Following this, DEGRAD simulations of the ERs in $SF_6$ were conducted and compared to the z-ranges calculated via the rise time of the preamplifier signals. These distributions agreed both qualitatively and quantitatively following a Kolmogorov-Smirnov two-sample test. This result, combined with the rejection of pile-up, strongly indicated that the longer preamplifier rise times observed during the $SF_6$ exposures were a direct result of the slower drift velocity of $SF_6^-$ ions.

Finally, the affect that the longer rise times had on electronic gain was investigated. By comparing the maximum preamplifier voltage to that of the shaper in both $CF_4$ and $SF_6$, it was found that the standard PHA method significantly underestimated the amount of charge during $SF_6$ measurements. The effective electronic gain using the integral of the shaper signal and the maximum voltage of the preamplifier provided better agreement between $CF_4$ and $SF_6$. However, this also highlighted that the preamplifier likely experienced a significant amount of ballistic deficit during the $SF_6$ measurements. A deconvolution algorithm, which accounted for the ballistic deficit, was compared to the signal integral method. This comparison indicated that the integral method provides consistent electronic gain between an electron and NID gas, which is not significantly affected by ballistic deficit. This finding further validated the large NI gas gains presented in Chapter 4.

# Chapter 6

# Charge Amplification in $SF_6$:He Mixtures with the Multi-Mesh ThGEM

This chapter is a reproduction of the journal article titled *"Charge Amplification in Low Pressure $CF_4$:$SF_6$:He Mixtures with a Multi-Mesh ThGEM for Directional Dark Matter Searches"* which was published in the *Journal of Instrumentation.* As the text was originally intended as a journal article, it is a self contained account which leads to some repetition with other chapters.

Due to the success of the large charge amplification produced by the MMThGEM in low pressure $SF_6$, demonstrated in Chapter 4 and validated in Chapter 5, the MMThGEM has proven to be a good candidate for a gain stage device in NID gases and mixtures. As discussed in Chapter 2, a CYGNUS target gas mixture preferably consists of a low partial pressure NID component like $SF_6$ and a large helium component ideally for atmospheric operation. In this chapter, $SF_6$:He mixtures are tested with incremental additions of helium followed by $CF_4$:$SF_6$:He mixtures.

Firstly, the experimental setup and gas mixing procedure is discussed in Section 6.2. Then baseline measurements are established in alternative low pressures of pure $SF_6$, in Section 6.3, before helium is added incrementally in Section 6.4. Following this, a low pressure $CF_4$:$SF_6$ base mixture is subjected to an optimisation procedure with the MMThGEM field strengths in Section 6.5. Finally, the optimised device is tested with incremental additions of helium, in Section 6.6 before conclusions are presented in Section 6.7

## 6.1 Introduction

There is overwhelming evidence for the existence of Dark Matter (DM) [1], constituting $\sim 85\%$ of the mass in the Universe [42]. A population of Weakly Interacting Massive Particles (WIMPs), hypothesised to have been created in the early Universe, provides a possible explanation. Many direct detection experiments have tried to measure rare elastic scattering events between WIMPs and nucleons and the sensitivity of these experiments has improved by several orders of magnitude since their inception [226]. Notable here are two-phase noble liquid Time Projection Chamber (TPC) DM experiments, like LZ and XENON [75, 76]. Their sensitivity is approaching the Neutrino Fog [79], the parameter space in which background neutrinos induce WIMP-like interactions. Current results show no excess in events near the Neutrino Fog [75, 76], indicating the need for future searches to probe below this parameter space. In this eventuality, two-phase noble liquid TPCs will likely fail to effectively discriminate between neutrino and potential WIMP induced Nuclear Recoil (NR) signals [79, 95, 227].

One method which could be exploited to search below the Neutrino Fog concerns the directional measurement of the recoiling nucleus [228]. This method enables discrimination between neutrino signals, predominantly originating from the Sun, and WIMP signals, which would appear to come from the Cygnus constellation due to the motion of the Solar System through the Galaxy. This galactic signature would change direction over the course of a sidereal day, depending on the detector's latitude on Earth, further evidencing its galactic origin [144]. Compared to an annual modulation signal, caused by Earth's motion around the Sun [108], an anisotropic directional galactic signature would be much more difficult to attribute to terrestrial phenomena [85, 86, 184]. However, evidence shows such a measurement is not possible with current two-phase noble liquid TPC detectors [112].

The DRIFT experiments have pioneered an alternative directional search method using low pressure gaseous back-to-back Multi-Wire Proportional Counters (MWPCs) filled with a Negative Ion Drift (NID) gas mixture of $CS_2$:$CF_4$:$O_2$ at a total pressure of 41 Torr (30:10:1 Torr) [151]. The NID gas $CS_2$ greatly enhanced DRIFT's position resolution by reducing diffusion in the drift region compared to electron drift gases [229]. However, generating sizeable avalanches in NID gases is more challenging. The NID gas $SF_6$ is now preferential to $CS_2$ due to its fluorine content, which is predicted to improve spin-dependant cross sections with a possible WIMP candidate, and because it is non-toxic and non-flammable [119, 153, 230, 231].

As indicated in DRIFT above, directional detectors have been operated at low pressure. The low pressure operation allows the extension of the NR ionisation track to the mm-scale to better match the position resolution of the available charge readout technology. This allows the principle axis of a recoiling nucleus to be determined by reconstructing the track of ionised charge left behind in the gas. Measuring the relative charge density at either end of the track, the so-called head-tail effect, can be used to determine the direction of the recoiling nucleus along that principle axis [146]. A detector capable of measuring the principle axis and head-tail effect in three dimensions can reduce the number of events needed for the positive identification of WIMPs to $\mathcal{O}(10)$ [109].

Clearly the low pressure requirement here has implications for the detector volume necessary to achieve a given sensitivity, something that can not be mitigated by increasing the pressure since this would reduce directional sensitivity. However, an alternative possibility is to add He. The low density of this gas implies no significant impact on NRs from the heavier target gases. The addition of He would improve the detectors target mass, sensitivity to lower mass WIMPs, and offer the potential of atmospheric operation which would reduce the cost of a containment vessel [122]. The demonstration of significant charge amplification in NID gas mixtures containing $SF_6$ and He is therefore highly desirable.

$CF_4$:He mixtures are the primary gas mixtures utilised by the CYGNO collaboration as these mixtures can provide a complementary scintillation and charge readout approach. Although $CF_4$ is not an NID gas, this property can be obtained using a small admixture of $SF_6$ [232]. It is therefore of interest to demonstrate significant charge amplification in $CF_4$:$SF_6$:He mixtures. A $CF_4$:$SF_6$:He gas mixture at nearly atmospheric pressure has been the subject of investigation by the CYGNO collaboration before [169], however the explicit measurement of the gas gain in such an NID mixture is yet to be realised.

As mentioned, one challenge of using NID gases is that their electronegative nature can result in reduced avalanche gains. This comes from the requirement to first strip the electron before charge amplification can take place [119]. Previous work with a Thick Gaseous Electron Multiplier (ThGEM) showed that a single amplification stage was not sufficient for significant charge amplification in $SF_6$ at pressures $< 100$ Torr [129]. It has been shown elsewhere that Gaseous Electron Multipliers (GEMs) and ThGEMs typically require double or even triple GEM configurations to produce substantial gas gains in NID gases at both low and close to atmospheric pressure [119, 169, 171]. Therefore, a multi-stage charge amplification device is likely required for successful NID detector operation. Recent results with a multi-stage Multi-Mesh ThGEM (MMThGEM) have demonstrated large (sub $10^5$) gas gains in low pressure pure $SF_6$ [233], which makes the device a promising candidate for testing $CF_4$:$SF_6$:He mixtures for the next generation of directionally sensitive DM detectors.

In this article, gaseous avalanche gain and energy resolution measurements, using the multi-stage MMThGEM, with low pressure pure $SF_6$ and a $CF_4$:$SF_6$ gas mixture are presented.

Following these initial measurements, He was gradually added to the mixtures, and the effect on gas gain and energy resolution is presented.

## 6.2 Experimental Apparatus and Gas Mixing Procedure

All studies undertaken in this work made use of a novel MMThGEM device developed by the authors in collaboration with CERN [129, 174]. The MMThGEM is a multi-stage charge amplification device, similar in design to a regular ThGEM, with the addition of intermediate mesh electrode layers seen to span across the holes in Figure 6.1a. The holes have a diameter of 0.8 mm and a pitch of 1.2 mm. As seen in Figure 6.1b, the electrode layers designated as top, meshes 1-4, and bottom divide the detecter into six distinct regions when mounted together with a cathode above the MMThGEM. These are the drift, collection, amplification 1, transfer 1, amplification 2 and transfer 2 regions. Each electrode layer can be biased individually with High Voltage (HV) supplies to set up electric fields of varying strengths in the different regions. The device has a total thickness of 2.6 mm and a total active area of 10 × 10 cm. Further details of the device and operation can be found in Ref. [129, 213, 233].

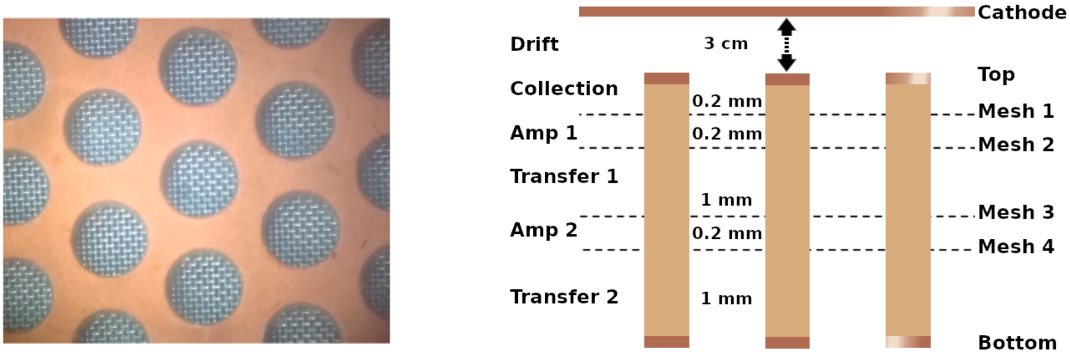

(a) (b)

Figure 6.1 (a) Image of the MMThGEM hole structure as viewed from above. (b) Cross sectional diagram of the MMThGEM device/TPC.

When operated with an NID gas, the detector is expected to perform in the following way. Following an ionising event in the target volume between the cathode and top layer of the MMThGEM, the initial ionisation electrons will bind to the gas molecules to form Negative Ions (NIs). The drift field transports the NIs towards the MMThGEM. The collection field between the top and mesh 1 layers then guides the charge into the holes. The high field strength of the first amplification field accelerates the charge and energetic collisions cause the electron to strip from the NI and an avalanche of ionisation ensues. Evidence of stripping and avalanching charge in the device has been found previously with fields greater than

19000 V/cm [129]. When the avalanche electrons reach the first transfer field, the lower field strength means that the electrons can bind again to gas molecules to form NIs. The NIs are transported towards the second amplification field. Once the NIs reach the second amplification field the electron is stripped again and a second avalanche occurs. When coupled to a micromegas, which is its intended use, the second transfer field transports the amplified charge towards the micromegas readout plane for x-y positional measurements. However, for the purpose of the measurements presented here, the micromegas is not present and the amplified charge is measured on mesh 4 immediately after the second amplification field. As mentioned, this device has been tested previously and, following an optimisation procedure, was found to produce significant charge amplification of $\sim 9 \times 10^4$ in 40 Torr of $SF_6$ [233]. This makes the device a suitable candidate for investigating charge amplification in $SF_6$:He mixtures.

Gain calculation was enabled by an $^{55}$Fe X-ray source positioned next to the MMThGEM TPC directed towards the centre of the drift volume. An average of $\approx 173$ electron-ion pairs are produced following the photoelectric absorption of such an X-ray in $SF_6$ [216]. Test pulses injected into a CR-111 charge sensitive preamplifier and CR-200-4$\mu$s shaper connected to mesh 4 were used to determine the amount of charge reaching mesh 4, thus providing the gain calibration. During measurements, the TPC was biased by setting the cathode to a negative HV, the top electrode was grounded, and meshes 1 to 4 were positively biased. The current draw on the electrodes was used only to monitor sparking by tripping of the HV current limiter. Energy spectra were recorded on mesh 4 over the course of 30 minutes. A Gaussian function was fitted to the photopeak observed in the energy spectra and the gain and energy resolution were ascertained from the mean and FWHM divided by the mean of the Gaussian fit function respectively. Error bars were determined from the uncertainties associated with the fitting procedure. The TPC setup, positioning of the $^{55}$Fe source, and method of gain calculation is identical to that presented in Ref. [233].

The diagram in Figure 6.2 illustrates the gas system used to fill the vacuum vessel. The filling procedure began by evacuating the vessel; with all gas bottles closed, valves V1-5 open, and the vacuum scroll pump turned on. The vessel was evacuated for a minimum of 48 hours achieving a vacuum $< 10^{-2}$ Torr. Following vessel evacuation, all valves were closed and the gas bottles briefly opened to reduce the pressure differential between the gas line and the lab. To begin filling, the $SF_6$ gas bottle and V1 were opened. Then V5 throttled the gas line to fill the vessel to the desired pressure. Then the $SF_6$ gas bottle, V1 and V5 were all closed. When a mixture was required, the gas line was first evacuated by opening V4 and turning on the pump between each addition. After 10 minutes of evacuating the gas line, V4 was closed and the pump was turned off again. Depending on whether He or $CF_4$ was

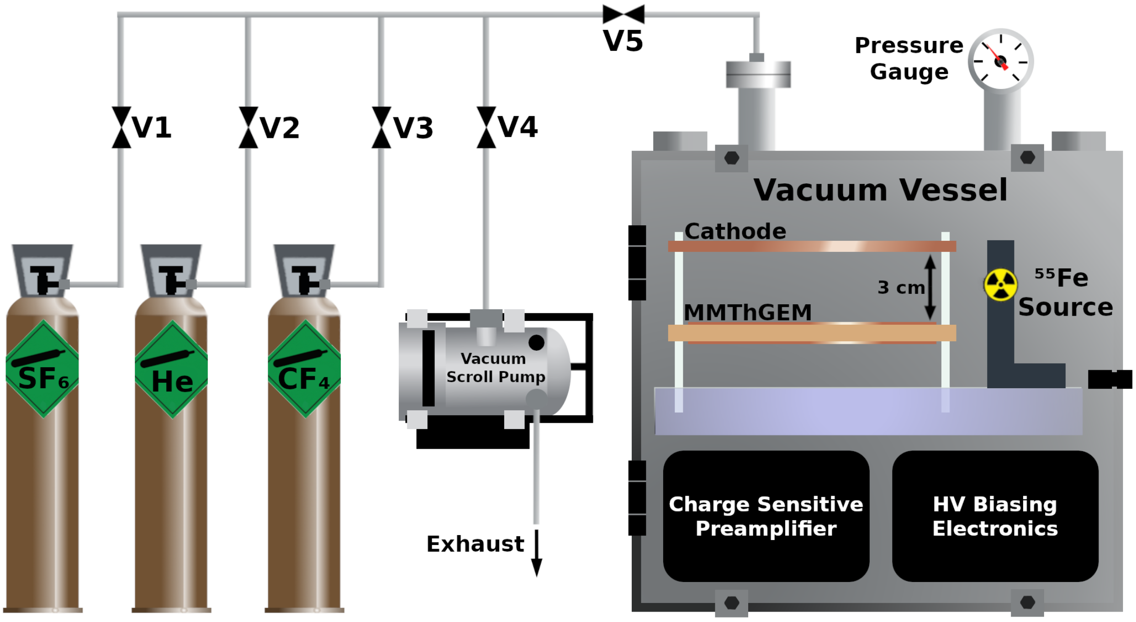

Figure 6.2 Diagram of the experimental setup and gas system used to fill the vacuum vessel with the desired mixture.

required, either the He gas bottle and V2 or the $CF_4$ bottle and V3 were opened respectively. V5 was again used to fill the vessel to the desired partial pressure. Once the desired gas mixture was achieved, all valves and gas bottles were closed and gas gain measurements were taken with the MMThGEM TPC. Following each successful run of measurements the vessel was returned to the evacuation phase.

## 6.3 Low Pressure Pure $SF_6$

To begin these measurements, the vessel was filled with pure $SF_6$ to a pressure of 30 and 50 Torr by following the filling procedure described in Section 6.2. This was done in order to establish a set of baseline measurements for a small range of pressures before He was introduced; as discussed, measurements have already been taken with the MMThGEM in 40 Torr of $SF_6$. The cathode voltage, mesh 1 voltage, and transfer 1 field were set constant at -500 V, 40 V, and 900 V/cm based on the previous optimisation [233]. The amplification fields were increased in tandem until an $^{55}$Fe photopeak could be resolved above the trigger threshold in the energy spectrum. The amplification fields were then increased in increments of 500 V/cm until sparking was observed on mesh 4. The result of these gain and energy resolution measurements, including previous measurements in 40 Torr [233], can be seen in Figure 6.3.

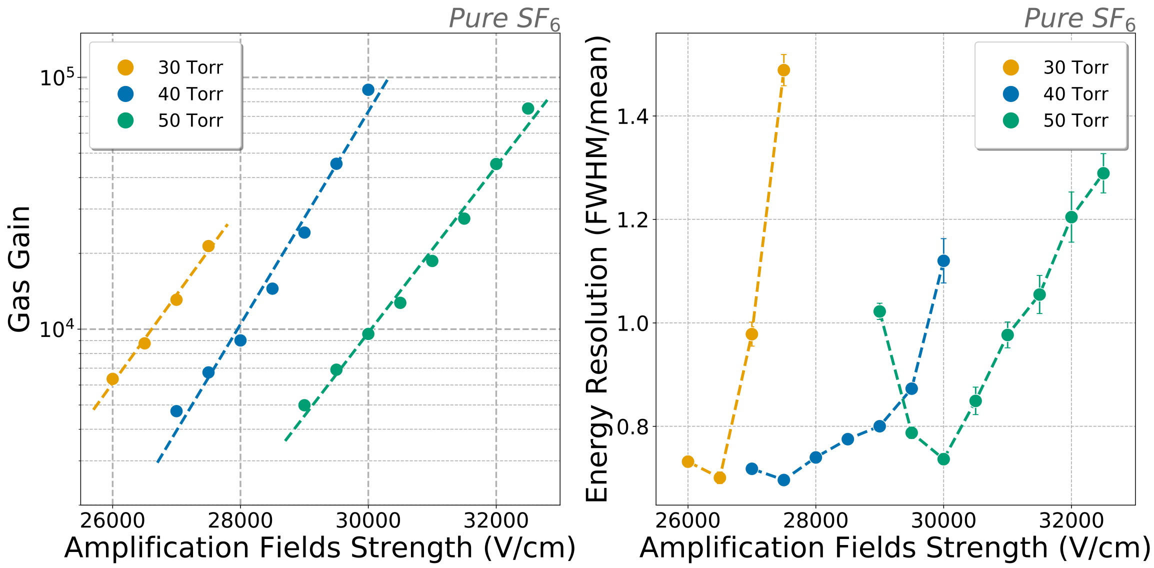

Figure 6.3 Effective gas gain vs amplification fields strength in 30, 40, and 50 Torr of pure $SF_6$ (left). Energy resolution vs amplification fields strength in 30, 40, and 50 Torr of pure $SF_6$ (right). Some error bars are smaller than the marker size and are therefore omitted from the graphs.

It is observed in Figure 6.3 (left) that the gas gain increases exponentially with increasing amplification fields strength; dashed lines represent an exponential curve fitted to the data. The gain curves are seen to shift to the right as the gas pressure increases and larger electric fields are required to produce comparable gas gains.

The maximum gas gains achieved before sparking occurred, $G_{max}$, are summarised in Table 6.1. Sparking and continuous ringing was observed in 30, 40, and 50 Torr at field strengths of 28000 V/cm, 30500 V/cm, and 33000 V/cm respectively; the observed ringing phenomena is discussed in more detail in Ref. [213]. It is interesting to note that the maximum stable gas gain at 30 Torr is smaller than both 40 and 50 Torr. This was caused by earlier onset continuous ringing during the 30 Torr ramp up. Additionally, self-regulating ringing events which were able to return to baseline without intervention were noted to be more frequent in the 30 Torr run than the 40 and 50 Torr runs. This suggests that the ringing effect could be suppressed at higher pressures. A minority of these self-regulating events could also be responsible for the slight deviation from the exponential trend lines fitted to the 40 and 50 Torr data during the highest stable field strength exposures.

Previous measurements in 30 Torr of pure $SF_6$ with the MMThGEM were only capable of producing a maximum stable gas gain around $\sim$ 3000 before sparking occurred [213].

Table 6.1 Summary of pure $SF_6$ results including maximum stable gas gain, $G_{max}$, and the minimum/maximum energy resolution, $ER_{min}$ and $ER_{max}$.

| Pressure (Torr) | $G_{max} \times 10^4$ | $ER_{min}$ | $ER_{max}$ |
|---|---|---|---|
| 30 | $2.32 \pm 0.04$ | $0.701 \pm 0.002$ | $1.49 \pm 0.03$ |
| 40 | $8.93 \pm 0.06$ | $0.697 \pm 0.001$ | $1.12 \pm 0.04$ |
| 50 | $7.53 \pm 0.05$ | $0.737 \pm 0.002$ | $1.29 \pm 0.04$ |

This notable improvement is likely due to the optimisation procedure conducted with the MMThGEM [233] and the lower drift field strength used since those initial measurements were taken. The lower drift field used here, 167 V/cm compared to 385 V/cm, likely reduces the charge density in the holes of the MMThGEM and therefore reduces the possibility of arcing between neighbouring electrodes.

The corresponding energy resolution curves are shown in Figure 6.3 (right). This shows that the energy resolution initially decreases with increasing amplification field strengths before increasing significantly. The degrading energy resolution with increasing amplification fields strength could be caused by inefficient transfer of charge between the different regions, combined with the disruptive stripping/recombination of electrons. This is likely dictated by the changing field ratios with the neighbouring collection and transfer fields. The minimum and maximum energy resolutions, $ER_{min}$ and $ER_{max}$, achieved during the measurements are summarised in Table 6.1. 40 Torr of $SF_6$ was subsequently selected as the base gas pressure for the following additions of He due to its superior gas gain and comparable energy resolution range [233].

## 6.4 Sub-atmospheric $SF_6$:He Mixtures

Once the optimum base pressure of pure $SF_6$ was determined, see Section 6.3, the vessel was once again evacuated and filled with 40 Torr of $SF_6$. Helium was added to the vessel to bring the total pressure up to 50, 75, 100, 150, 380, and 760 Torr. These pressures were chosen so that a dynamic range of low and sub-atmospheric pressures could be tested. For each gas mixture the drift, collection, and transfer fields were set to the optimised settings [233] and the amplification fields were again increased in tandem by increments of 500 V/cm. Spectra were recorded for stable operating voltages in each gas mixture and subsequent gas gains and energy resolutions were calculated. The results are presented alongside the 40 Torr pure $SF_6$ data in Figure 6.4.

As shown in Figure 6.4 (left), not all mixtures tested were able to produce measurable gas gains; this is because some mixtures did not yield a distinct $^{55}$Fe photopeak before sparking

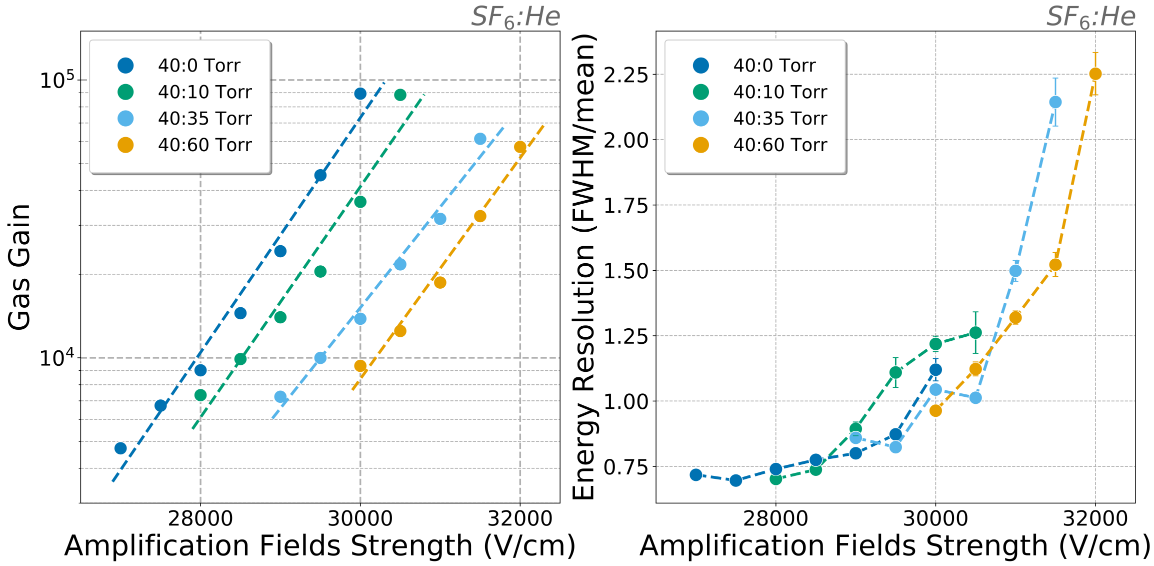

Figure 6.4 Effective gas gain vs amplification fields strength in $SF_6$:He mixtures (left). Energy resolution vs amplification fields strength in $SF_6$:He mixtures (right). Some error bars are smaller than the marker size and are therefore omitted from the graph.

occurred. However, the mixtures up to a total pressure of 100 Torr all exhibit exponential gas gain curves which shift to the right with increasing partial pressure of He. The maximum gas gains achieved for all $SF_6$:He mixtures are summarised in Table 6.2. Initially, a small addition of He does not appear to have any significant effect on the maximum gas gain, as the 40:10 mixture produces a similar maximum gas gain to pure $SF_6$. As more He is added to the vessel, the maximum stable gas gain begins to drop for the 40:35 and 40:60 mixtures. This suggests that as more He is added to the vessel the maximum stable gas gain could drop further.

Table 6.2 Summary of $SF_6$:He results including maximum stable gas gain, $G_{max}$, and the minimum/maximum energy resolution, $ER_{min}$ and $ER_{max}$.

| $SF_6$:He Pressure (Torr) | $G_{max} \times 10^4$ | $ER_{min}$ | $ER_{max}$ |
|---|---|---|---|
| 40:10 | $8.8 \pm 0.2$ | $0.70 \pm 0.01$ | $1.26 \pm 0.08$ |
| 40:35 | $6.1 \pm 0.2$ | $0.82 \pm 0.01$ | $2.14 \pm 0.09$ |
| 40:60 | $5.7 \pm 0.1$ | $0.96 \pm 0.01$ | $2.25 \pm 0.08$ |

The energy resolution measurements are also presented in Figure 6.4 (right). The minimum and maximum energy resolutions are summarised in Table 6.2. It can be seen that the energy resolution worsens significantly with increasing partial pressure of He. For example, both $SF_6$:He mixtures with ratios 40:35 and 40:60 Torr produced fractional energy resolutions > 2. This results in the lower end of the photopeak merging with low level noise and therefore becomes more difficult to distinguish. It is therefore unsurprising that gas gains could not be determined at higher pressures, 150 - 760 Torr, when more He was added to the vessel. Any observed variation in the shape of these energy resolution curves is likely subject to the changing gas composition, pressure, and field ratios between the collection/transfer field and the amplification regions.

These results demonstrate large gas gains, on the order of $10^4$, in a low pressure NID mixture containing He up to a total pressure of at least 100 Torr for the first time. This constitutes an order of magnitude improvement on what has previously been achieved with $CS_2$:He mixtures [170]. Furthermore, the small addition of He will improve the sensitivity of the target gas to low WIMP masses in the context of a directional DM search.

## 6.5 Low Pressure $CF_4$:$SF_6$ Mixture Optimisation

As discussed in Section 6.1, the CYGNO collaboration is interested in $CF_4$:$SF_6$:He mixtures due to the potential for a complementary light/charge NID readout approach. Before introducing He, a 38:2 Torr base mixture of $CF_4$:$SF_6$ was subjected to an optimisation procedure identical to that presented in Ref. [233]. Starting with the isolation of the collection field, the cathode voltage, amplification fields and transfer field 1 were held constant at -500 V, 25000 V/cm and 500 V/cm respectively. The collection field was then varied in isolation by increasing the mesh 1 voltage from 20 V to 100 V in increments of 10 V, the results of which are presented in Figure 6.5 (left).

Figure 6.5 (left) shows that, as the mesh 1 voltage increases from 20 to 50 V the gas gain increases from 5340 ± 30 to 6480 ± 20. As the voltage increases further to 100 V the gas gain decreases to 5730 ± 20. This trend is similar to what was observed in pure $SF_6$ however the peak occurs at 50 V rather than 40 V. This suggests that the optimisation could depend strongly on the gas mixture. As a clear peak is observed at 50 V, this voltage was taken as the optimum collection field for the $CF_4$:$SF_6$ base gas mixture.

The transfer field was optimised in a similar way by holding the cathode voltage, mesh 1 voltage, and amplification fields constant at -500 V, 50 V and 25000 V/cm respectively. The transfer field was then varied in isolation from 400 V/cm to 1400 V/cm in increments of 100 V/cm and gain measurements were made for each transfer field strength. Results are shown in Figure 6.5 (right).

As the transfer field increases from 400 to 600 V/cm the gas gain increases gradually from 6290 ± 40 to 8640 ± 20. Between 600 and 1100 V/cm the gas gain increases more rapidly to 23400 ± 100. Above 1200 V/cm the rate at which gas gain improves begins to

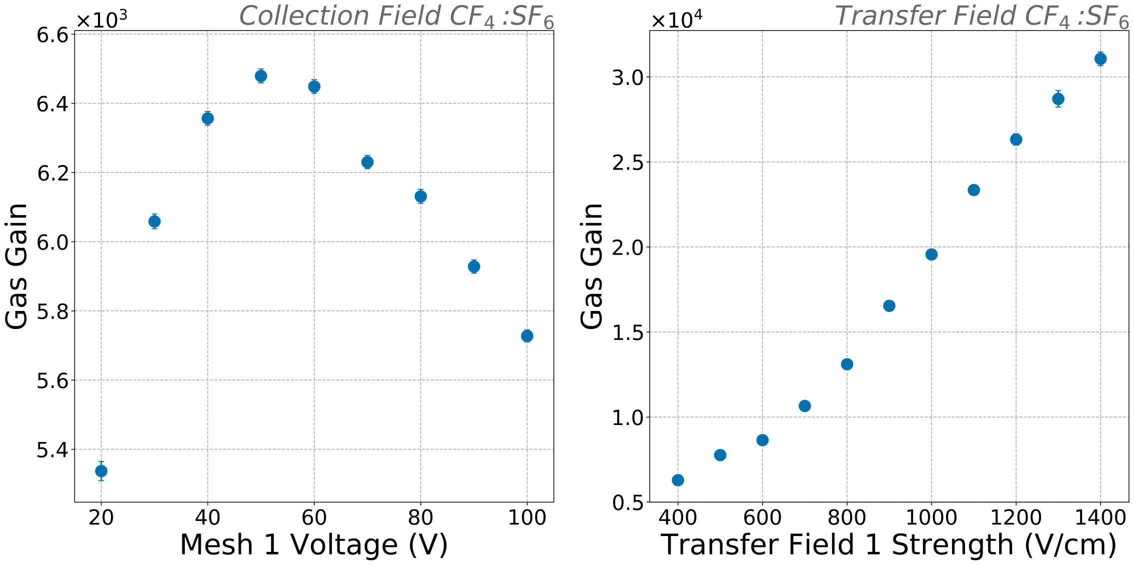

Figure 6.5 Effective gas gain vs mesh 1 voltage in a $CF_4$:$SF_6$ mixture with partial pressures 38:2 Torr (left). Effective gas gain vs transfer field 1 strength in a $CF_4$:$SF_6$ mixture with partial pressures 38:2 Torr (right). The majority of error bars are smaller than the marker size and are therefore not observed.

slow up to 1400 V/cm producing a gas gain of 31100 ± 400 before sparking was observed at 1500 V/cm. This trend is different to what was observed in 40 Torr of pure $SF_6$ which demonstrated a plateau above a field strength of 900 V/cm. As no plateau can be observed, the optimum transfer field was chosen to be 1400 V/cm as this produced the largest gas gain before sparking occurred.

## 6.6 Sub-atmospheric $CF_4$:$SF_6$:He Mixtures

Following the gain optimisation of the collection and transfer fields in the MMThGEM for operation with the $CF_4$:$SF_6$ base mixture, He was again added to the vessel. Measurements were taken for total pressures of 50, 75, 100, 150, 380, and 760 Torr. The cathode voltage, mesh 1 voltage and transfer field were set to -500 V, 50 V and 1400 V/cm respectively. Then the amplification fields were again increased in tandem in increments of 500 V/cm and gain measurements were taken for each mixture until sparking occurred. The results of this are presented in Figure 6.6.

Similar to the $SF_6$:He mixtures, the $CF_4$:$SF_6$:He mixtures were not able to produce measurable gas gains above a total pressure of 100 Torr. The gain curves which could be measured are seen in Figure 6.6 (left) and all exhibit exponential behavior and shift to the

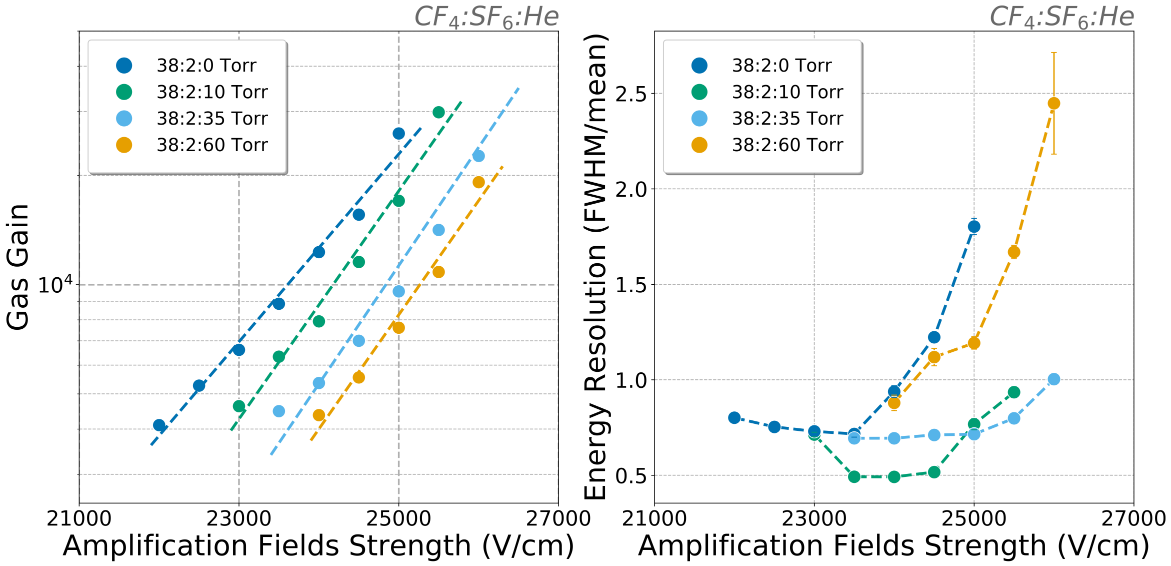

Figure 6.6 Effective gas gain vs amplification fields strength in $CF_4$:$SF_6$:He mixtures (left). Energy resolution vs amplification fields strength in $CF_4$:$SF_6$:He mixtures (right). Some error bars are smaller than the marker size and are therefore omitted from the graph.

right with increasing partial pressure of He. Considering the base mixture of $CF_4$:$SF_6$, and comparing this to the 40 Torr pure $SF_6$ gain curve in Figure 6.4, the amplification fields required to produce a comparable gas gain has been significantly reduced. For example, the amplification field strength required to produce a gas gain $> 10^4$ has reduced from $\sim$ 28500 V/cm to $\sim$ 24000 V/cm.

As He is added to the vessel, the maximum attainable gas gain initially rises very slightly with 10 Torr of He. As the partial pressure of He increases to 35 and 60 Torr the maximum gas gain drops. This suggests that the maximum gas gain could drop further as more He is added to the vessel. The maximum gas gains achieved for all $CF_4$:$SF_6$:He mixtures are presented in Table 6.3.

Table 6.3 Summary of $CF_4$:$SF_6$:He results including maximum stable gas gain, $G_{max}$, and the minimum/maximum energy resolution, $ER_{min}$ and $ER_{max}$.

| $CF_4$:$SF_6$:He Pressure (Torr) | $G_{max} \times 10^4$ | $ER_{min}$ | $ER_{max}$ |
|---|---|---|---|
| 38:2:0 | $2.61 \pm 0.03$ | $0.72 \pm 0.01$ | $1.80 \pm 0.04$ |
| 38:2:10 | $2.99 \pm 0.03$ | $0.49 \pm 0.03$ | $0.94 \pm 0.03$ |
| 38:2:35 | $2.26 \pm 0.08$ | $0.66 \pm 0.02$ | $1.00 \pm 0.01$ |
| 38:2:60 | $1.9 \pm 0.1$ | $0.86 \pm 0.04$ | $2.4 \pm 0.3$ |

Interestingly, the maximum stable gas gains observed in the $CF_4$:$SF_6$:He mixtures is considerably smaller than what was observed in the $SF_6$:He mixtures before sparking occurred, around $\sim 3 \times 10^4$ compared to $\sim 9 \times 10^4$. This could be due to the lower proportion of $SF_6$ molecules resulting in more of the avalanche electrons being able to propagate freely after the first amplification stage. This could make the probability of electrical breakdown in the second amplification stage more likely. Other possible compounding factors could include photon feedback, due to scintillation in these mixtures, and a reduced attachment cross section due to the larger transfer field strength.

The energy resolution has been evaluated for the various $CF_4$:$SF_6$:He mixtures and can be observed in Figure 6.6 (right). Additionally, the minimum and maximum energy resolutions measured are summarised in Table 6.3. With a small addition of 10 Torr of He the energy resolution appears to initially improve. However, as more He is added to the vessel, the energy resolution deteriorates significantly. Similar to the $SF_6$:He mixtures with larger partial pressures of He, the energy resolution was measured to be $> 2$ in the 38:2:60 Torr mixture. The worsening energy resolution with increasing partial pressure of He is likely the reason why gas gains could not be measured at 150, 380, and 760 Torr.

These results demonstrate gas gains on the order of $10^4$, in not only a low pressure NID gas mixture of $CF_4$:$SF_6$ but also, with additions of He up to a total pressure of 100 Torr. In addition to being an NID gas mixture containing He, these mixtures have the potential to scintillate due to the $CF_4$ component. Future work is therefore required to investigate the scintillating properties of these gas mixtures and further optimise the device for atmospheric mixtures.

## 6.7 Conclusions

In conclusion, the CYGNO collaboration is considering the use of He mixtures, which will extend directional sensitivity to lower WIMP masses. Ideally these mixtures will contain a low partial pressure of fluorine rich gases like $CF_4$ and most importantly the NID gas $SF_6$. A multi-stage MMThGEM has recently demonstrated significant charge amplification in the NID gas $SF_6$ at low pressure [233] and therefore makes a good candidate for testing mixtures containing $SF_6$ and He.

By first building on a previous optimisation of the MMThGEM, gas gain measurements were taken in 30 and 50 Torr and compared to the previous results in 40 Torr of pure $SF_6$. It was found that 40 Torr of $SF_6$ performed the best by producing the largest gas gain while also producing comparable energy resolutions to the 30 and 50 Torr runs. He was then added incrementally to 40 Torr of $SF_6$ and gas gain measurements were obtained up to a total pressure of 100 Torr. These results demonstrated that maximum gas gains on the order of $10^4$ are possible in $SF_6$:He mixtures up to at least 100 Torr. As the partial pressure of He increased the maximum stable gas gain began to recede and the energy resolution worsened significantly to $> 2$ in some cases. The worsening gain and energy resolution is likely the reason why measurements could not be achieved with further additions of He; at total pressures of 150, 380, and 760 Torr.

In an attempt to find a scintillating NID gas mixture containing He, which could potentially facilitate a complementary light/charge readout capability, a significant portion of the $SF_6$ base gas was replaced with $CF_4$ in proportions of 38:2 Torr $CF_4$:$SF_6$. A comprehensive optimisation procedure was carried out on the collection and transfer fields in the MMThGEM. Following this, He was added to the mixture gradually. It was found that gas gains on the order of $10^4$ could be achieved in $CF_4$:$SF_6$:He mixtures up to a total pressure of 100 Torr for the first time. Similar to the $SF_6$:He mixtures, the gain and energy resolution worsened with increasing partial pressure of He and is likely the reason why gain measurements could not be made at 150, 380, and 760 Torr.

Considering these results, the potential for lower cost atmospheric operation in the future could be realised by minimising the energy resolution via optimisation of the MMThGEM field strengths; improving the energy resolution would also benefit the measurement of the crucial head-tail effect [202]. As it was found that the MMThGEM optimisation could have some dependance on gas composition, an iterative optimisation procedure could be used in future following the initial additions of He. Finally, the light yield of similar $CF_4$:$SF_6$:He mixtures should be demonstrated in the interest of a complementary light/charge readout method for use in future CYGNO experiments.

# Chapter 7

# High Gain MMThGEM-Micromegas Operated in a CYGNUS-m$^3$ Scale Vessel

In the previous chapters, the MMThGEM has been successfully demonstrated as an excellent gain stage device in the NID gas $SF_6$; capable of producing gas gains comparable with the electron drift gas $CF_4$. The MMThGEM is therefore ideal for coupling to a strip readout detector like a micromegas to achieve a multi-dimensional NI readout plane which is potentially suitable for the scale up required by a CYGNUS search. In this chapter, the initial demonstration of such a MMThGEM-Micromegas in low pressure $SF_6$ is described. This includes detector characterisation in a small test vessel followed by the detection of NRs in a large cubic metre scale vessel for the first time. This work additionally featured charge sensitive electronics, specifically designed for use in multi-channel detectors like a micromegas, partially developed by Kobe University in Japan, who also provided access to the vessels where the work was performed.

In Section 7.1, the detector is first introduced, followed by a description of the experimental setup in a test vessel. The effective gas gain is established on the strips in Section 7.2 and the detector's directional response to alpha particles is evaluated in Section 7.3. Following the characterisation of the detector response in the test vessel, work is presented in Section 7.4 which describes an exposure to a $^{252}$Cf neutron source in a large CYGNUS-m$^3$ scale vessel alongside supplementary ER/NR simulations. Finally, conclusions are drawn in Section 7.5.

## 7.1 Detector Configuration and Experimental Setup

In Chapters 4 - 6, sub $10^5$ gas gains in the NID gas $SF_6$, and mixtures thereof, were demonstrated with the MMThGEM and subjected to validation. Provided that sufficient care is given to the design and optimisation of a charge amplification stage device, these gas gain measurements suggest that future directional DM searches, which utilise an NID gas for its high-fidelity, will be able to operate with a comparable level of charge amplification to conventional gaseous TPC targets like $CF_4$. The MMThGEM is therefore an excellent gain stage device for coupling to a high-granularity x-y charge readout plane. One possible technology, presented here, is a type of MPGD called a micromegas (introduced previously in Chapter 2).

### 7.1.1 Coupled MMThGEM-Micromegas Detector

The MMThGEM TPC, used in Chapters 4 - 6, was mounted 1 mm above a micromegas plane as shown in Figure 7.1. As discussed in Chapter 2, a micromegas detector is an MPGD which utilises a parallel plate avalanche region, established between a mesh electrode and a

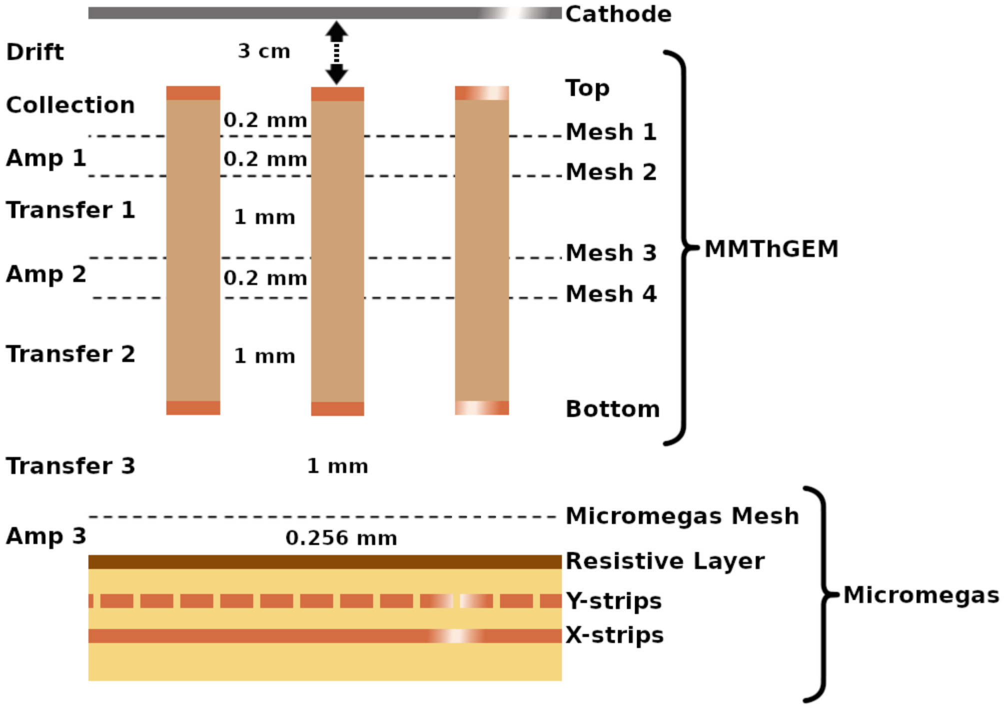

Figure 7.1 Cross sectional diagram of the coupled MMThGEM-Micromegas detector depicted with a 3 cm drift length used during small scale testing.

micro-strip plane; it was originally designed to help overcome the limitations of MWPCs, like those used in DRIFT, and micro-strip gas chambers [175]. The micromegas used in this work, depicted in Figure 7.1, has an amplification gap of 256 $\mu$m between the micromegas mesh and the surface of the micro-strip readout plane. The offset between the MMThGEM bottom and micromegas mesh, and the gap between the micromegas mesh and the strip readout plane are denoted as the third transfer and amplification regions respectively. The micro-strip readout plane consists of a Diamond Like Carbon (DLC) resistive anode layer on top of orthogonal x and y micro-strip electrode planes, which are embedded in a supportive printed circuit board. In this design, the y-strips are situated above the x-strips which have a width of 100 $\mu$m and 220 $\mu$m respectively with a pitch of 250 $\mu$m. The micromegas has an active area of $10 \times 10$ cm$^2$ which is identical to the MMThGEM.

A similar MMThGEM-Micromegas configuration has been used before in pure $SF_6$ [129]. However, these previous measurements were only able to accurately measure gas gains up to 9000 in low pressure $SF_6$. Additionally, the strips of the micromegas had to be grouped into pairs to improve the charge collection per channel; this made measurements with the lower available gas gains at the time more feasible. This means that the granularity of the micromegas strip readout was not used to its full potential.

The aforementioned measurements with this coupled detector preceded the results presented in Chapters 4 - 6. Due to the significant amount of work which has been dedicated to improving charge amplification with the MMThGEM, an evaluation of the coupled detector's performance with individually instrumented strips in low pressure pure $SF_6$ is presented in this chapter.

### 7.1.2 Experimental Setup in the Kobe Test Vessel

To begin the detector characterisation in the small test vessel, the coupled MMThGEM-Micromegas TPC was first assembled and mounted in the centre of an aluminium plate, shown in Figure 7.2a, with a 0.5 cm standoff from the plate. This plate was mounted to the door of the test vessel with an 8 cm standoff. Once assembled, the detector was then sealed inside by mounting the door to the test vessel. The test vessel also featured a thin kapton window, shown in Figure 7.2b, to aid calibration.

For the HV connections, a resistor chain was soldered to the MMThGEM electrodes to reduce the number of HV channels required for operation. A diagram depicting the resistor chain can be seen in Figure 7.3. The resistors, which divide the potential difference across the MMThGEM electrodes, are indicated as R1 - R6. The values of these resistors are based on the previous pure $SF_6$ optimisation presented in Chapter 4. Taking into account the additional amplification supplied by the third amplification region, in the micromegas, the resistor chain

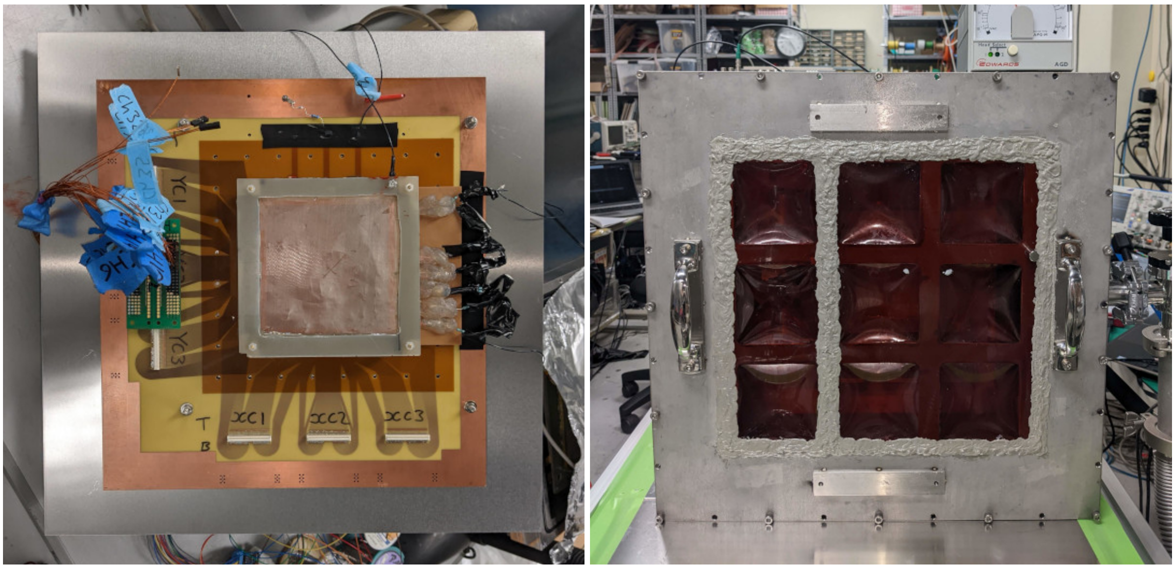

(a) (b)

Figure 7.2 (a) Image of the coupled MMThGEM-Micromegas TPC assembly mounted to the door of the test vessel. (b) Image of the test vessel with brown kapton window containing the coupled MMThGEM-Micromegas TPC assembly mounted inside.

was modelled after voltage settings which were capable of producing a gas gain $\approx 1 \times 10^4$; i.e. with M1 voltage, transfer and amplification field strengths of 40 V, 900 V/cm and 28000 V/cm respectively (see Chapter 4 for further details). The resistor chain divides the potential difference between $V_{in}$ and $V_{out}$ which were connected to two separate HV supplies. Series resistors, $R_s$, of magnitude 200 MΩ were also used to mediate the connection between the resistor chain and the MMThGEM electrodes. Two additional HV supplies were used for biasing the cathode and micromegas mesh separately, while the resistive layer and strips of the micromegas were connected to ground. All four HV channels were provided by CAEN A7030DP and A7030DN modules situated in a SY5527LC Universal Multichannel Power Supply System which was managed via the GECO 2020 control software on a dedicated PC.

To instrument the micromegas strips, a green breakout board with a 130 pin 2-way panasonic P5KS connector interfaced with the central y-strip connector on the micromegas, seen in Figure 7.2a. Connections were made between 32 pins on the breakout board and a feedthrough so that the strips could be instrumented externally with LTARS2018 charge sensitive electronics, discussed in the following section. These connections corresponded with 32 individual neighbouring y-strips with a central position in the TPC. This amounts to a total instrumented area of 7.85 mm × 10 cm.

Once the MMThGEM-Micromegas TPC was sealed inside the test vessel, the vessel was evacuated for 48 hours to allow for outgassing. Prior to measurements taking place, the

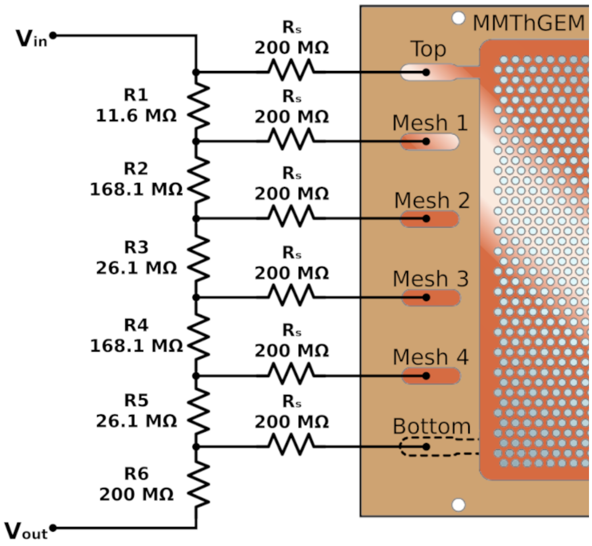

Figure 7.3 Circuit diagram of the MMThGEM resistor chain used for HV biasing.

vessel was filled with 40 Torr of $SF_6$. During measurements, the test vessel had a leak rate of 0.3 Torr per hour and measurements were typically completed within 1 hour of filling.

### 7.1.3 LTARS2018 Charge Sensitive Electronics

As mentioned, 32 micromegas y-strips were instrumented with LTARS2018 charge sensitive electronics. The Low-Temperature Analog Readout System (LTARS) is a versatile front-end readout system, depicted in Figure 7.4, which can provide the charge sensitive electronics for multi-channel detectors like a $\mu$-PIC or micromegas. The system was designed in collaboration between KEK and Kobe University partly for the purpose of NID gaseous TPC measurements [234]. A NEWAGE 2018 RO board, which utilises LTARS electronics, was purchased and taken to Kobe University for testing; a photograph of the board can be seen in Figure 7.4a.

One NEWAGE 2018 RO board is capable of providing the charge sensitive preamplifer and shaping electronics for 32 channels. Figure 7.4a highlights the main electrical components and illustrates the order in which the signals are processed by the board. As shown, 32 micromegas strips are connected to the input. Signals from the strips are amplified and shaped by the two LTARS2018 Application-Specific Integrated Circuit (ASIC) chips. Each LTARS2018 ASIC provides a High Gain (HG) and Low Gain (LG) output for 16 input channels. The HG and LG signals are passed to differential buffers which duplicate and invert the signal. The original and inverted HG and LG signals for all 32 channels are then passed to the input of a DELTA V2 Digitiser board seen in Figure 7.4b.

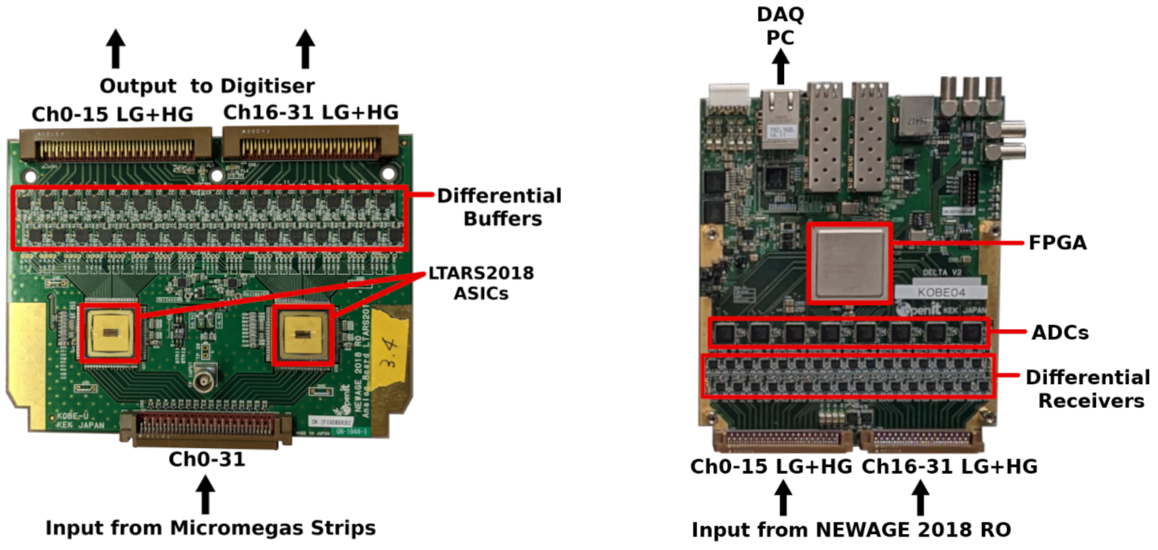

(a) (b)

Figure 7.4 (a) Annotated image of the NEWAGE 2018 RO board with LTARS2018 ASICs. (b) Annotated image of the DELTA V2 Digitiser board used at Kobe University.

The purpose of sending both the original and inverted signals is to reduce the influence of ElectroMagnetic Interference (EMI) before reaching the digitiser board. The differential receivers, highlighted in Figure 7.4b, combine the signals by subtracting the inverted signal from the original, thus removing any shared EMI induced noise. The outputs from the differential receivers are then passed to ADCs so that the analogue signals can be stored digitally. The board is controlled by a programmed FPGA chip on the digitiser which allows the board to interface via an ethernet connection with a data acquisition (DAQ) PC; from which the data collection can be managed.

### 7.1.4 Calibration of Electronics

In order to determine the amount of charge arriving on each instrumented strip, the electronics were first subjected to a calibration procedure. Square waves from an HP 8116A function generator were injected into the inputs of the LTARS2018 ASICs via 32 1 pF parallel capacitors and the amplitude was used to vary the amount of charge reaching the input. The amplitude was varied from 50 - 100 mV in increments of 10 mV and then from 100 - 2400 mV in increments of 100 mV, due to the dynamic range provided by the HG and LG channels. The average output maximum pulse height and signal integration (above a 5 mV threshold) for each input amplitude was recorded. The results of the calibration for both HG and LG channels can be seen in Figure 7.5.

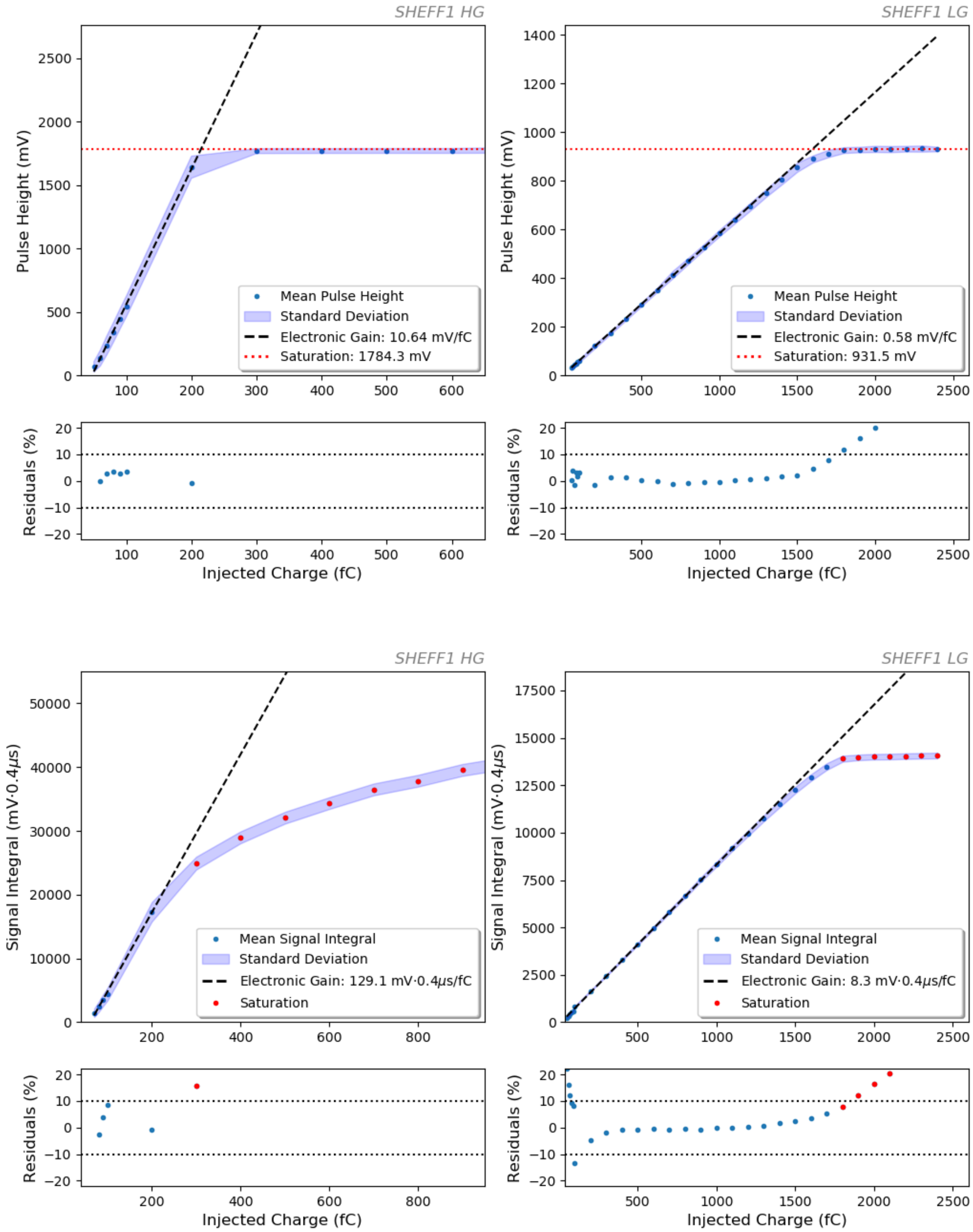

Figure 7.5 Average maximum pulse height calibration (top) and average signal integration calibration (bottom), for both HG (left) and LG channels (right).

The average maximum pulse height and signal integral for all 32 channels is plotted as a function of injected charge and the standard deviation is displayed as the blue shaded region. As the amount of injected charge increases, the output initially increases linearly. A linear regression analysis was performed and the resulting line of best fit was used for the purpose of charge calibration. The electronic gain was extracted from the gradient of these lines and is summarised in Table 7.1. These values are in good agreement with the conversion gain of the LTARS2018 chips demonstrated previously [235, 236]. As the shaping time of the LTARS ASIC is identical to the CREMAT shaper used in previous chapters (4 $\mu$s) [236], and because the signal integral method has been shown as a robust method in NID gases in Chapter 5, the signal integral method is used for charge conversion in this chapter.

Table 7.1 Electronic gain values and saturation voltages for HG and LG channels on the NEWAGE 2018 RO board.

| | Pulse Height Gain (mV/fC) | Signal Integral Gain (mV·0.4$\mu$s/fC) | Saturation Voltage (mV) |
|---|---|---|---|
| HG Channels | 10.64 ± 0.05 | 129.1 ± 0.5 | 1784.3 ± 0.3 |
| LG Channels | 0.58 ± 0.07 | 8.3 ± 0.6 | 931.5 ± 0.6 |

The percentage residuals can also be seen plotted below each calibration graph in blue with ± 10% limits displayed as black dotted lines. It can be seen for the HG channels that the linear relationship is maintained within a ± 10% uncertainty up to 200 fC and up to 1700 fC for the LG channels. Above which the residuals increased significantly and correspond with the plateau caused by saturation. The saturation voltage is also summarised in Table 7.1 and was calculated as the average maximum pulse height with residuals greater than 10%. The positive saturation of the HG channels was larger than previously demonstrated due to a negative pedestal offset which improved the positive-going (negative charge) dynamic range of the HG channels from 100 fC [235, 236] to 200 fC. This saturation voltage was used to veto events.

### 7.1.5 Source Positioning

Once the detector setup had been mounted inside the test vessel and was evacuated and filled with 40 Torr of $SF_6$, sources of ionising radiation were positioned around the instrumented TPC volume. The sources included an $^{55}$Fe X-ray source, 0.8 MBq, and an $^{241}$Am alpha particle source, $\mathcal{O}$(10 kBq). A diagram was created to aid the explanation of the source positions relative to the instrumented TPC volume and can be seen in Figure 7.6.

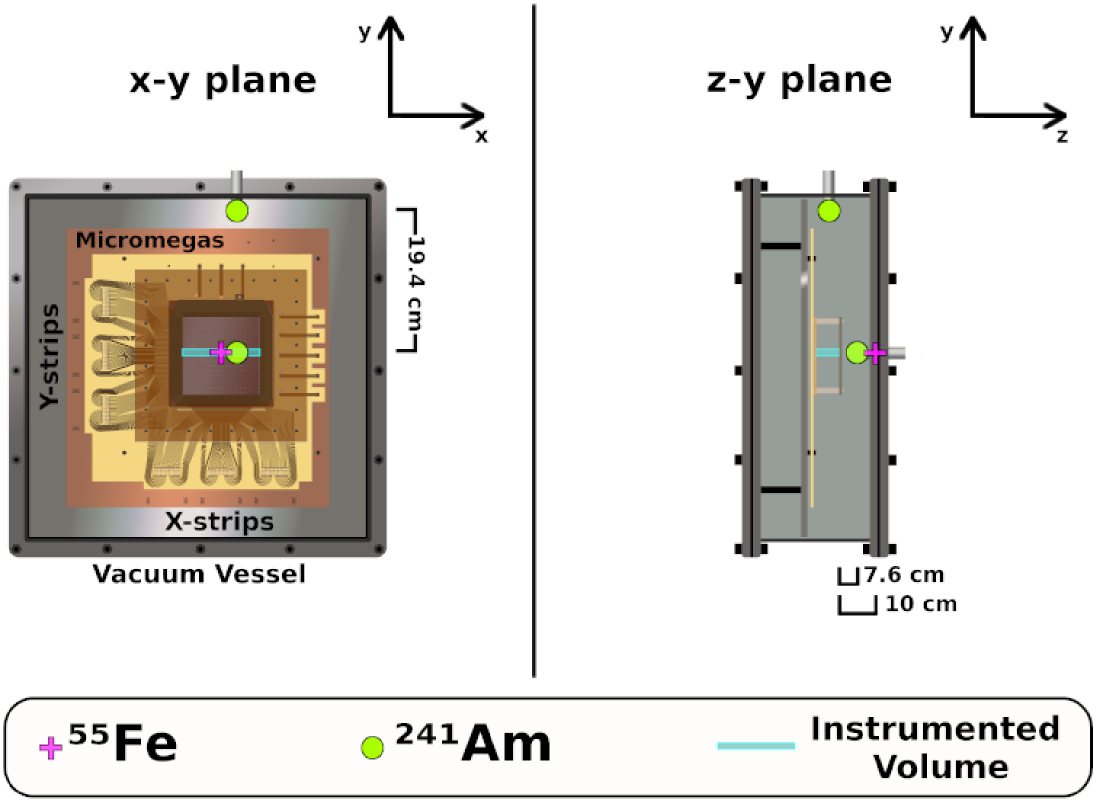

Figure 7.6 Diagram showing the positioning of radioactive sources around the TPC volume.

The panel on the left of Figure 7.6 shows a cross section of the detector mounted in the test vessel in the x-y plane, while the panel on the right shows a cross section in the z-y plane. The cross section of the instrumented TPC volume can be seen highlighted in cyan above the micromegas plane. The source positions can be seen indicated by a magenta plus and green circle icons for the $^{55}$Fe and $^{241}$Am positions respectively.

During the X-ray exposure, the $^{55}$Fe source was positioned externally in the kapton window of the test vessel. This placed the source directly in front of the instrumented strips in the x-y plane with an offset in the z-dimension of 10 cm from the instrumented volume.

For the purpose of orthogonal directional measurements, the $^{241}$Am source was given a y-axis and z-axis exposure position. During the y-axis exposure, the $^{241}$Am source was positioned internally, via a magnet, with a 19.4 cm distance in the y-dimension from the instrumented volume. During the z-axis exposures, it can be seen that the $^{241}$Am source was positioned directly in front of the instrumented volume with a separation in the z-axis of 7.6 cm.

## 7.2 $^{55}$Fe Gain Measurements on the Micromegas Strips

In this section, work which evaluates the gas gain measured on the detector strips, with optimised MMThGEM voltage settings obtained previously in Chapter 4, using the $^{55}$Fe source is presented. The HV biasing was set to be -2900 V, -1900 V, 100 V, and -530 V for the cathode, V$_{in}$, V$_{out}$ and micromegas mesh respectively. Using these voltage settings, $^{55}$Fe X-ray events were successfully detected on both the HG and LG channels; a range of voltage settings could not be determined due to the narrow range of stable voltages which conserved the optimised MMThGEM voltage settings and produced signals visible to both HG and LG channels.

### 7.2.1 Preprocessing of Event Signals

Before the detector's gain could be determined, the event waveforms required some preprocessing. During the measurements, a loose connection between the feedthrough and one strip resulted in a dead channel. This channel was identified as #16 and its null-response to an X-ray event can be observed on the left in Figure 7.7. Due to its central position, it would be detrimental to ignore the charge contribution of channel 16. To this avail, the voltage response of channel 16 was estimated by calculating the average instantaneous voltage of channels 15 and 17. The result of this interpolation can be seen on the right of Figure 7.7.

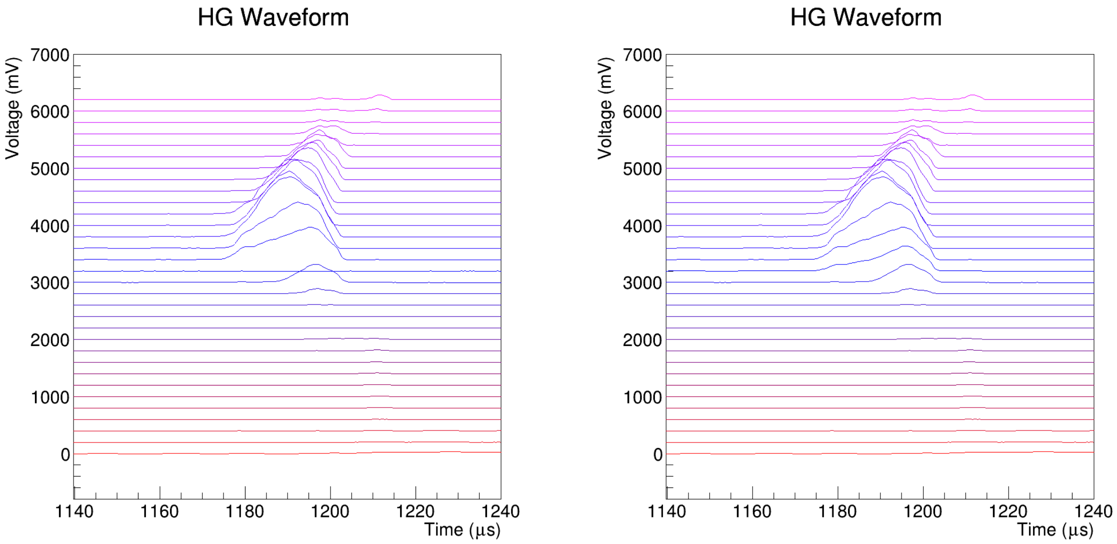

Figure 7.7 Example event before dead channel interpolation (left). The same event after dead channel interpolation (right). Vertical offset of channels used for clarity only.

Following the interpolation correction, events needed to be appropriately selected for the gain calculations. Due to charge dissipation in the resistive layer of the micromegas, events can span across several strips [129]. Therefore, a cut must be applied to the events close to the edge of the instrumented area. This cut ensures that the amount of charge registered per event is not artificially diminished due to charge falling outside the instrumented area. To perform this cut, the channel with the largest amplitude per event was determined, this channel was found to be centred within the cluster, and the event was cut if the channel number was less than 13 or more than 18. An example of an edge event cut from the gain calculations, with a peak channel number of 27, can be seen on the left in Figure 7.8. An example of a centred event accepted for the gain calculations, with a peak channel number of 13, can be seen on the right of Figure 7.8.

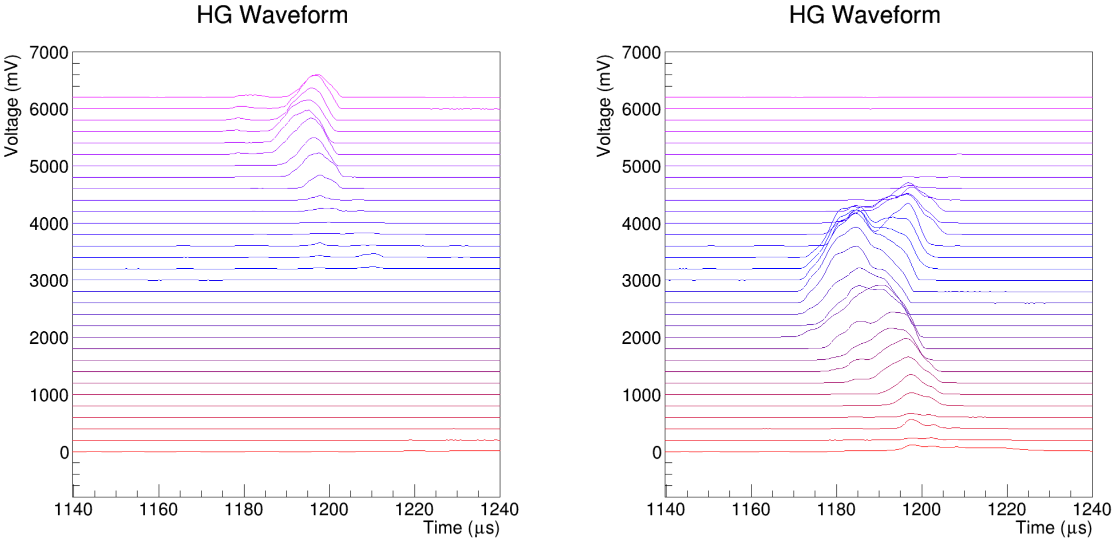

Figure 7.8 Example of edge event which was removed by the edge cut (left). Example of centred event accepted for the gain calculations (right). Vertical offset of channels used for clarity only.

## 7.2.2 Gain Determination

Once the events from the $^{55}$Fe exposure had been preprocessed, the events could be binned according to the signal integral; following application of the charge calibration presented in Table 7.1 and summation across all 32 strips. Figure 7.9 shows the signal integral spectrum from the $^{55}$Fe exposure in solid magenta and a background exposure, without any edge cuts applied, in hatched violet.

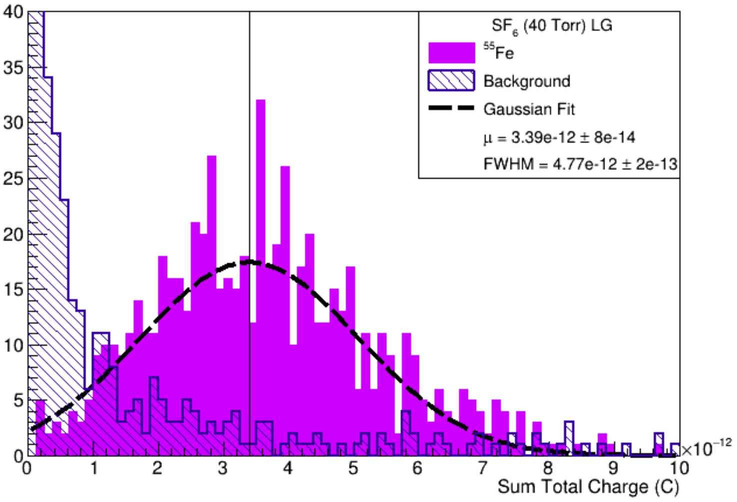

Figure 7.9 Sum total charge spectrum with the signal integral method as measured on the LG channels.

A Gaussian function was fit to the $^{55}$Fe exposure data and can be seen superimposed on top as a dashed black line with the mean of the Gaussian, $\mu$, indicated by a vertical black line. The gain was determined via the $^{55}$Fe X-ray energy, 5.89 keV, and W-value of SF$_6$, 34 eV [216]. It was found that the detector produced an effective gas gain of $1.22 \pm 0.08 \times 10^5$ with an energy resolution of $1.41 \pm 0.07$.

This result is significant because this is the first time a gas gain on the order of $10^5$ has been achieved with an NID gas; furthermore, this is more than two orders of magnitude larger than typical NID gas gains. This result is credible considering that the MMThGEM is known to be providing an amplification factor of $\approx 10^4$ and the micromegas mesh provides additional amplification; an apparent amplification factor $\approx 12.2$.

## 7.3 $^{241}$Am Principle Axis Reconstruction Algorithm

The instrumented micromegas y-strips now provide the opportunity to investigate 2-dimensional directionality. As highlighted in Chapter 2, determining the principle axis and identifying sense via $\frac{dE}{dx}$ signatures is important for directional searches. In this section, work in which a track reconstruction algorithm was developed, via exposures to an $^{241}$Am alpha particle source, is presented. Due to the highly ionising nature of alpha particles, the field strengths applied to the MMThGEM and micromegas had to be lowered slightly during these runs to reduce sparking. The voltages applied to the cathode, V$_{in}$, V$_{out}$, and the micromegas mesh were -2800 V, -1800 V, 100 V, and -500 V respectively.

### 7.3.1 Detector Response to Alpha Tracks

By using the aforementioned voltage settings, alpha tracks were successfully detected in both the y-axis and z-axis exposure directions, outlined in subsection 7.1.5. During the z-axis alpha particle exposure, events were observed to have discontinuity between consecutive charge clusters. An example of this artefact can be seen on the left of Figure 7.10. The channel number is plotted as a function of time dictated by the digitiser clock. The instantaneous voltage of each channel is indicated by the colour scale in mV. The points above a 40 mV threshold are indicated by magenta markers. Multiple charge clusters can be seen to arrive in quick succession and this was hypothesised to be caused by the MMThGEM hole pitch; this is illustrated by the image of two holes, superimposed on top of the event, which share the same approximate separation along the y-axis.

A diagram which aids the explanation of this hypothesis can be seen on the right of Figure 7.10. If the hole pitch is responsible for the discontinuity, then the ΔY separation (channel #) between consecutive clusters would be equivalent to the pitch of the MMThGEM holes. If true, the ΔZ (temporal) separation of clusters, i.e. the track discontinuity, could be explained by NIs, produced along the length of the track, clustering together as they enter the MMThGEM holes.

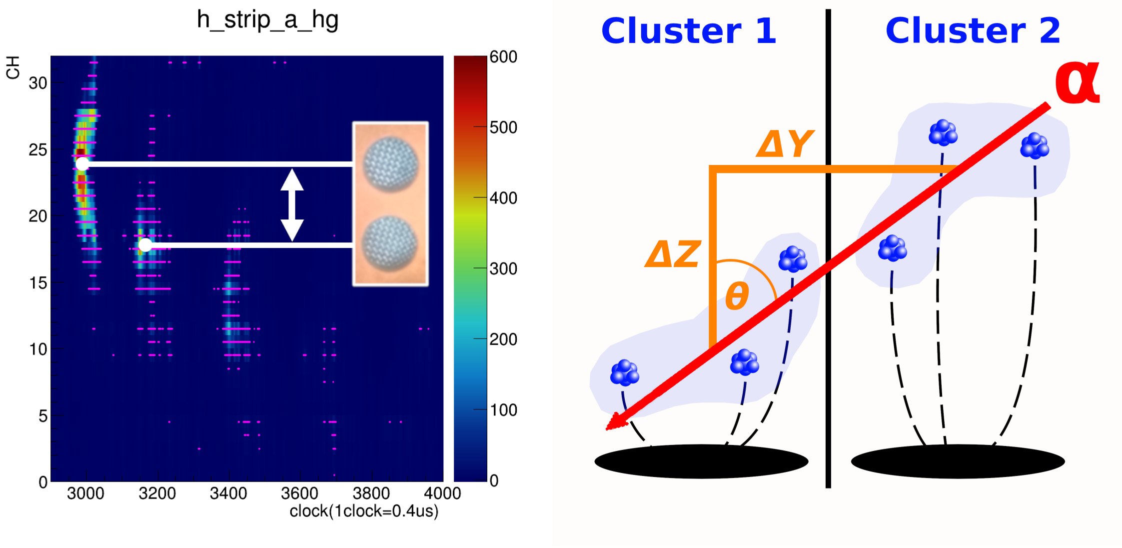

Figure 7.10 Example event exhibiting charge discontinuity with image of two MMThGEM holes indicating the expected y-separation between consecutive clusters (left). Diagram depicting the clustering of NIs in neighbouring MMThGEM holes following an alpha event (right).

This hypothesis was tested by measuring both the $\Delta$Y and $\Delta$Z separation between consecutive clusters in the first 100 alpha events measured during the z-axis exposure; shown in Figure 7.11. The histogram on the left shows the y-separation of consecutive clusters and also includes the mean (solid black line) $\pm$ the micromegas strip pitch (dashed black lines) and the MMThGEM hole pitch (solid red line). It can be seen that the mean $\Delta$Y separation is in good agreement with the MMThGEM hole pitch. Furthermore, the $\Delta$Z cluster separation, on the right of Figure 7.11, features a peak at $\sim$ 3 mm with a longer trailing tail on the right hand side up to $\sim$ 10 mm. These values correspond to a $\theta$ range between 6 - 20°, where $\theta$ represents the angle between the z-axis and the track, which is consistent with the source positioning. These findings strongly indicate that the track discontinuity is a result of the MMThGEM hole pitch.

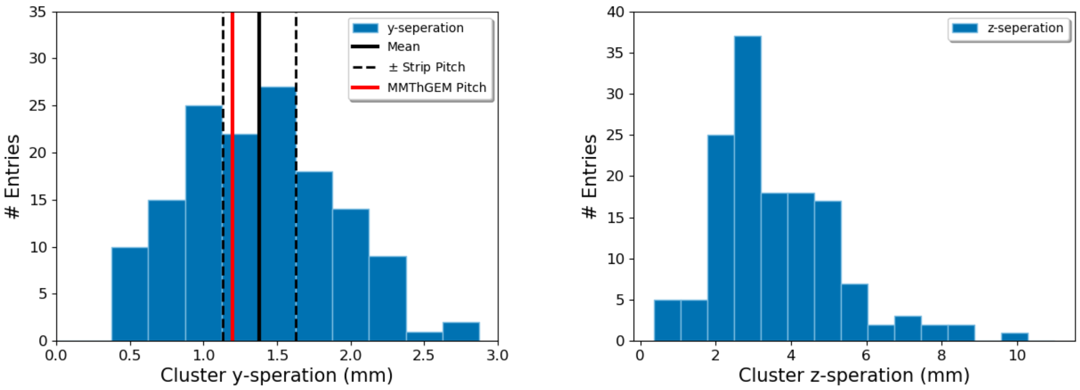

Figure 7.11 Histograms showing the separation of consecutive charge clusters in the first 100 z-axis exposure events measured in the y-axis (left) and z-axis (right).

### 7.3.2 Principle Track Reconstruction and Sense Recognition

Once the observed discontinuity in the arrival of charge on the micromegas strips was understood, a Total Linear Regression (TLR), also known as Deming regression, algorithm was developed for determining the principle axis of alpha tracks in the y-axis and z-axis exposures. A TLR algorithm was ideal for this purpose, as it accounts for the residuals in both axes and effectively handles the highly rectilinear nature of alpha particle tracks. This algorithm was implemented by first determining all the points above a 40 mV threshold, followed by the conversion of these coordinates to spatial units via the micromegas strip pitch and ion drift velocity. For each event, the gradient, m, and y-intercept, c, of the track in the z-y plane was calculated as [237]:

$$m = -p + \sqrt{1+p^2}, \quad c = \bar{Y} - m\bar{Z}, \quad \text{where} \quad p = \frac{S_{ZZ} - S_{YY}}{S_{ZY}},$$

$\bar{Y}$ and $\bar{Z}$ are the average y and z coordinates of those above threshold and $S_{ZZ}$, $S_{YY}$, and $S_{ZY}$ are defined as:

$$S_{ZZ} = \frac{1}{n}\sum_{i=1}^{n} Z_i^2 - \bar{Z}, \quad S_{YY} = \frac{1}{n}\sum_{i=1}^{n} Y_i^2 - \bar{Y}, \quad S_{ZY} = \frac{1}{n}\sum_{i=1}^{n} Z_i Y_i - \bar{Z}\bar{Y}, \tag{7.1}$$

where $n$ is the total number of points above threshold. By visual inspection, the algorithm performed well for track reconstruction during both perpendicular exposures. The result of this algorithm applied to a z-axis and y-axis exposure event can be seen overlaid in red in Figure 7.12.

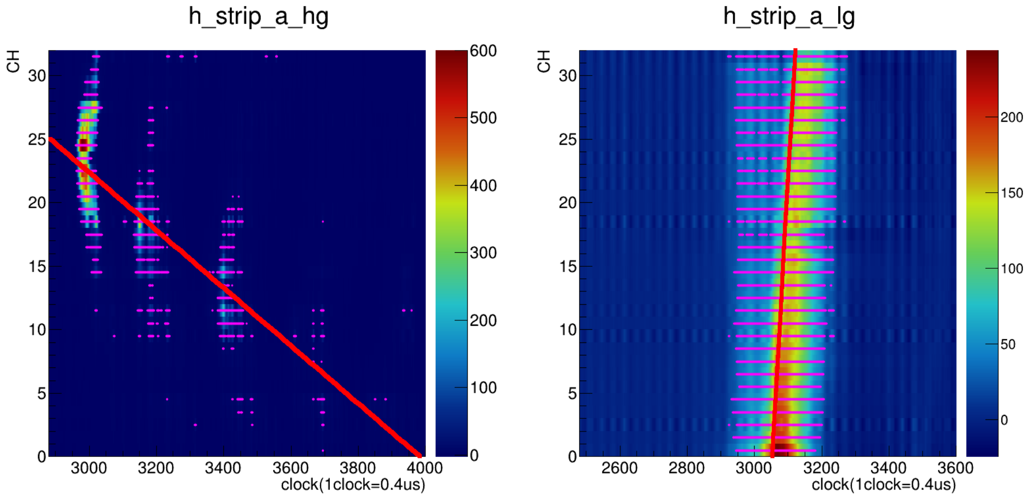

Figure 7.12 The TLR algorithm applied to a z-axis exposure event with HG channels (left) and a y-axis exposure event with LG channels (right). Points above a 40 mV threshold are indicated by magenta markers and the TLR fit is indicated by a red line.

The TLR algorithm was applied to all events in the z-axis and y-axis exposures and $\theta$, i.e. the angle between the z-axis and the reconstructed track, was calculated. The results of which, shown in Figure 7.13, display a clear angular separation between events from the two orthogonal exposures. The z-axis events peak at $\theta$ = 0° while the y-axis events peak at $\theta$ = 90°. This result highlights the effectiveness of the TLR algorithm for accurately determining the principle axis in 2-dimensions.

Another interesting feature of the events presented in Figure 7.12 regards the $\frac{dE}{dx}$ of the alpha particle along its track. The intensity of the charge clusters in the z-axis exposure event increases from right to left, in the direction of the alpha particles motion. While the intensity

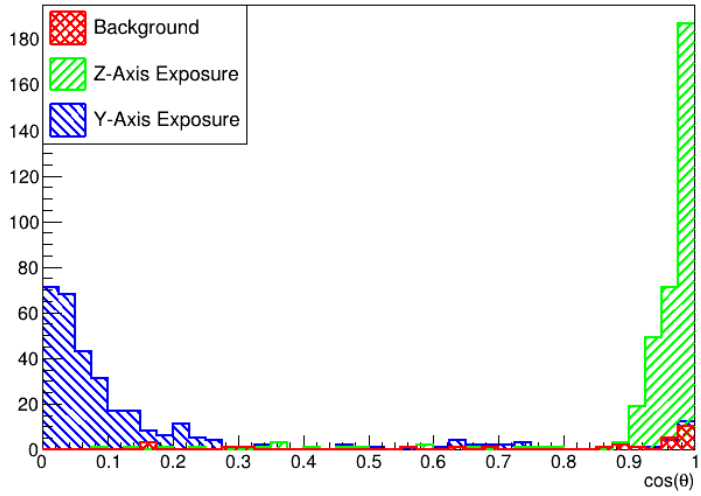

Figure 7.13 Distribution of the angle between the principle axis of an event and the z-axis determined via the TLR algorithm.

of the measured charge in the y-axis exposure event decreases along the length of the track; the alpha particle is travelling from channel 0 to 31. A SRIM (Stopping and Range of Ions in Matter) [238] simulation of the Bragg curve for 5.5 MeV alpha particles in 40 Torr of $SF_6$ was performed and the regions of interest for both the z-axis and y-axis exposures can be seen in Figure 7.14, highlighted in green and blue respectively. These regions of interest

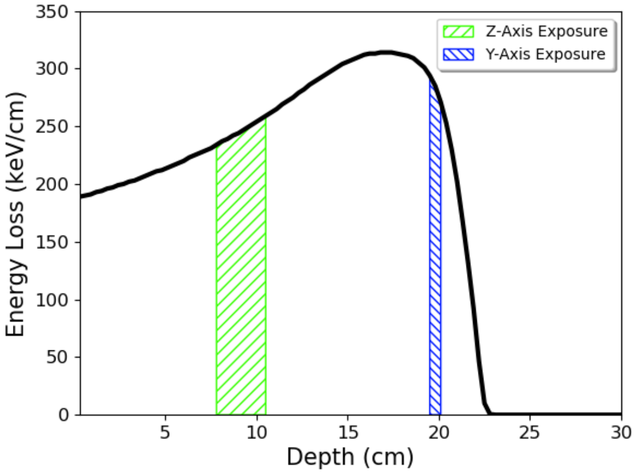

Figure 7.14 Bragg curve generated with 10,000 5.5 MeV alpha particles in 40 Torr of $SF_6$ using SRIM. Hatched regions indicate the section of the Bragg curve which was measured by the instrumented strips during the exposures.

correspond to the separation between the alpha source and instrumented volume during each exposure. As shown, the observed increasing and decreasing $\frac{dE}{dx}$ signatures along the length of the track, for the z-axis and y-axis exposures respectively, are found to be consistent with this simulation. This result is significant because it demonstrates that charge asymmetries, and therefore directional sense, can be resolved with this detector.

## 7.4 $^{252}$Cf Measurements in the Large BENTO Vessel

Following the successful characterisation of the MMThGEM-Micromegas detector in the test vessel, preliminary testing indicated that the detector was receptive to a $^{252}$Cf neutron source. Due to the limited drift length of the test vessel, the detector assembly was transferred to the Kobe University BENTO vessel to perform an initial large scale demonstration in low pressure $SF_6$. In this section, the detector installation in the BENTO vessel is discussed and results of an exposure to a $^{252}$Cf neutron source (0.3 MBq), including supplementary SRIM and SREM (Stopping and Range of Electrons in Matter) [239] simulations, are presented.

### 7.4.1 Experimental Setup in the BENTO Vessel

The BENTO vessel is a large CYGNUS-m$^3$ scale vessel which is capable of housing up to 18 small scale R&D detector readout planes. A diagram of the BENTO vessel can be seen on the left of Figure 7.15. As shown, the vessel has a height and width of 1.6 m and features a central cathode design with a 0.5 m drift length either side. This large drift distance is an important feature of the BENTO vessel as it is conducive for testing the capability of different readout technologies with a full scale CYGNUS drift length. To this effect, small scale detector modules can be mounted to the nine panels, highlighted in magenta, either side of the cathode. The door of the test vessel is conveniently designed to fit into these panels. This allowed the detector mounting on the test vessel door to be easily transferred to the central panel on one side of the BENTO vessel. The cathode used in the test vessel measurements was removed before installation. An image of the BENTO vessel following installation can be seen on the right of Figure 7.15.

After installation, the BENTO vessel was evacuated for $\sim$ 48 hours before being filled with 40 Torr of $SF_6$; this marks the first instance in which such a large volume of low pressure $SF_6$ has been utilised. The vessel was connected to a gas recirculation system which monitored gas conditions. Once filled, $V_{in}$, $V_{out}$ and the micromegas mesh voltages were once again set to -1900 V, 100 V, and -530 V while the cathode was set to -18.55 kV; this was done to replicate the field strengths used during the gas gain measurements in the test vessel,

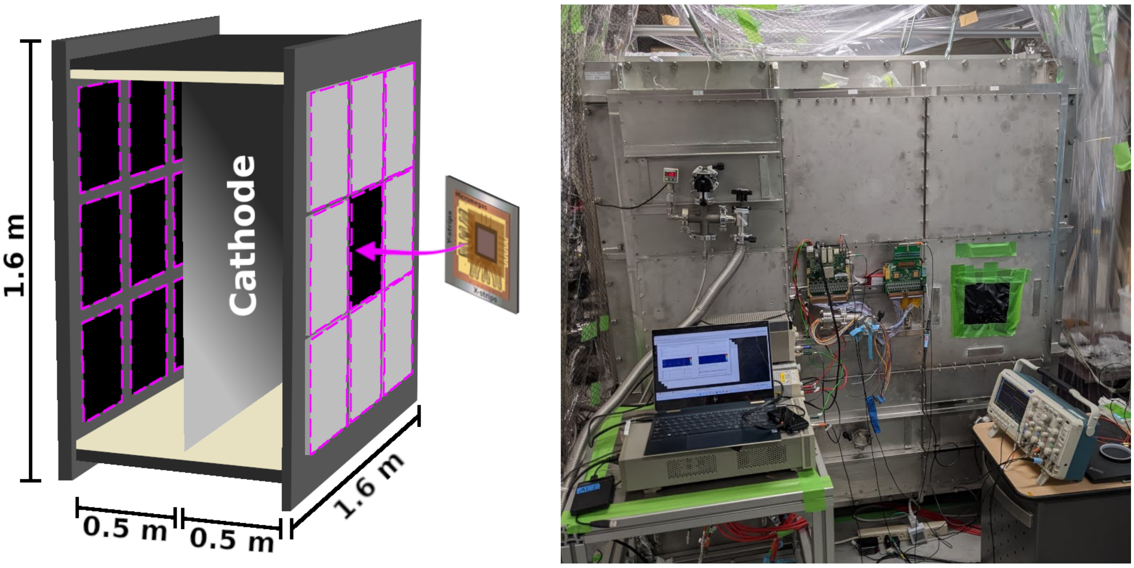

Figure 7.15 Diagram of the BENTO vessel depicting the vessel dimensions and installation of the MMThGEM-Micromegas detector (left). Image of the BENTO vessel following installation of the detector panel (right).

in Section 7.2. The $^{252}$Cf source was then placed externally in front of the central panel with a z-axis offset of 12.6 cm from the instrumented TPC volume, as illustrated in Figure 7.16.

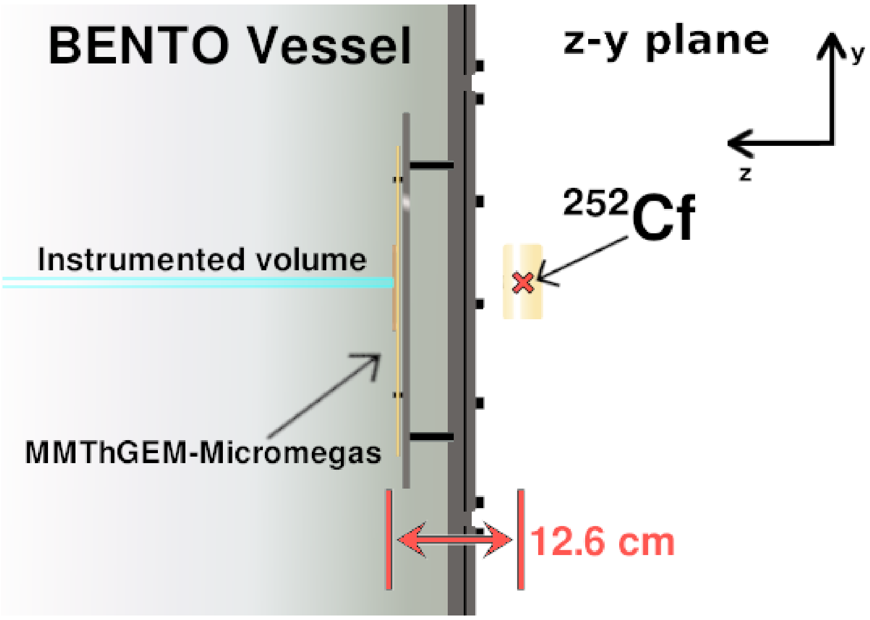

Figure 7.16 Cross sectional diagram depicting the $^{252}$Cf neutron source position relative to the MMThGEM-Micromegas assembly in the BENTO vessel.

Events were acquired over the course of 13 hours and the leak rate was negligible during this time.

### 7.4.2 Initial Inspection of Recoil Events

As a result of the exposure to the $^{252}$Cf neutron source in the BENTO vessel, 1210 events were successfully captured. Two example events from the exposure can be seen in Figure 7.17. The successful observation of events in such a large volume of low pressure $SF_6$ is a significant step forward for demonstrating the MMThGEM-Micromegas detector as a scalable readout technology for a future CYGNUS search.

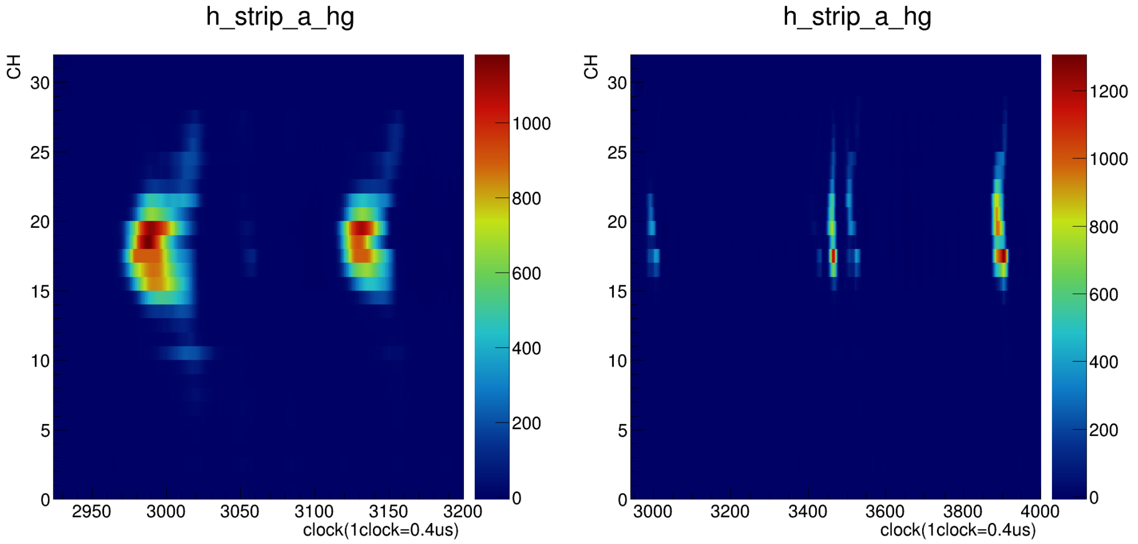

Figure 7.17 Examples of events which were captured during the $^{252}$Cf neutron source exposure in the BENTO vessel.

The event on the left of Figure 7.17 consists of two symmetric clusters of charge. This structure in most likely caused by the charge discontinuity effect, discussed previously in subsection 7.3.1. Interestingly, this particular event potentially exhibits some preliminary evidence of the head-tail effect, discussed previously in Chapter 2, as neutrons are incident from the left in this image and the leading cluster contains more charge than the trailing cluster. Further work is required to investigate the sensitivity of this readout technology to the head-tail effect in the future.

On the other hand, the event on the right of Figure 7.17 contains four charge clusters, which could be caused by two possible mechanisms. Either this event is purely subject to the charge discontinuity effect mentioned previously, or this event could also be displaying evidence of two $SF_5^-$ minority peaks, the concept of which was discussed previously in Chapter 2. However, the charge in the smaller leading clusters are estimated to contain $\sim 30\%$ of that in the larger respective trailing clusters, which is a significantly larger fraction than previously attributed to detectable $SF_5^-$ minority peaks at lower gas gains [119]. Furthermore, without access to the charge arriving on the x-strips, this is difficult to confirm or refute and should therefore be subject of future work.

The potential sensitivity to signatures like the head-tail effect and minority peaks is greatly promising for the future deployment of this technology and should be subject to further investigation. However, at this early stage, it is advantageous to first confirm the observation of events consistent with NRs. In order to aid the positive identification of potential NRs induced by neutrons from the $^{252}$Cf source, supplementary ER/NR simulations in low pressure $SF_6$ were conducted. These simulations utilised the software packages SRIM, used briefly in subsection 7.3.2 for simulating alpha particles, and SREM.

### 7.4.3 Supplementary Recoil Simulations

SRIM and SREM can be used to simulate NRs and ERs, respectively, in a target medium. Given the relative abundance of fluorine in $SF_6$, the recoil of 100 fluorine nuclei were simulated for every 1 keV increment between 1 and 150 keV in 40 Torr of $SF_6$; the energy was converted to keV$_{ee}$ via the Lindhard model discussed in Chapter 2. SREM was then used in a similar fashion to simulate 100 ERs for each 1 keV increment between 1 and 100 keV. Example events for 25 fluorine NRs (left) and 25 ERs (right) of energy 10 keV are shown in Figure 7.18.

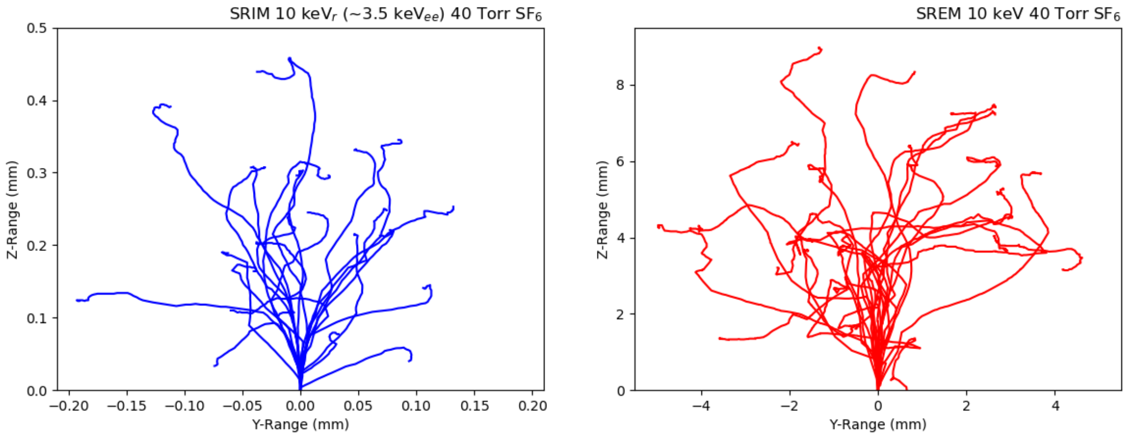

Figure 7.18 Example of 10 keV$_r$ ($\sim$ 3.5 keV$_{ee}$) fluorine recoils simulated in SRIM (left) and 10 keV electron recoils simulated in SREM (right).

The range in the z-y plane exhibited by NRs is an order of magnitude smaller than those displayed by the ERs of equivalent energy. In order to aid the discrimination between NRs and ERs, a parameter was defined to facilitate a $\frac{dE}{dx}$ cut such that:

$$\eta = E/R_2,$$

where $E$ is the electron equivalent energy and $R_2$ is the 2-dimensional range in the z-y plane. This is analogous to a parameter whose natural logarithm has previously been used for ER/NR discrimination in low pressure $CF_4$ [128] and $SF_6$ [232].

The natural logarithm of $\eta$ was calculated for each simulated event and plotted as a function of recoil energy, shown in Figure 7.19. As can be seen, the populations of NRs and ERs are well separated by this parameterisation. In an attempt to quantify the ER rejection ($ER_r$), two cuts were imposed in this parameter space. Firstly, a strict cut which included events above 10 keV$_{ee}$ with $ln(\eta) \geq 9$ (solid black line), and secondly a more lenient cut with $ln(\eta) \geq 8$ (dashed grey line). It was found that the strict cut was capable of $ER_r$ to 99% while the more lenient cut resulted in $ER_r$ to 98% for the simulated events. In the following

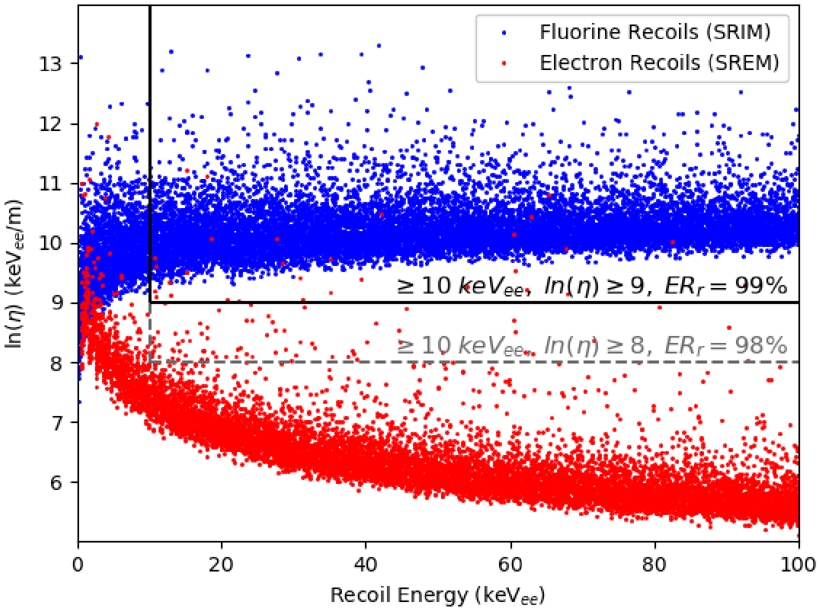

Figure 7.19 ln($\eta$) plotted as a function of electron equivalent recoil energy for simulated fluorine NRs (blue) and ERs (red) in 40 Torr of $SF_6$. Cuts which are able to successfully reject 99% (solid black line) and 98% (dashed grey line) of ERs are superimposed on the simulated data.

subsection, these simulated recoils are compared to the recoils obtained during the $^{252}$Cf neutron exposure in the BENTO vessel.

### 7.4.4 Comparison with Recoils in the BENTO Vessel

For comparison to the simulations, the recoil energies of measured events during the neutron run in the BENTO vessel were calculated by first converting the signal integral into charge, via the calibration presented in subsection 7.1.4, and then relating this measured charge to the initial amount of ionisation charge via the gas gain, determined to be $1.22 \times 10^5$ in Section 7.2. Finally this was related to the amount of electron equivalent energy via the $SF_6$ W-value, 34 eV [216]. The 2-dimensional recoil range was then calculated by first determining the z-range from the points above a 40 mV threshold. The y-range was then determined via the TLR algorithm, described in subsection 7.3.2, to minimise the influence of charge dissipation in the resistive layer. The resulting 2-dimensional range of each event can be seen plotted against the estimated recoil energy in Figure 7.20; indicated by the black cross markers. The NRs (pale blue) and ERs (pale red) from the SRIM and SREM simulations are also observed along with the simulated selection cuts described in the previous subsection.

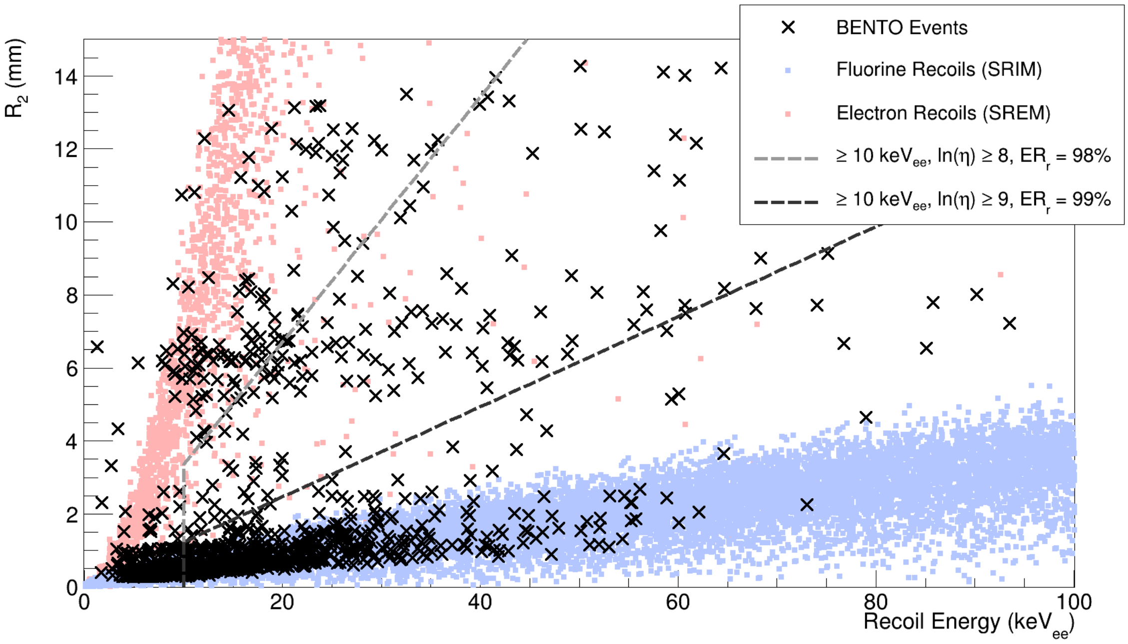

Figure 7.20 Two-dimensional range vs estimated recoil energy for events observed in the BENTO vessel during the $^{252}$Cf neutron exposure (black cross markers). The simulated NR and ER events from SRIM (pale blue) and SREM (pale red) are also observed along with the selection cuts described in the previous subsection.

As can be seen, a significant portion of events were found to be consistent with the simulated NR band, falling well within the strict, ER$_r$ = 99%, simulated selection cut. This result is significant because it suggests that these events are likely caused by NRs, in response to the $^{252}$Cf neutron source. Furthermore, this indicates the first potential observation of NRs in a large CYGNUS-m$^3$ vessel with the MMThGEM-Micromegas readout plane.

A significant portion of events can also be seen to fall within the more lenient, ER$_r$ = 98%, simulated selection cut. It is noted that, events which occur closer to the cathode will experience more notable diffusion, artificially broadening the measured range of these events. As diffusion has not been accounted for here, some NRs could be found to fall within the more lenient simulated selection cut; although this diffusion is anticipated to be $\lesssim$ 1 mm [119]. An alternative effect which could contribute to artificial range broadening of events, is the possible presence of unidentified minority peaks. Given the estimated ER$_r$ from this selection cut, these events are less likely to be attributed to ERs induced by background sources or the gamma-rays produced by the $^{252}$Cf source. However, due to their longer ranges, ERs which are not completely captured within the instrumented volume could also occupy this area of the parameter space. Therefore, further work is required to investigate these events. This would include scaling up the number of instrumented channels in both x and y-strip planes for complete 3-dimensional event reconstruction, as well as exposure to a high energy gamma-ray source for a more explicit ER/NR discrimination study.

Figure 7.21 presents a more focused view of the distribution of the measured recoil ranges (left) and energies (right) from the exposure in the BENTO vessel. Interestingly, with no selection cuts applied, events appear to accumulate in three distinct clusters in the range distribution. Upon inspection, it was observed that the majority of events with ranges less

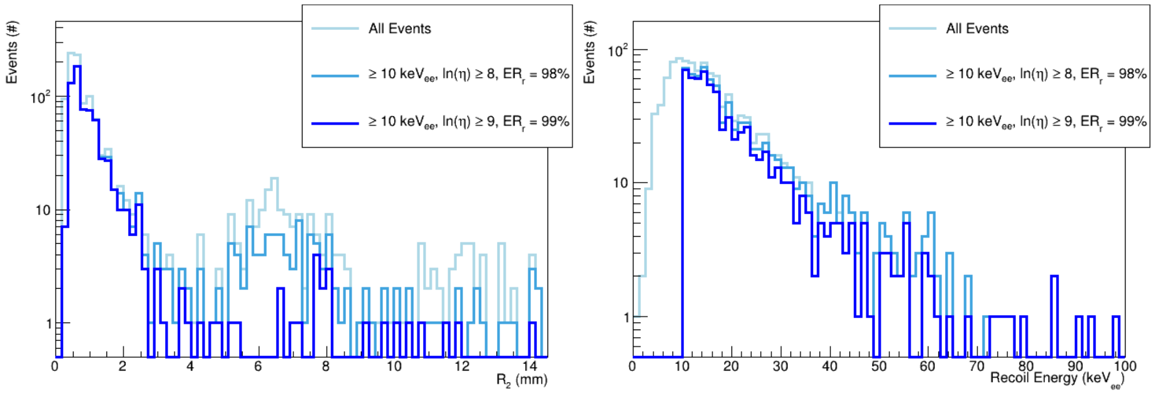

Figure 7.21 Histograms showing the measured ranges (left) and energies (right) of all recoil events (pale blue) and with the lenient (light blue) and strict (blue) simulated selection cuts applied.

than 4 mm contained 1-2 clusters of arriving charge, while those between 4 and 10 mm exhibited 2-3 clusters, and ranges exceeding 10 mm featured 3 or more clusters of arriving charge. This result indicates that the discontinuity caused by the MMThGEM hole pitch, discussed in subsection 7.3.1, is likely inducing a range quantisation artefact. This structure is not present following the strict selection cut, most likely due to the short (< 4 mm) range of NRs in this energy range. Finally, it is noted that the measured energy spectrum is consistent with that of a $^{252}$Cf neutron source demonstrated elsewhere in similar low pressure gaseous detector exposures [128, 129]. The combination of the range quantisation, short lengths of NRs, and the shape of the $^{252}$Cf energy spectrum explains the large population of events with low energy and short ranges.

These findings collectively provide strong evidence that NRs were successfully observed during operation in the large BENTO vessel. This result therefore represents a significant step towards realising this detector technology as a scalable readout option for a CYGNUS search. In the future, the confirmation of this finding would benefit from the instrumentation of more channels, including both x and y-strip planes, and an additional exposure to a high energy gamma-ray source for the purpose of an explicit ER/NR discrimination study.

## 7.5 Conclusions

In conclusion, this chapter described the operation of a coupled MMThGEM-Micromegas detector in low pressure SF$_6$. 32 y-strips were individually instrumented, demonstrating the largest area of individually instrumented strips in an NID gas with this detector to date. This was made possible by the large gas gain of $1.22 \pm 0.08 \times 10^5$. This is an improvement on the previous measurements with the isolated MMThGEM and demonstrates the first charge amplification of order $10^5$ in an NID gas; two orders of magnitude larger than typical NID gas gains previously seen. Complete 2-dimensional directionality was also demonstrated with alpha particle tracks by reconstruction of the principle axis, through development of a total linear regression algorithm; and by sense recognition, where $\frac{dE}{dx}$ signatures were found to be consistent with simulated alpha tracks.

Following characterisation in the test vessel, the detector was then installed in the BENTO vessel, a large CYGNUS-m$^3$ volume, and exposed to a $^{252}$Cf neutron source. Through comparison to simulated fluorine NRs and ERs, a large portion of events measured during this exposure were isolated and found to be consistent with simulated NRs; although, further work is required to explicitly determine the ER/NR discrimination capability of this detector and investigate the detector's sensitivity to the head-tail effect, for directional sense, and the possible observation of minority peaks, for fiducialisation. These findings demonstrate a significant step towards scaling up this readout technology for operation in a CYGNUS search. Finally, it is recommended that future design iterations of the coupled detector focus on the reduction of the MMThGEM hole pitch/diameter and removal of the resistive layer of the micromegas. This is due to challenges associated with track discontinuity, charge dissipation, and range quantisation.

# Chapter 8

# Testing Alternative Micromegas Designs for Directional Dark Matter Searches

In the previous chapter, the University of Sheffield (UoS) micromegas was coupled with a MMThGEM gain stage and successfully tested in a CYGNUS-m$^3$ SF$_6$ volume. However, the resistive DLC layer of the micromegas degrades the readout plane's resolution due to its dissipative effect [129, 240–243]. Considering the significant amount of work which has been devoted to improving charge amplification in SF$_6$, Chapter 4 - 6, this charge dissipation is counter productive to the reduced diffusion offered by this NID gas. As the resistive layer was originally introduced for protection in high event rate collider applications [240, 244–246], which is not a concern for low event rate DM experiments, it is argued that this layer could be removed to benefit a directional DM search. In this chapter, work is presented in which the UoS micromegas is compared to two alternative designs, owned by the University of Hawaii (UH), to investigate the benefits and drawbacks of including a resistive layer.

This work, carried out during a visit to the UH, also offered the opportunity to investigate different detector geometries including the effect of alternative strip widths on charge collection and sharing between the strip planes, which can benefit full 3-dimensional reconstruction in a directional detector. Additionally, this work facilitated the full area instrumentation of the micromegas readout area with an RD51 Scalable Readout System (SRS) [247]. This system increases the number of readout channels from 32 to hundreds, and offers scalability for future CYGNUS-m$^3$ modules requiring thousands of channels.

This chapter begins by first introducing the micromegas designs in Section 8.1, followed by the experimental setup in Section 8.2. A comparison, between the different detector designs, of charge measurements made on the micromegas mesh and strips are presented in Section 8.3 and 8.4 respectively. Finally, the results are concluded in Section 8.5.

## 8.1 Micromegas Detector Configurations

Three detector planes were subject to evaluation during this work: the UoS micromegas with DLC resistive layer; "UoS DLC", and the UH micromegas design with and without a DLC layer; "UH DLC" and "UH No DLC". The UH micromegas designs have the same 10 × 10 cm$^2$ active area as the UoS DLC. The major differences in detector design between the UoS and UH designs include the resistivity of the DLC layer, amplification gap, and the electrode strip pitch and width. These detector dimensions are illustrated in Figure 8.1.

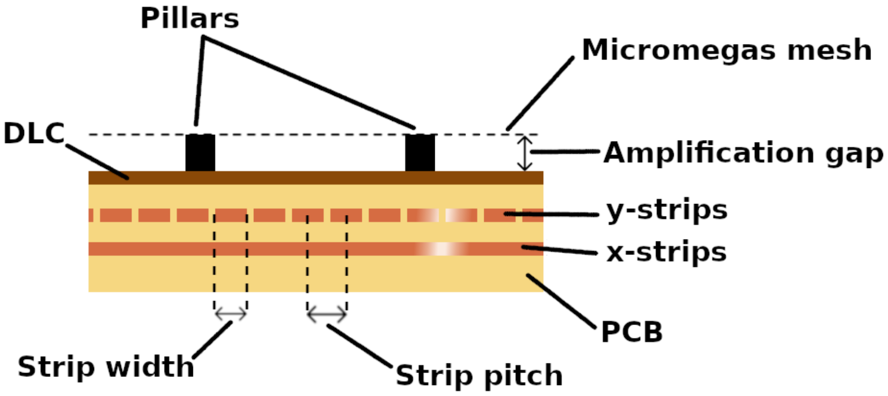

Figure 8.1 Cross sectional micromegas diagram illustrating the variable design parameters.

Additionally, the UH designs are segmented into quadrants to incorporate varying widths of the upper strip electrodes (y-strips). This unique design, illustrated in Figure 8.2, facilitates

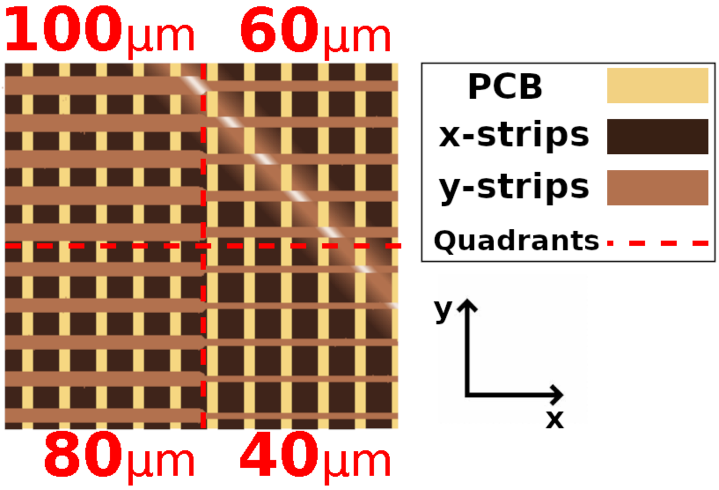

Figure 8.2 Diagram illustrating the UH y-strip width variation per quadrant.

four configurations per detector plane, totalling nine configurations for the comparison. The design specifications of the three detector planes are summarised in Table 8.1.

Table 8.1 Summary of the micromegas detector design specifications.

| Design Parameter | UoS DLC | UH DLC | UH No DLC |
|---|---|---|---|
| Active area ($cm^2$) | 100 | 100 | 100 |
| DLC resistance ($M\Omega/\square$) | 50 | 70 | N/A |
| Amplification gap size ($\mu$m) | 256 | 128 | 128 |
| Strip pitch ($\mu$m) | 250 | 200 | 200 |
| Segmented design ($\times/\checkmark$) | $\times$ | ✓ | ✓ |
| Y-strip width ($\mu$m) | 100 | 40, 60, 80, 100 | 40, 60, 80, 100 |
| X-strip width ($\mu$m) | 220 | 140 | 140 |
| Number of strips per axis | 358 | 500 | 500 |

## 8.2 Experimental Setup

A diagram of the experimental setup used for the measurements presented in this chapter can be seen in Figure 8.3. During all measurements, a cathode was mounted to the micromegas to create a drift length of 1.2 cm. The drift volume was enclosed by a gas box which was secured directly to the detector plane with screws. The cathode mounting screws were made leak tight with an application of epoxy to the underside of the detector plane. This enclosure was suitable for atmospheric operation and utilised a gas mixture of He:$CO_2$ with ratio 70:30. Despite lacking a fluorine or NID component for enhanced SD sensitivity and reduced diffusion, this gas mixture was selected for its helium content and proven stable atmospheric operation [202, 248, 249]. Gas was continuously flowed through the enclosure and vented via an exhaust on the opposite side; the flow rate was controlled with a Mass Flow Controller (MFC).

A junction box was mounted to the detector plane which enclosed the HV connections for the micromegas mesh, DLC layer, and cathode. The mesh and cathode were biased via negative HV power supplies whilst the DLC layer and strips were connected to ground. The cathode was connected directly to the HV supply and the mesh was connected via the biasing line on a CREMAT preamplifier CR-150 evaluation board. During all measurements, the potential difference between the cathode and micromegas mesh was set to 504 V.

Two separate DAQ systems were used during this measurement campaign. The first utilised the CREMAT charge sensitive electronics, used previously in Chapter 3 - 6, connected

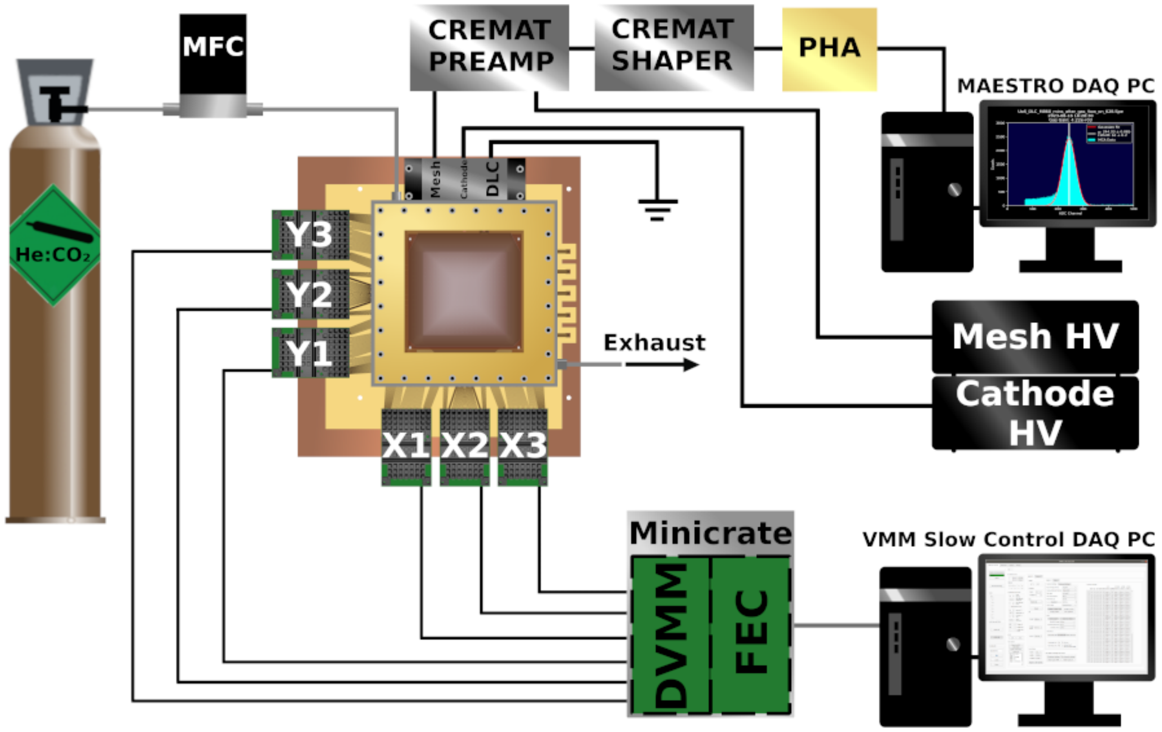

Figure 8.3 Diagram of the experimental setup showing the gas delivery system, HV biasing scheme, the CREMAT circuit connected to the mesh, and the SRS circuit connected to the strips.

to the micromegas mesh. The only difference was the use of an Ortec EASY-MCA Pulse Height Analyzer (PHA). The second system involved the RD51 SRS electronics. This required 3 VMM hybrids per axis for the UoS detector, labelled Y1-3 and X1-3 in Figure 8.3, and 4 per axis for the UH designs due to the smaller strip pitch. The VMM hybrids were connected to a Digital VMM adapter (DVMM) card situated in a SRS Technology minicrate via HDMI cables. The DVMM card was connected to a Front End Concentrator (FEC) card in the minicrate which interfaced with a dedicated DAQ PC, running the VMM slow control software [250], via an ethernet cable. This DAQ PC facilitated the calibration of the VMM chips, control of system settings including the trigger threshold, and saving the raw event information to disk.

The gas box design featured a thin kapton window directly above the TPC volume. As depicted in Figure 8.4, this allowed an $^{55}$Fe X-ray source to be centred directly above the readout plane. The source was assigned 5 positions on the kapton window, the main position was centred above the active area and the other four positions were centred in each of the quadrants as illustrated by the red dotted outlines in Figure 8.4. By connecting the CREMAT electronics to the micromegas mesh electrode, a positive charge polarity signal proportional to the electron avalanche in the amplification region can be registered. Calibration was performed by injecting a square wave via a function generator into the CREMAT test capacitor. The charge calibration of the SRS electronics connected to the strips is more complex and is described later in subsection 8.4.1. The gas gain was then determined via the W-value of the gas mixture, found from DEGRAD [221] simulations to be 35.2 eV, and the mean of a Gaussian function fitted to the $^{55}$Fe photopeak in the pulse height spectrum. The energy resolution was determined via the FWHM of the Gaussian peak divided by the mean.

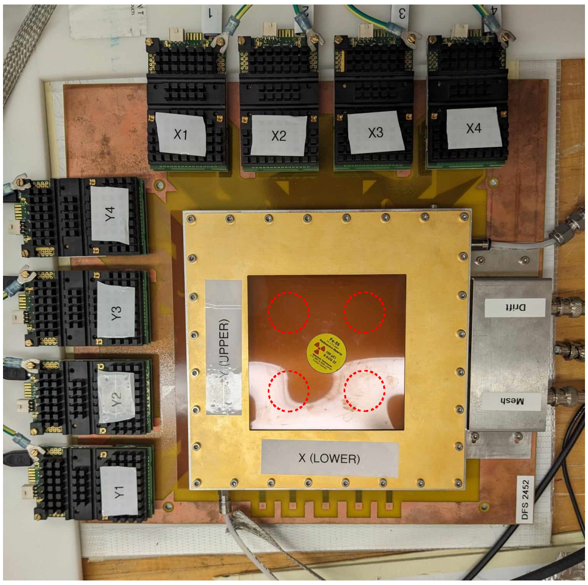

Figure 8.4 Photograph of UH No DLC experimental setup indicating the five source positions used during the measurement campaign. The yellow $^{55}$Fe X-ray source can be seen in the main centre position on the kapton window and the four alternative positions are indicated by the red dotted outlines.

## 8.3 Charge Measurements on the Mesh Electrode

The measurements which were conducted on the micromegas mesh electrode are covered in this section. As the gas system utilises a constant flow of the target gas mixture, these measurements are first used to establish the minimum amount of time required to purge the gas box for stable operation. Once stable conditions are established, a comparison of the effective gas gain and energy resolution on each mesh is presented. Finally the alternative source positions, outlined in Section 8.2, are utilised to test the avalanche uniformity across the detector plane, which is an important consideration for scaling up the readout area.

### 8.3.1 Gas Purity and Avalanche Stability

To begin the measurements, a stable gas purity must be established for repeatability of results. During preliminary testing it was found that the pulse height spectrum was significantly effected by low flow rates and the gas gain stability was closely linked with the purging time of the gas enclosure. In order to quantify the conditions for stable operation, the flow rate was set to 0.15 SLPM on the MFC which was large enough to provide a slight over pressure in the gas enclosure. With the source centred above the TPC, the pulse height spectra were recorded on the Maestro DAQ PC every 60 s following the initialisation of gas flow until a stable gas gain condition was achieved. The mesh voltage was set to -860 V and -640 V during the UoS and UH runs respectively. The results of this can be seen in Figure 8.5.

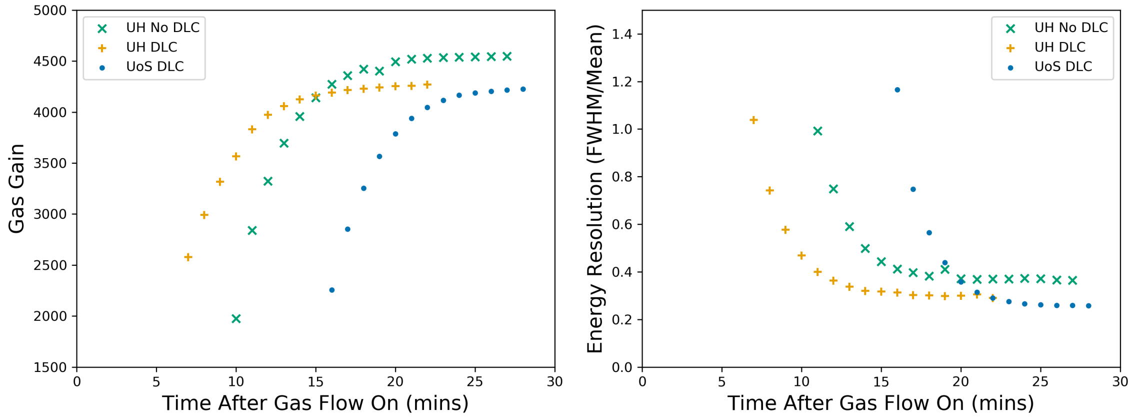

Figure 8.5 Effective gas gain and energy resolution measurements plotted as a function of time after the gas flow was turned on. Error bars have been omitted as they are smaller than the marker size.

The left of Figure 8.5 shows the gain response as a function of time after the gas flow was turned on and the right shows the corresponding energy resolution. The UH No DLC, UH DLC, and UoS DLC detectors are indicated by the green cross, orange plus and blue circle markers respectively. After a few minutes of gas flow, the X-ray photopeak appeared and could be resolved on the PHA spectrum. As time progressed, the measured gas gain continued to increase and slowly began to plateau. Within 30 minutes of gas flow, the gas gain varied less than 0.4% in all detectors. The energy resolution shows the inverse trend but still becomes stable with less than 0.5% change within the same period. A high flow rate test was performed at 0.225 SLPM after stability was reached in the UH DLC run but no further change was observed in gas gain or energy resolution. Consequently, the gas was flowed at a rate of 0.15 SLPM for 30 minutes prior to all further data acquisition.

### 8.3.2 Gas Gain and Energy Resolution Determination

Once the conditions for stable operation were determined, the mesh voltage on each detector was varied in increments of 10 V. The voltage range was determined from the point at which the $^{55}$Fe photopeak could be confidently resolved on the PHA spectrum above the electronic noise until sparking was indicated by triggering of the HV current limiter. The gas gain and energy resolution determinations as a function of amplification field strength can be seen presented in Figure 8.6.

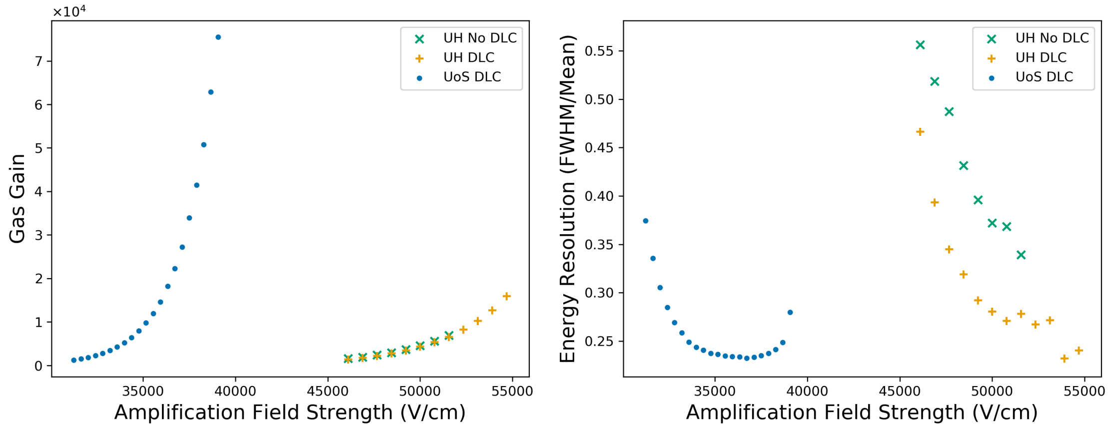

Figure 8.6 Effective gas gain (left) and energy resolution (right) measured on the mesh as a function of amplification field strength. Error bars are smaller than the markers and therefore not observed.

The gas gain curves, on the left of Figure 8.6, in both UH detectors are seen to be almost identical. This result is expected as the amplification gap is the same size in both UH detectors, as indicated in Table 8.1. One difference is that the UH DLC amplification field is able to maintain larger field strengths and therefore larger overall gas gains. Given that the only design difference between the UH detectors is the presence of a DLC layer, this result indicates that a resistive DLC layer is beneficial for charge amplification due to the suppression of sparking in the avalanche region.

The UoS effective gas gain curve is able to produce comparable gas gains to the UH detectors at much lower amplification field strengths. This is due to the fact that the amplification region is twice as large, as indicated in Table 8.1. This also improves the size of avalanches achieved before sparking occurs, allowing significantly larger gas gains to be observed.

The energy resolution measurements can be seen on the right hand side of Figure 8.6. As shown, the UH detectors exhibit a decreasing energy resolution with increasing amplification field strength. The observed energy resolution is seen to be better in the UH DLC compared to the UH No DLC detector. This result suggests that the presence of a resistive DLC layer not only improves the maximum gain capability but also the energy resolution. The UoS detector also shows an initial decrease in energy resolution, reaching a minimum comparable to the UH DLC, before increasing slightly at higher amplification field strengths.

### 8.3.3 Avalanche Uniformity

Good uniformity of charge amplification across the surface of a readout plane is important, particularly when anticipating the large area scale up to a CYGNUS-m$^2$ readout. Avalanche uniformity has been studied previously in several other MPGD designs [251–257]. In this comparison, the variation in strip width and presence/absence of a DLC layer presents a unique opportunity for investigation.

To quantify the variation in effective gas gain and energy resolution, the $^{55}$Fe source was placed on each of the five assigned positions indicated earlier in Figure 8.4. The mesh voltage was set to -660 V and -1000 V for the UH and UoS detectors respectively, as these were the largest stable voltages which could be achieved by both UH detectors and the UoS DLC. The effective gas gain and energy resolution was determined for each position and can be seen presented for each detector in Figure 8.7.

Each detector is indicated by a different colour scale in Figure 8.7: green for the UH No DLC, orange for the UH DLC and blue for the UoS DLC. The gain uniformity maps are shown in the left column and energy resolution uniformity maps are shown in the right column. The detector plane is shown divided into equal quadrants by the dotted black lines. The circular markers indicate the source position above the micromegas readout plane and the tone of the markers indicate the variation relative to the average gain and energy resolution according to the colour scale.

It can be seen that a relative increase in gain generally corresponds to a relative decrease in energy resolution as expected. The relative variation between quadrants is not consistent in the UH detectors, indicating that the variable strip widths do not contribute significantly to avalanche variation measured on the mesh. The largest variation, indicated by the colour scale, is exhibited by the UH No DLC micromegas and smallest by the UoS DLC micromegas. To help quantify this variation, the percentage Root Mean Square (RMS) was calculated for both the gain and energy resolution measurements in all three detectors and is summarised alongside the mean values in Table 8.2. The larger variation exhibited by the UH No DLC micromegas, particularly in energy resolution, could be due to the irregular surface potential of the exposed strip layer compared to the uniform surface potential which the DLC layer provides. This result suggests that the inclusion of a resistive DLC layer could improve

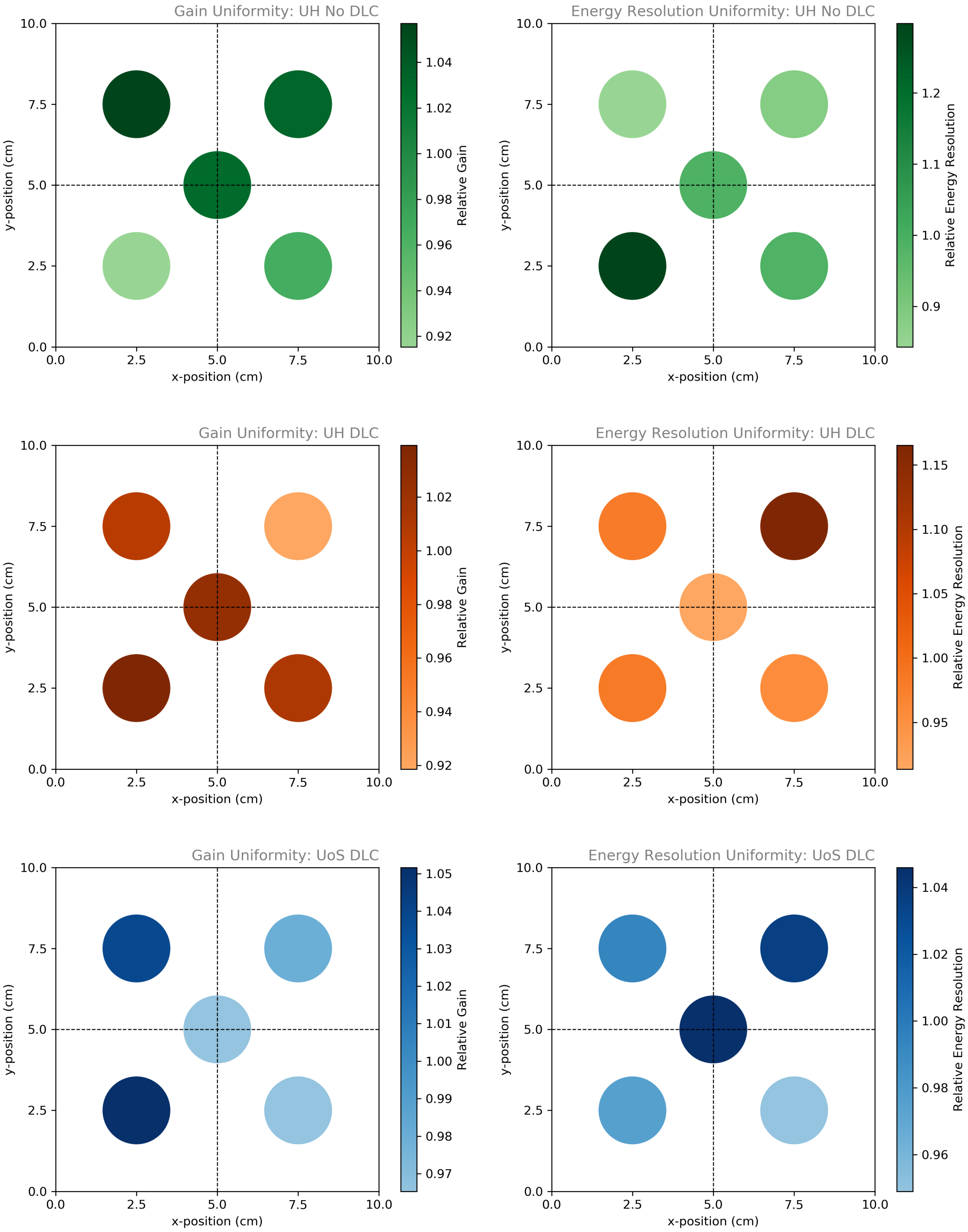

Figure 8.7 Effective gas gain and energy resolution uniformity maps for each micromegas as measured on the mesh. The UH No DLC, UH DLC and UoS DLC detectors are shown in green, orange and blue respectively.

uniformity across a large area device. However, all percentage RMS values are comparable to other MPGDs demonstrated elsewhere [251–257].

Table 8.2 Summary of avalanche uniformity measurements on the micromegas mesh.

| Detector | Mean Gain | RMS (%) | Mean Energy Resolution | RMS (%) |
|---|---|---|---|---|
| UH No DLC | 6700 ± 200 | 5.2 | 0.34 ± 0.02 | 16.0 |
| UH DLC | 6400 ± 100 | 4.2 | 0.28 ± 0.01 | 8.6 |
| UoS DLC | 78000 ± 1000 | 3.7 | 0.268 ± 0.004 | 3.6 |

## 8.4 Charge Measurements on the Strip Electrodes

This section contains the measurements conducted on the strips using the SRS electronics. The micromegas readout planes have hundreds of strips per axis and each strip requires a dedicated preamplifier and shaper. The VMM hybrids are manufactured with 2 VMM chips which each provide the charge sensitive electronics for 64 channels. As mentioned, the UH detectors required 4 hybrids per axis compared to 3 for the UoS detector totalling 512 and 384 electronic channels respectively. The number of channels is larger than the number of strips, indicated in Table 8.1, due to the strip-pin mapping. The charge calibration procedure for all these channels is more complex than previous calibrations with the CREMAT and LTARS electronics because it is performed via the VMM slow control software.

To begin, this charge calibration procedure is first presented. This is followed by a demonstration of event clustering which groups together strips exceeding the trigger threshold in quick succession. Once this has been successfully demonstrated, the effect of different strip widths and the presence/absence of a DLC layer on gas gain, energy resolution, charge sharing between electrode planes, and charge dissipation is tested.

### 8.4.1 SRS Calibration

To begin the calibration, the VMM Slow Control DAQ PC, shown in Figure 8.3, was used to configure the VMM hybrids to respond to charge of negative polarity and set the electronic gain. The electronic gain was set to 4.5 and 9 mV/fC in the upper (y) and lower (x) strips respectively in the UH detectors. The electronic gain was set to 1 mV/fC for all channels in the UoS detector due to higher levels of observed noise. The software was then used to execute protocols which performed several calibrations including the threshold, ADC response and BCID timings to ensure uniform calibration across the micromegas readout plane.

The calibration requires several protocols to be sent to the VMMs, starting with the calibration of the Digital-to-Analog Converters (DACs). Each VMM chip has two global 10-bit DACs, one is used for the test pulser and the other for the threshold setting. The VMM slow control is first used to scan a range of DAC settings in the pulser and threshold DACs, and measure the true analogue voltages. Example graphs produced by these protocols can be seen in Figure 8.8 showing the linear relationship between the measured analogue value in mV and the digital DAC setting.

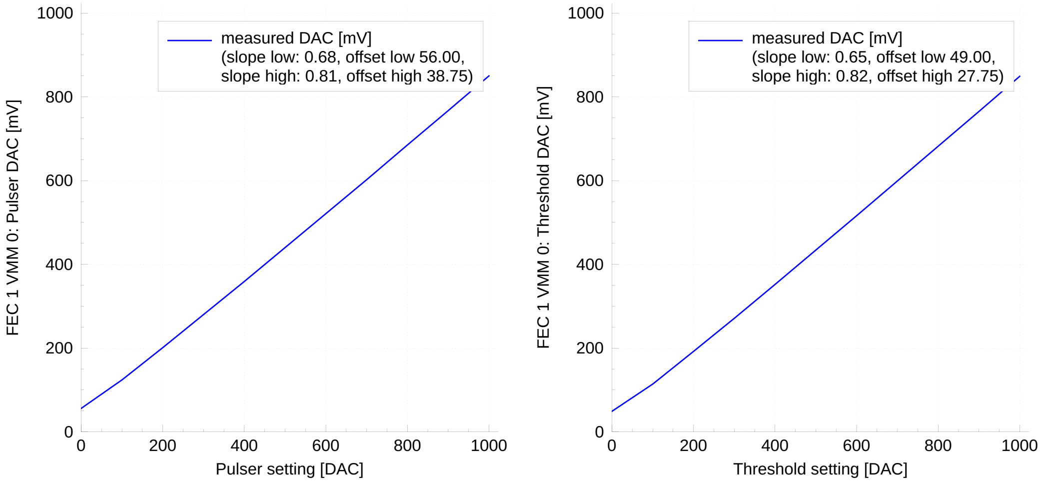

Figure 8.8 Example of global DAC calibration graphs as measured for the pulser DAC (left) and threshold DAC (right).

Next a suitable threshold above the pedestal must be chosen, this was done by first measuring the pedestal of each channel. An example of the pedestal measurement for one VMM can be seen on the left of Figure 8.9. Then, by referring to the threshold DAC calibration, a threshold DAC setting corresponding to 100 mV above the pedestal was chosen. This sets a global threshold for each VMM, however there is still some variation across channels. Therefore, a threshold calibration was performed which adjusts a 5-bit trimmer on each channel to bring the threshold of all channels into alignment. The results of this calibration can be seen on the right of Figure 8.9 which shows all possible trimmer values for each channel from lowest in blue to highest in black. The desired and closest calibrated thresholds are shown in red and green respectively. Another method for threshold selection above the noise regards the S-curve protocol, although this is known to have instabilities [258] and was not used to inform the threshold in this case.

The next step of the calibration concerns the ADC and BCID/TDC time calibrations. Due to the way that the VMMs are powered, median channels on the VMM chips amplify the signal more than the channels further from the power supply [259]. This results in an inverse

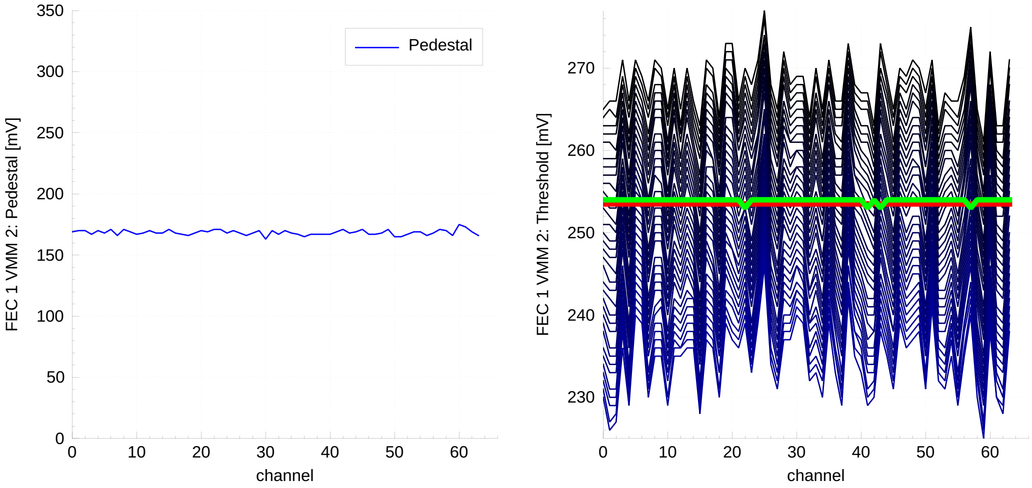

Figure 8.9 Example pedestal measurement for all channels on one VMM (left). Example threshold calibration for all channels on one VMM (right).

"U" shape response of the ADC values across the channels on the VMM. An example of this measured response to the DAC pulser can be seen on the left of Figure 8.10. A calibration must be applied which makes the electronic gain uniform across all channels. The input DAC value is shown in blue, the raw ADC response is shown in black and the corrected response is shown in red. The BCID/TDC calibration, shown on the right of Figure 8.10, is important to synchronise timing information across all channels as this can help improve the clustering of events. The raw BCID timings are shown in black and the result of the calibration in red.

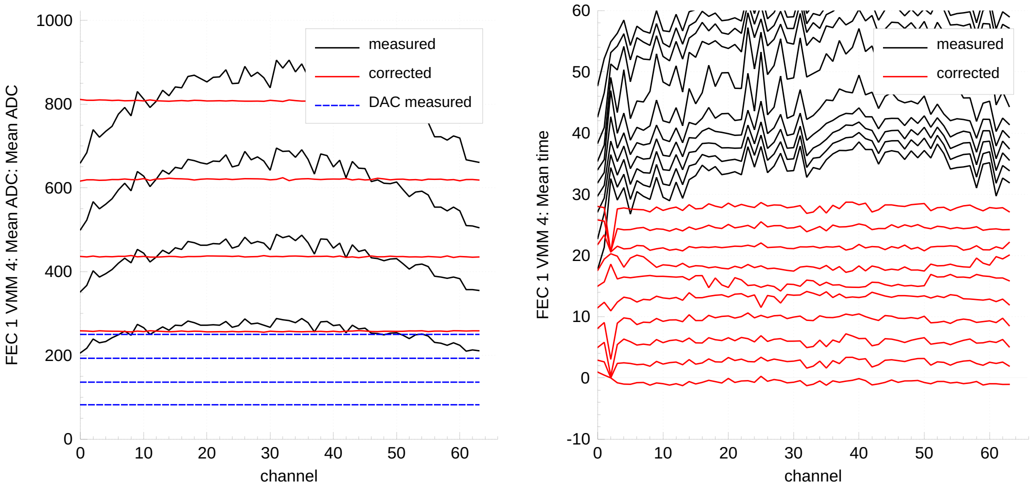

Figure 8.10 Example calibration of the ADC response (left) and BCID/TDC synchronisation (right) of one VMM.

The final step of the calibration is required to relate the ADC value to the true measured charge. This can be done by carrying out a procedure similar to the CREMAT/LTARS calibrations done previously. This is shown for an electronic gain of 9 mV/fC in Figure 8.11 by extracting the data from the ADC calibration and plotting the measured charge, determined via the VMM hybrid onboard capacitor and the measured DAC pulser value, against the measured ADC value after the inverse "U" shape calibration is applied. The line of best fit can then be used to convert the ADC response to the actual amount of charge measured. This graph also demonstrates the importance of the ADC inverse "U" shape calibration because, before the calibration was applied, the ADC values varied by more than 100 for a given pulser setting.

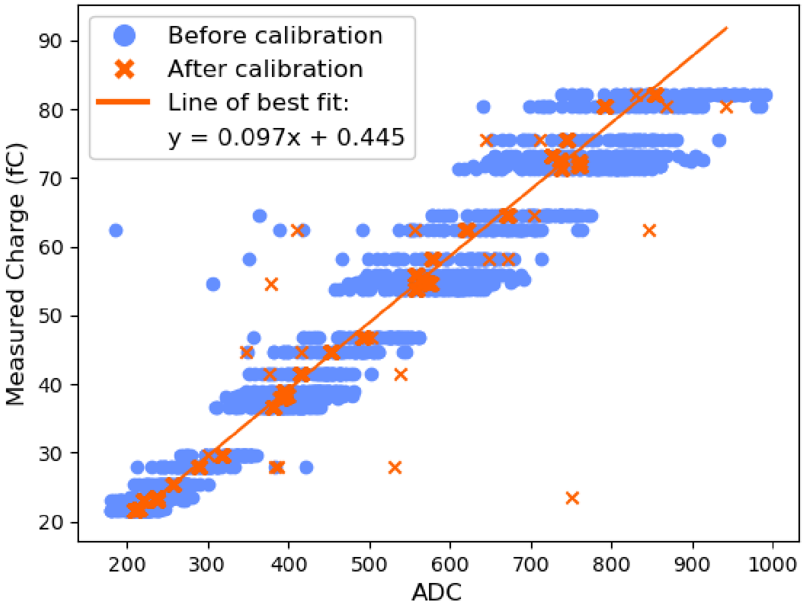

Figure 8.11 Charge conversion graph for the 9 mV/fC electronic gain setting before (blue circles) and after (orange crosses) the inverse "U" shape calibration is applied. The line of best fit representing the charge calibration is shown in orange.

### 8.4.2 Strip Hit Clustering and Event Reconstruction

Once the charge conversion calibration was established, the $^{55}$Fe source was placed on the central position on the kapton window and exposures of 30 minutes were acquired. During the exposure all strip hits which were above the calibrated threshold were captured as network packages on the VMM Slow Control DAQ PC. Following the exposure, concurrent hits were reconstructed into clustered events using the VMM-sdat software [260] and a user generated detector mapping file. The parameters which established the conditions for clustering are summarised in Table 8.3.

Table 8.3 Summary of the parameters used for clustering events in the VMM-sdat software.

| Parameter | Parameter Description | Assigned Value |
|---|---|---|
| *th* | Minimum ADC threshold per hit | 0 |
| *cs* | Minimum number of hits per plane | 2 |
| *ccs* | Minimum number of hits combined | 4 |
| *mst* | Maximum number of missing strip hits | 1 |
| *dt* | Maximum time between strip hits | 200 |
| *spc* | Maximum time span of hits per plane | 1500 |
| *dp* | Maximum time between clusters in both planes | 200 |
| *crl* | Minimum charge ratio between plane 0 and plane 1 | 0 |
| *cru* | Maximum charge ratio between plane 0 and plane 1 | 1000 |

An example X-ray image of the UH DLC detector, with mesh voltage of -660 V, after hit clustering can be seen in Figure 8.12. This graph shows the frequency of clustered hits in the x and y axes. In this X-ray image, the frequency of events clearly indicates that the source has been centred directly above the micromegas readout plane. Additionally, the grid of equally spaced pillar structures which support the micromegas mesh can also be observed as they prevent the charge from being deposited onto the DLC layer. Some vertical and horizontal lines caused by a few dead channels are also present. The quadrant boundaries are delimited by white dotted lines. The observed frequency of clustered events in the different quadrants begins to indicate some variation caused by the differing strip widths of the UH designs.

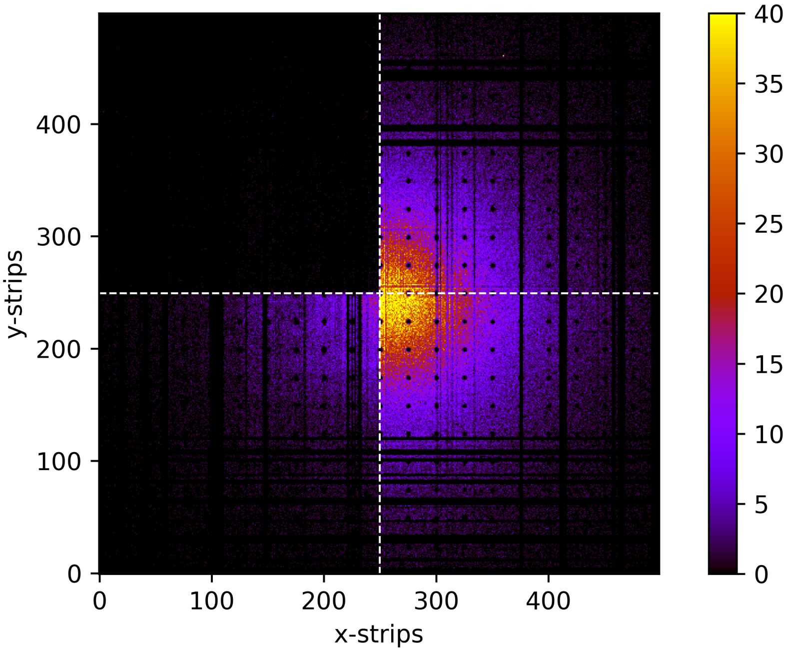

Figure 8.12 X-ray image of clustered events in the UH DLC detector with a mesh voltage of -660 V.

### 8.4.3 Gas Gain and Energy Resolution Determination

The charge measured in each of the four quadrants was isolated via the strip numbers. The quadrant boundaries were denoted by xL, xH, yL and yH; where L and H indicate low and high strip numbers respectively. For the UH detectors, low strip numbers range from 0-249 and high strip numbers range from 250-499. For the UoS detector, low strip numbers range from 0-178 and high strip numbers range from 179-357.

The effective gas gain and energy resolution was then determined via the W-value and X-ray energy by first applying the charge calibration to each strip, summing together clustered events, and extracting the mean and FWHM from a Gaussian function fitted to the photopeak in the summed charge spectrum; analogous to the CREMAT mesh measurements. This was performed for each quadrant as a function of increasing amplification field strength and can be seen in Figure 8.13. The three detectors are colour coded and presented separately for clarity; ordered UH No DLC (green), UH DLC (orange), and UoS DLC (blue) from top to bottom. The left hand column shows the effective gas gain results and the right hand column shows the energy resolution results. The four quadrants denoted as "xL-yL", "xL-yH", "xH-yL", and "xH-yH" are differentiated by the different marker shapes: triangle, circle, cross, and square respectively.

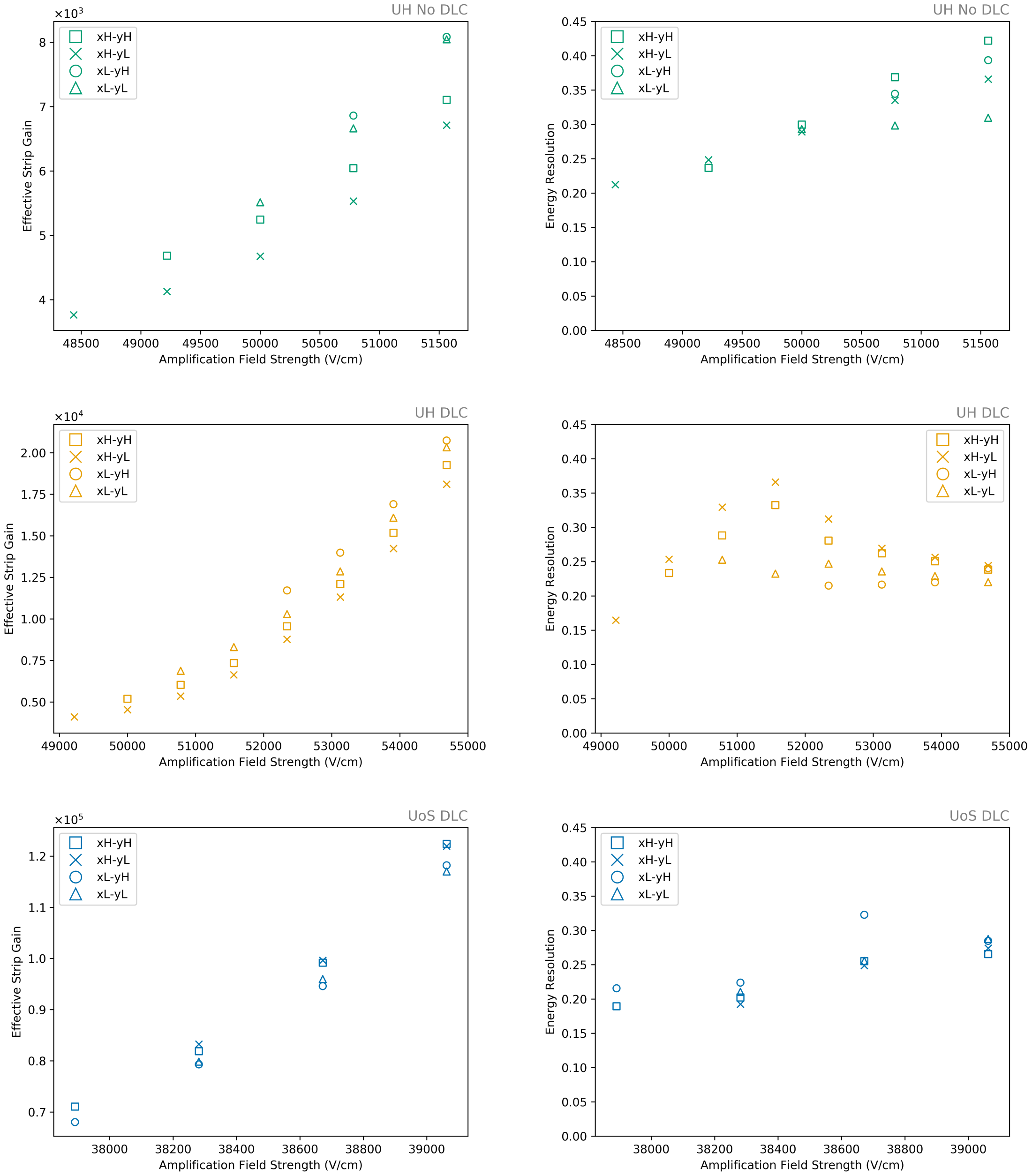

Figure 8.13 Effective gas gain and energy resolution uniformity measurements for each micromegas as measured on the strips. Error bars are smaller than the marker sizes and therefore not observed.

The effective gas gain measured on the UH detector strips varies between the quadrants in a way which is consistent across both detectors. The effective gain measured on each quadrant for a given amplification field strength increases in the order of xH-yL, xH-yH, xL-yL, xL-yH. This is an interesting result as this corresponds with an increasing y-strip width. The minimum amplification field strength at which clustering was sufficient enough to begin determining the gas gain also varies between quadrants. Clustering between the two planes was found to occur at lower amplification field strengths with decreasing strip width. This result suggests that the y-strip width could significantly influence the charge sharing between the two planes. It is important to note that these trends are only observed in the UH detectors, confirming that this is caused by the varying strip widths.

The energy resolution measurements do not exhibit a trend with the y-strip width which is consistent between both UH detectors. However, as the amplification field strength increases up to 51500 V/cm, the variation in energy resolution is seen to broaden. Above 51500 V/cm, the energy resolution exhibited by the UH DLC detector begins to decrease; converging towards $\sim 0.24$. The initial increase in energy resolution is likely caused by charge losses due to less efficient clustering at lower gas gain. This could also explain why the UH DLC energy resolution begins decreasing at higher amplification fields, as the clustering efficiency improves, in a similar manner to the mesh measurements.

The variation of the effective gas gain and energy resolution demonstrated by the UoS detector is smaller than both UH detectors. This suggests that the varying strip width has a significant influence on uniformity. To compare the uniformity measured on the strips, the percentage RMS was evaluated and the smallest variation achieved by each detector is summarised in Table 8.4. Similar to the mesh measurements, these results also indicate that the presence of a DLC layer reduces the variation in both the effective gas gain and energy resolution.

Table 8.4 Summary of the best avalanche uniformity measurements on the micromegas strips.

| Detector | Min. Gas Gain RMS (%) | Min. Energy Resolution RMS (%) |
|---|---|---|
| UH No DLC | 7.9 | 7.5 |
| UH DLC | 5.2 | 3.9 |
| UoS DLC | 1.9 | 3.2 |

### 8.4.4 Charge Sharing between Electrode Planes

In the previous subsection, the UH micromegas designs exhibited quadrant dependant charge collection and clustering of events in both planes. These factors clearly influence the effective gas gain, but would also likely effect the efficient 3-dimensional tracking of recoils in the TPC volume; i.e. if events can not be clustered and reconstructed in both axes, then the reconstruction could be limited to 2-dimensions. It is therefore an important consideration for future micromegas designs to investigate how charge is shared between the upper and lower strip electrode planes.

The charge sharing is hypothesised to vary as a function of strip width and should therefore not be influenced by other factors like effective gas gain. To investigate this, the charge sharing of the UH DLC and UoS DLC detectors are presented in Figure 8.14 as a function of amplification field strength. The charge fraction is defined here as the charge measured on the y-strips, $q_y$, divided by the total charge measured on both the x and y-strips, $q_{total}$, per event. On the left, the UH DLC detector demonstrates a constant charge fraction with increasing amplification field strength and the average in each quadrant is indicated by a horizontal dotted line. Therefore the charge sharing is not influenced by the effective gas gain. The charge fraction varies significantly between quadrants from $0.713 \pm 0.002$ to $0.913 \pm 0.004$; with increasing charge fraction corresponding to a larger y-strip width. For comparison, the UoS DLC detector also exhibits a constant charge fraction with increasing amplification field strength and has very little variation between quadrants, indicating that the differing strip width of the UH DLC is responsible for the observed variation in charge sharing.

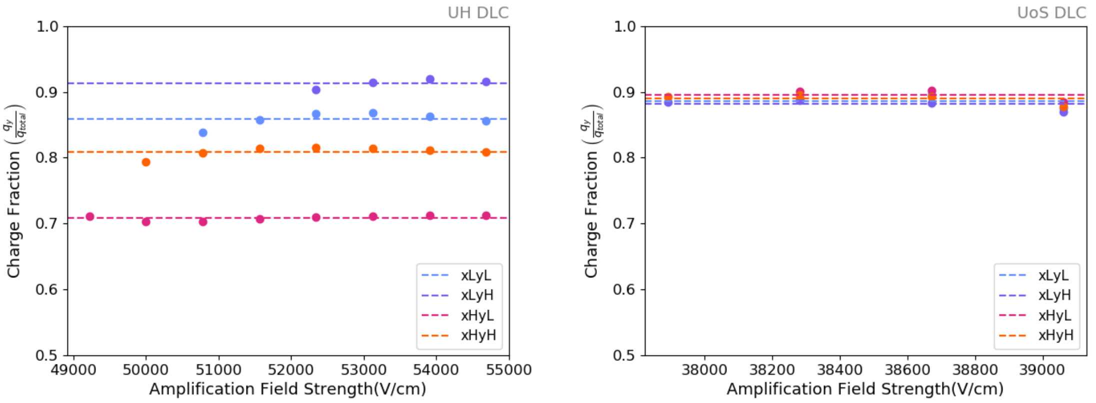

Figure 8.14 Charge fraction observed on the upper y-strips in the UH DLC (left) and UoS DLC (right) as a function of amplification field strength for each quadrant.

Ideally, in order to establish efficient clustering of events between the two planes, the charge fraction should be 0.5 to ensure that x and y positional information can be acquired even for less energetic events; otherwise this will have implications for the energy threshold of events which can be effectively reconstructed in 3-dimensions. It is thought that this charge fraction depends on the surface visibility of the x-strips, i.e. the area of the x-strips which is not intercepted by the y-strips above. It is therefore likely to depend on both the y-strip width and pitch. To investigate this, the average charge fraction on the y-strips has been plotted as a function of the y-strip width/pitch ratio for all three detectors in Figure 8.15.

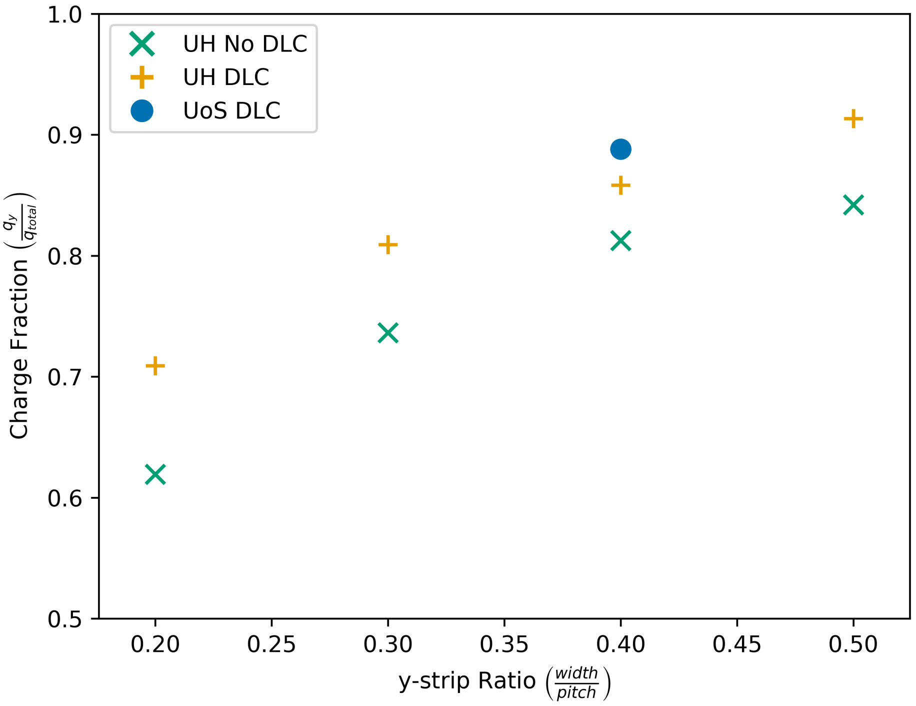

Figure 8.15 Average charge fraction observed on the upper y-strips plotted as a function of the y-strip width/pitch ratio.

Figure 8.15 shows that the charge fraction observed on the y-strips rises with increasing y-strip ratio. This result suggests that the charge sharing improves with the x-strips surface visibility, i.e. decreasing y-strip ratio. It would therefore be advantageous to reduce the y-strip ratio further to more extreme ratios $< 0.20$ in future designs. Another interesting observation here is the better charge sharing found in the UH No DLC detector, up to $\sim 10\%$. This result suggests that the presence of a DLC resistive layer hinders charge sharing in the lower electrode layer.

### 8.4.5 Cluster Size and Charge Dissipation in DLC Layer

As mentioned, the DLC resistive layer has been shown to exhibit a charge dissipation effect [129] which has also been noted in similar designs elsewhere [240–243]. The DLC layer was originally introduced to reduce the damage of strip electrodes and charge sensitive electronics caused by sparking events [240, 244–246]. This protective precaution is well justified for collider physics applications due to the large particle fluxes which are experienced. However, in the context of a directional DM search, the event rate is very low which reduces the possibility for damage to accrue over long term operation. It is therefore argued that the DLC could be removed in order to preserve the positional resolution, particularly in cases where NID gases are used; thereby improving sensitivity to asymmetries, like the head-tail effect, which are highly desirable for directional DM searches.

This is investigated here by comparing the measured X-ray cluster sizes for both UH detectors as a function of amplification field strength, presented in Figure 8.16. It can be seen that both detectors begin with a cluster size of 2 strips, due to the minimum clustering conditions in Table 8.3, and begin to increase with increasing amplification field strength. This broadening of the signal is likely due to the higher effective gas gain and hence larger avalanche of charge.

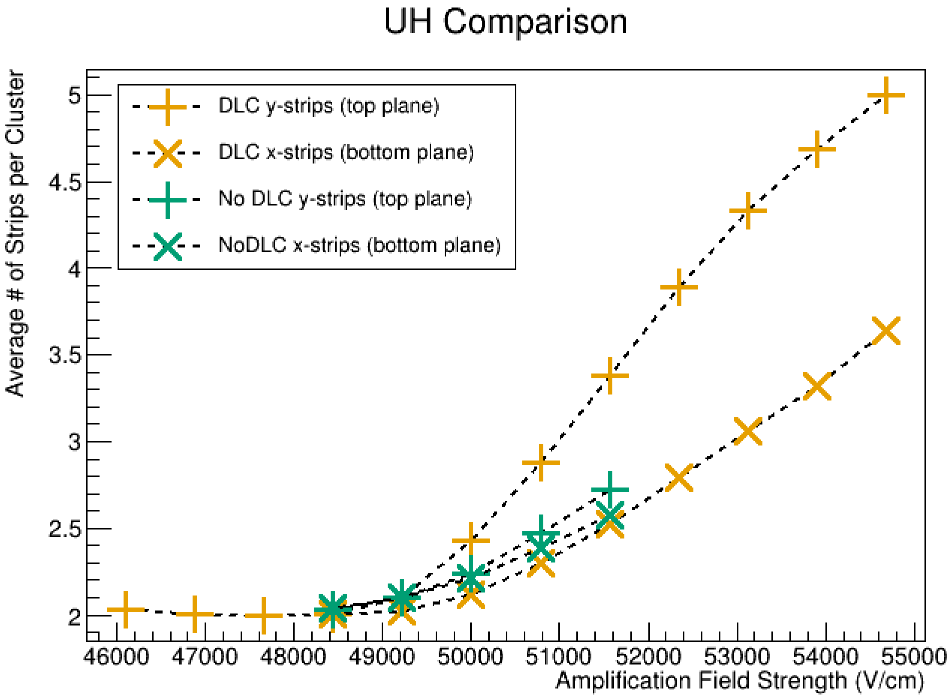

Figure 8.16 Average number of strips above threshold per cluster plotted as a function of amplification field strength.

The average x-axis cluster size is smaller than the y-axis cluster size in both detectors. This is consistent with expectations due to the charge sharing between planes. The x-axis cluster size is marginally smaller in the UH DLC compared to the UH No DLC, which agrees with the worse charge sharing noted in Figure 8.15. A significant difference is observed between the UH DLC and No DLC detectors in the y-strips at fields $\geq$ 50000 V/cm. The average number of y-strips per cluster in the UH DLC detector begins to increase at a greater rate than the UH No DLC detector. Considering that the only difference is the presence of the DLC resistive layer, this discrepancy must be caused by the charge dissipation in the resistive DLC layer alone. As the amplification field increases, so does the discrepancy between the DLC and No DLC. The maximum discrepancy associated with the presence of a DLC layer here is 0.655 ± 0.002 strips.

This result demonstrates that the DLC layer alone can degrade the positional resolution up to 131.0 ± 0.4 $\mu$m, which is greater than the amount of normalised electron diffusion in this gas mixture (129 $\mu\mathrm{m}\,/\sqrt{\mathrm{cm}}$ ) [248]. This scale of signal broadening would be particularly detrimental and counter productive when applied to an NID gas. Despite the apparent benefits of the DLC layer, including higher effective gas gain, lower energy resolution, and improved surface uniformity, the significant signal broadening observed here could justify removing it for a directional DM search with an NID gas target.

## 8.5 Conclusions

In conclusion, by comparing mesh and strip measurements on several micromegas designs, it was found that the DLC resistive layer provided benefits to detector designs including larger available effective gas gains before sparking was observed, lower energy resolution, and improved avalanche uniformity across the detector surface. Despite these benefits, the presence of a DLC resistive layer was found to induce artificial event broadening, up to 131 ± 0.4 $\mu$m due to charge dissipation, and $\sim$ 10% reduction in charge sharing between the y and x-strip layers. These findings are pertinent for future directional searches with an NID gas as the charge dissipation will likely degrade the high-fidelity benefits of using a gas like $SF_6$ and because poor charge sharing has implications on the energy threshold of events which can be reconstructed in 3-dimensions.

This measurement campaign at the UH also presented the opportunity to compare the effect of varying strip widths on charge collection and charge sharing. It was found that total charge collection improves with larger y-strip widths, however charge sharing improves with smaller y-strip widths. Furthermore, the UoS micromegas has now been demonstrated with full area instrumentation for the first time using SRS electronics. This is significant because micromegas detectors require hundreds of charge sensitive electronic readout channels in order to instrument a relatively small area of 10 × 10 cm$^2$. As this will scale to thousands of readout channels when implemented in a CYGNUS-m$^3$ detector module, it is important to pursue systems which are capable of handling this quantity of channels like the SRS technology solution.

As a result of the findings presented in this chapter, two main recommendations can be made for future detector design iterations suitable for a directional DM search. Firstly, more extreme y-strip width pitch ratios < 0.20 should be tested in order to improve charge sharing to around 50%. Secondly, as the event rate in a DM search is low, the DLC resistive layer could be removed because its protective function is non-essential and it only serves to reduce charge sharing and degrade the positional resolution through charge dissipation. Additionally, the larger available gas gain provided by the presence of a DLC layer is redundant if a dedicated gain stage device, similar to the MMThGEM, is used instead.

# Chapter 9

# First Low Pressure Gaseous Detector Operated with SRS Electronics

The SRS electronics are well-suited for handling the high-throughput demand associated with sub-mm granularity micromegas detectors which utilise hundreds of charge readout channels. The full area of the UoS micromegas has now been instrumented with an SRS setup in an atmospheric mixture of $CO_2$:He in Chapter 8. However, this mixture does not conform to the ideals of a CYGNUS detector because it does not contain a fluorine or NID component for improved SD sensitivity and high-fidelity event reconstruction. In this chapter, work is described in which the full readout plane is instrumented with SRS electronics and operated in low pressure $CF_4$ gas as, although it is not an NID gas, this is more conducive to a future directional DM search. This presents some significant challenges regarding thermal management of the VMM hybrids as this is the first time that they have been implemented in a low pressure gaseous TPC environment.

To begin, the concerns regarding the overheating of electronics are discussed and methods of mitigation are tested in Section 9.1. Following this, the experimental setup and first engineering demonstration of a low pressure gaseous TPC instrumented with SRS electronics is presented in Section 9.2. Then the effective Townsend parameters, mean free path, primary ionisation cross section, and ionisation potential were extracted in Section 9.3. Thereafter, future plans for testing the novel low pressure SRS setup are outlined in Section 9.4 before finally drawing conclusions in Section 9.5.

## 9.1 Low Pressure Thermal Management of VMM Hybrid

The SRS setup demonstrated in the previous chapter was operated in atmospheric conditions with a sub-optimal gas mixture for a directional DM search. As outlined in Chapter 2, the ultimate goal for a CYGNUS-m$^3$ gas target is a helium mixture with a low partial pressure of $CF_4$ or ideally $SF_6$. However, as discussed in Chapter 3 and 6, it is advantageous to initially prioritise low pressure operation in $CF_4/SF_6$ to preserve directionality before introducing helium.

The gas enclosure used in the previous SRS measurements, in Chapter 8, is not rated for low pressure operation and thus the micromegas detector must be sealed inside a vacuum chamber. By doing so, the VMM hybrids must therefore also be situated inside the vessel because they are designed to be connected directly to the detector plane. Furthermore, introducing additional lengths of wire between the strip and VMM channels, to facilitate external positioning, would induce adverse electronic noise. This means that the hybrids will be subject to the same low pressure gaseous environment as the TPC volume.

The VMM hybrids are known to heat up under normal operation due to the large power consumption required to handle the readout for hundreds of channels. It is recommended that the temperature of the VMM chips should be less than 50 °C and ideally in the range 30 - 40 °C to prevent rapid degradation of the chip's lifetime at higher temperatures [261]. This is particularly important considering the extended exposure times of DM detection experiments which typically run for several years. Any downtime of the detector required for the replacement of burnt-out electronics would be detrimental to the exposure time of the search.

Some of the recommended options for cooling the VMM chips are presented in Figure 9.1. As standard, the VMM hybrids are manufactured with a Radian heatsink and bottom cooler plate which are thermally coupled to the VMM chips with thermal paste, so that excess heat can be dissipated via natural convection cooling. This is suitable for atmospheric operation where the gaseous molecules available for thermal heat exchange are numerous. However, if operated in a low pressure environment, the density of the thermal fluid which serves the heatsink decreases. This has been shown to effect the efficiency of convection cooling by significantly reducing the convection heat transfer coefficient [263]. It is therefore important to investigate alternative mitigation for the VMM hybrids in a low pressure environment.

Peltier coolers have also been suggested as a method of thermal mitigation. These are semiconductor devices which can transfer heat from one side of a plate to the other, thereby cooling the chip. This thermal energy is not efficiently dissipated and therefore these coolers are often coupled to a fan to aid convection cooling of the Peltier device. This option is

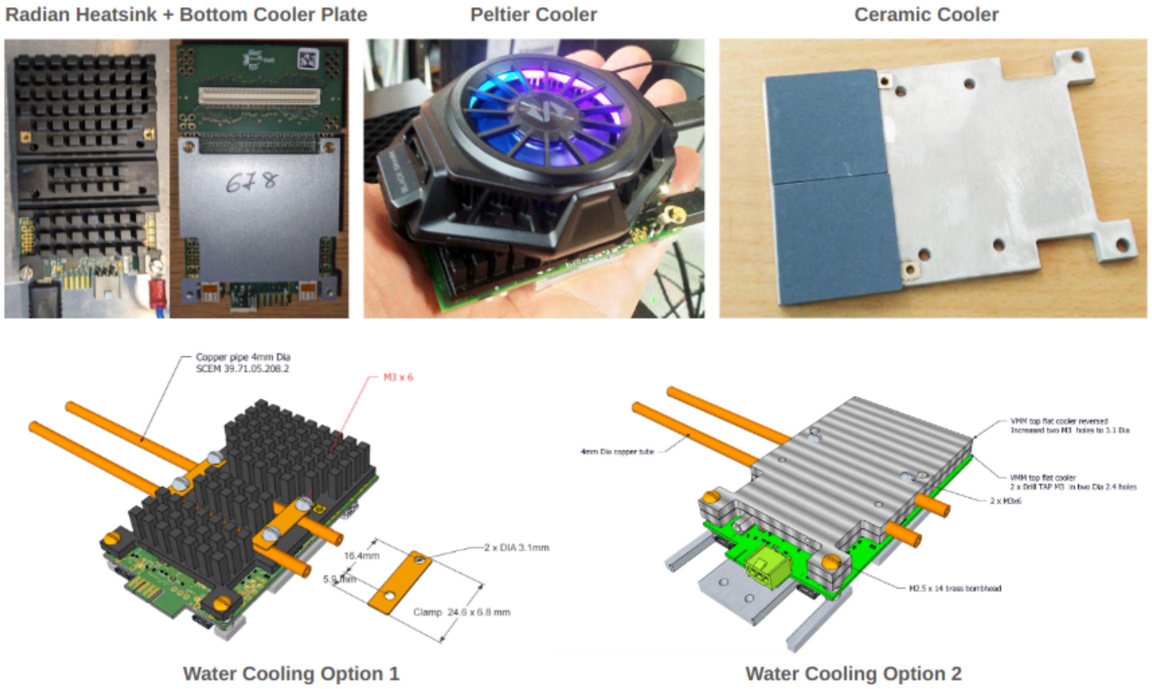

Figure 9.1 Compilation of the various methods of thermal mitigation recommended by SRS technologies. Top row: Default Radian heatsink and aluminium bottom cooler plate (left), portable USB Peltier cooler (middle), and ceramic coolers as a low profile alternative to the Radian heatsink (right). Bottom row: Water cooling option 1 coupled to Radian heatsink (left), and water cooling option 2 coupled to specially designed "sandwich" cooler plate (right). Adapted from Ref. [262].

not considered to be a practical solution here due to the turbulence which is expected to be produced in the TPC volume by the cooling fan.

Another alternative, is a water cooling solution which couples to the grooves on the top surface of the heatsink or to a custom "sandwich" top plate, option 1 and 2 respectively in Figure 9.1 [262]. However, introducing a water cooling solution to the vacuum vessel could be very problematic and even detrimental to the gas mixture; the effect of humidity on the transfer and amplification of charge in gaseous TPCs has only been tested at atmospheric pressure [264–266]. Other than these options, ceramic coolers have been suggested as a low profile substitute for the Radian heatsink, however this still relies on convection cooling. As all of these solutions are not ideal for a low pressure gaseous environment, it is suggested here that the VMM hybrid could be thermally coupled to the steel vacuum vessel to provide supplementary conduction cooling. This thermal coupling could be further aided by the application of heat sink compound, a thermally conductive paste, between the VMM hybrid and the vessel.

### 9.1.1 VMM Hybrid Thermal Testing Setup and Method

A diagram of the experimental setup used to investigate the thermal management of the VMM hybrids in a low pressure environment is shown in the top panel of Figure 9.2. One hybrid was placed inside a vacuum vessel, initially with no mitigation on top of a layer of low-density polyethylene (LDPE) to ensure no thermal contact with the vessel; an image of which can be seen in the bottom left panel of Figure 9.2. Communication with the DVMM card was established via a custom made pin connector feedthrough on the vessel. The wire pairs inside the HDMI cables had to be twisted together, at the feedthrough interface, to reduce crosstalk. The VMM slow control DAQ PC connected to the FEC could then be used to probe the VMM hybrid.

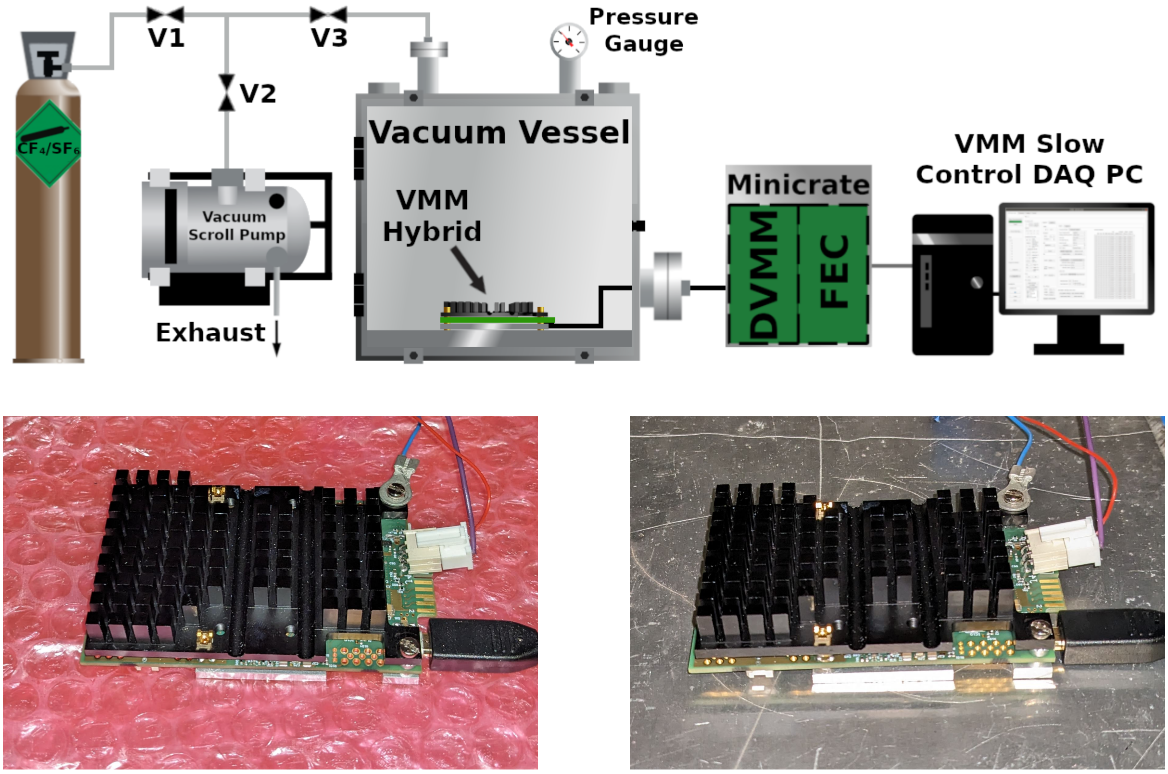

Figure 9.2 Diagram of the experimental setup used to measure the temperature of the VMM chips under different environmental pressure conditions (top). Image of VMM V5 hybrid with no thermal mitigation placed on top of insulating LDPE packing material (bottom left) and thermal coupling with the vessel floor (bottom right).

A vacuum scroll pump was used to evacuate the air from the vessel to test different pressures: ambient pressure (∼ 750 Torr), 1/2 atm (380 Torr), 1/4 atm (180 Torr), 1/8 atm (95 Torr) and a typical low operating pressure (40 Torr). The VMM slow control software was then used to monitor the analogue temperature sensors on the VMM hybrid once a minute over the course of 30 minutes. This procedure was repeated at each pressure. The ambient temperature in the laboratory was also recorded with a ThermoPro TP357 environmental sensor.

These measurements were repeated again with the LDPE layer removed and the bottom cooler plate of the hybrid placed in thermal contact with the vessel floor, shown in the bottom right panel of Figure 9.2. This was done both with and without the application of Dow Corning 340 HeatSink Compound (HSC) between the vessel floor and the bottom cooler plate. As the thermal conductivity of $CF_4$ and $SF_6$ is lower than air [267], all measurements were repeated with 40 Torr of each gas to replicate realistic operating conditions. This was achieved by first evacuating the vessel to < 0.01 Torr and then filling with the desired gas.

A simple model was then applied to the temperature measurements to better predict the equilibrium temperature of the chips. This model for the chip temperature, $T$, as a function of time, $t$, takes the form [268]:

$$T(t) = a - be^{-\frac{t}{c}}, \tag{9.1}$$

where:

$$a = PR + T_0, \;\; b = PR + T_0 - T_1, \;\; c = RC. \tag{9.2}$$

In this parameterisation, $P$ is the radiative power of the chip, $R$ is the thermal resistance of the system, $T_0$ is the ambient laboratory temperature, $T_1$ is the initial temperature of the chip, and $C$ is the heat capacity of the system. Most importantly, $a$ is the equilibrium temperature reached after long term operation. Equation 9.1 was fit to the data and the equilibrium temperature was extracted.

### 9.1.2 VMM Hybrid Thermal Management Results

The results of the thermal testing under different environmental conditions inside the vessel can be seen in Figure 9.3. From top to bottom, the graphs show the results for no mitigation, thermal coupling, and thermal coupling with HSC. The colour of the three different shaded regions indicates the recommended temperature ranges: 30 - 40 °C, acceptable long term temperature range (green); $\leq 50$ °C, recommended maximum temperature bound (yellow); and > 50 °C, the lifetime of the chip could degrade rapidly (red).

As can be seen, with no mitigating precautions, the temperature of the VMM chip increased rapidly and exceeded the recommended long term temperature range after 5 minutes in all environmental conditions. After 30 minutes, the temperature was found to

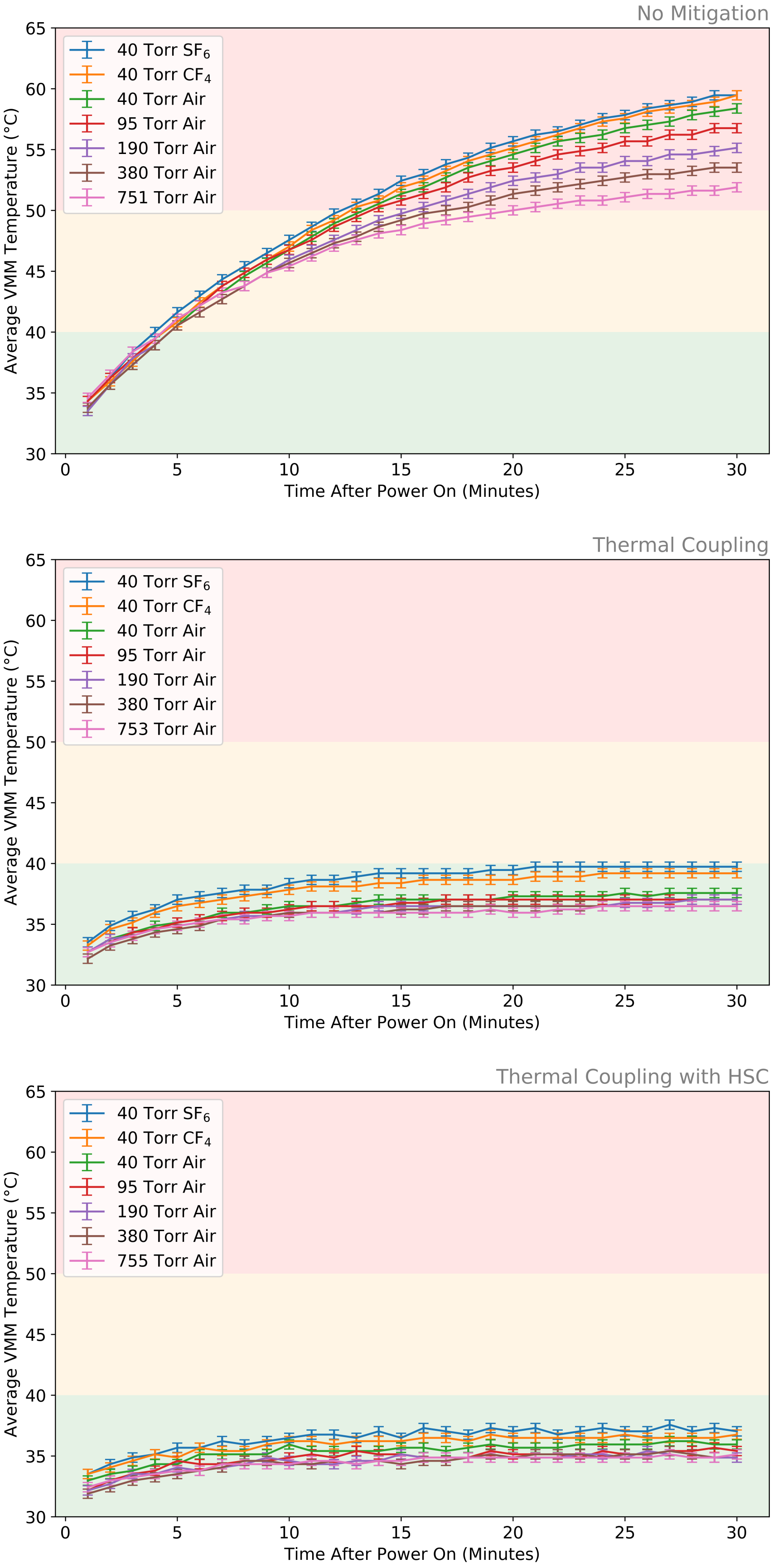

Figure 9.3 VMM temperature plotted as a function of time since the power was switched on with no mitigation (top), thermal coupling to vessel (middle), and thermal coupling to vessel with HSC (bottom).

be higher with decreasing pressure. Moreover, all pressures resulted in temperatures which were greater than 50 °C, and were found to still be rising, indicating that long term operation would likely impact the lifetime of the chips. Furthermore, in agreement with their respective thermal conductivities, both $CF_4$ and $SF_6$ runs resulted in slightly higher temperatures than 40 Torr of air. It is therefore obvious that some thermal mitigation will be required for long term operation, even in atmospheric conditions.

When the hybrid was thermally coupled to the vessel, the temperature after 30 minutes improved by as much as 20 °C. As a result, all tests conducted in air were found to remain within the ideal long term temperature range. However, in the case of $SF_6$, the temperature was borderline.

When the HSC was applied to the bottom cooler plate, a further improvement in temperature was observed after 30 minutes. This improvement was most significant in the case of $CF_4$ and $SF_6$ at 40 Torr. As observed, the application of HSC was able to maintain

Table 9.1 Summary table showing the equilibrium temperatures for each run with different levels of mitigation in various gases and pressures.

| **Mitigation** | **Gas** | **Pressure (Torr)** | **Lab. Temp. (°C)** | **Eq. Temp. (°C)** |
|---|---|---|---|---|
| None | Air | 751 | 26.4 ± 0.1 | 52.6 ± 0.4 |
| | | 380 | 26.5 ± 0.1 | 55.1 ± 0.4 |
| | | 190 | 26.4 ± 0.1 | 57.4 ± 0.4 |
| | | 95 | 25.2 ± 0.1 | 59.7 ± 0.4 |
| | | 40 | 25.6 ± 0.1 | 62.2 ± 0.4 |
| | $CF_4$ | 40 | 25.5 ± 0.1 | 64.2 ± 0.4 |
| | $SF_6$ | 40 | 25.6 ± 0.1 | 63.8 ± 0.4 |
| Thermal Coupling | Air | 753 | 26.1 ± 0.1 | 36.3 ± 0.4 |
| | | 380 | 26.5 ± 0.1 | 36.5 ± 0.4 |
| | | 190 | 26.9 ± 0.1 | 36.8 ± 0.4 |
| | | 95 | 26.9 ± 0.1 | 37.1 ± 0.4 |
| | | 40 | 26.8 ± 0.1 | 37.5 ± 0.4 |
| | $CF_4$ | 40 | 26.7 ± 0.1 | 39.1 ± 0.4 |
| | $SF_6$ | 40 | 26.5 ± 0.1 | 39.8 ± 0.4 |
| Thermal Coupling with HSC | Air | 755 | 26.5 ± 0.1 | 35.0 ± 0.4 |
| | | 380 | 26.8 ± 0.1 | 35.1 ± 0.4 |
| | | 190 | 26.9 ± 0.1 | 35.0 ± 0.4 |
| | | 95 | 26.8 ± 0.1 | 35.2 ± 0.4 |
| | | 40 | 26.8 ± 0.1 | 35.9 ± 0.4 |
| | $CF_4$ | 40 | 26.7 ± 0.1 | 36.6 ± 0.4 |
| | $SF_6$ | 40 | 26.7 ± 0.1 | 37.2 ± 0.4 |

a temperature which was well within the recommended range between 30 - 40 °C in all environmental conditions.

As the temperature was found to still be increasing after 30 minutes in some cases, the model described by Equation 9.1 was applied to the data and the results can be seen presented in Table 9.1. As shown, all conditions which utilised thermal coupling with HSC equilibrate below 40 °C. This indicates that this is an acceptable method of thermal management which does not necessitate the use of unfavourable techniques like water cooling.

## 9.2 Low Pressure Demonstration of Micromegas with Full Area SRS Readout

Once the concerns for the thermal management of VMM hybrids under low pressure conditions was addressed to a satisfactory level, the SRS electronics could be confidently implemented without damaging the VMM chips. The UoS micromegas was placed inside the vacuum vessel and the whole $10 \times 10$ cm$^2$ area was instrumented with the SRS electronics. In this section, the experimental detector setup and first engineering demonstration of the SRS electronics with a low pressure gaseous detector is presented.

### 9.2.1 Experimental Setup

The experimental setup utilised for the measurements presented in this section can be seen photographed on the left of Figure 9.4. As can be seen, the micromegas was set up with a cathode, which was positioned 3 cm above the readout plane, to form a TPC. The MMThGEM was not required at this stage for operation in $CF_4$; however, it will be coupled to the micromegas for NI operation in $SF_6$ in the future, as done previously in Chapter 7. Thermal coupling with the vessel floor was achieved with HSC and a metal bracket. This was found to provide sufficient conductive cooling during full scale measurements.

The electrical circuitry inside the vacuum vessel is depicted in the diagram on the right of Figure 9.4. The TPC electrodes were biased in the same way as the measurements presented in Chapter 8: the cathode was connected directly to a HV supply, $V_{cathode}$; the micromegas mesh was biased via the HV line on the CREMAT evaluation board, $V_{mesh}$; and the DLC layer and strips were grounded. The mesh signal from the CR-111 preamp on a CR-150 evaluation board was connected to a CR-200-4$\mu$s shaper on a CR-160 evaluation board. This interfaced with the software package Maestro via an Ortec 926 ADCAM MCB NIM module. The VMM hybrids were connected to the micromegas strips and interfaced with the VMM slow control software via the DVMM and FEC. The electronic gain of the VMM

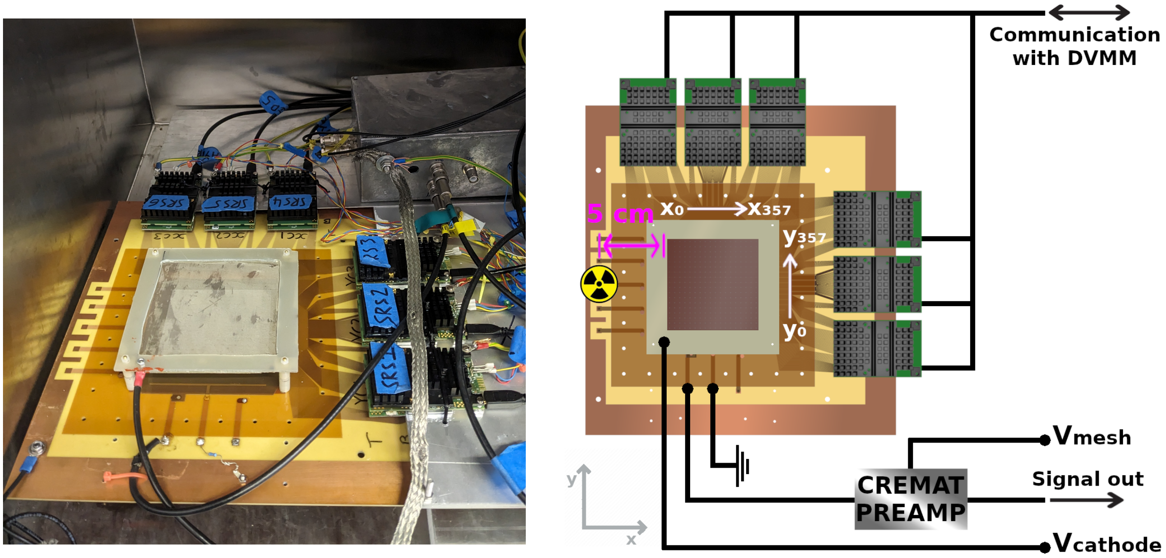

Figure 9.4 Photograph of experimental setup inside the vacuum vessel (left) and diagram of the experimental setup indicating the strip numbering, electrical connections, and source positioning (right).

hybrids was set to 9 mV/fC for the (upper) y-strips and 12 mV/fC for the (lower) x-strips. The calibration procedure for the CREMAT and SRS electronics can be found in Chapter 3 and 8 respectively.

An $^{55}$Fe X-ray source was then positioned 5 cm from the active area of the micromegas directed towards the centre of the TPC volume, as depicted in the diagram. The vacuum vessel was sealed and evacuated for 48 hours prior to data acquisition runs. The vessel was then filled with 40 Torr of $CF_4$ and the HV supplies were switched on and ramped up. Gas gain and energy resolution measurements were established by fitting the pulse height spectrum with a function consisting of an exponentially falling component and a Gaussian function. The mean and FWHM of the Gaussian was extracted and the charge calibration applied; in line with the calibration methods described in Chapter 3 and 8 for the CREMAT and SRS electronics respectively. The gain was determined via the energy of the X-ray, 5.89 keV, and W-value of $CF_4$, 34 eV [201]. The leak rate of the vessel was found to be $< 0.1$ Torr per day and all measurements were conducted within the first hour of filling the vessel with gas.

### 9.2.2 Gas Gain and Energy Resolution on the Mesh

Once filled with 40 Torr of $CF_4$, the electronics were switched on and the HV was applied to the TPC electrodes. The potential difference between the cathode and the micromegas mesh, $\Delta V_{Drift}$, was set constant at 500 V for all measurements. The potential difference between the micromegas mesh and the DLC layer/strips, $\Delta V_{Micromegas}$, was increased by 5 V increments between 535 - 570 V. For each voltage increment, the pulse height spectrum was recorded for signals on the micromegas mesh for a duration of 5 minutes. The gas gain and energy resolution determinations can be seen in Figure 9.5.

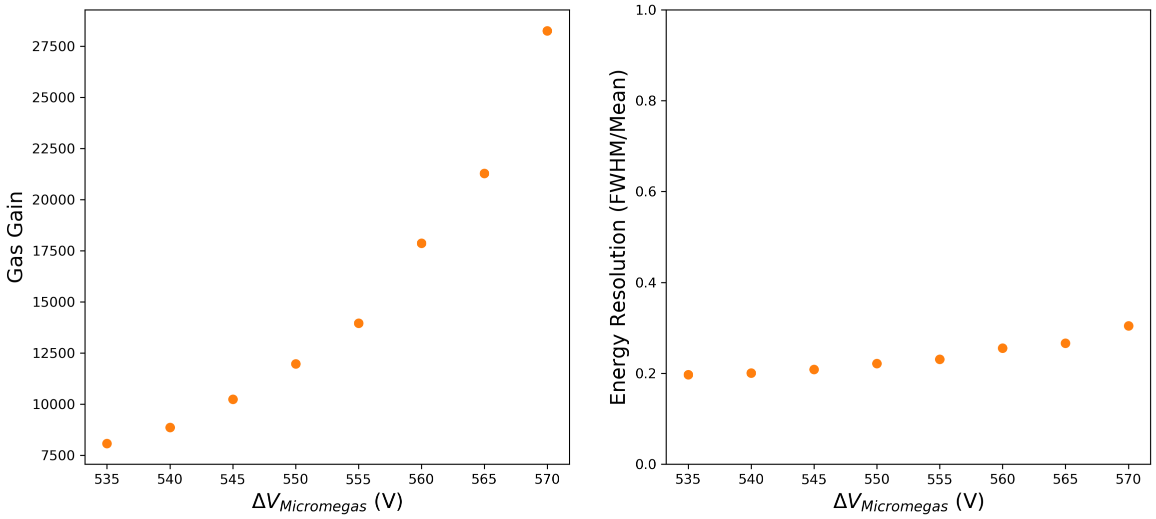

Figure 9.5 Gas gain (left) and energy resolution (right) plotted as a function of $\Delta V_{Micromegas}$.

As expected the gas gain can be seen to increase with exponential behavior as $\Delta V_{Micromegas}$ increases. The gas gain ranged from $8073 \pm 1$ at 535 V to $28250 \pm 10$ at 570 V. The energy resolution initially has a relatively constant response and begins to increase slightly at larger values of $\Delta V_{Micromegas}$. The energy resolution was found to vary from $0.1966 \pm 0.0004$ at 535 V to $0.305 \pm 0.001$ at 570 V. These measurements establish a baseline for comparison with the following measurements conducted on the strip electrodes.

### 9.2.3 Event Clustering on the Strips

Following the baseline measurements established with the CREMAT electronics on the micromegas mesh, the SRS setup was then used to take measurements on the micromegas strips. An initial 30 minute long exposure was conducted with $\Delta V_{Drift}$ and $\Delta V_{Micromegas}$ set to 500 V and 570 V respectively. Multiple strips per event were found to exceed the threshold, which was set 205 mV above the pedestal. When triggered, the system acquires the maximum ADC value above threshold, per triggered strip, along with identifying parameters such as the corresponding strip number. Strips were clustered together to form events; the clustering conditions used were identical to those used in the previous chapter shown in Table 8.3. The results of this exposure and event clustering can be seen in Figure 9.6.

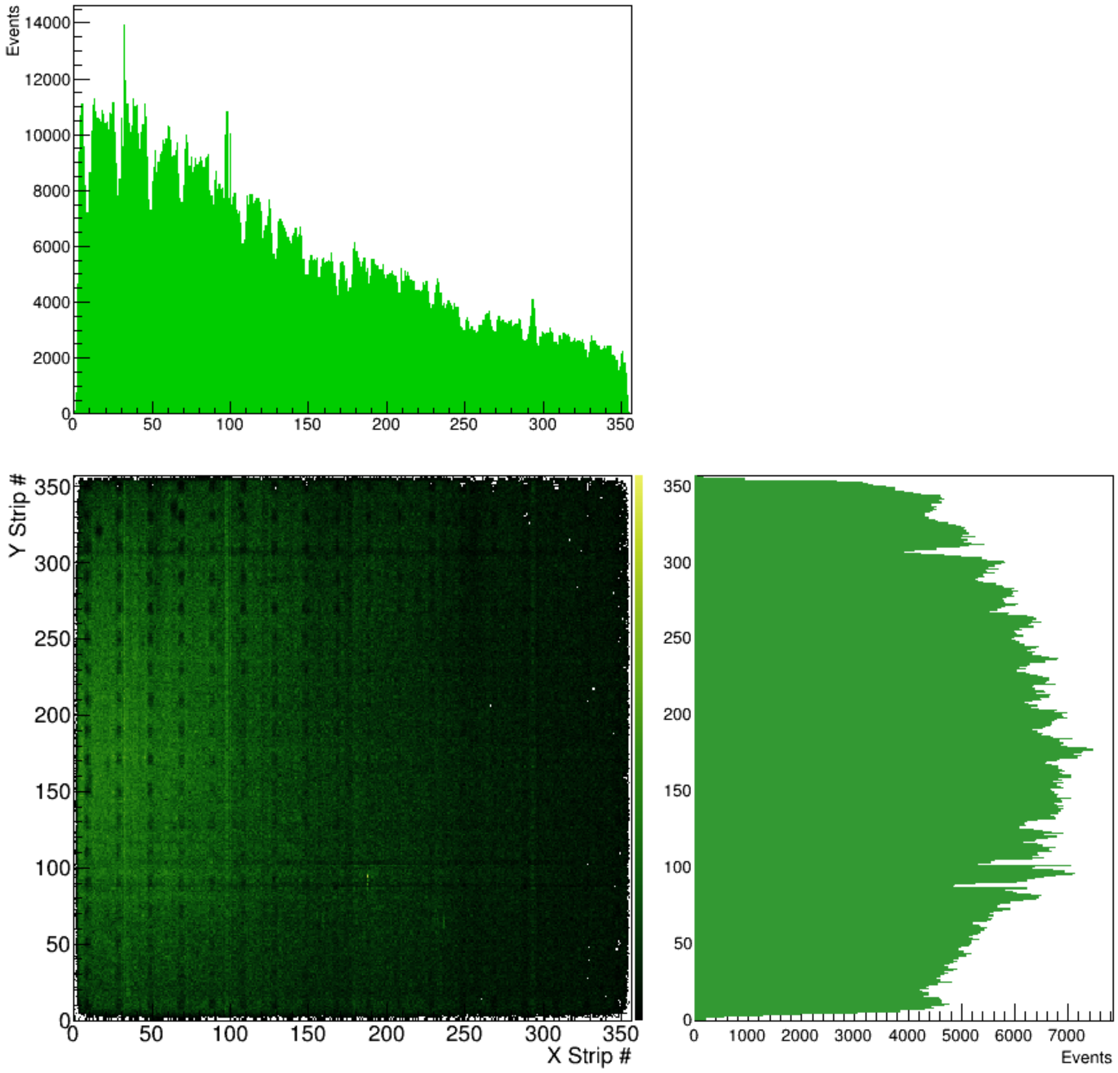

Figure 9.6 X-ray image of clustered events on the micromegas strips (bottom left panel) and 1-dimensional histograms showing the projection of the clustered events in the x (top panel) and y (bottom right panel) axes.

The X-ray image of the micromegas readout plane, seen in the bottom left panel of Figure 9.6, demonstrates event clustering in both strip planes. This is evidenced by the visibility of the pillars, which support the micromegas mesh, observed as the regularly spaced grid of low event regions. Additionally, a source position dependant signature can be observed in the X-ray image due to the non-uniform irradiation of the micromegas readout plane. As per the experimental setup diagram, on the right of Figure 9.4, the $^{55}$Fe source was positioned to the left of this X-ray image. The intensity of the X-ray image indicates that a higher event rate was experienced by x-strips with a closer proximity to the source.

To explore this further, the top panel in Figure 9.6 shows the projection of the X-ray image along the x-axis. Ignoring the channels close to the edge of the detector volume, the event rate is shown to exhibit an approximately inverse square relationship with distance from the source. The y-axis projection (bottom right panel) also shows a source position dependent response. The event rate can be seen to peak in the centre of the y-axis and decrease towards the edge of the TPC volume. In both the x and y-axis projections, a regularly spaced decrease in the event rate is observed to coincide with the pillar intervals. These observations provide qualitative verification of the detectors response to the X-ray source.

Unlike the previous measurements with the SRS electronics in Chapter 8, 100% of the channels and corresponding strips were operational during this exposure. This result demonstrates the first complete and uninterrupted instrumentation of the UoS micromegas plane with SRS electronics. Furthermore, this is the first demonstration of the SRS electronics with a low pressure gaseous detector.

### 9.2.4 Gas Gain and Energy Resolution on the Strips

Following confirmation of event clustering, $\Delta V_{Drift}$ was set to be constant at 500 V and $\Delta V_{Micromegas}$ was varied from 535 V to 570 V; in an identical way to the mesh measurements. For each amplification field strength, 60 second exposures were captured using the VMM slow control software. With the charge calibration applied, the total charge spectrum was obtained by summing all the charge on the x and y-strips per clustered event. The gain and energy resolution was then extracted from the spectrum and can be seen plotted as a function of $\Delta V_{Micromegas}$ in Figure 9.7.

The gas gain is seen to increase exponentially from $5341 \pm 7$ at 530 V to $24020 \pm 20$ at 570 V, similar to the observations on the mesh. The corresponding energy resolution is observed to initially decrease from $0.574 \pm 0.002$ to $0.319 \pm 0.003$ as $\Delta V_{Micromegas}$ increases from 530 to 560 V. The energy resolution is then seen to increase slightly to $0.358 \pm 0.002$ at 570 V.

These results demonstrate some discrepancies between the effective gas gain and energy resolution measured on the mesh and strips. Interestingly, the effective gas gain measured on the mesh was on average a factor of 1.29 larger than that observed on the strips. This is

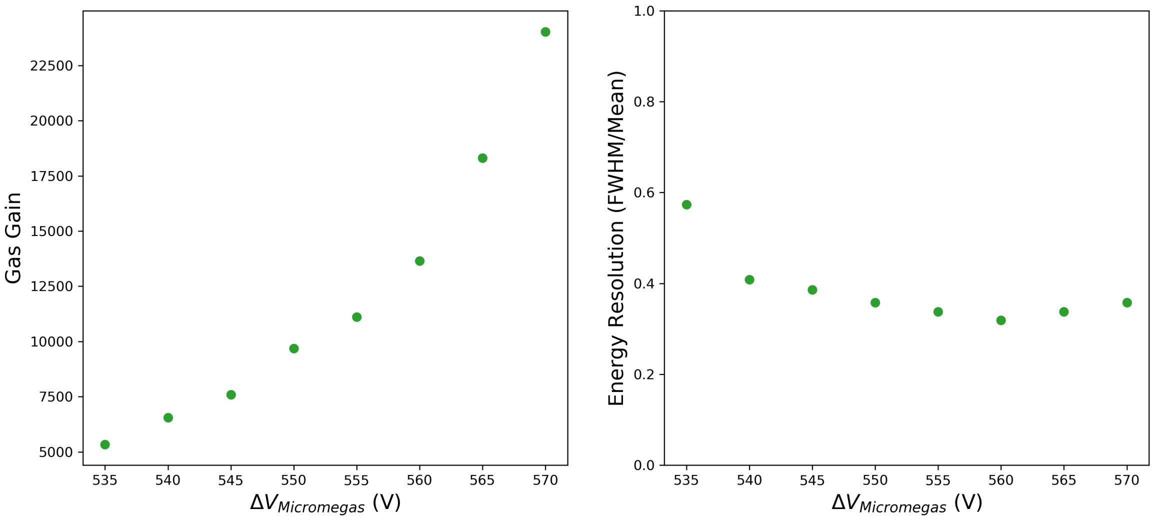

Figure 9.7 Gas gain (left) and energy resolution (right) measurements on the micromegas strips plotted as a function of $\Delta V_{Micromegas}$.

consistent with the difference between the mesh and strip measurements seen in the previous chapter and is likely due to charge losses on the inter-electrode gaps between strips. This hypothesis is explored in more detail through the extraction of Townsend and Rose-Korff parameters in the next section.

## 9.3 Effective Townsend Parameters

The absolute gas gain in the micromegas amplification region, i.e the multiplication factor between the initial number of electrons and the final number of electrons following the avalanche, is the same regardless of whether the measurements are taken on the mesh or the strips. However, the effective gas gain, which takes into account secondary effects like charge collection efficiency, has persistently been lower on the strip electrodes. As the effective strip gas gain was shown to depend on the micromegas strip widths in the previous chapter, it is likely that this discrepancy is caused by the electrode geometry resulting in less efficient charge collection on the strips. It is therefore hypothesised that the effective gas gain on the mesh more accurately represents the absolute gas gain.

This hypothesis was investigated by formulating the effective gas gain measurements in terms of the Townsend and Rose-Korff equations. The Townsend parameters can be determined via the gain measurements by rearranging Equation 2.8 in the form:

$$ln(ln(Gain)) = ln(APd) - \frac{BP}{E}, \tag{9.3}$$

this yields a linear relationship between $ln(ln(Gain))$ and $1/E$ from which the Townsend parameters, $A$ and $B$, can be extracted from the intercept and gradient respectively. By taking a similar approach the mean free path, $\lambda$, and ionisation energy, $I_e$, can be estimated by rearranging Equation 2.9 in the form:

$$ln(ln(Gain)) = ln\left(\frac{d}{\lambda}\right) - \frac{I_e}{\lambda E}, \tag{9.4}$$

where the intercept and gradient can be used to extract $\lambda$ and subsequently $I_e$.

Figure 9.8 shows the results of plotting $ln(ln(Gain))$ as a function of $1/E$ for both the mesh and strip measurements. As can be seen, a linear regression analysis was applied to both sets of results. The gradient and y-intercept were extracted from the fit functions and the Townsend parameters, mean free path, and ionisation energy were determined; the extracted values can be seen in Table 9.2.

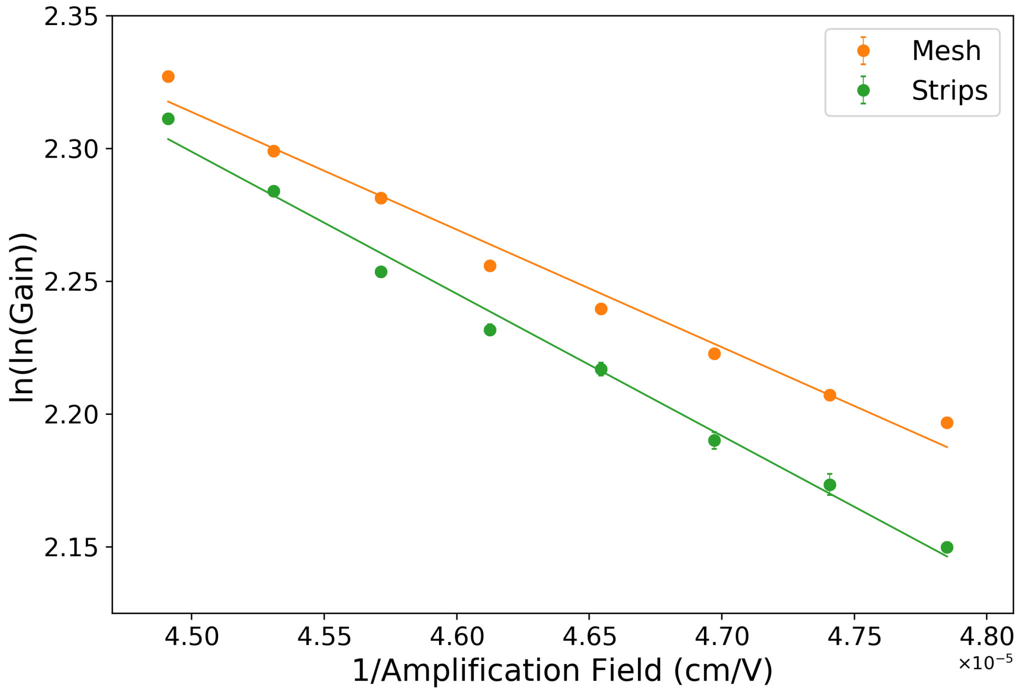

Figure 9.8 $ln(ln(Gain))$ plotted as a function of $1/E$ for both the micromegas mesh and strip measurements in 40 Torr of $CF_4$.

Table 9.2 Summary of the effective Townsend parameters, mean free path, primary ionisation cross section, and ionisation energy determined via the gain measurements on the micromegas mesh and strips.

| **Parameter** | **Mesh** | **Strips** |
|---|---|---|
| $A$ ($\mathrm{cm^{-1}Torr^{-1}}$) | $72 \pm 2$ | $110 \pm 10$ |
| $B$ ($\mathrm{V\ cm^{-1}Torr^{-1}}$) | $1107 \pm 8$ | $1340 \pm 60$ |
| $\lambda$ ($\mu$m) | $3.45 \pm 0.01$ | $2.3 \pm 0.2$ |
| $\sigma_p$ ($\mathrm{m^{-2}}$) | $2.20 \pm 0.08 \times 10^{-19}$ | $3.3 \pm 0.4 \times 10^{-19}$ |
| $I_e$ (eV) | $15.3 \pm 0.4$ | $12.4 \pm 0.8$ |

As anticipated the effective Townsend parameters were found to be different between the mesh and the strips; both $A$ and $B$ were found to be smaller on the mesh. These values are slightly larger than what could be extrapolated from previous ThGEM measurements at 40 Torr [125]. However this discrepancy is likely caused by the different detector geometries, i.e. the amplification field strength in the hole of a ThGEM is non-uniform and weaker than an equivalent parallel plate geometry field [123]. This comparison of the Townsend parameters is therefore limited.

Alternatively, the Rose-Korff formulation provides us with physical parameters which can be directly compared with literature. The mean free path, $\lambda$, determined on both the mesh and strips was used to calculate the primary ionisation cross section, $\sigma_p$, via Equation 2.10; assuming a molecular number density of $N_m = 1.32 \times 10^{24}\ \mathrm{m^{-3}}$. This is also presented in Table 9.2 and is compatible with literature [269]. Furthermore, literature values of $I_e$ for $CF_4$ range from 15.3 - 16.5 eV [270] which is in remarkable agreement with the value obtained on the mesh. However, a discrepancy with these literature values is noted on the strips.

This result indicates that the mesh measurements provide a more reliable proxy for the absolute gas gain produced in the amplification region. This finding thereby supports the hypothesis that significant charge losses likely occur on the strips and highlights that further work could be undertaken to optimise the strip geometry for more efficient charge collection and, as discussed in the previous chapter, charge sharing between x and y-strip planes. Such an optimisation in the future would likely benefit the detection threshold of events which can be effectively reconstructed in 3-dimensions in a directional DM search.

## 9.4 Future Work

In this chapter, the first engineering demonstration of a micromegas detector with full area SRS instrumentation in low pressure $CF_4$ has been presented. Going forward, there exists two pipelines for future work which are outlined in Figure 9.9. Pipeline 1 regards the direct continuation of the work presented in this chapter with the micromegas in low pressure $CF_4$. The next step here is a demonstration with neutrons to investigate the detectors capability for ER/NR discrimination, track reconstruction, and head-tail sensitivity. As $CF_4$:He mixtures at atmospheric pressure have already shown success with a ThGEM in Chapter 3, these mixtures should be tested with the micromegas and subject to neutron exposures in parallel with low pressure pure $CF_4$.

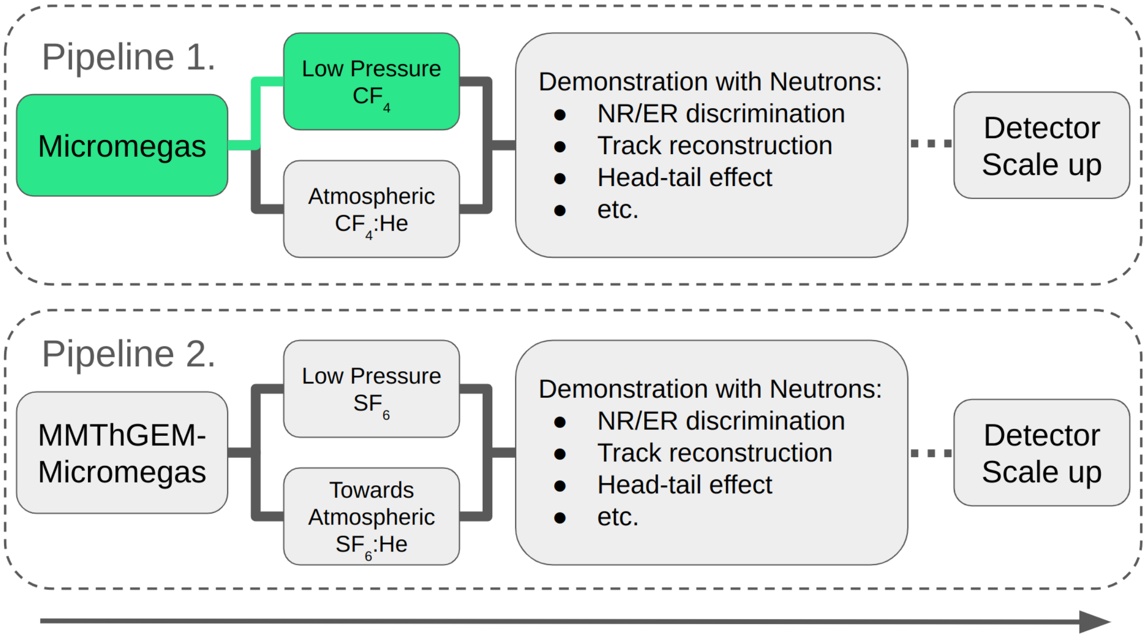

Figure 9.9 Flow chart diagram indicating the two major pipelines for future work towards a CYGNUS-m$^3$ scale demonstrator with SRS electronics. Sections highlighted in green indicate the current phase in the pipeline.

As the ultimate goal is operation with an NID gas, pipeline 2 begins with the SRS instrumentation of the coupled MMThGEM-Micromegas detector which was found to function well in low pressure $SF_6$ in Chapter 7. Similar to pipeline 1, the goal of pipeline 2 is to demonstrate the detectors response to NRs in the hope that it can be used in a future WIMP search. A parallel objective is the demonstration with an atmospheric $SF_6$:He mixture which could still require some optimisation of the MMThGEM gain stage.

Depending on the small scale detector performance, a tentative future step towards scale up has also been included in both pipelines with the aim of reaching a CYGNUS-m$^3$ scale demonstrator. This would include studies to understand the scalability and stability of the detector under long term operation. Additionally, due to being prominent greenhouse gases, constant scrubbing of impurities from large volumes of $CF_4$ and $SF_6$ gas using technologies like molecular sieves [271–273] must be demonstrated for sustainable long term operation. Finally, it is also advantageous to investigate the radiopurity of detector materials similar to the Low $\alpha$ emitting $\mu$-PIC [152].

## 9.5 Conclusions

In summary, this chapter saw the first successful engineering demonstration of a low pressure gaseous TPC implemented with SRS electronics. This began by addressing the thermal management of the system under low pressure conditions. It was found that the VMM chips quickly exceeded 50 °C without any thermal mitigation; this would have not been suitable for long term operation in a DM search. However, when thermally coupled to the steel vacuum vessel with HSC, the chips were able to equilibrate below the recommended 40 °C limit under realistic low pressure operating conditions.

Tests then began with the micromegas in 40 Torr of $CF_4$ by instrumenting the mesh with CREMAT electronics and the full area of the strip readout plane with the SRS electronics. Baseline gas gain and energy resolution measurements were first taken on the mesh as a function of $\Delta V_{Micromegas}$ which ranged from 8073 ± 1 to 28250 ± 10 and 0.1966 ± 0.0004 to 0.305 ± 0.001 respectively. Measurements were then taken on the strips and demonstrated event clustering with 100% utilisation of the micromegas strip plane in a low pressure gas for the first time. Gas gain and energy resolution measurements were then established on the strips which were found to range from 5341 ± 7 to 24020 ± 20 and 0.319 ± 0.003 to 0.574 ± 0.002 respectively.

On average the gain was found to be a factor of 1.29 larger on the mesh. Townsend and Rose-Korff parameters were extracted in an attempt to address this discrepancy. Some of which showed remarkable agreement with literature values, suggesting that the larger gas gains observed on the mesh were more accurate and provided additional evidence that a significant amount of charge is lost in the strip measurements. This finding further reinforced the idea that an optimisation of the strip geometry could be performed to improve charge utilisation for 3-dimensional reconstruction.

Finally, future plans for testing the response of the novel low pressure SRS setup to NRs were discussed. This included two main pipelines of future work: 1.) low pressure pure

$CF_4$ and atmospheric $CF_4$:He mixtures with the micromegas, and 2.) NI operation with the coupled MMThGEM-Micromegas in low pressure pure $SF_6$ and steps towards atmospheric $SF_6$:He mixtures.

# Chapter 10

# Conclusions

In Chapter 1, a historical review of the evidence for Dark Matter (DM) was presented. It was shown that the majority of mass in the Universe, $\approx 84\%$, is attributed to non-baryonic DM. One well motivated candidate known as a Weakly Interacting Massive Particle (WIMP) has been the subject of many direct search experiments. The current world leading searches with two-phase Time Projection Chambers (TPCs) are beginning to probe the region of the WIMP-nucleon cross section vs WIMP mass search parameter space known as the Neutrino Fog. Without a method of discriminating between WIMP and neutrino induced events, these experiments will struggle to produce irrefutable evidence of WIMP-nucleon scattering.

A further discussion which elaborated on the challenges of the Neutrino Fog was presented in Chapter 2. Particular focus was paid to the concepts of directional detection which is largely considered to be the most robust method for identifying a DM signature, especially in light of the neutrino background. Several directional detector technologies were highlighted, but the most developed and widely used technology is that of the low pressure gaseous TPC. There are multiple approaches to this technology currently being investigated for the next generation of directionally sensitive nuclear recoil observatories with the CYGNUS and CYGNO collaborations. Major avenues for small scale research and development include: new target gas mixtures which can ideally operate at atmospheric pressure, contain a fluorine component, and a Negative Ion Drift (NID) component; charge amplification and readout technologies, which are capable of producing large charge amplification in NID gases with high-granularity readouts; and scalable charge sensitive readout systems, which can keep up with the demand of new high-granularity detectors.

To begin studying new gas mixtures which can operate at atmospheric pressure, a ThGEM TPC was constructed to demonstrate charge amplification in $CF_4$:He mixtures. Results presented in Chapter 3 demonstrated gas gains on the order of $10^4$ in both low pressure and atmospheric mixtures which prioritised the low partial pressure of $CF_4$ in the interest of preserving directionality. As a result of these measurements, it was recommended that a mixture consisting of $CF_4$:He with ratio 40:720 Torr should be used in the future.

It has been previously demonstrated that low pressure $SF_6$, an NID gas, is limited to low gas gains on the order of $10^3$, with ThGEM technology. Therefore, a novel multi-stage Multi-Mesh ThGEM (MMThGEM) was employed for charge amplification measurements presented in Chapter 4. Measurements were compared to previous work with the device and an optimisation procedure was presented which demonstrated large gas gains in 40 Torr of $SF_6$ on the order of $10^4$; indicating an order of magnitude improvement in what was previously considered possible with an NID gas. These results showed that, an NID gas is capable of producing charge amplification comparable to conventional drift gases, provided careful consideration is given to the design and optimisation of the gain stage technology. Further work is required to optimise the device for improved energy resolution while maintaining high gas gain.

The signal integration method used to calculate the gas gains measured in low pressure $SF_6$, with the MMThGEM, was validated by work presented in Chapter 5. This began by identifying the long preamplifier rise time associated with events in $SF_6$ compared with those in $CF_4$ and excluding pile-up as a possible explanation for the unique appearance of $SF_6$ signals. Instead, the long rise time was found to be a physical effect caused by the slow arriving Negative Ions (NIs), compared to fast electrons, via simulations which utilised the software package DEGRAD. Following this, the integral method used for gain calculations was validated against a deconvolution algorithm applied to the preamplifier signal, which removed the suspected effects of ballistic deficit caused by the slow rise times. The effective electronic gain between the deconvolved preamplifier and integral of the shaper was found to be almost identical for the fast electron signal in $CF_4$ and the slow NI signal in $SF_6$, suggesting that the integral method is a valid approach for gain calculations which is not influenced by ballistic deficit.

Following the validation of the integral method in pure $SF_6$, the MMThGEM was then subjected to $SF_6$:He and $CF_4$:$SF_6$:He mixtures in Chapter 6. With the aim of prioritising the directional potential of these mixtures, this process began with low partial pressures of $SF_6$, and a $CF_4$:$SF_6$ base gas mixture, proceeded by gradual additions of helium. These mixtures were able to produce gas gains on the order of $10^4$, for the first time in an NID gas containing helium, up to a total pressure of 100 Torr. Further work is required to optimise the energy resolution of the device with the aim of achieving atmospheric operation in a mixture containing $SF_6$ and helium.

As the MMThGEM proved to be a proficient gain stage device in $SF_6$, the device was coupled to a high-granularity micromegas detector instrumented with 32 channels on the y-axis in Chapter 7. The coupled detector was able to achieve an extremely large, of order $10^5$, gas gain in low pressure $SF_6$ for the first time; this result offers an improvement of 2 orders of magnitude compared to typical charge amplification previously seen in an NID gas. Following this, 2-dimensional directionality was demonstrated with alpha particles via the development of a total linear regression algorithm for principle axis reconstruction and directional sense via comparison to a SRIM (Stopping and Ranges of Ions in Matter) simulation. The coupled detector was then installed in a large CYGNUS-$m^3$ scale vessel and nuclear recoils were observed, identified with the aid of SRIM and SREM (Stopping and Ranges of Electrons in Matter) simulations, for the first time in a such a large volume of $SF_6$. Recommendations included reducing the hole pitch of the MMThGEM in future designs.

The demonstration of the MMThGEM-Micromegas detector in a CYGNUS-$m^3$ volume was a significant accomplishment. However, the resistive Diamond Like Carbon (DLC) layer in the micromegas, originally introduced for protection in high event rate applications, resulted in charge dissipation which is detrimental to the reconstruction of events. For the purpose of investigating the benefits and challenges associated with a DLC layer, work which compared the micromegas to two alternative detector designs was discussed in Chapter 8. This work also presented the opportunity to implement a Scalable Readout System (SRS) which increased the number of channels from 32 to hundreds; providing full area instrumentation with the potential for 3-dimensional event reconstruction. By comparing all three designs, it was found that the DLC layer worsened the charge sharing between upper (y-strip) and lower (x-strip) electrodes and induced an artificial broadening, to a level which was comparable to the amount of normalised electron diffusion in the detector, thereby degrading the positional resolution. As this is counterproductive to the goal of NID gases, and the event rate in DM detection experiments is not high enough to warrant its use, it is recommended that micromegas detectors used for directional searches be manufactured without a resistive layer in the future.

Finally, given the success of the SRS system during the micromegas comparison, work in which the micromegas was instrumented with SRS electronics and operated in low pressure $CF_4$, a more conducive gas target for a directional DM search, was discussed in Chapter 9. This involved testing thermal management options for operating the system in a novel low pressure environment. It was found that the system can operate in an ideal long term temperature range by thermal coupling to the steel containment vessel. The micromegas was instrumented with a full scale SRS system in 40 Torr of $CF_4$ and demonstrated the first novel operation of the SRS electronics in a low pressure gas. Furthermore, a comparison between gain measurements on the micromegas mesh and strips indicated that charge is likely lost on the strip measurements in agreement with results presented in Chapter 8. Further work is still required to realise the full potential of this system with $CF_4$:He mixtures and coupling with the MMThGEM to demonstrate the setup in low pressure $SF_6$ and $SF_6$:He mixtures. Future studies of scalability, stability and sustainability under long term operation, and radiopurity of detector materials are also required for demonstrating the feasibility of this technology in a full scale CYGNUS search.

# Bibliography

[1] G. Bertone and D. Hooper, "History of Dark Matter", Reviews of Modern Physics **90**, 045002 (2018).

[2] F. Zwicky, "Die Rotverschiebung von Extragalaktischen Nebeln", Helvetica Physica Acta **6**, 110 (1933).

[3] F. Zwicky, "Republication of: The Redshift of Extragalactic Nebulae", General Relativity and Gravitation **41**, 207 (2009).

[4] F. Zwicky, "On the Masses of Nebulae and of Clusters of Nebulae", The Astrophysical Journal **86**, 217 (1937).

[5] S. M. Faber and J. S. Gallagher, "Masses and Mass-To-Light Ratios of Galaxies", Annual Review of Astronomy and Astrophysics **17**, 135 (1979).

[6] V. C. Rubin and J. W. Kent Ford, "Rotation of the Andromeda Nebula from a Spectroscopic Survey of Emission Regions", The Astrophysical Journal **159**, 379 (1970).

[7] M. Persic et al., "The Universal Rotation Curve of Spiral Galaxies - I. The Dark Matter Connection", Monthly Notices of the Royal Astronomical Society **281**, 27 (1996).

[8] K. Begeman et al., "Extended Rotation Curves of Spiral Galaxies: Dark Haloes and Modified Dynamics", Monthly Notices of the Royal Astronomical Society **249**, 523 (1991).

[9] J. Magee et al., "Rotation Curve Measurement of Dark Matter Content of a z 0.5 Galaxy", Research Notes of the AAS **7**, 110 (2023).

[10] A. Eilers et al., "The Circular Velocity Curve of the Milky Way from 5 to 25 kpc", The Astrophysical Journal **871**, 120 (2019).

[11] M. Milgrom, "A Modification of the Newtonian Dynamics as a Possible Alternative to the Hidden Mass Hypothesis", The Astrophysical Journal **270**, 365 (1983).

[12] M. Milgrom, "A Modification of the Newtonian Dynamics: Implications for Galaxies", The Astrophysical Journal **270**, 371 (1983).

[13] M. Milgrom, "A Modification of the Newtonian Dynamics : Implications for Galaxy Systems", The Astrophysical Journal **270**, 384 (1983).

[14] P. van Dokkum et al., "A Galaxy Lacking Dark Matter", Nature **555**, 629 (2018).

[15] P. van Dokkum et al., "A Second Galaxy Missing Dark Matter in the NGC 1052 Group", The Astrophysical Journal Letters **874**, 8 (2019).

[16] M. Montes et al., "The Galaxy “Missing Dark Matter” NGC 1052-DF4 is Undergoing Tidal Disruption", The Astrophysical Journal **904**, 12 (2020).

[17] K. Chae, "Breakdown of the Newton–Einstein Standard Gravity at Low Acceleration in Internal Dynamics of Wide Binary Stars", The Astrophysical Journal **952**, 128 (2023).

[18] I. Banik et al., "Strong Constraints on the Gravitational Law from Gaia DR3 Wide Binaries", Monthly Notices of the Royal Astronomical Society **527**, 4573 (2024).

[19] I. Banik and H. Zhao, "From Galactic Bars to the Hubble Tension: Weighing Up the Astrophysical Evidence for Milgromian Gravity", Symmetry **14**, 1331 (2022).

[20] A. Einstein, "Die Grundlage der allgemeinen Relativitätstheorie", Annalen der Physik **354**, 769 (1916).

[21] B. P. Abbott et al., "Observation of Gravitational Waves from a Binary Black Hole Merger", Physical Review Letters **116**, 061102 (2016).

[22] B. P. Abbott et al., "GW151226: Observation of Gravitational Waves from a 22-Solar-Mass Binary Black Hole Coalescence", Physical Review Letters **116**, 241103 (2016).

[23] B. P. Abbott et al., "GW170104: Observation of a 50-Solar-Mass Binary Black Hole Coalescence at Redshift 0.2", Physical Review Letters **118**, 221101 (2017).

[24] B. P. Abbott et al., "GW170814: A Three-Detector Observation of Gravitational Waves from a Binary Black Hole Coalescence", Physical Review Letters **119**, 141101 (2017).

[25] T. Treu, "Strong Lensing by Galaxies", Annual Review of Astronomy and Astrophysics **48**, 87 (2010).

[26] R. Massey et al., "The Dark Matter of Gravitational Lensing", Reports on Progress in Physics **73**, 086901 (2010).

[27] A. J. Shajib et al., "Strong Lensing by Galaxies", arXiv:2210.10790 (2022).

[28] P. Natarajan et al., "Strong Lensing by Galaxies Clusters", Space Science Reviews **220**, 19 (2024).

[29] A. Refregier, "Weak Gravitational Lensing by Large-Scale Structure", Annual Reviews of Astronomy and Astrophysics **41**, 645 (2003).

[30] R. Gavazzi et al., "The Sloan Lens ACS Survey. IV. The Mass Density Profile of Early-Type Galaxies out to 100 Effective Radii", The Astrophysical Journal **667**, 176 (2007).

[31] D. Clowe et al., "Weak-Lensing Mass Reconstruction of the Interacting Cluster 1E 0657–558: Direct Evidence for the Existence of Dark Matter", The Astrophysical Journal **604**, 596 (2004).

[32] D. Clowe et al., "A Direct Empirical Proof of the Existence of Dark Matter", The Astrophysical Journal **648**, L109 (2006).

[33] B. Marusa et al., "Revealing the Properties of Dark Matter in the Merging Cluster MACS J0025.4-1222", The Astrophysical Journal **687**, 959 (2008).

[34] W. A. Dawson et al., "Discovery of a Dissociative Galaxy Cluster Merger with Large Physical Separation", The Astrophysical Journal **747**, 6 (2012).

[35] S. W. Allen et al., "Cosmological Parameters from Observations of Galaxy Clusters", Annual Review of Astronomy ans Astrophysics **49**, 409 (2011).

[36] D. N. Spergel et al., "First-Year Wilkinson Microwave Anisotropy Probe (WMAP) Observations: Determination of Cosmological Parameters", The Astrophysical Journal Supplement Series **148**, 175 (2003).

[37] D. N. Spergel et al., "Three-Year Wilkinson Microwave Anisotropy Probe (WMAP) Observations: Implications for Cosmology", The Astrophysical Journal Supplement Series **170**, 377 (2007).

[38] G. Hinshaw et al., "Five-Year Wilkinson Microwave Anisotropy Probe Observations: Data Processing, Sky Maps, and Basic Results", The Astrophysical Journal Supplement Series **180**, 225 (2009).

[39] E. Komatsu et al., "Seven-Year Wilkinson Microwave Anisotropy Probe (WMAP) Observations: Cosmological Interpretation", The Astrophysical Journal Supplement Series **192**, 18 (2011).

[40] C. L. Bennett et al., "Nine-Year Wilkinson Microwave Anisotropy Probe (WMAP) Observations: Final Maps and Results ", The Astrophysical Journal Supplement Series **208**, 54 (2013).

[41] P. A. R. Ade et al., "Planck 2013 Results. XVI. Cosmological Parameters", Astronomy and Astrophysics **571** (2014).

[42] P. A. R. Ade et al., "Planck 2015 Results. XIII. Cosmological Parameters", Astronomy and Astrophysics **594** (2016).

[43] N. Aghanim et al., "Planck 2018 Results VI. Cosmological Parameters", Astronomy and Astrophysics **641** (2020).

[44] F. Iocco et al., "Primordial Nucleosynthesis: From Precision Cosmology to Fundamental Physics", Physics Reports **472** (2009).

[45] A. Coc, "Big-bang Nucleosynthesis: A Probe of the Early Universe", Nuclear Instruments and Methods in Physics Research A **611**, 224 (2009).

[46] J. Beringer et al., "Review of Particle Physics", Physical Review D **86**, 010001 (2012).

[47] B. D. Fields et al., "Big-Bang Nucleosynthesis after Planck", Journal of Cosmology and Astroparticle Physics **03** (2020).

[48] P. Tisserand, "Limits on the MACHO Content of the Galactic Halo from the EROS-2 Survey of the Magellanic Clouds", Astronomy and Astrophysics **469**, 387 (2007).

[49] T. D. Brandt, "Constraints on MACHO Dark Matter from Compact Stellar Systems in Ultra-Faint Dwarf Galaxies", The Astrophysical Journal Letters **824**, L31 (2016).

[50] J. L. Feng, "Dark Matter Candidates from Particle Physics and Methods of Detection", Annual Review of Astronomy and Astrophysics **48**, 495 (2010).

[51] G. Jungman et al., "Supersymmetric Dark Matter", Physics Reports **267**, 195 (1996).

[52] S. P. Martin, "A Supersymmetry Primer", arXiv:hep-ph/9709356v7 (2016).

[53] G. Bertone and T. M. P. Tait, "A New Era in the Search for Dark Matter", Nature **562**, 51 (2018).

[54] D. Hooper and S. Profumo, "Dark Matter and Collider Phenomenology of Universal Extra Dimensions", Physics Reports **453**, 29 (2007).

[55] A. Hook, "TASI Lectures on the Strong CP Problem and Axions", Proceedings of Science **333** (2019).

[56] J. M. Pendlebury et al., "Revised Experimental Upper Limit on the Electric Dipole Moment of the Neutron", Physical Review D **92**, 092003 (2015).

[57] R. D. Peccei, "The Strong CP Problem and Axions", arXiv:hep-ph/0607268 (2006).

[58] A. Boyarsky et al., "Sterile Neutrino Dark Matter", Progress in Particle and Nuclear Physics **104** (2019).

[59] M. Schumann, "Direct Detection of WIMP Dark Matter: Concepts and Status", Journal of Physics G: Nuclear and Particle Physics **46**, 103003 (2019).

[60] J. M. Gaskins, "A Review of Indirect Searches for Particle Dark Matter", Contemporary Physics **57**, 496 (2016).

[61] F. Kahlhoefer, "Review of LHC Dark Matter Searches", International Journal of Modern Physics A **32**, 1730006 (2017).

[62] L. Baudis, "Direct Dark Matter Detection: The Next Decade", Physics of the Dark Universe **1**, 94 (2012).

[63] G. Giroux, "Search for Dark Matter with the PICO-500 Experiment", Journal of Physics: Conference Series **2156**, 012068 (2022).

[64] F. Aubin et al., "Discrimination of Nuclear Recoils from Alpha Particles with Superheated Liquids", New Journal of Physics **10**, 103017 (2008).

[65] C. Amole et al., "Dark Matter Search Results from the PICO-60 $C_3F_8$ Bubble Chamber", Physical Review Letters **118**, 251301 (2017).

[66] C. Amole et al., "Dark Matter Search Results from the Complete Exposure of the PICO-60 $C_3F_8$ Bubble Chamber", Physical Review D **100**, 022001 (2019).

[67] R. Bernabei et al., "The DAMA/LIBRA Apparatus", Nuclear Instruments and Methods in Physics Research A **592**, 297 (2008).

[68] G. F. Knoll, *"Radiation Detection and Measurement"*, John Wiley & Sons, 4th edition, 2010, Chap. 8.

[69] T. Shutt et al., "Measurement of Ionization and Phonon Production by Nuclear Recoils in a 60 g Crystal of Germanium at 25 mK", Physical Review Letters **69**, 3425 (1992).

[70] S. Zatschler, "Status and Prospects of the SuperCDMS Dark Matter Experiment at SNOLAB", Proceedings of Science **441**, 076 (2024).

[71] P. D. Gangi et al., "The Xenon Road to Direct Detection of Dark Matter at LNGS: The XENON Project", Universe **7**, 313 (2021).

[72] D. S. Akerib et al., "The LUX-ZEPLIN (LZ) Experiment", Nuclear Instruments and Methods in Physics Research A **953**, 163047 (2020).

[73] E. Aprile et al., "The XENONnT Dark Matter Experiment", arXiv:2402.10446 (2024).

[74] A. Abdukerim et al., "PandaX-xT: a Multi-ten-tonne Liquid Xenon Observatory at the China Jinping Underground Laboratory", arXiv:2402.03596 (2024).

[75] J. Aalbers et al., "First Dark Matter Search Results from the LUX-ZEPLIN (LZ) Experiment", Physical Review Letters **131**, 041002 (2023).

[76] E. Aprile et al., "First Dark Matter Search with Nuclear Recoils from the XENONnT Experiment", Physical Review Letters **131**, 041003 (2023).

[77] W. Ma et al., "Search for Solar $^8$B Neutrinos in the PandaX-4T Experiment Using Neutrino-Nucleus Coherent Scattering", Physical Review Letters **130**, 021802 (2023).

[78] L. Baudis, "Dual-phase Xenon Time Projection Chambers for Rare-event Searches", Philosophical Transactions of the Royal Society A **382**, 20230083 (2024).

[79] C. A. J. O'Hare, "New Definition of the Neutrino Floor for Direct Dark Matter Searches", Physical Review Letters **127**, 251802 (2021).

[80] J. Aalbers et al., "DARWIN: Towards the Ultimate Dark Matter Detector", Journal of Cosmology and Astroparticle Physics **11**, 017 (2016).

[81] L. Baudis, "DARWIN/XLZD: a Future Xenon Observatory for Dark Matter and Other Rare Interactions", arXiv:2404.19524 (2024).

[82] F. Froborg and A. R. Duffy, "Annual Modulation in Direct Dark Matter Searches", Journal of Physics G: Nuclear and Particle Physics **47**, 094002 (2020).

[83] J. Josephides, "WIMP Wind Infographic", Swinburne Astronomy Productions (Swinburne University of Technology) (2019).

[84] R. Bernabei et al., "Recent Results from DAMA/LIBRA and Comparisons", Moscow University Physics Bulletin **77**, 291 (2022).

[85] J. Klinger and V. A. Kudryavtsev, "Muon-Induced Neutrons Do Not Explain the DAMA Data", Physical Review Letters **114**, 151301 (2015).

[86] J. H. Davis, "Fitting the Annual Modulation in DAMA with Neutrons from Muons and Neutrinos", Physical Review Letters **113**, 081302 (2014).

[87] D. Buttazzo et al., "Annual Modulations from Secular Variations: Relaxing DAMA?", Journal of High Energy Physics **2020**, 137 (2020).

[88] A. Messina et al., "Annual Modulations from Secular Variations: Not Relaxing DAMA?", Journal of Cosmology and Astroparticle Physics **2020**, 037 (2020).

[89] G. Adhikari et al., "An Induced Annual Modulation Signature in COSINE-100 Data by DAMA/LIBRA's Analysis Method", nature **13**, 4676 (2023).

[90] J. Amare et al., "The ANAIS-112 Experiment at the Canfranc Underground Laboratory", Journal of Physics: Conference Series **1342**, 012056 (2020).

[91] The COSINE-100 Collaboration, "An Experiment to Search for Dark-matter Interactions using Sodium Iodide Detectors", Nature **564**, 83 (2018).

[92] I. Coarasa et al., "ANAIS-112: Updated Results on Annual Modulation with Three-year Exposure", Proceedings of Science - XVIII International Conference on Topics in Astroparticle and Underground Physics (TAUP2023) **441** (2024).

[93] H. S. Lee, "COSINE-100 Experiment", Proceedings of Science - XVIII International Conference on Topics in Astroparticle and Underground Physics (TAUP2023) **441** (2024).

[94] G. Heusser, "Low-Radioactivity Background Techniques", Annual Review of Nuclear and Particle Science **45**, 543 (1995).

[95] J. Billard et al., "Implication of Neutrino Backgrounds on the Reach of Next Generation Dark Matter Direct Detection Experiments", Physical Review D **89**, 023524 (2014).

[96] C. A. J. O'Hare et al., "Recoil Imaging for Directional Detection of Dark Matter, Neutrinos, and Physics Beyond the Standard Model", arXiv: 2203.05914 (2022).

[97] M. Anderson et al., "Measurement of the $^8$B Solar Neutrino Flux in SNO+ with Very Low Backgrounds", Physical Review D **99**, 012012 (2019).

[98] J. N. Bahcal et al., "Solar Models: Current Epoch and Time Dependences, Neutrinos, and Helioseismological Properties", The Astrophysical Journal **555**, 990 (2001).

[99] T. K. Gaisser, "Atmospheric Neutrinos", arXiv: 1910.08851 (2019).

[100] J. F. Beacom, "The Diffuse Supernova Neutrino Background", Annual Review of Nuclear and Particle Science **60**, 439 (2010).

[101] L. Ludhova and S. Zavatarelli, "Studying the Earth with Geoneutrinos", Advances in High Energy Physics **2013**, 425693 (2013).

[102] M. Baldoncini et al., "Reference Worldwide Model for Antineutrinos from Reactors", Physical Review D **91**, 065002 (2015).

[103] F. Ruppin et al., "Complementarity of Dark Matter Detectors in Light of the Neutrino Background", Physical Review D **90**, 083510 (2014).

[104] J. H. Davis, "Dark Matter vs. Neutrinos: the Effect of Astrophysical Uncertainties and Timing Information on the Neutrino Floor", Journal of Cosmology and Astroparticle Physics **2015**, 012 (2015).

[105] S. Sassi et al., "Solar Neutrinos and Dark Matter Detection with Diurnal Modulation", arXiv:2103.08511 (2021).

[106] Z. Bo et al., "First Measurement of Solar $^8$B Neutrino Flux through Coherent Elastic Neutrino-Nucleus Scattering in PandaX-4T", arXiv:2407.10892 (2024).

[107] F. Gao, "New Results from XENONnT", Identification of Dark Matter, 2024.

[108] D. N. Spergel, "Motion of the Earth and the Detection of Weakly Interacting Massive Particles", Physical Review D **37**, 1353 (1988).

[109] B. Morgan et al., "Directional Statistics for Realistic Weakly Interacting Massive Particle Direct Detection Experiments", Physical Review D **71**, 103507 (2005).

[110] S. E. Vahsen et al., "Directional Recoil Detection", Annual Review of Nuclear and Particle Science **71**, 189 (2021).

[111] C. O'Hare, "The Future of Directional Searches", Identification of Dark Matter, 2024.

[112] P. Agnese et al., "Constraints on Directionality Effect of Nuclear Recoils in a Liquid Argon Time Projection Chamber", The European Physical Journal **84**, 023–12312–1 (2024).

[113] E. Daw et al., "The DRIFT Directional Dark Matter Experiments", EAS Publication Series **53**, 11 (2012).

[114] J. Lindhard et al., "Integral Equations Governing Radiation Effects", Matematisk-fysiske Meddelelser Det Kongelige Danske Videnskabernes Selskab **33** (1963).

[115] P. Sorensen, "Atomic Limits in the Search for Galactic Dark Matter", Physical Review D **91**, 083509 (2015).

[116] W. Blum et al., *"Particle Detection with Drift Chambers"*, Springer-Verlag, 2008.

[117] F. Sauli, *"Gaseous Radiation Detectors: Fundementals and Applications"*, Cambridge University Press, 2023.

[118] Y. M. Gavrilyuk et al., "High-resolution Ion Pulse Ionization Chamber with Air Filling for the $^{222}$Rn Decays Detection", Nuclear Instruments and Methods in Physics Research A **801**, 27 (2015).

[119] N. S. Phan et al., "The Novel Properties of $SF_6$ for Directional Dark Matter Experiments", Journal of Instrumentation **12**, P02012 (2017).

[120] D. Loomba, "Low Pressure TPCs: Techniques and Applications", RD51 collaboration meeting and topical workshop on New Horizons in Time Projection Chambers, 2020.

[121] T. Ohnuki et al., "Measurement of Carbon Disulfide Anion Diffusion in a TPC", Nuclear Instruments and Methods in Physics Research A **463**, 142 (2001).

[122] S. E. Vahsen et al., "CYGNUS: Feasibility of a Nuclear Recoil Observatory with Directional Sensitivity to Dark Matter and Neutrinos", arXiv:2008.12587 (2020).

[123] S. Bressler et al., "The Thick Gas Electron Multiplier and its Derivatives: Physics, Technologies and Applications", Progress in Particle and Nuclear Physics **130**, 104029 (2023).

[124] D. Attié et al., "Current Status and Future Developments of Micromegas Detectors for Physics and Applications", Applied Science **11**, 5362 (2021).

[125] J. Burns et al., "Characterisation of Large Area THGEMs and Experimental Measurement of the Townsend Coefficients for $CF_4$", Journal of Instrumentation **12**, T10006 (2017).

[126] F. J. Iguaz et al., "Characterization of Microbulk Detectors in Argon- and Neon-based Mixtures", Journal of Instrumentation **7**, P04007 (2012).

[127] M. E. Rose and S. A. Korff, "An Investigation of the Properties of Proportional Counters. I", Physical Review **59**, 850 (1941).

[128] N. S. Phan et al., "GEM-based TPC with CCD Imaging for Directional Dark Matter Detection", Astroparticle Physics **84**, 82 (2016).

[129] C. Eldridge, "New Negative Ion Time Projection Chamber Technology for Directional Detection of Dark Matter, Neutrinos and Fast Neutrons", Thesis, University of Sheffield (2021).

[130] B. Morgan et al., "Directional Statistics for Realistic Weakly Interacting Massive Particle Direct Detection Experiments. II. 2D Readout", Physical Review D **72**, 123501 (2005).

[131] D. Dujmic et al., "Observation of the “Head-tail” Effect in Nuclear Recoils of Low-energy Neutrons", Nuclear Instruments and Methods in Physics Research A **584**, 327 (2008).

[132] A. Scarff, "Developments Towards a Scaled-Up One-Dimensional Directional Dark Matter Detector", Thesis, University of Sheffield (2018).

[133] H. Sekiya et al., "Measurements of Anisotropic Scintillation Efficiency for Carbon Recoils in a Stilbene Crystal for Dark Matter Detection", Physics Letters B **571**, 132 (2003).

[134] R. Bernabei et al., "$ZnWO_4$ Anisotropic Scintillator for Dark Matter Investigation with the Directionality Technique", EPJ Web of Conferences **136**, 05002 (2017).

[135] V. Caracciolo et al., "The ADAMO Project and Developments", Journal of Physics: Conference Series **718**, 042011 (2016).

[136] V. Caracciolo, "The ADAMO Project for the Dark Matter Directionality Approach", 9th International Conference on New Frontiers in Physics, 2020.

[137] N. D'Ambrosio et al., "Nuclear Emulsions as a Very High Resolution Detector for Directional Dark Matter Search", Journal of Instrumentation **9**, C01043 (2014).

[138] T. Asada et al., "The Development of a Super-fine-grained Nuclear Emulsion", Progress of Theoretical and Experimental Physics **2017**, 063H01 (2017).

[139] A. Alexandrov et al., "Directionality Preservation of Nuclear Recoils in an Emulsion Detector for Directional Dark Matter Search", Journal of Cosmology and Astroparticle Physics **2021**, 047 (2021).

[140] N. D. Marco et al., "NEWS: Nuclear Emulsions for WIMP Search", Journal of Physics: Conference Series **718**, 042018 (2016).

[141] S. A. Gorbunov and N. S. Konovalova, "New Experiment NEWSdm for Direct Searches for Heavy Dark Matter Particles", Physics of Atomic Nuclei **83**, 83 (2020).

[142] M. C. Marshall et al., "Directional Detection of Dark Matter with Diamond", Quantum Science and Technology **6**, 024011 (2021).

[143] G. J. Alner et al., "The DRIFT-I Dark Matter Detector at Boulby: Design, Installation and Operation", Nuclear Instruments and Methods in Physics Research A **535**, 644 (2004).

[144] B. Morgan et al., "DRIFT: a Directionally Sensitive Dark Matter Detector", Nuclear Instruments and Methods in Physics Research A **513**, 226 (2003).

[145] N. J. C. Spooner et al., "Simulations of the Nuclear Recoil Head–tail Signature in Gases Relevant to Directional Dark Matter Searches", Astroparticle Physics **34**, 284 (2010).

[146] J. B. R. Battat et al., "First Measurement of Nuclear Recoil Head-tail Sense in a Fiducialised WIMP Dark Matter Detector", Journal of Instrumentation **11**, P10019 (2016).

[147] D. P. Snowden-Ifft, "Discovery of Multiple, Ionization-created $CS_2$ Anions and a New Mode of Operation for Drift Chambers", Review of Scientific Instruments **85**, 013303 (2014).

[148] J. B. R. Battat et al., "First Background-free Limit from a Directional Dark Matter Experiment: Results from a Fully Fiducialised DRIFT Detector", Physics of the Dark Universe **9** (2015).

[149] S. Higashino et al., "First Reconstruction of Absolute Three-dimensional Position of Nuclear Recoils using a Negative Ion $\mu$-TPC for Dark Matter Search Experiments", arXiv: 2302.10725 (2023).

[150] T. Shimada et al., "Direction-sensitive Dark Matter Search with 3D-vector-type Tracking in NEWAGE", Progress of Theoretical and Experimental Physics **2023**, 103F01 (2023).

[151] J. B. R. Battat et al., "Low Threshold Results and Limits from the DRIFT Directional Dark Matter Detector", Astroparticle Physics **91**, 65 (2017).

[152] T. Hashimoto et al., "Development of a Low-$\alpha$-emitting $\mu$-PIC as a Readout Device for Direction-sensitive Dark Matter Detectors", Nuclear Instruments and Methods in Physics Research A **977**, 164285 (2020).

[153] J. Ellis and R. A. FLores, "Elastic Supersymmetric Relic-nucleus Scattering Revisited", Physics Letters B **263**, 259 (1991).

[154] K. Nakamura et al., "NEWAGE", Journal of Physics: Conference Series **469**, 0120003 (2013).

[155] M. Leyton, "Directional Dark Matter Detection with the DMTPC Experiment", UCLA Dark Matter, 2016.

[156] F. D. Amaro et al., "A 50 l CYGNO Prototype Overground Characterization", The European Physical Journal C **83**, 946 (2023).

[157] C. Tao, "MIMAC MIcro-tpc MAtrix of Chambers for Directional Dark Matter Detection and Neutron Spectroscopy", CYGNUS Workshop 2019, 2019.

[158] S. Ahlen et al., "First Dark Matter Search Results from a Surface Run of the 10-L DMTPC Directional Dark Matter Detector", Physics Letters B **695**, 124 (2011).

[159] M. Leyton et al., "Directional Dark Matter Detection with the DMTPC m$^3$ Experiment", Journal of Physics: Conference Series **718**, 042035 (2016).

[160] F. D. Amaro et al., "The CYGNO Experiment", Instruments **6**, 6010006 (2022).

[161] D. J. G. Marques et al., "Directional Dark Matter searches with CYGNO", Identification of Dark Matter 2024, 2024.

[162] D. Santos et al., "MIMAC: A Micro-TPC Matrix of Chambers for Direct Detection of Wimps", Journal of Physics: Conference Series **65**, 012012 (2007).

[163] D. Santos, "Dark Matter Directional Detection with MIMAC", Journal of Physics: Conference Series **1029**, 012005 (2018).

[164] J. Billard et al., "Exclusion Limits from Data of Directional Dark Matter Detectors", Physical Review D **82**, 055011 (2010).

[165] W. P. Wood and J. Heicklen, "Kinetics and Mechanism of the Carbon Disulfide Oxygen Explosion", Journal of Physical Chemistry **75**, 861 (1971).

[166] S. Higashino et al., "Development of Negative-ion Gaseous TPC using Micro Pattern Readout for Direction-sensitive Dark Matter Search", Journal of Instrumentation **18**, C06012 (2023).

[167] M. Bianco, "Micropattern Gaseous Detectors Technologies", EURIZON Detector School, 2023.

[168] F. Sauli, "The Gas Electron Multiplier (GEM): Operating Principles and Applications", Nuclear Instruments and Methods in Physics Research A **805**, 2 (2016).

[169] E. Baracchini et al., "Negative Ion Time Projection Chamber Operation with $SF_6$ at Nearly Atmospheric Pressure", Journal of Instrumentation **13**, P04022 (2018).

[170] J. Miyamoto et al., "GEM Operation in Negative Ion Drift Gas Mixtures", Nuclear Instruments and Methods in Physics Research A **526**, 409 (2004).

[171] H. Ishiura et al., "MPGD Simulation in Negative-ion Gas for Direction-sensitive Dark Matter Searches", Journal of Physics: Conference Series **1498**, 012018 (2020).

[172] K. Pushkin and D. Snowden-Ifft, "Measurements of W-value, Mobility and Gas Gain in Electronegative Gaseous $CS_2$ and $CS_2$ Gas Mixtures", Nuclear Instruments and Methods in Physics Research A **606**, 569 (2009).

[173] M. Cortesi et al., "Multi-layer Thick Gas Electron Multiplier (M-THGEM): A New MPGD Structure for High-gain Operation at Low-pressure", Review of Scientific Instruments **88**, 013303 (2017).

[174] R. de Olivera and M. Cortesi, "First Performance Evaluation of a Multi-layer Thick Gaseous Electron Multiplier with In-built Electrode Meshes—MM-THGEM", Journal of Instrumentation **13**, P06019 (2018).

[175] Y.Giomataris et al., "Micromegas: a High-granularity Position-sensitive Gaseous Detector for High Particle-flux Environments", Nuclear Instruments and Methods in Physics Research A **376**, 29 (1996).

[176] A. Ochi et al., "A New Design of the Gaseous Imaging Detector: Micro Pixel Chamber", Nuclear Instruments and Methods in Physics Research A **471**, 264 (2001).

[177] G. J. Alner et al., "The DRIFT-II Dark Matter Detector: Design and Commissioning", Nuclear Instruments and Methods in Physics Research A **555**, 173 (2005).

[178] A. C. Ezeribe et al., "Demonstration of ThGEM-multiwire Hybrid Charge Readout for Directional Dark Matter Searches", Nuclear Instruments and Methods in Physics Research A **987**, 164847 (2021).

[179] F. Mayet et al., "Micromegas μTPC for Direct Dark Matter Search with MIMAC", Journal of Physics: Conference Series **179**, 012011 (2009).

[180] J. Derré and I. Giomataris, "Spatial Resolution and Rate Capability of Micromegas Detector", Nuclear Instrumentation and Methods in Physics A **461**, 74 (2001).

[181] A. C. Ezeribe et al., "Performance of 20:1 Multiplexer for Large Area Charge Readouts in Directional Dark Matter TPC Detectors", Journal of Instrumentation **13**, P02031 (2018).

[182] J. Billard et al., "Direct Detection of Dark Matter—APPEC Committee Report", Reports on Progress in Physics **85**, 056201 (2024).

[183] C. J. Copi et al., "Directional Sensitivity, WIMP Detection, and the Galactic Halo", Physics Letters B **461**, 43 (1999).

[184] V. A. Kudryavtsev et al., "The Expected Background Spectrum in NaI Dark Matter Detectors and the DAMA Result", Journal of Physics: Conference Series **203**, 012039 (2010).

[185] V. A. Bednyakov et al., "Superlight Neutralino as a Dark Matter Particle Candidate", Physical Review D **55**, 503 (1997).

[186] P. C. Divari et al., "Shell Model Calculations for Light Supersymmetric Particle Scattering off Light Nuclei", Physical Review C **61**, 054612 (2000).

[187] S. Ahlen et al., "The Case for a Directional Dark Matter Detector and the Status of Current Experimental Efforts", International Journal of Modern Physics A **25** (2010).

[188] C. Deaconu et al., "Measurement of the Directional Sensitivity of Dark Matter Time Projection Chamber Detectors", Physical Review D **95**, 122002 (2017).

[189] C. Deaconu, "A Model of the Directional Sensitivity of Low-pressure $CF_4$ Dark Matter Detectors", Thesis, Massachusetts Institute of Technology (2015).

[190] K. Miuchi et al., "Direction-sensitive Dark Matter Search Results in a Surface Laboratory", Physics Letters B **654**, 58 (2007).

[191] M. M. F. R. Fraga et al., "The GEM Scintillation in He–$CF_4$, Ar–$CF_4$, Ar–TEA and Xe–TEA Mixtures", Nuclear Instruments and Methods in Physics Research A **504**, 88 (2003).

[192] L. M. S. Margato et al., "Time Analysis of the Light Pulses on Gaseous Active Scintillators using GEMs with He/$CF_4$", Nuclear Instruments and Methods in Physics Research A **504**, 374 (2003).

[193] S. Vahsen et al., "Tests of Gases in a Mini-TPC with Pixel Chip Readout", Nuclear Instruments and Methods in Physics Research A **738**, 111 (2014).

[194] A. E. C. Coimbra et al., "Photoelectron Extraction Efficiency from a CsI Photocathode and THGEM Operation in He-$CF_4$ and He-$CH_4$ Mixtures", Journal of Instrumentation **11**, P03025 (2016).

[195] E. Baracchini et al., "Stability and Detection Performance of a GEM-based Optical Readout TPC with He/$CF_4$ Gas Mixtures", Journal of Instrumentation **15**, P10001 (2020).

[196] F. D. Amaro et al., "The CYGNO Experiment, a Directional Detector for Direct Dark Matter Searches", Nuclear Instruments and Methods in Physics Research A **1054**, 168325 (2023).

[197] R. Chechik et al., "Thick GEM-like (THGEM) Detectors and Their Possible Applications", SNIC Symposium, Stanford, California (2006).

[198] S. Bressler et al., "A Concept for Laboratory Studies of Radiation Detectors Over a Broad Dynamic-range: Instabilities Evaluation in THGEM-structures", Journal of Instrumentation **9**, P03005 (2014).

[199] M. Pitt et al., "Measurements of Charging-up Processes in THGEM-based Particle Detectors", Journal of Instrumentation **13**, P03009 (2018).

[200] A. Inc, "MAESTRO Multichannel Analyzer Emulation Software", https://www.ortec-online.com/products/software/maestro-mca, (2024).

[201] G. F. Reinking et al., "Studies of Total Ionization in Gases/Mixtures of Interest to Pulsed Power Applications", Journal of Applied Physics **60**, 499 (1986).

[202] T. N. Thorpe and S. E. Vahsen, "Avalanche Gain and its Effect on Energy Resolution in GEM-based Detectors", Nuclear Instruments and Methods in Physics Research A **1045**, 167438 (2023).

[203] A. E. C. Coimbra et al., "THGEM Operation in High Pressure Ne/$CF_4$", Journal of Instrumentation **7**, C02062 (2012).

[204] M. Cortesi et al., "Operation of a THGEM-based Detector in Low-pressure Helium", Journal of Instrumentation **10**, P02012 (2015).

[205] D. collaboration, "First Model Independent Results from DAMA/LIBRA-phase2", Nuclear Physics and Atmoic Energy **19**, 307 (2018).

[206] D. S. Akerib et al., "Results from a Search for Dark Matter in the Complete LUX Exposure", Physical Review Letters **118**, 021303 (2017).

[207] E. Aprile et al., "First Dark Matter Search Results from the XENON1T Experiment", Physical Review Letters **119**, 181301 (2017).

[208] R. Agnese et al., "Search for Low-Mass Weakly Interacting Massive Particles with SuperCDMS ", Physical Review Letters **112**, 241302 (2014).

[209] G. Adhikari et al., "Search for a Dark Matter-Induced Annual Modulation Signal in NaI(Tl) with the COSINE-100 Experiment", Physical Review Letters **123**, 031302 (2019).

[210] M. Marafini et al., "Study of the Performance of an Optically Readout Triple-GEM", IEEE Transactions on Nuclear Science **65**, 604 (2018).

[211] T. Isobe et al., "Development of a Time Projection Chamber using $CF_4$ Gas for Relativistic Heavy Ion Experiments", Nuclear Instruments and Methods in Physics Research A **564**, 190 (2006).

[212] L. Ounalli et al., "New Gas Mixtures Suitable for Rare Event Detection using a Micromegas-TPC Detector", Journal of Instrumentation **4**, P01001 (2009).

[213] C. Eldridge et al., "Directional Dark Matter Readout with a Novel Multi-mesh ThGEM for $SF_6$ Negative Ion Operation", Journal of Instrumentation **18**, P08021 (2023).

[214] A. Breskin et al., "A Concise Review on THGEM Detectors", Nuclear Instruments and Methods in Physics Research A **598**, 107 (2009).

[215] E. Jones et al., "SciPy: Open source scientific tools for Python, scipy.integrate.simpson", https://docs.scipy.org/doc/scipy-1.12.0/reference/generated/scipy.integrate.simpson.html, Accessed: 09/09/2024.

[216] I. Lopes et al., "Ionisation of Gaseous and Liquid Sulphur Hexafluoride by $^60$Co $\gamma$-radiation", Journal of Physics D **19**, 107 (1986).

[217] G. F. Knoll, *"Radiation Detection and Measurement"*, John Wiley & Sons, 4th edition, 2010, Chap. 17.

[218] C. Inc, "CR-111-R2.1 Charge Sensitive Preamplifier: Application Guide", https://www.cremat.com/CR-111-R2.1.pdf, Accessed: 13/02/2024.

[219] C. Inc, "CR-200 Gaussian Shaping Amplifier: Application Guide", https://www.cremat.com/CR-200-R2.1.pdf, Accessed: 11/02/2024.

[220] J. H. Hubbell and S. M. Seltzer, "Tables of X-Ray Mass Attenuation Coefficients and Mass Energy-Absorption Coefficients from 1 keV to 20 MeV for Elements Z = 1 to 92 and 48 Additional Substances of Dosimetric Interest", https://www.nist.gov/pml/x-ray-mass-attenuation-coefficients, Accessed: 12/02/2024.

[221] S. Biagi, "DEGRAD - Transport of Electrons in Gas Mixtures", https://degrad.web.cern.ch/degrad/, Accessed: 05/02/2024.

[222] D. Pfeiffer et al., "Interfacing Geant4, Garfield++ and Degrad for the Simulation of Gaseous Detectors", Nuclear Instruments and Methods in Physics Research A **935**, 121 (2019).

[223] S. F. Biagi, "Auger Cascade Model for Electron Thermalisation in Gas Mixtures Produced by Photons or Particles in Electric and Magnetic Fields", https://indico.cern.ch/event/245535/contributions/531797/attachments/420757/584265/cern.rd51.2013.pdf, Accessed: 05/02/2024.

[224] R. Morrow, "A Survey of the Electron and Ion Transport Properties of $SF_6$", IEEE Transactions on Plasma Science **PS-14**, 234 (1986).

[225] S. Kotz and N. L. Johnson, *"Breakthroughs in Statistics: Methodology and Distribution"*, volume 2, Springer, 1st edition, 1992.

[226] P. Cushman et al., "Snowmass CF1 Summary: WIMP Dark Matter Direct Detection", arXiv:1310.8327 (2013).

[227] M. Abdullah et al., "Coherent Elastic Neutrino-nucleus Scattering: Terrestrial and Astrophysical Applications", arXiv:2203.07361 (2022).

[228] F. Mayet et al., "A Review of the Discovery Reach of Directional Dark Matter Detection", Physics Reports **627** (2016).

[229] C. J. Martoff et al., "Suppressing Drift Chamber Diffusion without Magnetic Field", Nuclear Instruments and Methods in Physics Research A **440**, 355 (2000).

[230] M. Cannoni et al., "Scheme for the Extraction of WIMP-nucleon Scattering Cross Sections from Total Event Rates", Physical Review D **83**, 075010 (2011).

[231] P. Gondolo et al., "Effective Theory of Nuclear Scattering for a WIMP of Arbitrary Spin", Physical Review D **104**, 063017 (2021).

[232] R. J. Lafler, "Studying The Properties of $SF_6$ Gas Mixtures For Directional Dark Matter Detection", Thesis, University of New Mexico (2019).

[233] A. G. McLean et al., "Gas Gains Over $10^4$ and Optimisation using $^{55}$Fe X-rays in Low Pressure $SF_6$ with a Novel Multi-Mesh ThGEM for Directional Dark Matter Searches", Journal of Instrumentation **19**, P03001 (2024).

[234] M. Nakazawa et al., "Prototype Analog Front-end for Negative-ion Gas and Dual-phase Liquid-Ar TPCs", Journal of Instrumentation **14**, T01008 (2019).

[235] T. Kishishita et al., "LTARS: Analog Readout Front-end ASIC for Versatile TPC-applications", Journal of Instrumentation **15**, T09009 (2020).

[236] T. Kosaka et al., "Development of Low Temperature Analog Readout (LTARS 2018) for LAr-TPCs", Journal of Physics: Conference Series **2374**, 012077 (2022).

[237] P. Glaister, "85.13 Least Squares Revisited", The Mathematical Gazette **85**, 104 (2001).

[238] J. F. Ziegler, "The Stopping and Range of Ions in Matter", http://www.srim.org/, Accessed: 05/02/2024.

[239] P. Hovongton and D. Drouin, "The Stopping and Range of Electrons in Matter", http://www.srim.org/SREM.htm, Accessed: 05/02/2024.

[240] M. S. Dixit et al., "Position Sensing from Charge Dispersion in Micro-pattern Gas Detectors With a Resistive Anode", Nuclear Instruments and Methods in Physics Research A **518**, 721 (2004).

[241] M. S. Dixit and A. Rankin, "Simulating the Charge Dispersion Phenomena in Micro Pattern Gas Detectors with a Resistive Anode", Nuclear Instruments and Methods in Physics Research A **566**, 281 (2006).

[242] D. Attie et al., "Characterization of Resistive Micromegas Detectors for the Upgrade of the T2K Near Detector Time Projection Chambers", Nuclear Instruments and Methods in Physics Research A **1025**, 166109 (2022).

[243] L. Ambrosi et al., "Characterization of Charge Spreading and Gain of Encapsulated Resistive Micromegas Detectors for the Upgrade of the T2K Near Detector Time Projection Chambers", Nuclear Instruments and Methods in Physics Research A **1056**, 168534 (2023).

[244] P. Fonte et al., "A Spark-protected High-rate Detector", Nuclear Instruments and Methods in Physics Research A **431**, 154 (1999).

[245] I. Giomataris, "High Rate Applications of Micromegas and Prospects", arXiv: 0610153 (2006).

[246] T. Alexopoulos et al., "A Spark-resistant Bulk-micromegas Chamber for High-rate Applications", Nuclear Instruments and Methods in Physics Research A **640**, 110 (2011).

[247] "SRS Technology", https://www.srstechnology.ch/, Accessed: 04/09/2024.

[248] P. M. Lewis et al., "Absolute Position Measurement in a Gas Time Projection Chamber via Transverse Diffusion of Drift Charge", Nuclear Instruments and Methods in Physics Research A **789**, 81 (2015).

[249] S. E. Vahsen et al., "3-D Tracking in a Miniature Time Projection Chamber", Nuclear Instrumentation and Methods in Physics Research A **788**, 95 (2015).

[250] D. Pfeiffer, "vmmsc", https://gitlab.cern.ch/rd51-slow-control/vmmsc, 2024.

[251] B. Ketzer et al., "Triple GEM Tracking Detectors for COMPASS", IEEE Transactions on Nuclear Science **49**, 2403 (2002).

[252] R. N. Patra et al., "Measurement of Basic Characteristics and Gain Uniformity of a Triple GEM Detector", Nuclear Instruments and Methods in Physics Research A **862**, 25 (2017).

[253] S. Bazylev et al., "Study of the GEM Detector Performance in BM@N Experiment", EPJ Web of Conferences **177**, 04004 (2018).

[254] S. Chatterjee et al., "Study of Uniformity of Characteristics Over the Surface for Triple GEM Detector", Nuclear Instruments and Methods in Physics Research A **936**, 491 (2019).

[255] M. Baruzzo et al., "Direct Measurements of the Properties of Thick-GEM Reflective Photocathodes", Nuclear Instruments and Methods in Physics Research A **972**, 164099 (2020).

[256] W. Jia et al., "Gap Uniformity Study of a Resistive Micromegas for the Multi-purpose Time Projection Chamber (MTPC) at Back-n White Neutron Source", Nuclear Instruments and Methods in Physics Research A **1039**, 167157 (2022).

[257] V. Kumar et al., "A Novel Technique for Measuring Position Resolution of Gas Electron Multipliers (GEM)", Nuclear Instruments and Methods in Physics Research A **1058**, 168836 (2024).

[258] L. Scharenberg, "S-curve Noise Measurements with VMM3a/SRS", Presented at RD51 Mini Week, CERN, 2021.

[259] L. Scharenberg, "VMM3a/SRS Software Installation and Operation Overview", https://indico.cern.ch/event/1071632/contributions/4615369/attachments/2345888/4000941/VMM-SRS-SoftwareInstallation-Scharenberg.mp4.

[260] D. Pfeiffer, "vmm-sdat", https://github.com/ess-dmsc/vmm-sdat, 2023.

[261] V. Polychronakos et al., "ATLAS NSW Electronics Specifications Component: VMM3a", https://drive.google.com/drive/folders/1e0sFGAI4nTdauhI0-tgycQtn7mPvzLOI, 2018.

[262] H. Muller, "VMM Hybrid Assembly Cooling, Cabling, Programming, Powering, Test", https://drive.google.com/drive/folders/1WtmT-qbRNbRY_SGfcOCGpSkIDEZzYN27, 2022.

[263] M. Saidi and R. H. Abardeh, "Air Pressure Dependence of Natural-Convection Heat Transfer", Proceedings of the World Congress on Engineering **2** (2010).

[264] R. Guida et al., "Effects of Gas Mixture Quality on GEM Detectors Operation", Journal of Physics: Conference Series **1498**, 012036 (2020).

[265] H. Fribert et al., "Studying the Impact of Humidity on the Performance of THGEMs", Journal of Instrumentation **18**, C06015 (2023).

[266] S. Chatterjee et al., "Effect of Relative Humidity on the Long-term Operation of a Single Mask Triple GEM Chamber", Nuclear Instrumentation and Methods in Physics Research A **1046**, 167747 (2023).

[267] M. L. Huber and A. H. Harvey, "Thermal Conductivity of Gases", https://www.nist.gov/publications/thermal-conductivity-gases, 2011.

[268] B. H. Thang et al., "Application of Multiwall Carbon Nanotubes for Thermal Dissipation in a Micro-processor ", Journal of Physics: Conference Series **187**, 012051 (2009).

[269] L. G. Christophorou et al., "Electron Interactions with $CF_4$", Journal of Physical and Chemical Reference Data **25**, 1341 (1996).

[270] P. J. Linstrom and W. G. Mallard, "The NIST Chemistry Webbook: a Chemical Data Resource on the Internet", Journal of Chemical & Engineering Data **46**, 1059 (2001).

[271] A. C. Ezeribe et al., "Demonstration of Radon Removal from $SF_6$ using Molecular Sieves", Journal of Instrumentation **12**, P09025 (2017).

[272] R. R. M. Gregorio et al., "Test of Low Radioactive Molecular Sieves for Radon Filtration in $SF_6$ Gas-based Rare-event Physics Experiments", Journal of Instrumentation **16**, P06024 (2021).

[273] R. R. M. Gregorio et al., "Molecular Sieve Vacuum Swing Adsorption Purification and Radon Reduction System for Gaseous Dark Matter and Rare-event Detectors", Journal of Instrumentation **19**, P03012 (2024).